THE UNIVERSITY OF HULL

"High Pulse Repetition Frequency XeCl Laser and its Applications"

being a Thesis submitted for the Degree of
Doctor of Philosophy
in the University of Hull

by

Gary J. Bishop, B.Sc., Dip. App. Phys. (Hull), M.Sc. (Essex)

September 1990

Abstract of the Thesis Submitted for the Ph.D Degree in Applied Physics

by

Gary J. Bishop, B.Sc., Dip. App. Phys. (Hull), M.Sc. (Essex)

on

"High Pulse Repetition Frequency XeCl Laser and Its Applications"

This thesis discusses the development, characterisation and evaluation of a compact, medium power, XeCl laser operating at pulse repetition frequencies (prf) >1kHz. The use of this laser to cut polymer films by ablative etching is also presented.

The device uses a closed-cycle gas flow loop, constructed from stainless-steel for corrosive gas compatibility, and a total volume of 6 litres and a working pressure of 4 atmospheres. A magnetically coupled, tangential fan provides the gas flow and, with appropriate flow shaping into the $0.8\text{x}1.5\text{x}22.0\text{cm}^{-3}$ discharge region, produces a maximum flow velocity of 40m.s^{-1}. Electrical excitation is provided by a conventional, thyratron switched, capacitor discharge circuit, coupled with an internal, capacitively loaded, uv spark preionisation scheme, resulting in a rapid energy deposition into the discharge.

Investigations of the effects of discharge perturbations on the maximum repetition rate capability of this laser, indicate that repetition rates up to 1800Hz should be feasible. In operation, the laser has proven to be capable of 16W at 1kHz, and 22W at 700Hz, with a 10nF charging capacitor. Qualitative studies of the effect of resonator configuration on the beam profile, have shown that the use of folded cavities will produce more uniform beam profiles.

Experiments have been carried out, using this laser, to cut thin polyethylene teraphthalate (PET) film at rates up to 1.3m.s^{-1}. The 8x15mm output beam from the laser, was brought to a 5.4mm long line-focus with a full width of 140µm. It is shown that the effective etch rate, and corresponding cutting efficiency, is markedly dependent on prf due, it is thought, to cummulative heating.

This thesis is dedicated to
my wife, Margaret, and
my parents, Eileen and John.

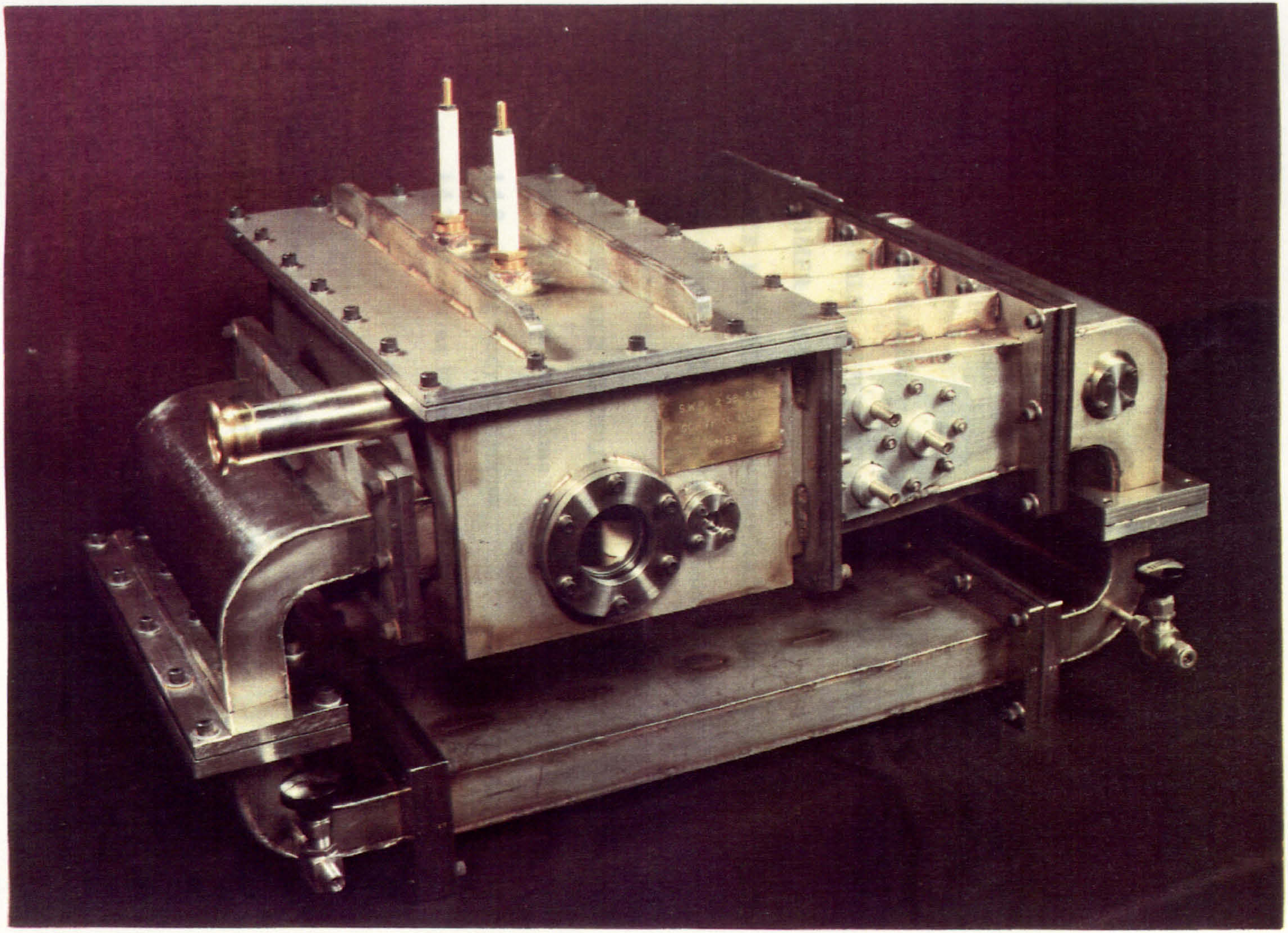

HIGH PULSE REPETITION FREQUENCY XeCl LASER AND ITS APPLICATIONS

CONTENTS

PAGE

ACKNOWLEDGEMENTS

I wish to express my appreciation to my supervisor, Professor Peter E. Dyer, for his guidance and support throughout this work, and to Dr. Douglas J. James who guided my writing of this thesis in Canada.

I should also like to give a special mention to Messrs. Brian L. Tait and Paul Monk who provided technical support: without them a lot of what took place may never have happened.

I should like to thank Harold Pashby, Eric Norman and John Metheringham (heads of the Applied Physics and Physics mechanical workshops, and the Applied Physics Electronics workshop respectively) and their staff. Special thanks goes to Tom Cherry and Robin Murray whose attention to detail in the production of the finished laser head enabled all the parts to fit together easily.

I would like to thank Dr. Christopher A. Hill, whose unflagging ability to keep nagging me to finish, from all corners of the globe, has finally paid off.

Finally, I have to give a big thankyou to my wife, Margaret, for her support throughout this endeavour, and for her patience in proof reading this manuscript.

FOREWORD

The experimental work reported in this thesis was carried out between the dates:

October 1981 → April 1985

The goal of the work described in this thesis was to design and develop a compact excimer laser, capable of operation at pulse repetition frequencies in excess of 1000Hz, and producing an output power of 10W at 1kHz. It will be shown that powers in excess of 15W at 1kHz, and 20W at 700Hz, were achieved. Applications for such a device could be far reaching, and some preliminary investigations into its applicability will be presented.

The first chapter provides an overview of the excimer laser field, with particular reference to the development of high repetition rate (hrr) devices. A brief introduction is made to the complexities of an excimer discharge, and the difficulties that must be overcome to produce a stable excimer discharge.

The second chapter outlines the design and evaluation of the flow system for this laser device, and also the external electrical drive circuit. Measurements made on the finished wind tunnel are also presented, including details of modifications made to the ductwork to optimise the flow of gas through the discharge region. Experiments comparing thyratron switch technology, suitable for high repetition rate operation, with that of spark-gap operation is discussed. Finally, there is a description of the external pulse power circuitry, with particular reference to obtaining the low inductance necessary to produce discharges suitable for laser excitation.

Chapter three deals with the optimisation of the internal laser discharge circuit. Results of the gas mixture optimisation, carried out at both low and high repetition rates, are described. In addition, preliminary investigations of methods to prolong the gas lifetime are presented, including the use of an electrostatic precipitator which gave a four-fold increase in lifetime. Various methods of preionisation are reported, and their ability to improve pulse energy, and to sustain this at high repetition rates, is evaluated. These include capacitively loaded and resistively ballasted uv sparks, corona and axial x-ray preionisation techniques.

The fourth chapter is primarily concerned with high pulse repetition frequency operation. A brief explanation is made of instabilities introduced by the expanding, heated, gas slug caused by the discharge. A simple experimental arrangement is described that was used to monitor the effect of the disturbance on the "clearing ratio" of the laser. Further investigations of gas lifetime are presented involving hydrogen, in small quantities, added to the discharge. Finally, operation of the laser at high pulse repetition frequencies is reported for both XeCl (308nm) and CO_2 (10.6μm) operation. In each case optimisation of the operating parameters, including the resonator configuration, is discussed.

The potential use of a high repetition rate laser in various applications is discussed in chapter five. An experimental investigation of cutting thin polymeric films (Melinex®) using a line focussed beam from the XeCl laser at high repetition rates is described. High cut rates are attained for thin films (~$1.2 m.s^{-1}$) using ablative etching, although beyond ~100Hz thermal effects became increasingly apparent.

Chapter six provides a review of the work conducted. Suggestions for improvements, and modifications to laser, and future experiments that could be carried out are discussed, including a brief review of where this laser stands today with respect to the continuing research efforts, and commercially available high pulse repetition frequency devices. Finally, the main conclusions that can be drawn from the studies are described.

1. EXCIMER LASERS

1.1 AN HISTORICAL OVERVIEW

In 1930 Hopfield [1.1], using a disruptive discharge, detected a strong emission continuum in the region 50 to 112.5nm which was attributed to the $He_2[^1\Sigma_u^+]$ to $He_2[^1\Sigma_g^+]$ transition. This broadband emission was later explained by Mrozowski [1.2] in terms of the transition from a bound excited state to a repulsive ground state (apart from some weak Van der Waals binding) (Fig. 1.1). Later in 1954, Tanaka and Zelikoff discovered the Xenon (147 → 220 nm) [1.3] and Krypton (123.6 → 133 nm) [1.4] continua using a microwave discharge. Tanaka closely followed these discoveries with that of the argon continuum [1.5] using, this time, a disruptive discharge. This later work also produced results more closely analogous to that of Hopfield.

In 1960, at the same time as Maiman invented the first optical maser, Houtermans [1.6] pointed out that the repulsive nature of the ground states coupled with the excited bound state would allow a population inversion to be very easily achieved. It was also at this time, that the term excimer was introduced to describe a bound excited state dimer which readily dissociates in its ground state.

More than a decade passed before Basov *et al* [1.7] detected the first laser emission from electron-beam pumped cryogenic liquid Xenon (176 nm) in 1971. A year later, the first gas-phase excimer laser was demonstrated by Koehler *et al* [1.8] using Xenon (172 nm) at several atmospheres pressure. Other rare-gas excimer lasers based on high pressure Krypton (146 nm) and Argon (126 nm) were soon demonstrated by Hoff *et al* [1.9] and Hughes *et al* [1.10] respectively. Much to the disappointment of the researchers at that time, it

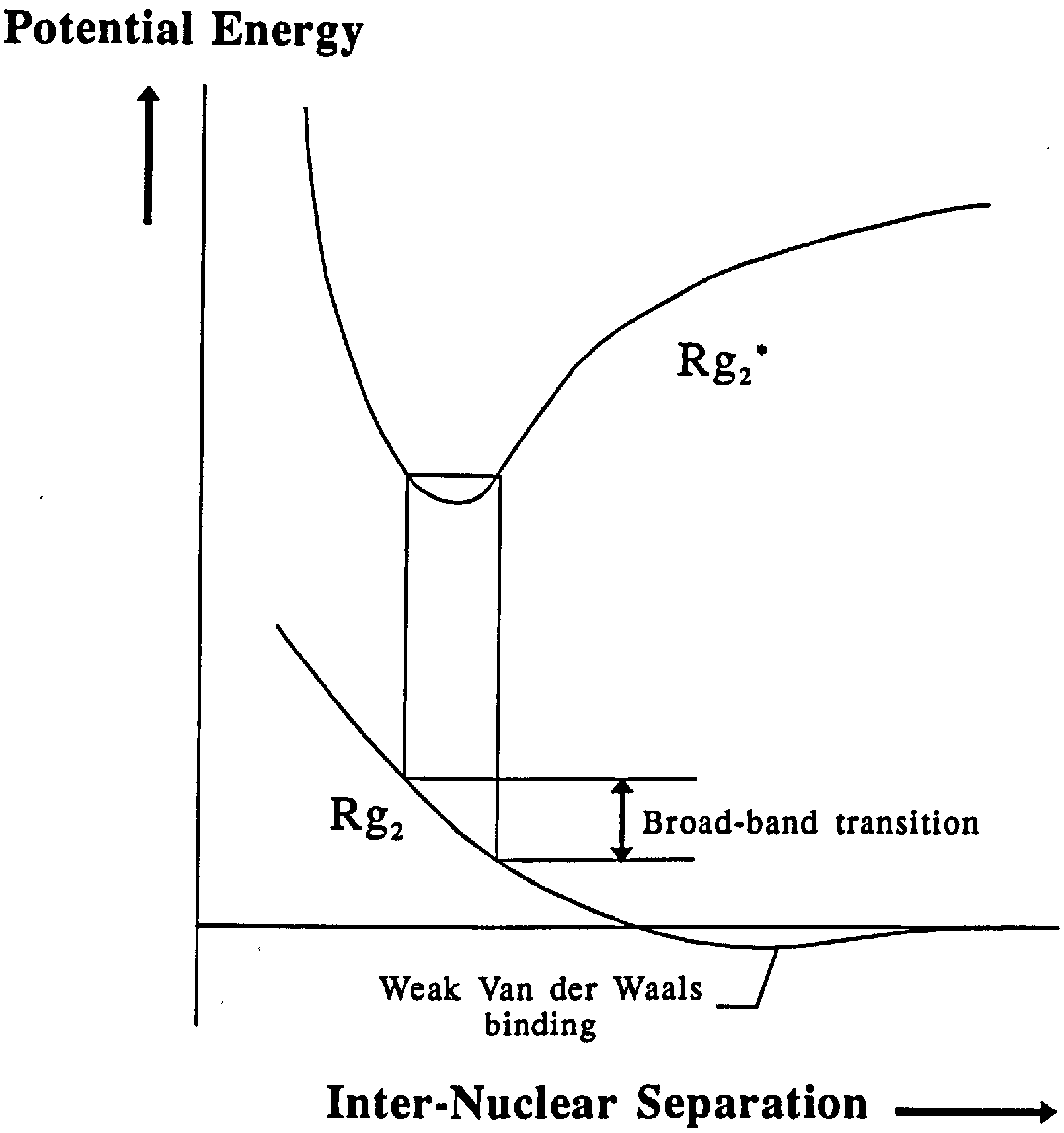

Fig. 1.1 Potential energy curves for a typical excimer molecule

was found that the overall laser efficiencies were rather low even though the rare-gas excimers have high fluorescence efficiencies. An explanation of this was given by Werner *et al* [1.11] using a model in which they predicted that excited state absorption would limit the laser efficiency.

The discovery of the rare-gas excimer laser, and the coincident development of electron-beam devices capable of producing them with high efficiency, soon led to the quest for new excimer media. Golde and Thrush in 1974 [1.12] made the first major breakthrough in this quest with the discovery of the ArCl (167 → 178 nm) exciplex† continuum. In the same year Powell *et al* [1.13] produced lasing from the XeO (540 nm) and KrO (558 nm) exciplexes by electron-beam pumping of rare-gases containing oxygen-bearing impurities at high pressures. Lasing from ArO (558 nm) was reported soon after [1.14]. Probably the greatest step taken in the excimer laser field since its discovery, was that made by Searles and Hart in 1975 [1.15] when they reported laser emission from XeBr (282 nm) the first rare-gas halide (RGH) laser. Since this point, rapid progress has been made in the development of this new class of excimer laser such that several diatomic and triatomic RGH species have been made to lase (Table 1.1).

The development and understanding of the RGH lasers with e-beam pumping has subsequently led to the utilisation of avalanche discharge pumped excimers, similar in configuration to those used in pulsed TE CO_2 laser devices. The first attempt at this was made by Burnham *et al* [1.16] and

---

† EXCIPLEX - this is the name given to describe ***exc****it*ed com***plex****es* and although technically more correct the trend is to use the term 'excimer' to describe this class of laser.

Wavelength (nm)	Species	Wavelength (nm)	Species
126	Ar_2^*	351	XeF^*
146	Kr_2^*	430	Kr_2F^*
172	Xe_2^*	485	XeF^* (C→A)
175	$ArCl^*$	502	$HgBr^*$
193	ArF^*	520	Xe_2Cl^*
222	$KrCl^*$	540	XeO^*
249	KrF^*	558	ArO^*
282	$XeBr^*$	558	KrO^*
308	$XeCl^*$	558	$HgCl^*$

Table 1.1 Wavelength of Excimer Lasers Transitions

Wang *et al* [1.17] in 1976, using a configuration similar to that used for nitrogen lasers, with operation limited to less than atmospheric pressures due to no preionisation being employed. Burnham *et al* [1.18] soon followed these results using uv-preionisation with working pressures up to three atmospheres.

During the period from the early seventies to the present day, several reviews have been made on excimer lasers [1.19 → 1.25] plus one on rare-gas avalanche discharge lasers [1.26].

1.2 HIGH PULSE-REPETITION-FREQUENCY (PRF) EXCIMER LASERS

The quest for a high average power, high prf excimer device in the mid-seventies took full advantage of an already existing CO_2 laser technology of the same nature.

One of the first of these studies was reported by Wang in 1978 [1.27], for which a fast transverse flow and rapidly pulsed, fast, electric discharge was used. This system incorporated a thyratron, in place of a low inductance spark-gap switch, for high prf and long life operation. The problem of gas recirculation and cooling was overcome in this device by operating the system in a burst mode configuration, achieved by discharging a high pressure supply tank into a low pressure dump tank, with nozzles controlling the pressure and velocity into the laser cavity. This experiment achieved a repetition rate of 500 Hz, 3 mJ/pulse, and an average power of 1.5 W with the device operating with XeF at a pressure of 0.85 atmospheres with a flow velocity across the discharge of $14 m.s^{-1}$.

Wang followed up his prediction of multi-kilohertz operation [1.27] with a demonstration of 2kHz laser operation [1.28]. Using the same "blow-down" arrangement as before, but with an increased flow velocity of 25m.s^{-1} between the electrodes 2kHz, 12mJ/pulse operation of XeF was achieved giving an average power of 24W. In 1979, Tulip *et al* [1.28] reported a closed-cycle RGH discharge with a maximum prf of 900Hz. Here the discharge circuit was of the Blumlein type, constructed from a coaxial cable which was pulse charged from a high prf Marx bank generator and switched from a high prf segmented rail-gap incorporating a thyratron switch. Gas flow, at 2.0 atmospheres pressure, was produced by a radial blower after which a converging section brought the velocity across the electrodes up to 110m.s^{-1}.

In the same year, a miniature high prf RGH laser was reported by Sze and Scott [1.29] where 1.25kHz operation was achieved with KrF and 850Hz with XeCl. Since that time, other groups have reported the construction of high prf devices [1.30→1.37]. Of these, Fahlen [1.31] has reported the highest average power of 210W at 1kHz with a uv-preionised discharge and Butcher *et al* [1.34] 200W at 500Hz for a device using transverse x-ray preionisation.

1.3 LASER KINETICS - AN INTRODUCTION

Gas lasers, depending on the nature of their active medium, can be divided into three main catagories: atomic, ionic and molecular. This class of laser is usually pumped by means of an electric discharge achieved by applying an electric field between a pair of electrodes. Electrons in this discharge are accelerated by the field such that they collide with the atoms, ions or molecules, and induce transitions to higher energy states. With suitable transitions and sufficient pump power density, a population inversion is achieved.

Of interest here is that class of gas laser known as the molecular laser and in particular excimer lasers operating in the uv region of the spectrum. The excimer laser is one of two main pulsed gaseous media operating in the uv, the other being the nitrogen laser (337.1nm) where transitions occur between bound electronic excited states.

There is also considerable interest in long-pulse and continuous wave (cw) operation of such devices in the uv, but before this can be achieved the following criteria must be satisfied:

(i) the upper state of the lasing transition must be long-lived,

(ii) the lower state must be rapidly depopulated.

The problem with the nitrogen system is that the upper-state lifetime is very short (5ns) and the lower-state lifetime is approximately three orders of magnitude longer. The consequence of this is that as the number of atoms in the lower state increases the stimulated output is re-absorbed causing a loss that increases with time. This eventually results in the self-termination of laser action in a time comparable to that of the lifetime of the upper state.

For practical purposes, the design of uv lasers for cw and pulsed operation requires an efficient energy storage medium. It has been shown that the excited states of the nitrogen molecule are so short lived that they cannot serve as efficient stores of energy. The concept, put forward by Houtermans [1.6], for transitions between excited bound and repulsive ground states for possible laser action has been shown to provide an efficient store of energy. However, the short radiative lifetimes of most excimers and the build-up of absorbing species tends to prevent a nett gain being achieved for long-pulse and continuous wave operation.

1.3.1 Excimer Gain Coefficient and Saturation Intensity [1.21]

For simplicity, take the case of an ideal excimer where Frank-Condon transitions from the lowest vibrational level of the first excited state terminate high on the dissociative lower level (Fig. 1.1). Here, the possibility of reabsorption is unlikely and hence this lower level can be neglected.

This simplifies the rate equations such that there are now two variables, the excimer number density, N, and the photon density, ρ. Thus for a beam of light which is amplified in the medium, whilst travelling in the x-direction, the rate equations are,

$$\frac{dN}{dt} = R - \frac{N}{\tau} - \sigma c \rho N \qquad \text{. . . (1.1)}$$

$$\frac{d\rho}{dt} = \frac{\partial \rho}{\partial t} + c\frac{\partial \rho}{\partial x} = \sigma c \rho N \qquad \text{. . . (1.2)}$$

where R is the pump rate into the upper level, τ is the lifetime of the upper level, σ is the average stimulated emission cross-section, c is the velocity of light, and $\sigma c \rho N$ is the rate of stimulated emission per unit volume.

Defining the irradiance as $I = hc\nu\rho$, where h is Plancks constant and ν is the transition frequency, then gives from Eqs. (1.1) and (1.2) in the steady state:

$$\frac{\partial I}{\partial x} = \frac{\alpha_0 I}{1 + \frac{I}{I_s}} \qquad \text{. . . (1.3)}$$

Here, $\alpha_0 = R\sigma\tau$ is the small signal gain coefficient and $I_S = \frac{h\nu}{\sigma\tau}$ is the saturation intensity.

For the small signal case, $I \ll I_S$, (1.3) becomes,

$$I_{OUT} = I_{IN}\, e^{(\alpha_0 l)} \qquad \ldots (1.4)$$

and for the large signal case, $I \gg I_S$,

$$I_{OUT} = I_{IN} + \alpha_0 I_S l \qquad \ldots (1.5)$$

where l is the length of the amplifying medium.

These solutions are shown graphically in Fig. 1.2. Since bound-free transitions have a wide bandwidth, σ is small, as is the lifetime τ for most excimers; this leads to a low value for the product $\sigma\tau$ is which implies that the saturation intensity for such devices is very high. Another implication of this is that excimer lasers are inherently high power devices capable of achieving gain up to high intensities. However, it can be shown that the pump rate, R, required to attain a useful gain needs to be very large since $\alpha_0 = R\sigma\tau$. For example, using appropriate values for the XeCl laser at 308 nm of $\sigma = 4.5\times10^{-16}$cm, $\tau = 11\times10^{-9}$s, and a gain coefficient of $\alpha_0 = 0.1\text{cm}^{-1}$, gives

$$I_S = \frac{h\nu}{\sigma\tau} \approx 130\text{kW.cm}^{-2}$$

and

$$R = \frac{\alpha_0}{\sigma\tau} \approx 2 \times 10^{22}\text{cm}^{-3}.\text{s}^{-1}$$

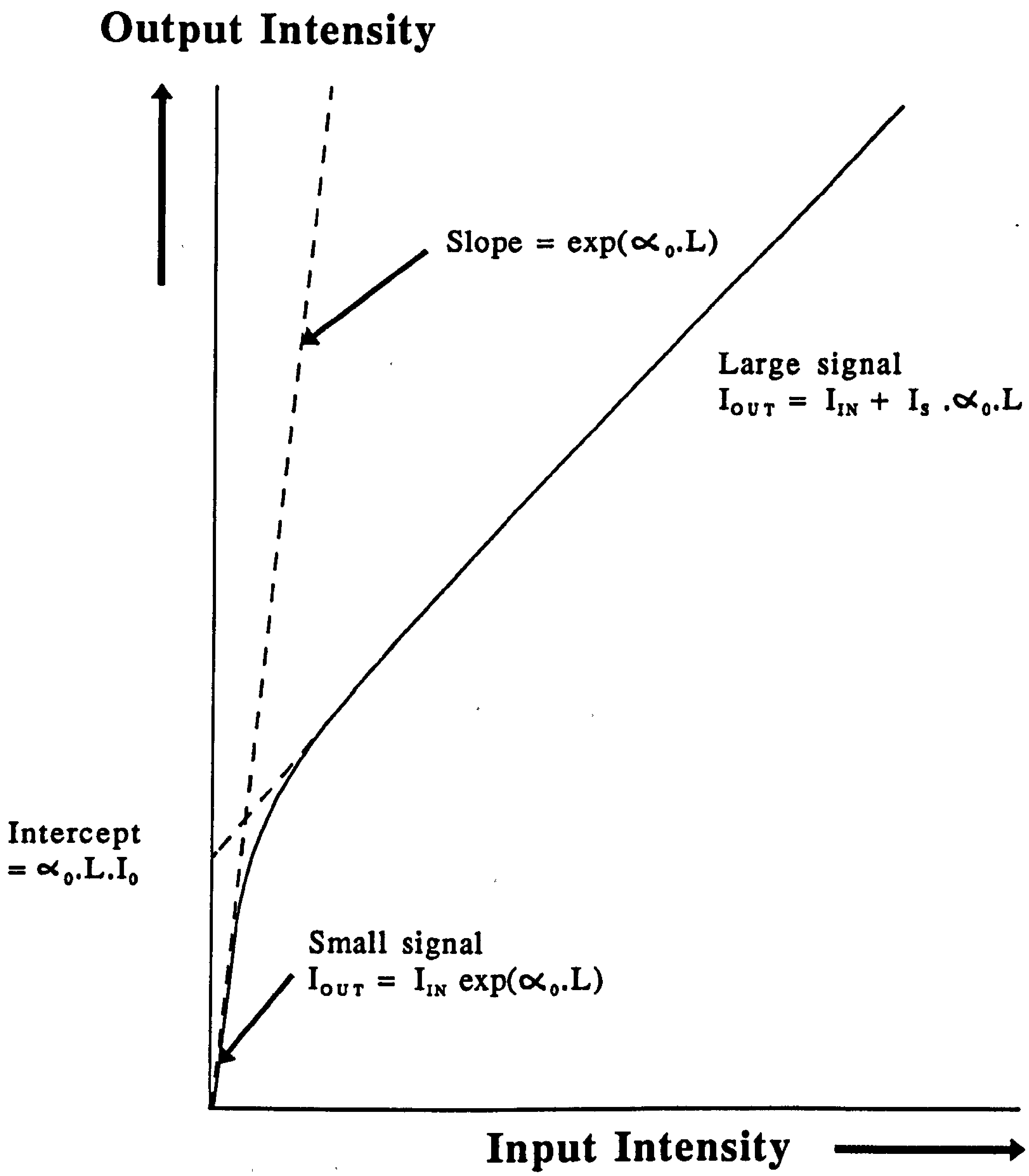

Fig. 1.2 Output intensity as a function of input intensity for a laser amplifier showing both small and large signal characteristics

The minimum pump power density required to attain this level of gain is therefore

$$Rh\nu \approx 13kW.cm^{-3}$$

indicating that high power excitation is required for practical devices. (Although operation at lower gain is possible, the pump power density must be sufficiently large to overcome background absorption, mirror losses, and allow the output pulse to be obtained prior to medium degradation due to arcs or absorption loss.)

1.4 EXCIMER AND EXIPLEX LASERS

The formation of excimer/exciplex molecules fall into two catagories:

(i) ionic channels

(ii) metastable channels

both of which involve the excited and the neutral gas atoms.

1.4.1 Chemical Reactions

Take the case of the excited rare gas atom reacting with the halogen containing donor molecule. The nature of this reaction is closely analogous to that of an alkali and halogen molecule where a "harpooning" reaction is observed. The ionic terms come about when the particle separation is still large, but the interaction in the initial channel is still relatively small. The excited atom "transfers" its electron to the halogen containing molecule, thereby creating a Coulombic interaction between the particles (hence the term "harpooning"). The Coulombic interaction brings the particles closer together such that the system can make a transition into an electronic term.

Since this transition leads to a restructuring of the molecule, the distance at which this transition takes place has to be comparable to the particle dimensions.

The important parameter in this process is the critical distance between the nuclei, r_c, at which the electronic terms of the system A^*-RX and A^+-RX^- intersect (where A is the rare gas atom and X the halogen atom). Assuming that r_c greatly exceeds the dimensions of the colliding particles, and that the last interaction is a purely Coulombic one then, in atomic units,

$$r_c = (J - EA)^{-1} \qquad \ldots (1.6)$$

where J is the ionisation potential of atom A^*, and EA the binding energy of the electron in the RX^- ion.

The electronic terms split due to exchange interaction and, if this splitting is relatively large while the collision velocity is low, then the system remains in the lower term. In this case, the colliding particles approach each other to distances of the order of their dimensions and hence a chemical reaction can occur.

1.4.2 Three-body Collisions

The other excimer formation process involves three-body collisions of excited atoms of the form

$$A^* + B^* + C \rightarrow AB^* + C \qquad \ldots (1.7)$$

The third particle C plays a fundamental role in that it takes up the excess energy and momentum produced from the interaction of particles A and B. If, after such a three-bodied collisional process, the energy transferred to C exceeds the kinetic energy of the particles A and B, then A and B remain bound. The three-body process just described is the only means of forming excimer molecules if the two-body process is forbidden [1.38]. At higher gas densities, it is possible for the three-body process to dominate the two-body process even if the latter is allowed.

1.4.3 Rare-gas mono-halide spectroscopy

Since the discovery of the first rare-gas mono-halide laser [1.15], the attention shown to such devices has made them the most highly developed of the excimer species. The reason for this is that, at present, they offer the highest efficiences and output pulse energies.

The emission spectrum of rare-gas mono-halide exciplex molecules is explained in terms of the energy level diagram shown in Fig. 1.3. Here, the ground state concerns a ground state rare-gas atom, Rg, and a ground state neutral halide atom, X. $^2\Sigma_g$ and $^2\Pi_g$ molecular states are formed which are chemically unstable except for the potential energy minimum which is due to Van der Waals binding. This well-depth is found to increase with increasing atomic number.

The higher molecular states with electronically excited atoms ($Rg+X^*$ and Rg^*+X) are similar to the ground state in that they are essentially repulsive and have only a shallow mimium due to Van der Waals binding. The lowest excited state of the rare-gas halide, RgX^*, will be an ionic state of fairly large binding energy at infinite separation, $Rg^+ + X^-$, and is usually some 10eV

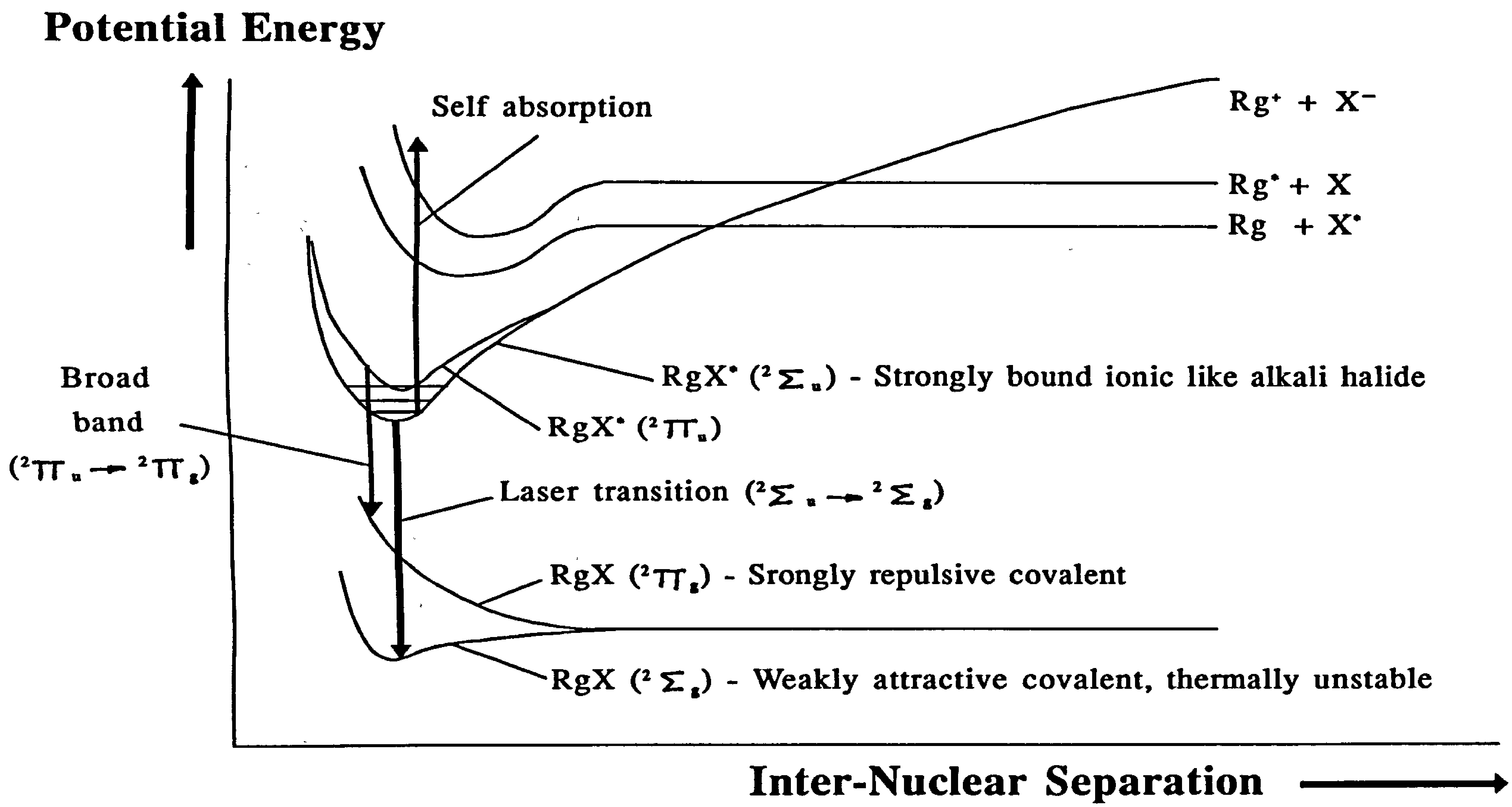

Fig. 1.3 Schematic potential energy diagram, illustrating the electronic structure of the rare-gas mono-halides

greater than that of many electronically excited states of the atom. Therefore, this ionic curve will cross excited covalent curves, as shown, providing a route for the population of the RgX^* state from an electronically excited meta-stable rare-gas atom Rg^*. The $Rg^+ + X^-$ ion pair in fact has associated with it two RgX^* molecular terms given by $^2\Sigma_u$ and $^2\Pi_u$ which are usually referred to as the B- and C-states respectively. In the pressure ranges usually employed in such devices, the vibrational ground state of B is mainly populated. As stated previously the Frank-Condon transitions are favoured and hence emission spectra are usually due to the B→X ($^2\Sigma_u \rightarrow {}^2\Sigma_g$) transition. Typical formation reactions are given by,

$$Xe^* \text{ (meta-stable)} + HCl \rightarrow XeCl^* + H$$

and

$$Xe^+ \text{ (ion)} + Cl^- + M \rightarrow XeCl^* + M$$

where M is the buffer gas required to conserve both the momentum and energy of the reacting partners.

Atomic absorption by X or Rg, by the B-state, by atomic metastables and by other molecules such as rare-gas di-halides result in parasitic absorptions and can seriously handicap power scaling. It could also be a restriction in the development of other excimer laser species.

REFERENCES

[1.1] J.J.HOPFIELD, Phys. Rev., **35**, 1133 (1930a) Phys. Rev., **36**, 784 (1930b)

[1.2] S.MROZOWSKI, Z. Phys., **76**, 38 (1932)

[1.3] Y.TANAKA & M.ZELIKOFF, Phys. Rev., **93**, 933 (1954)

[1.4] Y.TANAKA & M.ZELIKOFF, J. Opt. Soc. Am., **45**, 254 (1954)

[1.5] Y.TANAKA, J. Opt. Soc. Am., **45**, 710 (1955)

[1.6] F.G.HOUTERMANS, Helv. Phys. Acta, **33**, 933 (1960)

[1.7] N.G.BASOV, V.A.DANILYCHEV & Yu.M.POPOV, Sov. J. Quant. Elec., **1**, 18 (1971)

[1.8] H.A.KOHLER, L.J.FERDERBER, D.L.REDHEAD & P.J.EBERT, Appl. Phys. Lett., **21**, 198 (1972)

[1.9] P.W.HOFF, J.C.SWINGLE & C.K.RHODES, Appl. Phys. Lett., **23**, 245 (1973)

[1.10] W.M.HUGHES, J.SHANNON & R.HUNTER, Appl. Phys. Lett., **24**, 488 (1974)

[1.11] C.W.WERNER, E.V.GEORGE, P.W.HOFF & C.K.RHODES, IEEE J. Quant. Elec., **13**, 769 (1977)

[1.12] M.F.GOLDE & B.A.THRUSH, Chem. Phys. Lett., **29**, 485 (1974)

[1.13] H.T.POWELL, J.T.MURRAY & C.K.RHODES, Appl. Phys. Lett., **25**, 730 (1974)

[1.14] W.M.HUGHES, N.T.OLSON & R. HUNTER, Appl. Phys. Lett., **28**, 81 (1976)

[1.15] S.K.SEARLES & G.A.HART, Appl. Phys. Lett., **27**, 243 (1975)

[1.16] R.BURNHAM, N.W.HARRIS & N.DJEU, Appl. Phys. Lett., **28**, 86 (1976)

[1.17] C.P.WANG, H.MIRRELS, D.G.SUTTON & S.N.SUCHARD, Appl. Phys. Lett., **28**, 326 (1976)

[1.18] R.BURNHAM, F.X.POWELL & N.DJEU, Appl. Phys. Lett., **29**, 30 (1976)

[1.19] C.K.RHODES, IEEE J. Quant. Elec., **10**, 153 (1974)

[1.20] A.V.ELETSKII, Sov. Phys. Usp., **21**, 502 (1978)

[1.21] M.J.SHAW, Prog. Quant. Elec., **6**, 3 (1979)

[1.22] M.H.R.HUTCHINSON, Appl. Phys., **21**, 95 (1980)

[1.23] T.J.McKEE, La Phys. Au Canada, **36**, 41 (1980)

[1.24] D.BASTING, EPA Newsletter, **64** (1980)

[1.25] I.S.LAKOBA & S.I.YAKOVLENKO, Sov. J. Quant. Elec., **10**, 389 (1980)

[1.26] R.C.SZE, IEEE J. Quant. Elec., **15**, 1338 (1979)

[1.27] C.P.WANG, Appl. Phys. Lett., **32**, 360 (1978)

[1.28] J.TULIP, H.SEGUIN & P.N.MACE, Rev. Sci. Inst., **50**, 1108 (1979)

[1.29] R.C.SZE & P.B.SCOTT, SPIE, **190**, 305 (1979)

[1.30] J.L.MILLAR, J.DICKIE, J.DAVIN, J.SWINGLE & T.KAN,
Appl. Phys. Lett., **35**, 912 (1979)

[1.31] T.S.FAHLEN, IEEE J. Quant. Elec., **16**, 1260 (1980)

[1.32] R.C.SZE & E.SEEGMILLER, IEEE J. Quant. Elec., **17**, 81 (1981)

[1.33] P.E.CASSADY, G.MULLANEY & S.R.BYRON, SPIE, **279**, 18 (1981)

[1.34] R.R.BUTCHER, R.A.TENNANT, G.F.ERIKSON, S.L.SWISHER
W.L.WILLIS, OSA, RENO, NEVADA (1983)

[1.35] V.Yu BARANOV, V.M.BORISOV, A.Yu VINOKHODOV, F.I.VYSIKAILO
& Yu B.KIRYUKHIN, Sov. J. Quant. Elec., **13**(3), 318 (1983)

[1.36] MATHEMATICAL SCIENCES NORTHWEST,
Private Communication (1983)

[1.37] M.L.SENTIS, B.L.FONTAINE & B.M.FORRESTIER,
5th GCL Symp., 233 (1984)

[1.38] B.M.SMIRNOV, Sov. Phys. Usp., **26**, 31 (1983)

2. LASER DESIGN AND CONSTRUCTION

In this thesis, the primary objective was to design develop and characterise a high prf excimer laser operating typically at >1 kHz. In any excimer laser, where long lifetimes are required, considerable attention must be given to the halogen compatibility of the system. In a high prf device employing closed-cycle gas recirculation, this must be extended to the ducting system. Gas life extension in a kHz laser is particularly necessary since 10^6 shots will be accumulated in approximately 17 minutes, a duration which is of limited value for practical applications of such a device. The aim is thus to keep contamination and halogen depletion to a minimum with the view to extending lifetime of such a device to $>10^7$ shots per gas fill.

2.1 MATERIALS SELECTION

A report by Tennant [2.1] outlines an investigation he has made of these corrosive excimer laser mixtures on various metals (Table 2.1). The evidence clearly points to nickel being the only metallic material that shows no appreciable deterioration except for the pitting of electrodes due to arcing. Stainless-steel shows promise when kept dry, but on exposure to the atmosphere shows signs of corrosion. This problem can be circumvented by nickel electroplating the stainless-steel. Corrosion arises because metallic chlorides, which are hygroscopic by nature, form on the laser parts, and when exposed to moisture from the atmosphere become wet and highly corrosive. Therefore materials must be chosen carefully.

Extensions to Tennants original work, by Tennant & Peterson [2.2], also showed that plastics and epoxies will form volatile chlorocarbon compounds which are absorbing at the laser wavelength. The use of fluorocarbon based

Laser Materials After 7.5 x 10^7 Pulses	
Copper	Coating flakes badly
Aluminium	Uniform white powder coating
Brass Electrodes	Zinc leaches out leaving a pitted copper surface
Stainless & Carbon Steels	Rusts after being exposed to air
Monel	Turns green after exposure to air
Nickel Electrodes	Shows little attack other than where arcs impinge

Table 2.1 [Ref. 2.1]

plastics helps since they are less reactive, but they still produce chlorocarbons. The reaction of fluoroplastics, such as Kynar and Teflon, or Viton-A for 'o'-rings, with both F_2 and HCl can be reduced by conditioning the device with F_2 or HCl for several days before use.

(N.B. Conditioning with fluorine is the preferred method since it helps form a much harder passivation layer on the metal surfaces; also the fluoride based compounds formed are less hygroscopic than their chloride counterparts. Another benefit of fluorine passivation mixtures is that can form a discharge. Hence, with low water flow and the discharge running, the discharge vessel becomes warm increasing the rate of out-gassing of unwanted contaminants from the various materials in the system. However, care must be taken when passivating with F_2 since this technique should only be used with less reactive materials; with some materials fluorine can lead to the production of more contaminants.)

Another material finding increasingly more use in the commercial excimer laser of today is high density, high purity alumina. This ceramic material is relatively inert to the highly reactive gases and has the added benefit of being a dielectric. Alumina is finding increasing use in areas of construction where the use of metals is prohibited (i.e. high voltage) and the material is also in contact with the laser gas mixture. The major disadvantage of alumina over fluorocarbon based plastics is cost. Not only is material expensive, but also the methods of manufacturing components can require tooling, thus putting this material out of reach of some potential research applications.

Conclusions drawn from these results, and those of other system designs [2.3 & 2.4], led to the laser body and recirculation system in the present work being made of stainless-steel with the option of nickel electroplating being applied. The electrodes were initially constructed from solid nickel and the supporting gantry of nickel-plated mild steel with PTFE supports, since these components are in close proximity to the hot reactive gases of the excimer discharge.

2.1.1 Materials Cleaning Procedure

Prior to final assembly this laser was de-greased to remove any residual cutting fluid, or other form of contaminant. Once degreased all the components were thoroughly washed down with ethanol.

The cleaning procedure followed religiously whenever the laser electrode gantry, or any other component in contact with the laser gas, was removed for modification was as follows:

(i) The laser vessel was kept open for the minimum amount of time by careful preparation beforehand, and closing the lid as soon as the component had been remove. Whilst the component was being remove a stream of helium was kept flowing out of the laser vessel to minimise ingress of moisture from the air.

(ii) The laser vessel was then evacuated, purged with helium, and left in a pressurised state whilst the modification took place.

(iii) The component that had been removed was then washed down with copious quantites of ethanol in a well ventilated area. The component(s) were then dried using a hair dryer and wrapped in tissue paper so as to minimise absorbtion of moisture by any residual metal chlorides.

2.2 FAN SELECTION AND TESTING

From reports on the development of high prf excimer lasers by various groups [2.4 → 2.7], it was concluded that, with careful design, 1kHz operation could be achieved with a minimum discharge clearing ratio of four. The clearing ratio, CR, is defined as:

$$CR = \frac{\text{Gas flow velocity at the electrodes} \times \text{Interpulse time}}{\text{Discharge width in the flow direction}}$$

This meant for a 1cm discharge width the gas flow velocity required was 40m.s^{-1}. This flow rate would be difficult to obtain by means of conventional small fans, but the use of a venturi contraction with a ratio of input-to-output area of four would bring this down to 10m.s^{-1} at the fan. Within the Molecular Gas Laser (M.G.L.) group at Hull, 4m.s^{-1} was previously the highest flow rate achieved with axial flow fans. Since the discharge cross-section is rectangular, the use of a tangential (or cross-flow) fan was chosen to provide the simplest method of gas movement bearing in mind the need to use non-contaminating bearings.

Fan rotation speeds of the order of 6000 rpm were required, and to produce this a Parvalux SD-1 ($^1/_6$hp) AC motor was used in conjunction with an aluminium Airwheel, 240mm long x 60mm diameter, tangential vortex fan. In initial testing of the fan and motor on the bench, it was found that considerable bowing of the rotor blades occured at revolution rates approaching 7000rpm. The blades of the fan were supported by struts at either end and in the middle, in essence being comprised of two 120mm sections (Fig. 2.1a)). To try and reduce the bowing, two loops of nickel-chromium wire were linked and tightened midway between each pair of struts. Bowing was considerably reduced, allowing the rotation rate to be

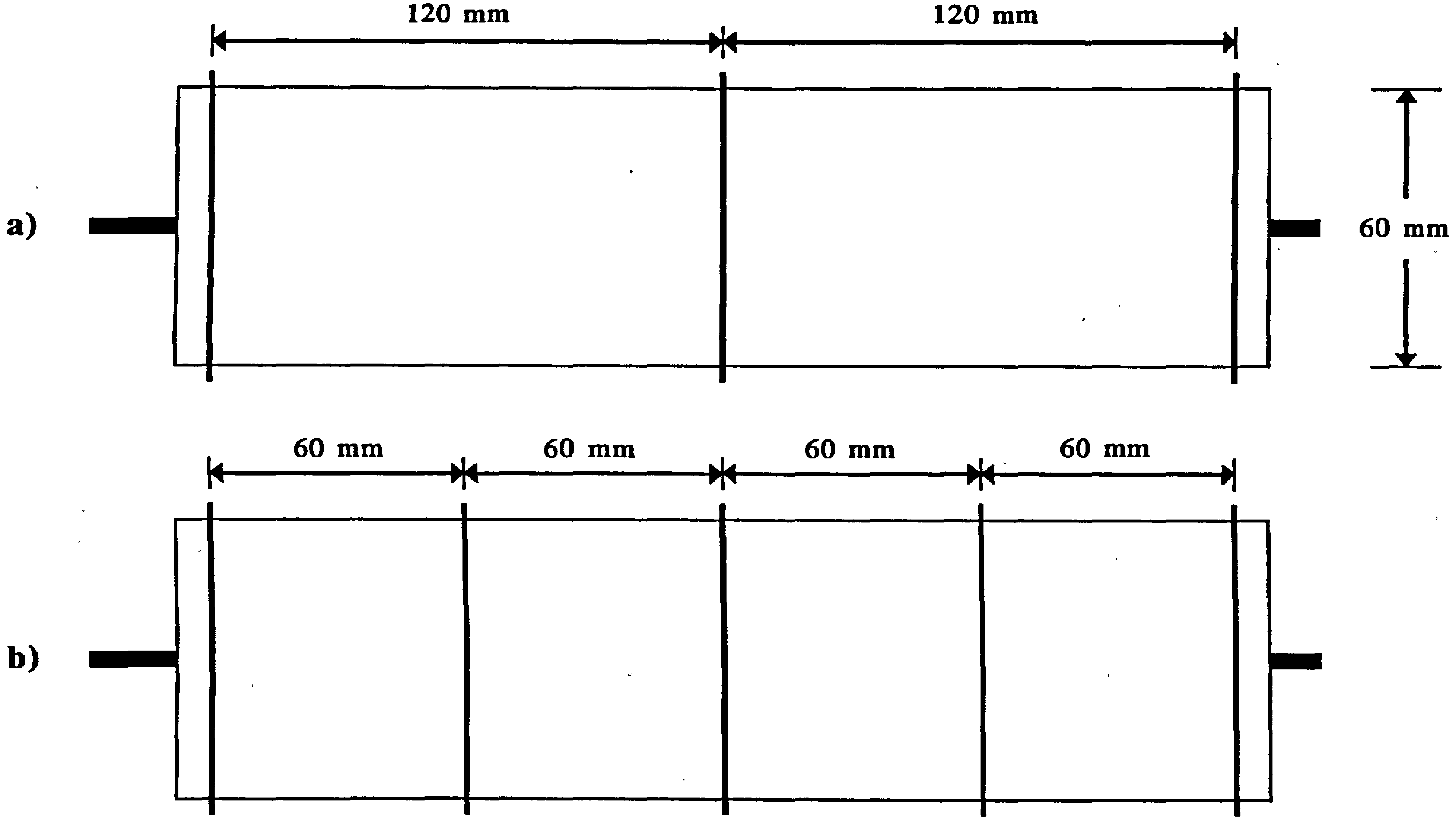

Fig. 2.1 Tangential cross-flow fan designs
a) prototype ; b) custom design

increased to greater than 8000rpm. Flow velocities were measured with a pitot-static tube attached to a micro-manometer and the corresponding rate of rotation with a stroboscope; the results of flow velocity versus rotation rate shown in Fig. 2.2 are for the fan operating in air at atmospheric pressure. This motor-fan combination was then operated for up to six hours a day, and for several days, over a period of weeks.

Custom built fans, of the same type but with struts replacing the wire loops (Fig. 2.1b)), were then purchased and tested. Results indicated that even less bowing occured than with the wire loops and that the structure was more rigid, which led to reduced noise and vibration.

2.3 SEALED FAN COUPLINGS

Previous use of tangential fans with magnetic couplings, within the M.G.L. group, had been restricted in speed of rotation due to motor-fan decoupling. This problem is futher complicated when a sealed-coupling is required between the shaft of the AC motor and the shaft of the tangential fan, through the wall of the duct.

2.3.1 Ferrofluidic Seals

Magnetic fluids [2.8] have the potential to solve difficult sealing problems. This is achieved by controlling the position of magnetic particles in a fluid by the application of a magnetic field. This type of seal is attractive as it can accomodate rotation without the introduction of contaminants or the escape of toxic gases. These seals can also be designed for high pressure and/or high speeds (~10,000rpm) operation.

Fig. 2.2 Air flow velocity as function of the fan rotation speed

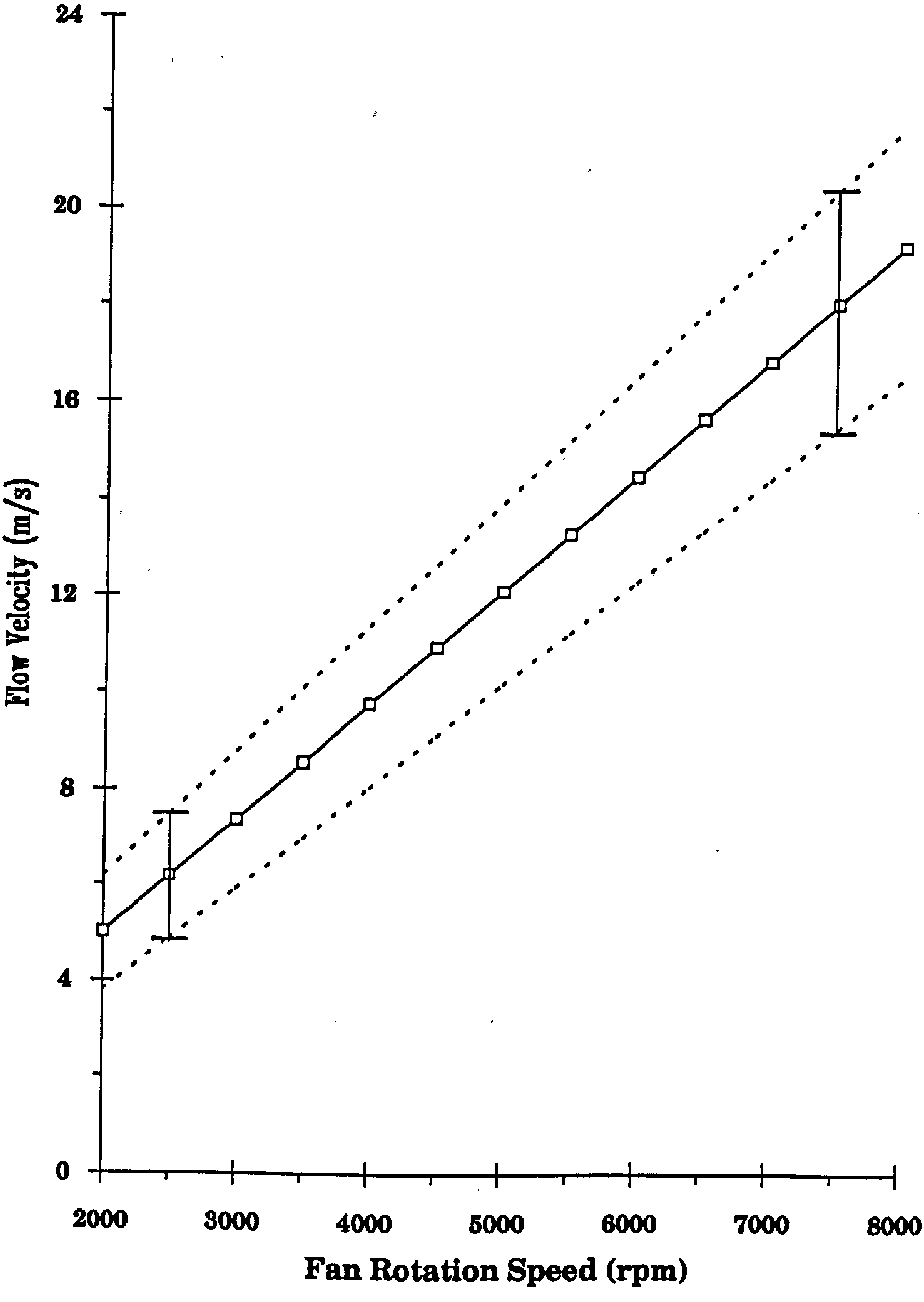

Ferrofluids consist of submicroscopic magnetic particles colloidally suspended in a carrier liquid which gives the fluid its magnetic properties. These particles are typically 10nm in diameter and are made from magnetic materials such as magnetite (Fe_3O_4). The stability of the suspension is maintained by coating the particles with a surface active agent (surfactant) resulting in their dispersion in the fluid. The application of a magnetic field orientates the suspended particles along the applied field gradient causing the transportation of the whole suspension by osmotic forces. The removal of the applied field results in the suspension becoming demagnetised due, once again, to the random orientation of the particles.

In a Ferrometic® seal, specially developed low vapour pressure magnetic fluids are held in discreet stages between the shaft and stationary elements by a magnetic field (Fig. 2.3). Each stage is a barrier to the passage of gases and contaminants and can support a differential pressure of typically 3psi. Thus, the use of several stages allows operation in a positive pressure gradient or vacuum.

Experiments carried out with this type of coupling did not prove successful. The first attempt lasted only a few days and was returned to the manufacturer for analysis and refurbishment. Based on their findings a pressure cup was designed to fit around the outside of the seal to minimise the effective differential pressure. This design enabled us to keep the maximum pressure differential to no more than one atmosphere. This solution proved more resilient, but eventually gave way to corrosion of the seals by the hydrogen chloride gas contained within the mixture.

Ferrometic® is a registered trademark of the Ferrofluidics Corporation.

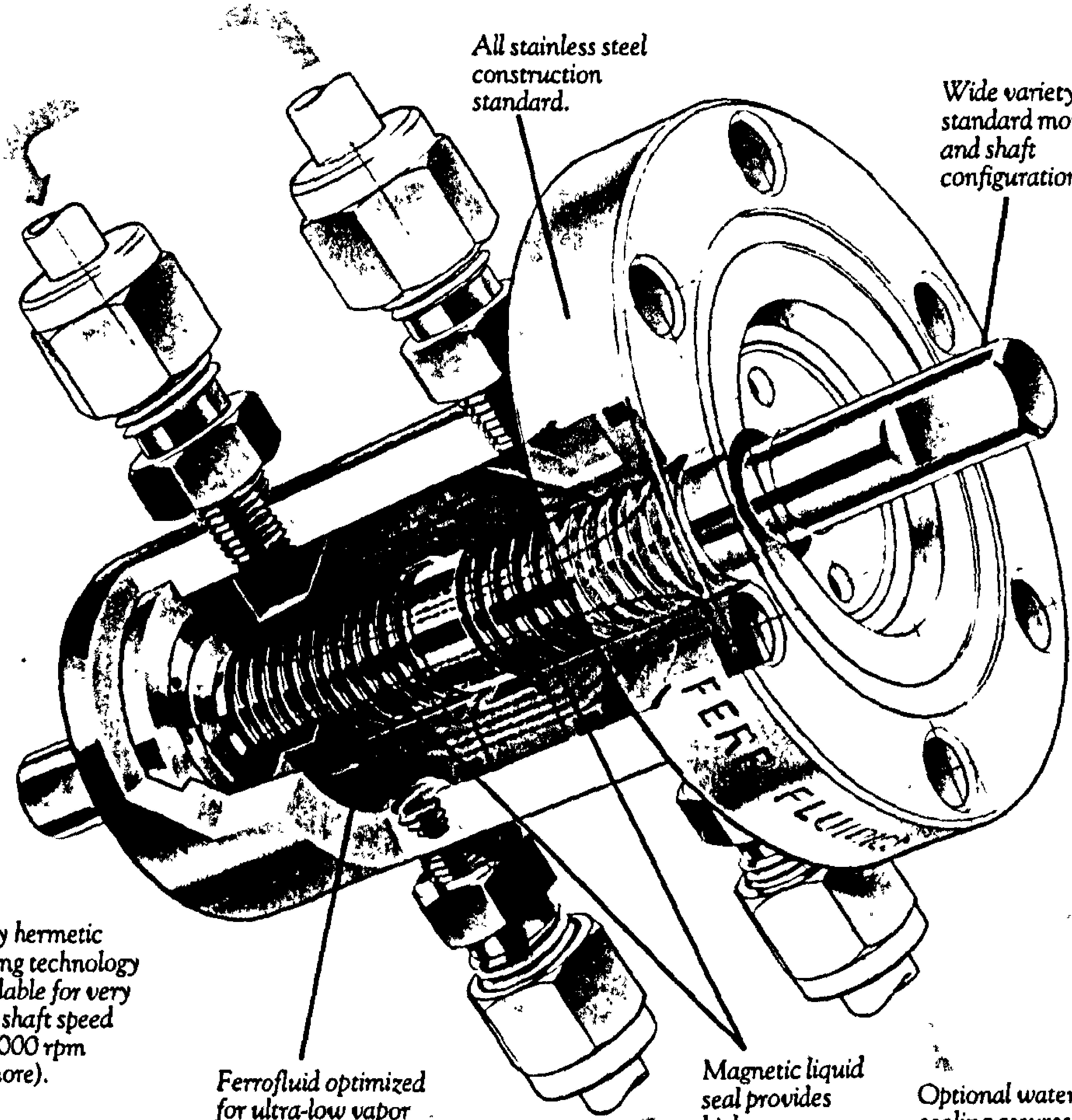

All stainless steel construction standard.

Wide variety of standard mounting and shaft configurations.

Only hermetic sealing technology available for very high shaft speed (10,000 rpm or more).

Ferrofluid optimized for ultra-low vapor pressure.

Magnetic liquid seal provides high vacuum integrity without rubbing, friction, or wear.

Optional water cooling assures long life under high ambient temperatures and/or high shaft speed conditions.

Fig. 2.3 Principle of ferrometic seal operation

Ferrofluidics, intrigued with this problem, refurbished the seal free of charge, but this time with a more chemically inert fluid. This fluid proved even more resilient but still failed after approximately a month of operation. They then flew in some special fluorocarbon based fluid from their home base in the U.S.A., and refurbished the seal once again, this time having to replace the stainless-steel shaft which had now also suffered from attack of the halogenated gas. Once again this was a further improvement, but eventually failed, leaving no option but to look to conventional magnetic couplings for a solution.

2.3.2 Magnetic Couplings

Magnetic drives are probably the simplest devices to implement, since they are constructed from two magnets, one that connects to the fan shaft on the inside of the chamber and one on the outside connected to the motor drive shaft. The external magnet is placed in close proximity to the internal magnet. When the external magnet is rotated, by the drive motor, the magnetic coupling between it and the inner magnet induces the inner magnet to rotate at the same speed. In order to maintain high rpm's without de-coupling occuring, high quality, high cost, magnetic materials such as samarium cobalt must be used.

The drives can be operated in two configurations shown in Fig. 2.4. The first, Fig. 2.4a), is the more conventional, where the inner magnetic core is located inside a thin, non-magnetic (e.g. 300 series stainless-steel) cup and aligned concentrically with the external magnetic core such that the maximum amount of the core overlaps. This will produce the maximum amount of coupling, and hence maximise the power handling capability of the drive before it will eventually de-couple. This latter point is important when

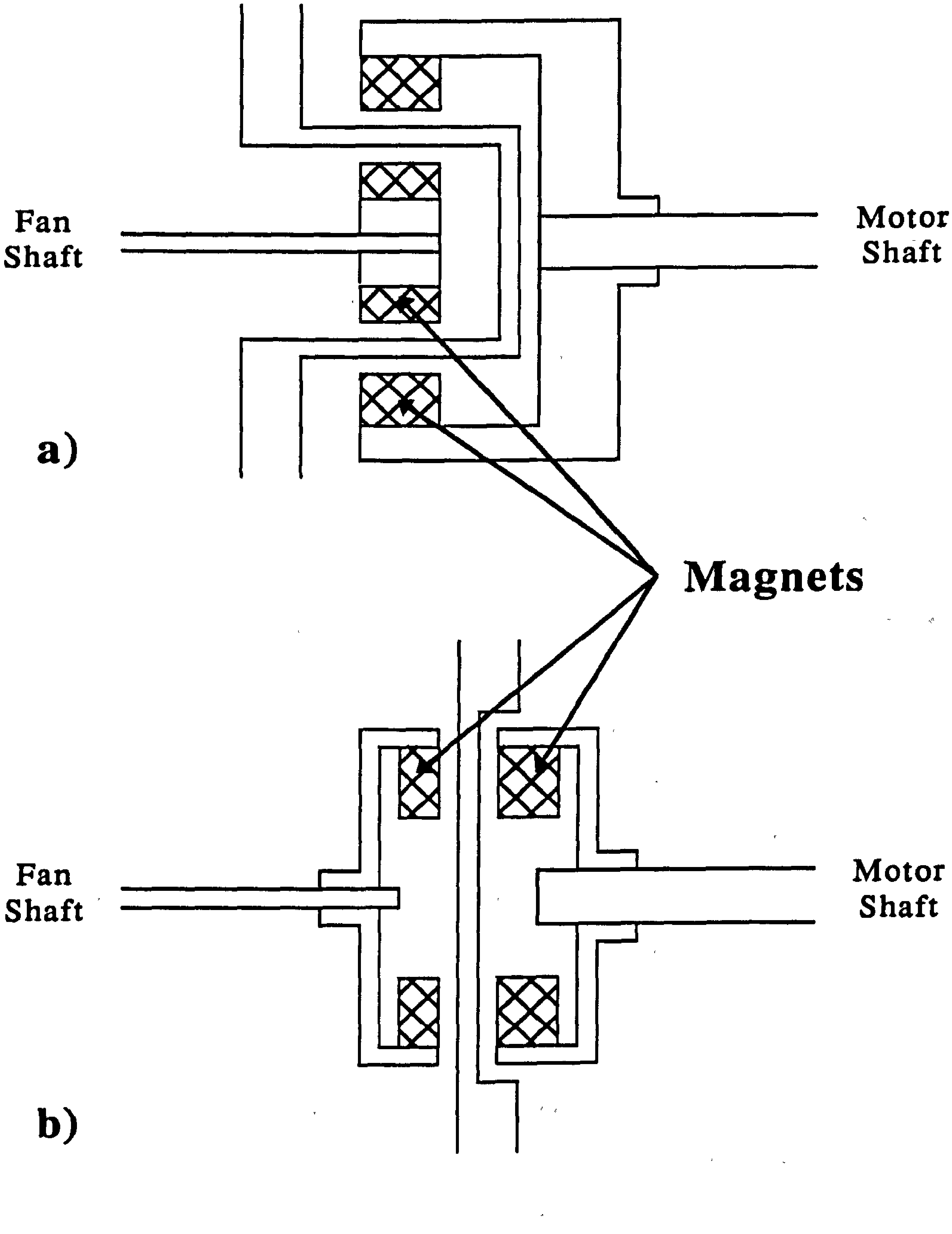

Fig. 2.4 Typical magnetic drive schemes:
a) concentrically coupled;
b) face-centred coupling

operating at high rpm, since the power is directly propotional to the rpm of the motor for a given torque. The second technique, Fig. 2.4b), uses a face-centred magnet design that is less widely used, and will result in an end-load being applied to the shaft of the fan.

In both cases the thin walled interface, made of a non-magnetic material, must be kept as thin as possible to minimise eddy currents being generated, thus minimising power loss from the magnetic drive and heating of the surrounding materials.

In experiments carried out on this design, a magnetic drive designed to couple a $^1/_2$ hp motor to a pump was used. In order to get experiments running with this technique, it was necessary to have the first cup made from PVC while the 304 stainless-steel cup was being fabricated. One of the consequences of choosing PVC was that the wall thickness had to be substantially increased to withstand the pressure without bowing. This cup, after several hours of running, would get very hot due to the eddy currents being generated in the magnetic field, resulting in the eventual failure due to over expansion of the cup and the side walls rubbing against the magnetic drive.

The arrival of the thin walled stainless-steel cup design made a dramatic improvement not only in reducing the eddy currents (and hence the heat generated) but also in increasing the clearance between the magnets and the outer wall of the cup. This design proved capable of attaining greater than 8000rpm using a $^1/_3$hp motor. No further leaking or eddy current problems were encountered with this design, and it is still functioning to-date.

2.4 WIND TUNNEL DESIGN

Wind tunnels usually fall into two main classes; high- and low-speed tunnels. For all practical purposes, the wind tunnel in this laser design can be regarded as a low-speed tunnel since it has a low Mach number (0.13).

2.4.1 Constraints [2.9]

In the design of this wind tunnel the following constraints were adhered to:

(i) the fans and other likely sources of turbulence were placed downstream of the discharge region of the laser. By this arrangement the disturbances introduced by the fan have a considerable time in which to decay before the working section is reached.

(ii) the gas downstream of the discharge but upstream of the fan should not be expanded into the suction side of the fan but contracted into it. This reduces any pressure drop in the loop.

(iii) the flow should be nozzeled down into the discharge region. This is achieved using a venturi type nozzle with the downstream end close-up to the electrodes because the gas will expand at between 30° and 45° on exit from the nozzle into a large volume.

It was also planned to incorporate turning vanes into the bends, to direct the flow and alleviate problems of boundary layer separation. However, due to the complexities of installing these at the time of construction, it was decided to omit them from the present design.

2.4.2 Irregularities in the Flow

The irregularities of the flow which are present in a wind tunnel usually fall into the following catagories, the most important of which is turbulence.

Spatial Non-Uniformity. The mean velocity may not be uniform over the cross-section of the tunnel ducting. This may be overcome by dissipating the regions of high velocity into heat by some form of resistance placed across the stream. The use of gauze, screens and honeycombs can achieve this, although it invariably involves heavy losses in the flow rate as well inducing further heating of the lasing medium.

Swirl. Rotation of the flow about an axis parallel to the direction of motion results in the direction, and often the magnitude, varying over the cross-section. Honeycomb can be used to reduce these directional fluctuations.

Low Frequency Pulsations. Surges in the mean flow velocity can exist. This can be a particular problem in the long arm of the return circuit where the source is difficult to locate. The removal of other irregularities can result in the disappearance of these surges.

Turbulence. Small eddies of varying size and intensity always present in these systems are referred to collectively as turbulence. Principal methods used for the reduction of turbulence in an airstream are gauzes, contractions of the ductwork and honeycombs.

Sound. As the intensity of the turbulence is progressively reduced, by the methods indicated above, a point is reached where the effects of sound in the tunnel become comparable. Noise in a closed-circuit tunnel has two main sources; the fan, and the irregular eddy motion in the boundary layer. In a pulsed laser system there is, however, also a third source; the pulse discharge itself where both shock and acoustic waves are produced periodically. The introduction of honeycombs to reduce the turbulence results in a drop in flow velocity and in order to compensate for this the fans rotational speed must be increased. Consequently, an increase in the noise is brought about. Thus efficient design of the ductwork is required to keep the fan rotation speed to a minimum.

2.5 EVALUATION OF THE FINISHED TUNNEL DESIGN

As has previously been noted, the wind tunnel ducting and laser housing was constructed of stainless-steel. The tunnel (Fig. 2.5) was constructed using a segmented duct design in order to facilitate its expansion, should it prove necessary, and allow further evaluation of laminar and turbulent flow in the discharge region of the laser. With this design, the modification to individual sections can be made without affecting the rest of the closed-loop. In Appendix-1, an estimate of the pressure drop in the recirculation loop is presented which shows that it is quite small for the design used.

2.5.1 Description of the Finished Tunnel Design

The initial tunnel design (Fig. 2.5), moving from the top centre in a clockwise direction, consisted of the main laser discharge chamber, a heat exchanger section, the blower housing, and the return ducting back to the laser chamber. The overall dimensions of the tunnel were approximately 36"(wide) x 18"(high) x 15"(deep).

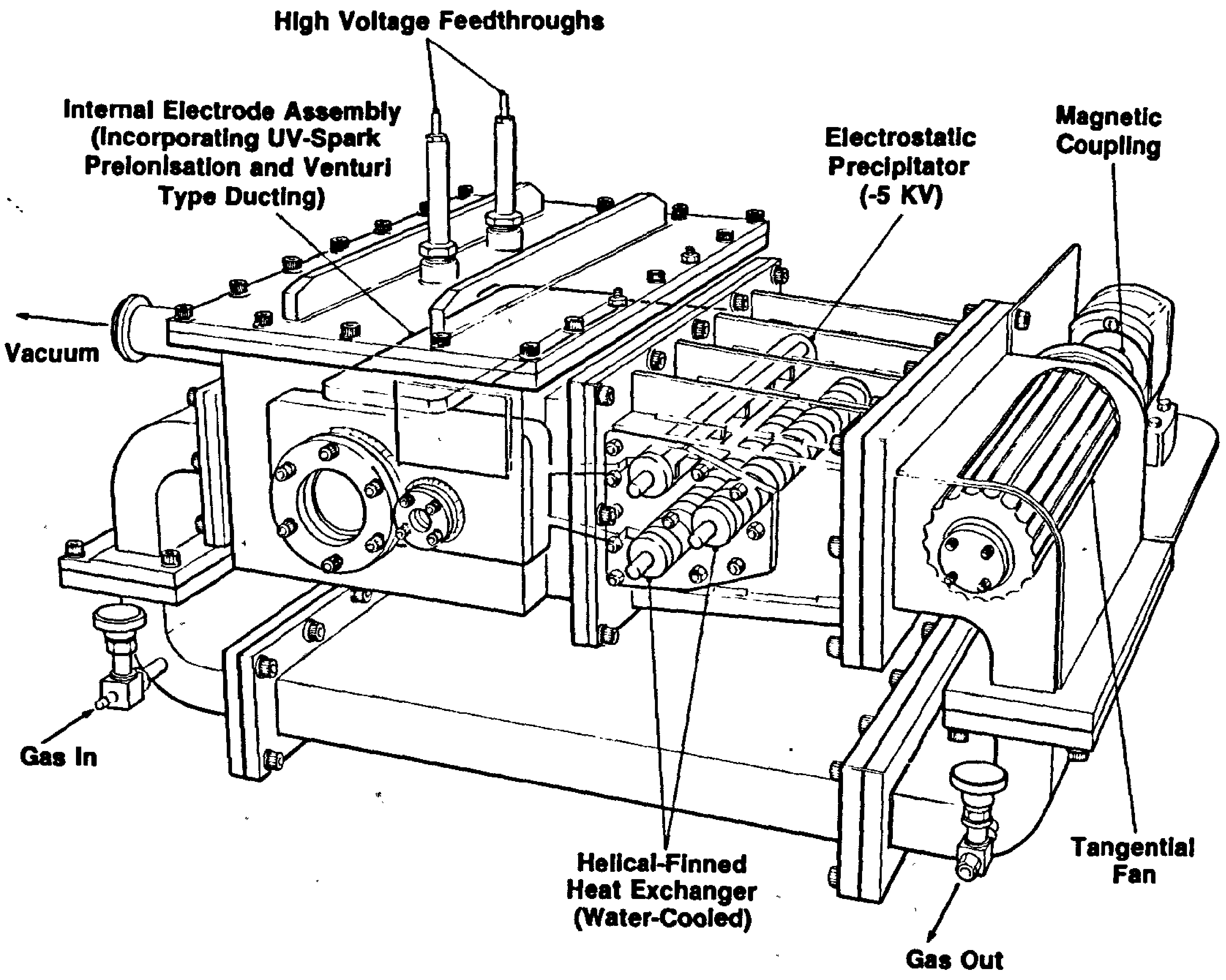

Fig. 2.5 Sectioned view of the high pressure, high prf excimer laser wind tunnel

The Laser Discharge Chamber.

The entrance to the laser discharge chamber from the exit of the ducting was 24cm(wide) x 3.6cm(high). The exit was a larger port, designed to minimise areas of the working section that could trap pockets of stale gas. This port extended to the base of the chamber and was 24cm(wide) x 10cm(high). A range of optic ports were included in this design. There are the front and rear optic mounting ports, designed to take 2" optics, and also a viewing port to the right of the output port that was used to monitor the state of the discharge. This port also provide the ability to carry out gain measurements of the discharge using the side-light fluorescence of the discharge. A large, 1" diameter, vacuum exhaust port was provided to facilitate fast and efficient pump down times. The chamber was closed by a $^3/_8$" thick stainless-steel plate which incorporated the two high voltage feedthroughs.

Heat Exchanger Section.

This section incorporated three 0.75" diameter, helically coiled, finned copper heat exchanger tubes from Yorkshire Imperial Metals. These tubes were sealed using "o"-ring compression cups placed around the bare copper tube that extended out of the duct section used to attach cooling pipes. The duct section also supplied a modest contraction, of a few degrees, of the gas prior to it entering the blower section in order to smooth out any eddy's that may have occured in the gas expansion after the laser chamber.

Fan Housing.

The fan used in this design was the Airwheel Ltd., 240mm x 60mm diameter, custom designed, tangential vortex fan unit described in Section 2.2. The fan unit drive was supplied initially via a Ferrofluidic seal coupled to the fan at one end. The support at the other end of the fan was supplied by a machined piece of Glacier 'DQ', bronze loaded teflon, dry bearing material. An "o"-ring sealed cap provided the closure to this side of the duct section. A more detailed appraisal of the performance of this fan housing is given later in this section.

The Closing Duct Sections.

The final four sections of the duct consisted of three curved sections and linear section, each if which had a 24cm (wide) x 3.6cm (high) internal cross-section. The curved sections were hollow, contained no guide vanes, and the ratio of inner-to-outer radii followed standard guidelines [2.10]. The long support duct, however, did include three supporting struts that ran the length of the duct. These were necessary to meet pressure vessel safety requirements.

2.5.2 Preliminary Testing of the Finished Tunnel Design

Upon completion of the full duct assembly, water and gas pressure tests were carried out in excess of 70psig, with only minor modifications being needed. Soon after these tests, the vessel was passed as being safe to a working pressure of 2.53 atmospheres gauge [2.11].

At the initial trial of the finished design, it was felt that the flow pressure of 0.30 torr ($\sim 8 m.s^{-1}$), measured by a in-house built pitot-static tube and micro-manometer (Furness MDC FC001) at the entrance to the laser head (Fig. 2.6), did not seem strong enough. Also, there was some noise eminating from the ductwork presumably due to buffeting. The fan section of the ducting was then removed and tested separately.

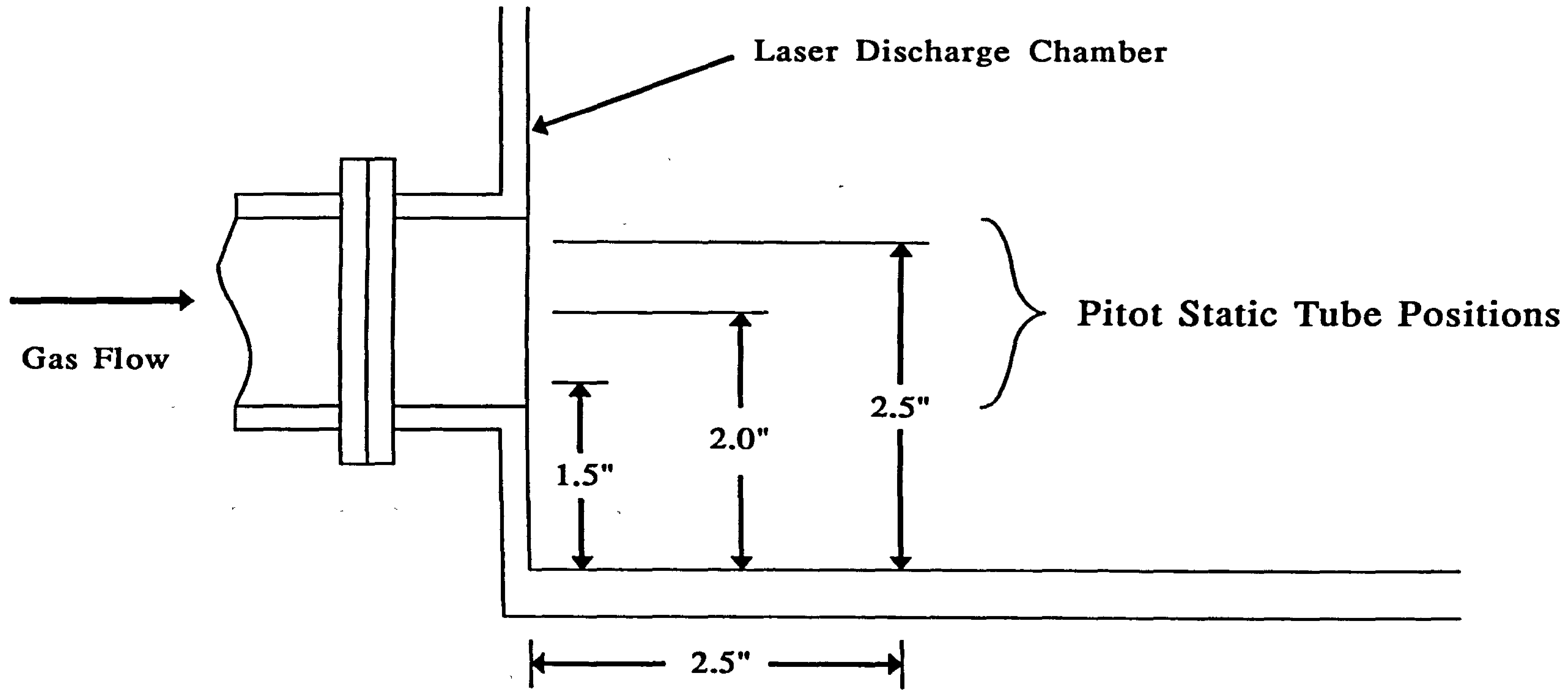

Fig. 2.6 Schematic of initial flow measurement set-up using a pitot static tube

2.5.3 Optimisation of the Fan Section

There was a considerable back-draft generated by the fan which interfered with the air being sucked in by the fan. This caused the fan to pulsate, thus reducing the effectiveness of the flow. The problem arose due to the complexities of the construction of the fan section where, in the final design, a radius was used as the inside of the duct (Fig. 2.7b)) instead of a right-angle as in the original design (Fig. 2.7a)).

Looking at the duct design used by the fan manufaturer Airwheel, it was noticed that they partially obstructed the entrance (Fig. 2.7c)). This was tried, and resulted in an increase in flow pressure by a factor 1.5. Since a factor of ~10 was required the matter was pursued still further. A thin sheet of metal plate was slid into the entrance of the fan section as indicated in Fig. 2.8a) such that it could overlap the exit port from the fan. The plate was then moved back and forth until an optimum pressure reading on the micro-manometer was achieved. This resulted in a factor of three improvement of the flow velocity. At this point, the plate was tilted towards the fan itself such that it nearly came into contact (Fig. 2.8b)). This produced a massive upsurge in the flow pressure by a factor of 8. The final design (Fig. 2.8c)) was made out of stainless-steel, for gas compatibility, and incorporated a lip bent back into the exit port of the duct to stop any of the directed flow from being trapped under the plate.

The final design was reinstalled into the main ducting and, after final fine adjustments, produced flow velocities in air of 17.5m.s^{-1}, 79% of that measured exiting the fan section by itself.

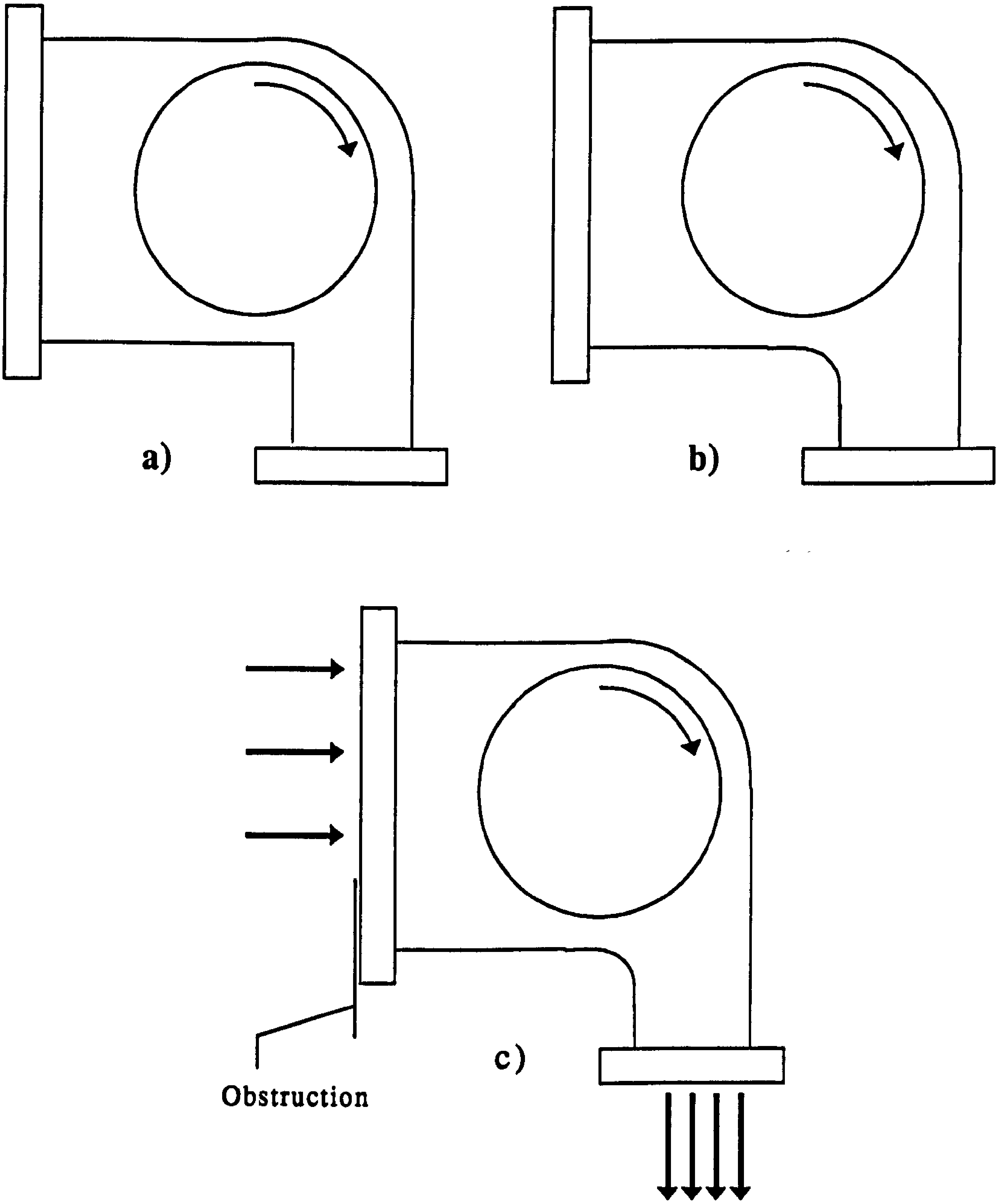

Fig. 2.7 Fan duct design: a) proposed; b) finished product; c) Airwheel design

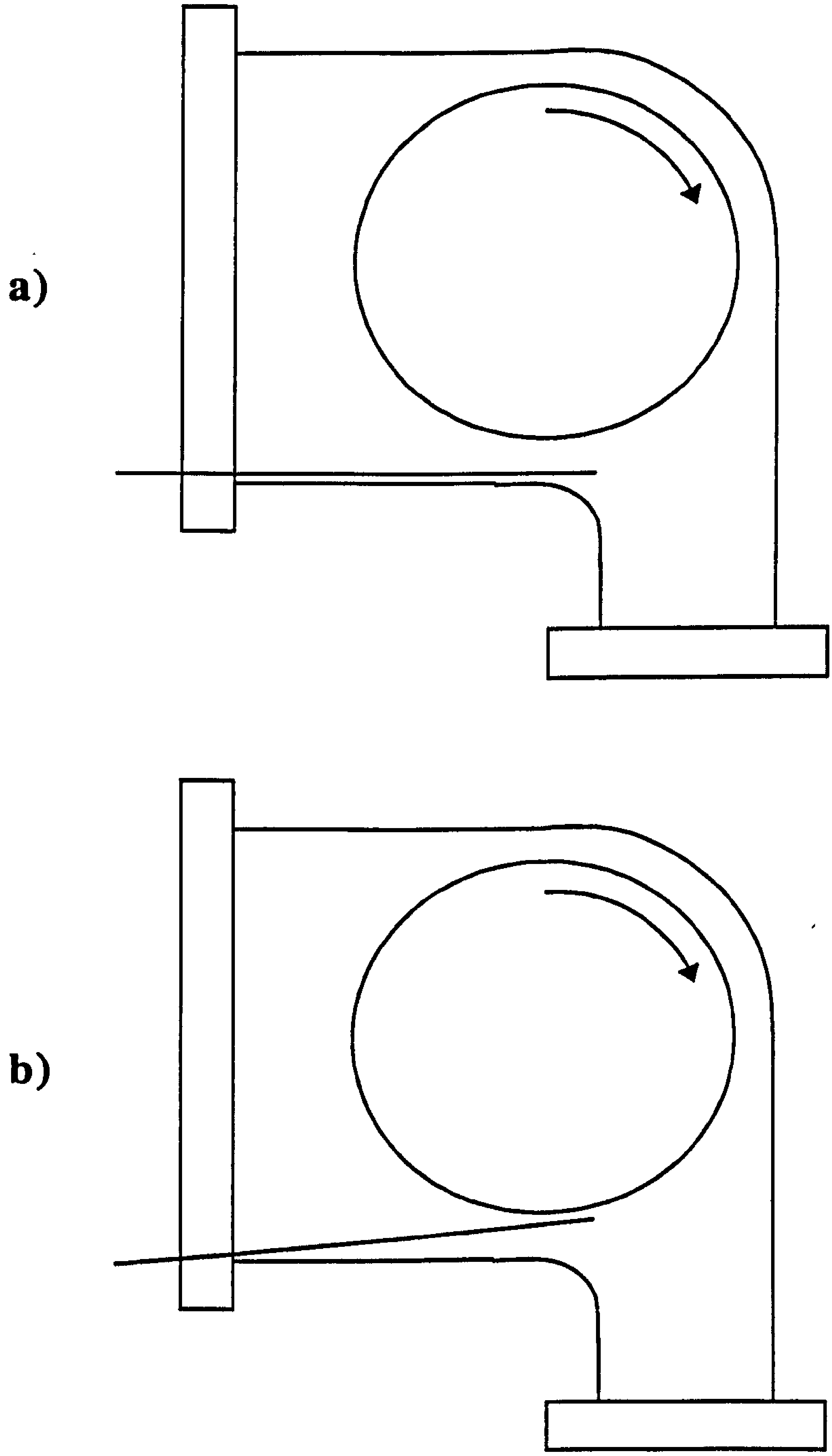

Fig. 2.8 Fan duct optimisation

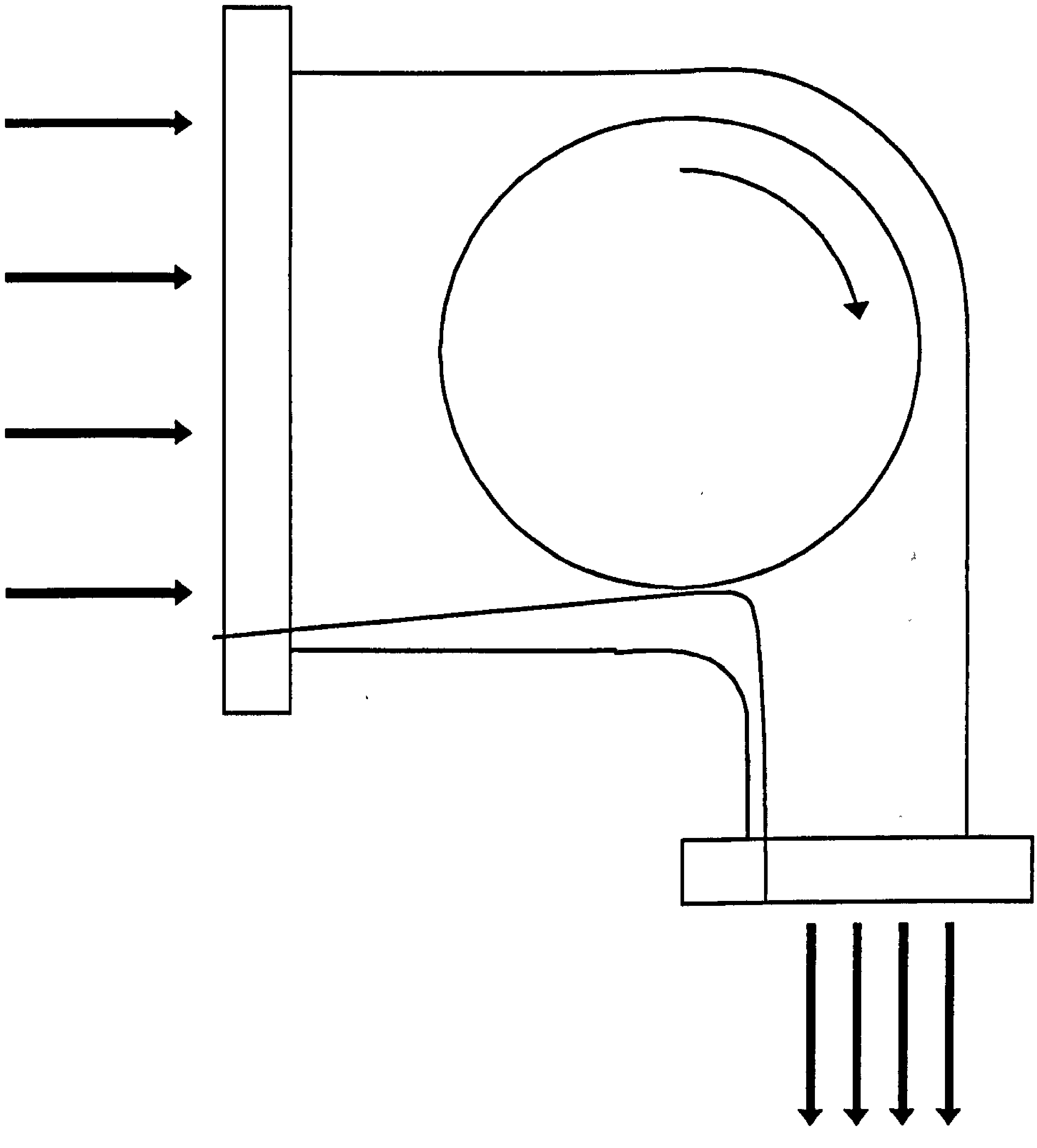

Fig. 2.8c) Final fan duct configuration

2.5.4 Flow Profile Measurements at the Laser Head

The velocity profile of the gas, at the entrance to the laser head, was determined to allow evaluation of the extent that the inclusion of a venturi flume would have on the velocity passing through the discharge region.

Measurements were made at the exit of the duct (Fig. 2.9a) and at a distance 2.5" from the duct (Fig. 2.9b) i.e. at the position the electrodes would eventually reside. In each case, the flow profile was measured in the long direction at various heights in relation to the duct (Fig. 2.6). At the exit of the duct, the flow pressure is a maximum at the top of the duct dropping to almost half at the bottom. Also, it should be noted that the three support struts in the base section of the flow duct, show up in the flow profile. This effect becomes more pronounced 2.5" away from the duct.

Preliminary laser operation of the set-up so far was carried out for a nitrogen laser discharge consisting of a ratio of $1\,N_2 : 5\,He$ at atmospheric pressure. Given the limits of the 250W Vinculum power supply that was available, a maximum repetition rate of 40Hz was achieved. This was deemed successful given that no constraint on the flow direction of the gas was being made after it exited the duct system.

N.B. A detailed account of the electrode gantry design and components is given in Chapter 3 of this thesis.

2.5.5 Construction of the Venturi Flume

The contraction stage of the venturi flume was designed experimentally using the pitot static tube to optimise the flow. The pitot tube was positioned at

Fig. 2.9a) Flow pressure across the duct at the duct exit

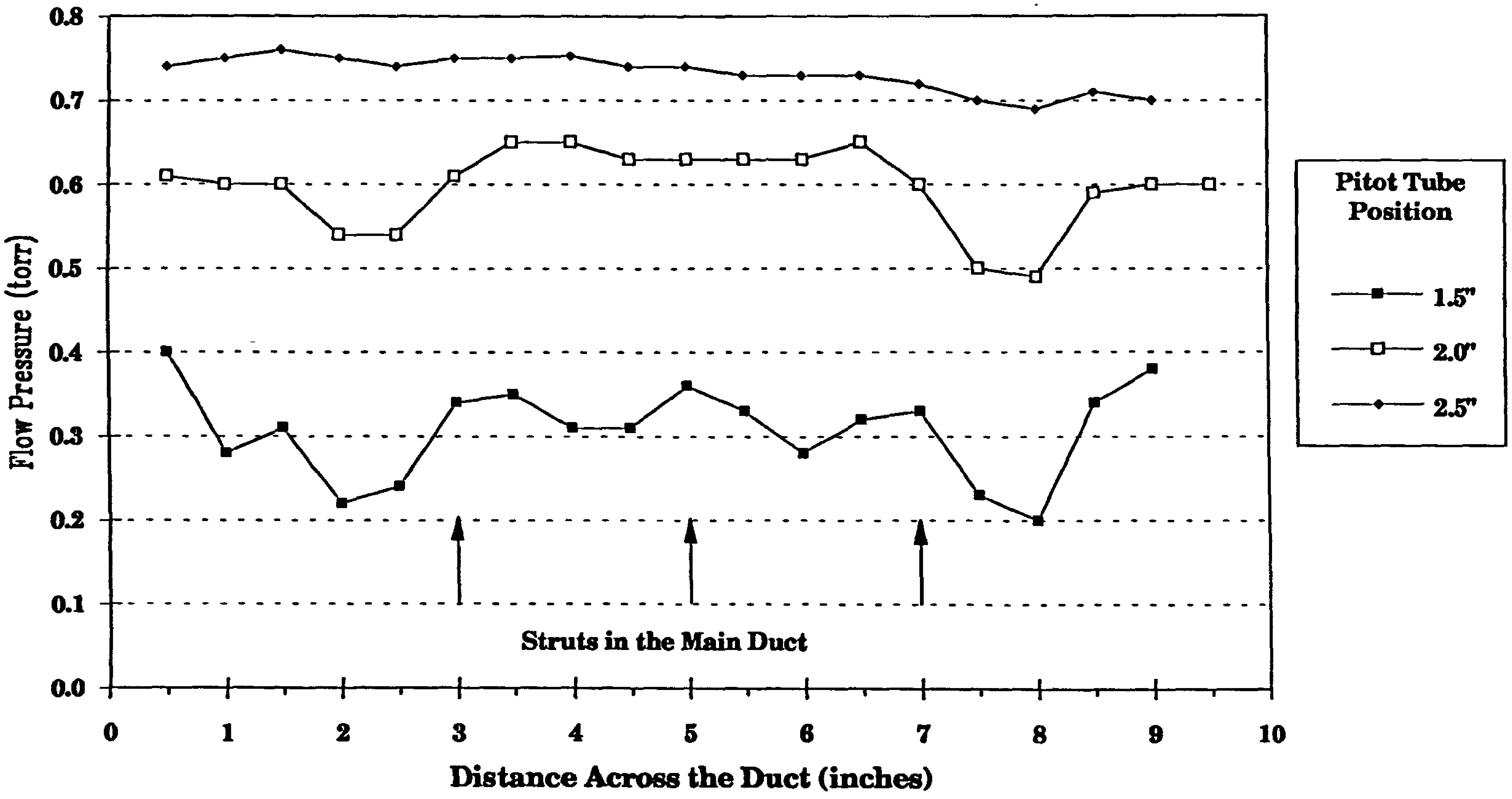

Fig. 2.9b) Flow pressure across the duct at a distance 2.5" from the duct exit

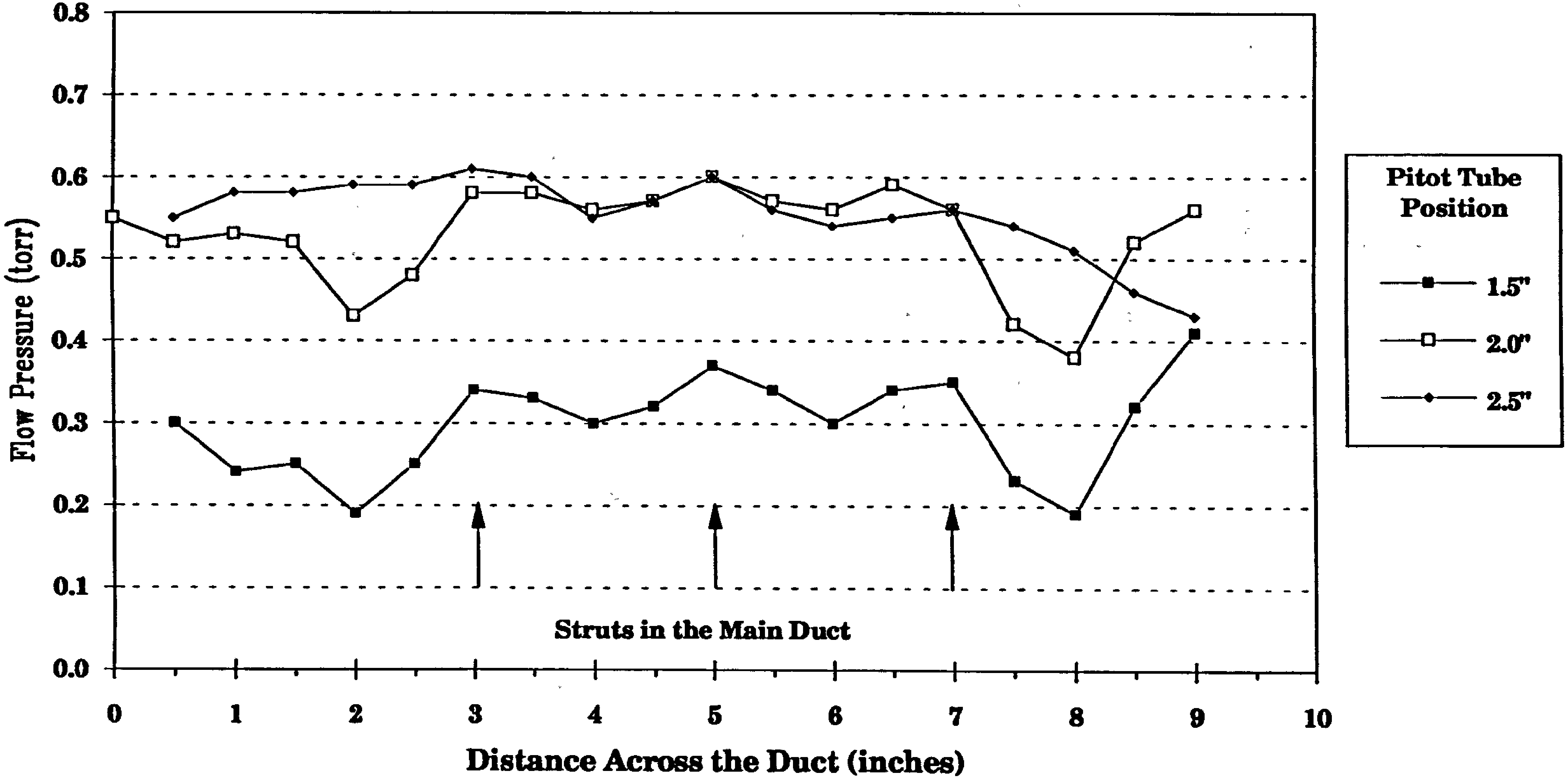

the eventual location of the electrodes, with adjustment to the flow being made by changing the angle of two pieces of sheet aluminium, used to guide the flow from the duct exit to the pitot tube. Using a further two pieces of sheet aluminium, the length of which was determined by the distance to the cooling pipes in the heat exchanger section, the optimum angle for the effuser was determined to be 6° full angle (Fig. 2.10). Although, the venturi by itself gave a considerable increase in flow pressure, the addition of the effuser improved the movement of the gas to the fan section resulting in a further increase in the flow velocity due primarily to the fan working more efficiently. The buffeting of the air being pushed around the tunnel was also noticeably reduced. The result of these measurements can be seen in Fig. 2.11a) where an increase in flow pressure of a factor x4 over the earlier results without ducting was achieved. Using the following relationship (see Appendix-2),

$$v = \sqrt{\frac{2 \times 1.01325 \times 10^5 \text{ (Pascals/atm.)} \times \Delta p}{760 \text{ (torr/atm.)} \times \rho}}$$

where Δp is the gas pressure change monitored on the micro-manometer (torr) and ρ the effective gas density, the gas flow velocity, v ($m.s^{-1}$), was calculated.

Fig. 2.11b) shows this result in terms of flow velocity as a function of distance. The flow velocity was also measured at the centre of the discharge region as a function of the fan motor voltage, (Fig. 2.12) with a near linear dependance being obtained.

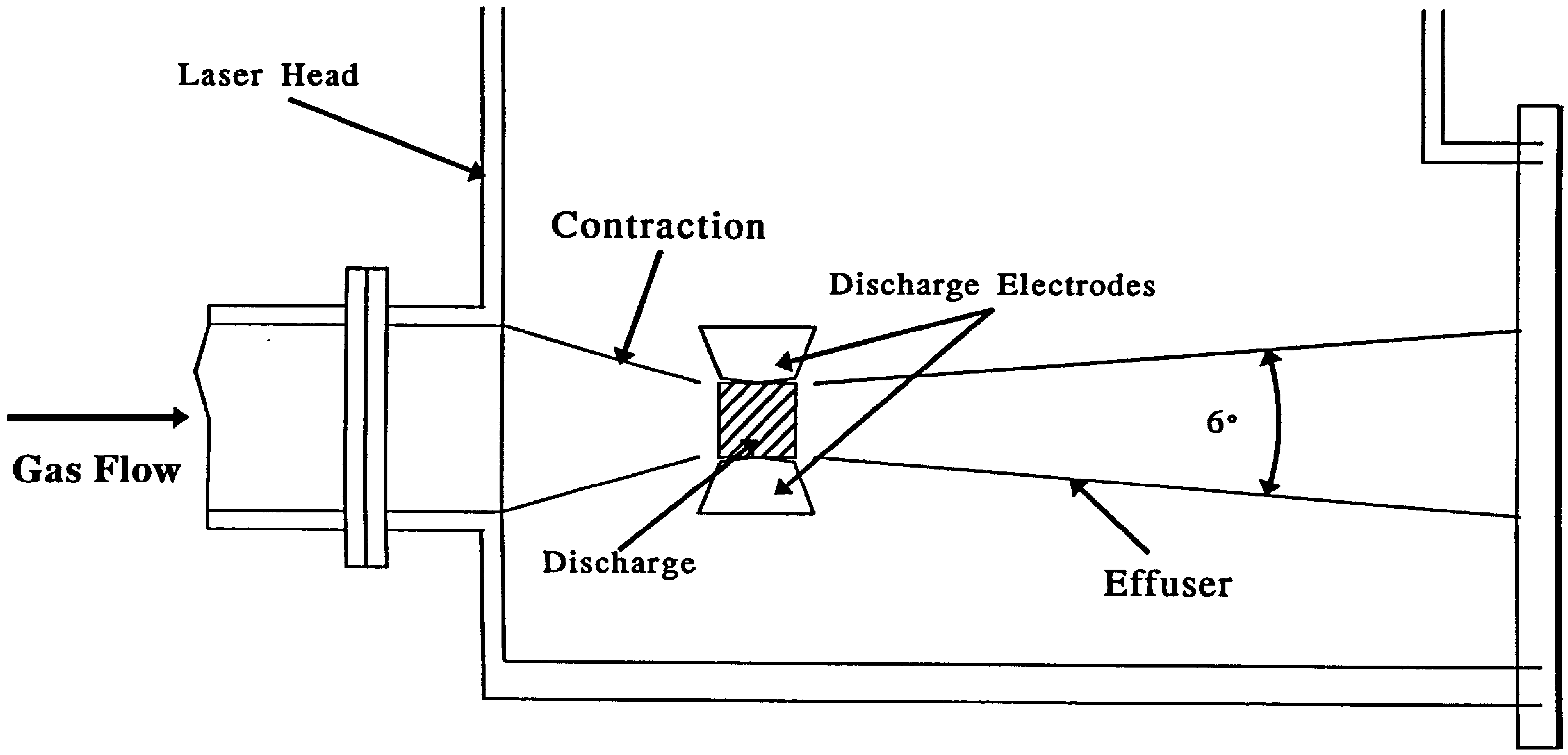

Fig. 2.10 Schematic diagram of the venturi flume

Fig. 2.11a) Flow pressure as a function of distance across the venturi, 2.5' from the duct exit.

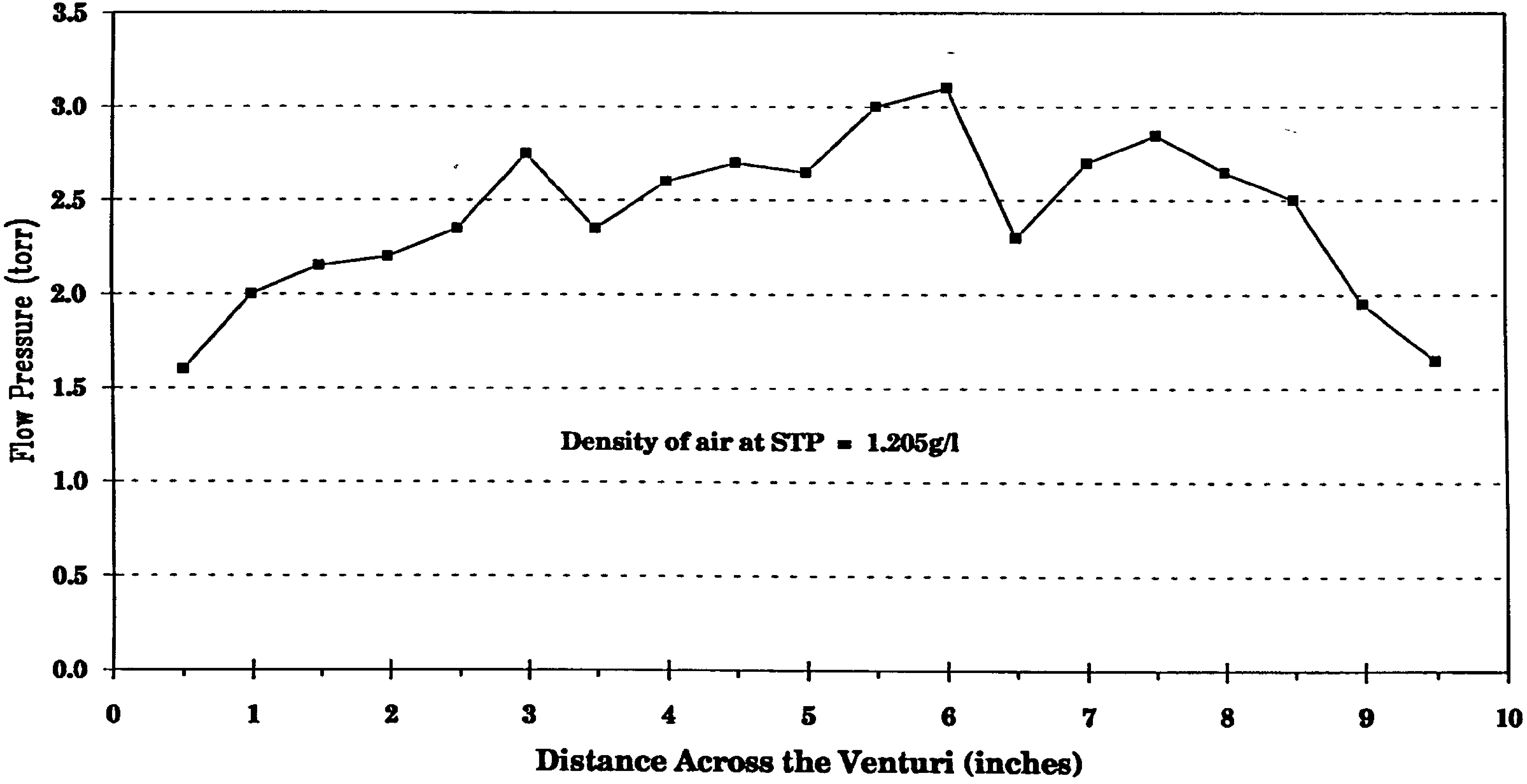

Fig. 2.11b) Flow velocity as a function of distance across the venturi, 2.5" from the duct exit.

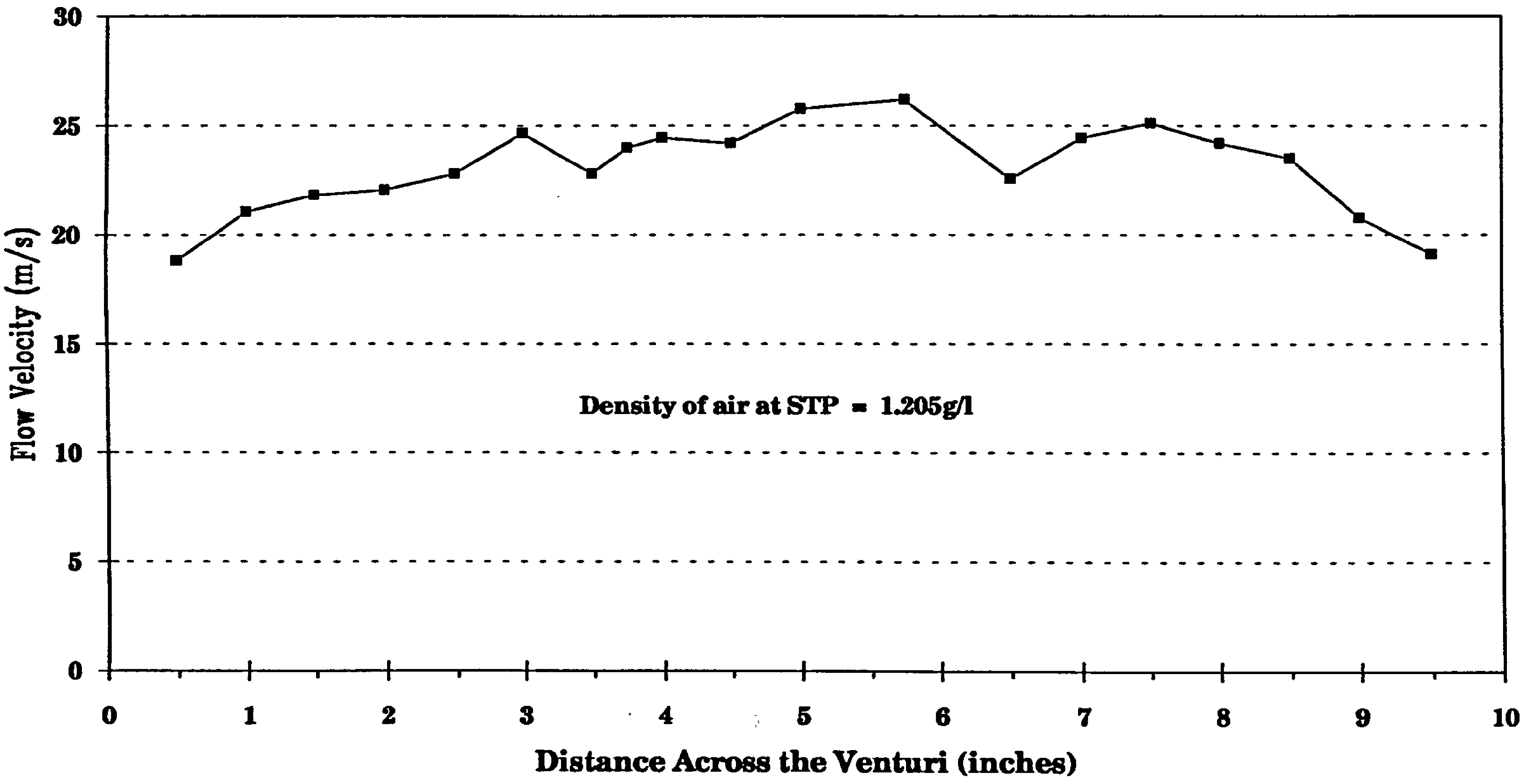

Fig. 2.12 Flow velocity, at the centre of the venturi, as a function of the fan motor voltage

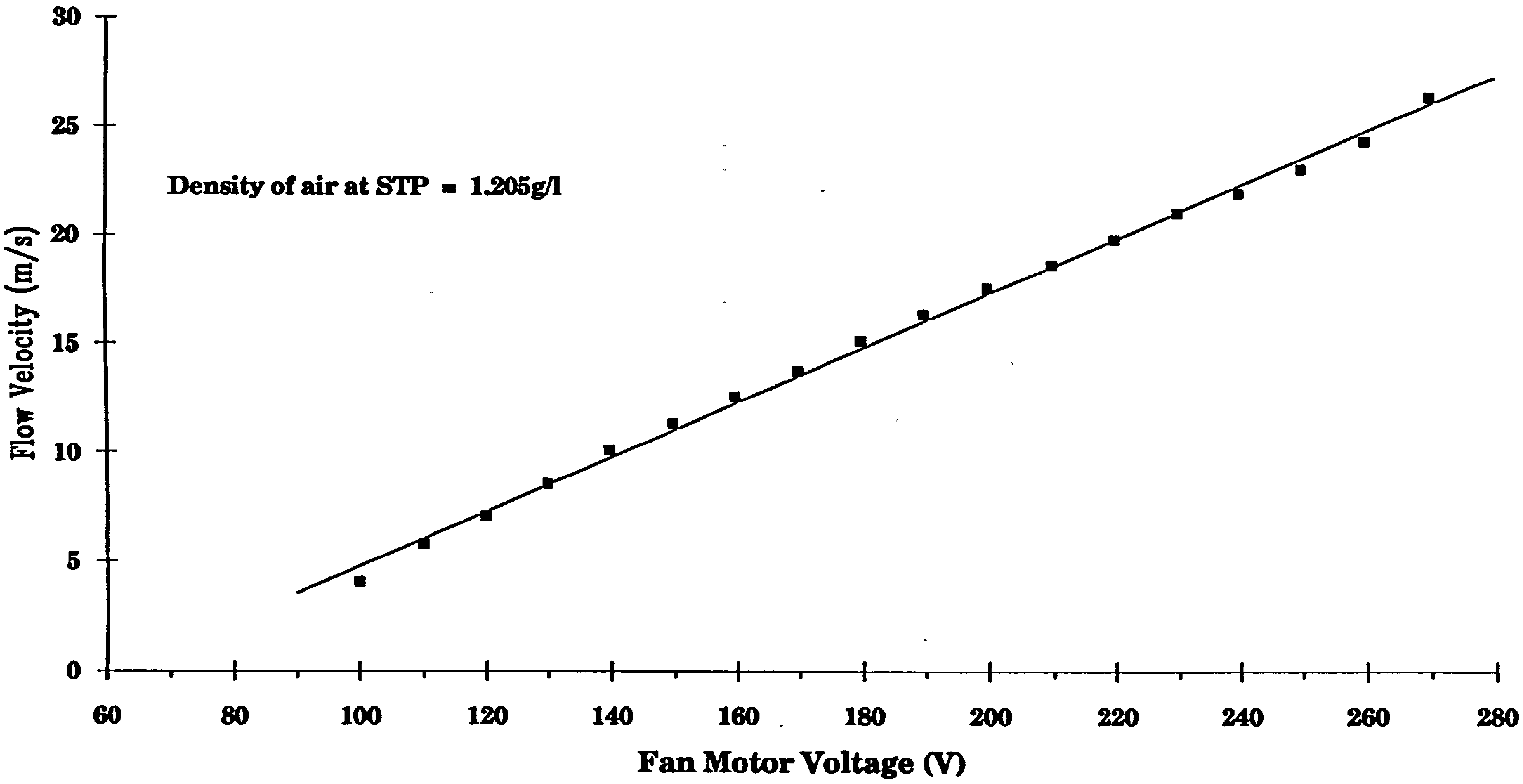

It should be pointed out that it is necessary to get a significant increase in the flow pressure to get a noticeable increase in the flow velocity, since the latter is directly proportional to the square root of the pressure differential.

As a footnote, it was ironic that, shortly after these measurements were made, a book by Pankhurst *et al* on wind tunnel design [2.12] was found that confirmed all of the venturi flume design results.

2.5.6 Ducted Electrode Assembly Evaluation

The first ducted electrode design was made from PVC with side walls, which acted also as the electrode gantry spacers, angled in the vertical plane just like the venturi produced in the horizontal plane, Fig. 2.13. PVC was chosen since it was a chloride based polymer and it was felt that it would react less with the halogen environment to which it would be exposed. It had also been the basis of other fabricated parts used in other excimers within the M.G.L. group. Once this ducted electrode gantry was in place, a measurement was made of the flow velocity to confirm that the flow rates in the finished design were still being met.

It was to be found later, after considerable running of the laser, that the material bleached from its original bright red colour to a paler pink. There was obviously a colouring agent used in the material's production that was reacting with the gas.

This result led to the final improved electrode gantry design (Fig. 2.14). It was made from a relatively inert, non-coloured PTFE, and formed the basis for the majority of the high prf experimental results to be found in this thesis. Here, because of the high cost of PTFE, the side walls were made of

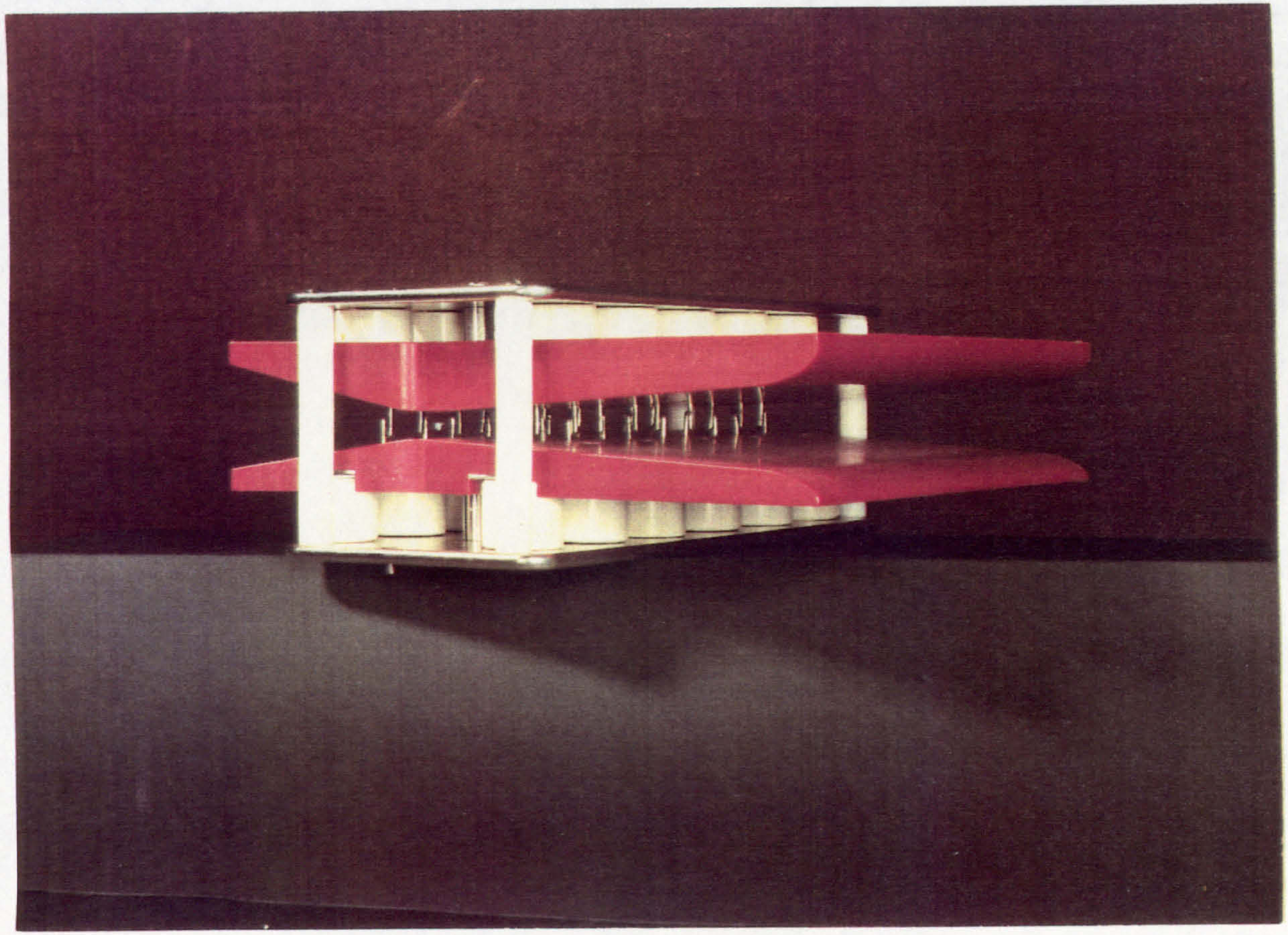

Fig. 2.13 Initial electrode gantry design: the ductwork was constructed from PVC

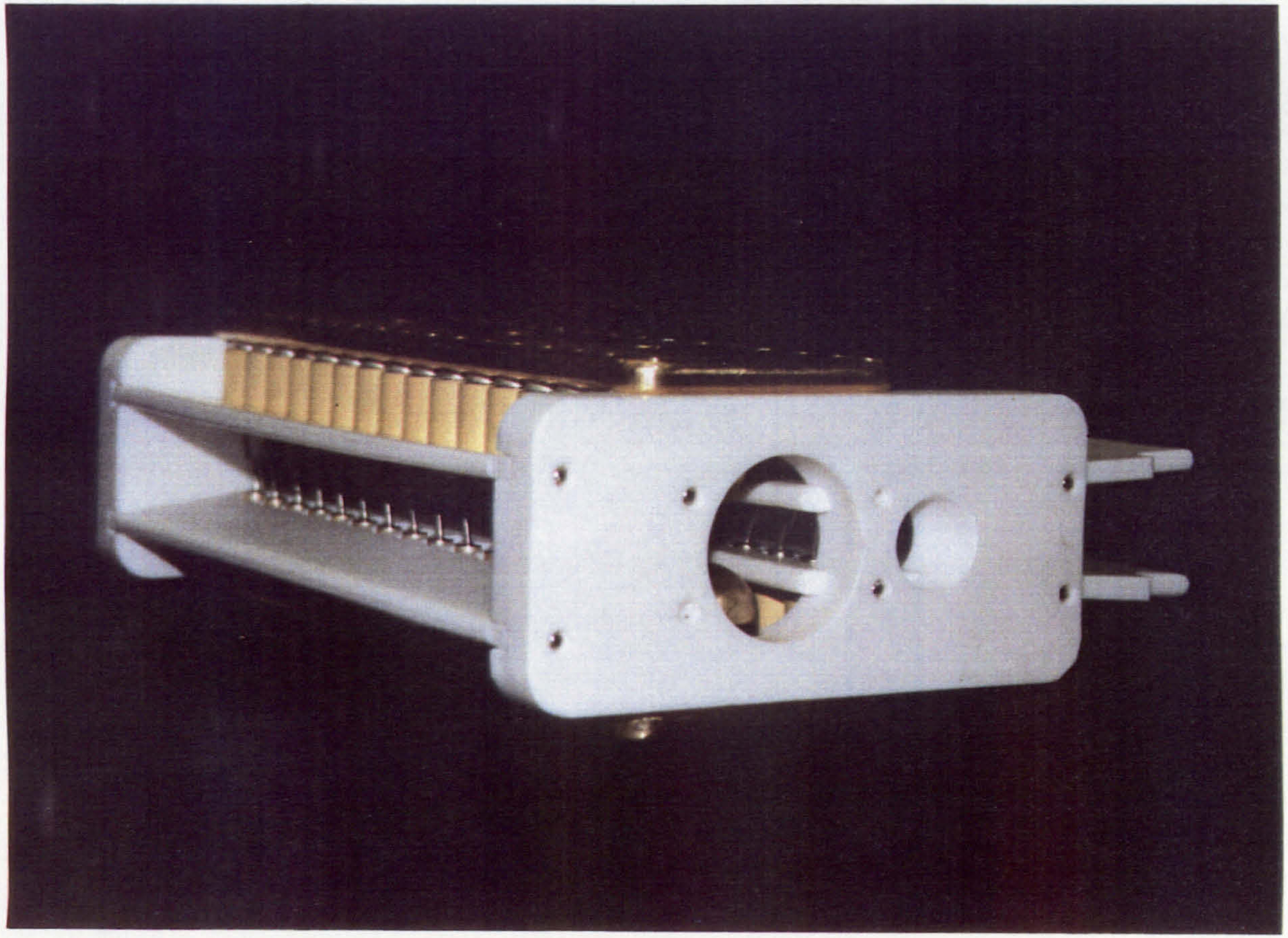

Fig. 2.14 Final electrode gantry design: the ductwork was constructed from PTFE

inch thick PTFE plate that were flat, and aligned with the edges of the ducting, to constrain the flow in the vertical plane. Sheets of 0.25" thick PTFE were then embedded into the side walls at the already pre-determined optimum angles found in section 2.4.5. This design resulted in flow velocities exceeding $45 m.s^{-1}$ as can be seen in Fig. 2.15.

2.6 THE HYDROGEN THYRATRON

The requirements of a switch to initiate the discharge of a pulse forming network are:

(a) it should be non-conducting during the charging period.

(b) it should be capable of closing very rapidly at predetermined times.

(c) the switch resistance should be as small as possible during the discharge of the network.

(d) it is not required to interrupt the current pulse, since the current drops to approximately zero at the end of the pulse.

(e) it should regain its non-conducting state rapidly after the end of the pulse.

In the early days of radar development, rotary spark-gaps were able to meet the above requirements satisfactorily. However, they also had three disadvantages: they were not particularly suited for high prf's; they have an inherent uncertainty in the firing time; and they are not able to be adapted for applications which require airtight enclosures. This has led to the development of fixed spark-gaps and thyratrons. For brevity, only the thyratron will be discussed here, since it is the only device capable of operating at the repetition rates and powers required.

Fig. 2.15 Flow velocity through the discharge region as a function of fan discharge voltage (for a 1/3rd HP Parvalux DC motor).

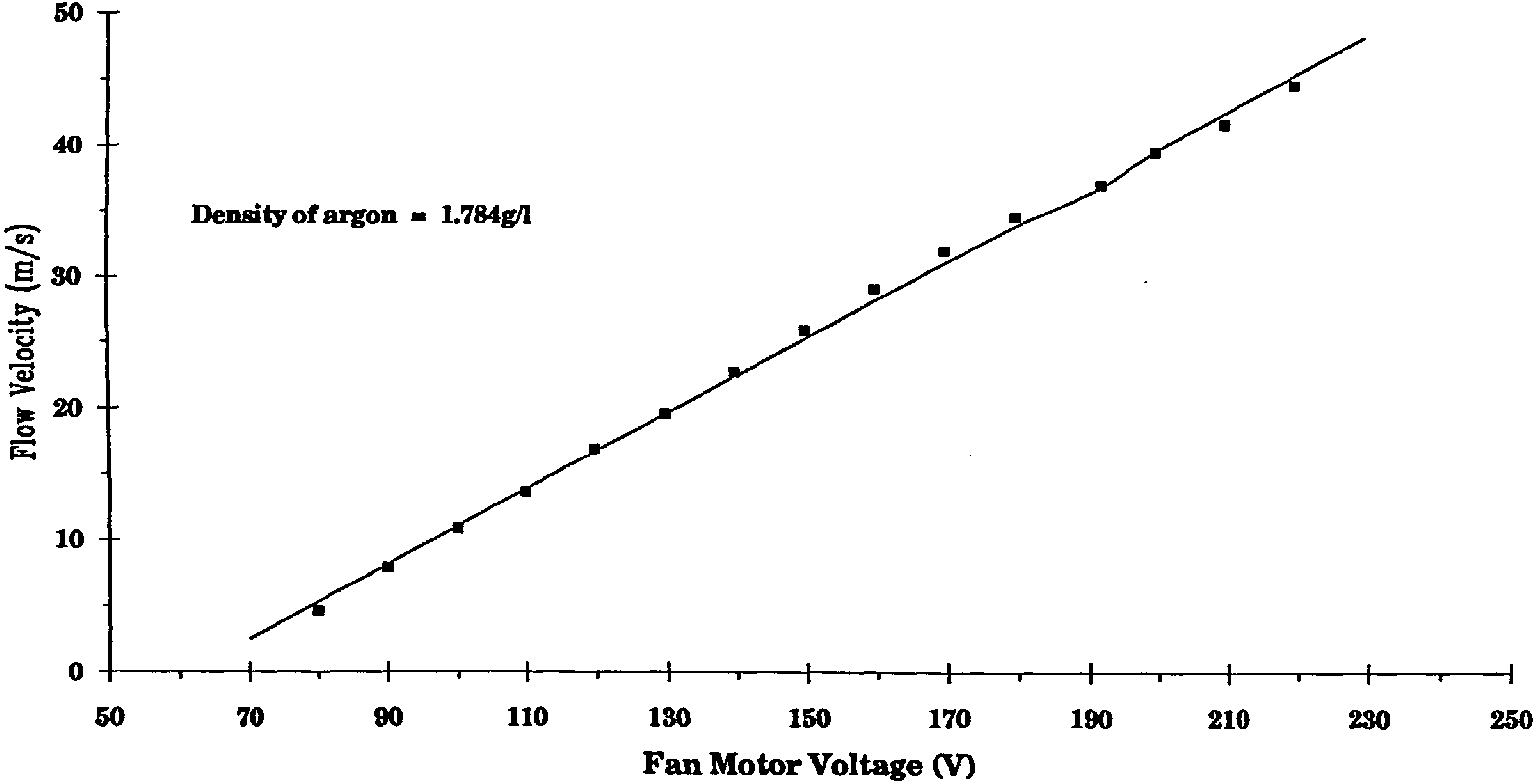

The advantages of the thyratron are that it is relatively small and light, can be triggered accurately by applying high-voltage pulses to the grid, has a high efficiency, and can be operated over a wide range of anode voltages. The early mercury thyratron suffered from its temperature sensitivity. Other difficulties encountered with pulsed operation were long deionising times and low voltage drops which lead to the destruction by ion bombardment of the cathode.

Development work on pulsed thyratrons led to the use of hydrogen as the medium, because it enables high current pulses to traverse the thyratron without a resulting voltage drop great enough to destroy the cathode. The hydrogen-filled tube also has a short deionisation time - about an order of magnitude less than that of mercury-, argon- or xenon-filled thyratrons.

Hydrogen-filled thyratrons do suffer from the disappearance of the gas during operation because of gas "clean-up". This is caused mainly by the great chemical activity of hydrogen which combines readily with many substances including the oxide cathode under certain conditions. Thus, great care must be taken to prevent the inclusion of any substance that can react chemically with hydrogen. Pressure "clean-up" has largely been eliminated with the development of these thyratrons by proper design and processing, and the use of selected materials such that the tube life is not seriously impaired.

The mass reducing action of hydrogen on the oxide cathode becomes serious at high temperatures, making it necessary to maintain the cathode temperature well below ~900°C. However, there is a restriction with this philosophy, in that below about 800°C cathode emission decreases rapidly. Therefore it is necessary to keep the temperature at a maximum of 850°C, although somewhat lower is preferable. Thus, as indicated in the thyratron data sheets, the cathode heater voltage must remain very stable.

The lifetime of hydrogen-filled tubes is further increased by the inclusion of a hydrogen reservoir. This is achieved using a metal capsule of titanium hydride which is heated to the required temperature. Under these conditions the titanium, hydrogen and hydride are in thermal equilibrium, and any variation of the amount of hydrogen within the tube envelope causes a readjustment of the equilibrium condition, so that a constant gas pressure is maintained.

Deuterium, which is chemically similar to that of hydrogen, is being increasingly used since its greater mass lends itself to a decrease in mobility and hence surface recombination effects are reduced and the arc drop lower. However, this reduction in mobility also leads to an increase of the recovery time by $\sqrt{2}$ for the same geometry. Deuterium is therefore used in high-power tubes where the hold-off voltage and dissipation are of particular importance.

2.6.1 Principles of Operation

In its basic form, the thyratron consists of an anode; a control grid; and a thermionic cathode in an envelope with a filling of mercury vapour, inert gas or hydrogen. The tube will remain in a non-conducting state with a positive voltage on the anode, if a sufficiently negative voltage is applied to the grid. The value of this voltage depends on the magnitude of the anode voltage and the geometry of the tube. Thus, as the grid voltage is made less negative, the ability to hold-off the anode voltage is reduced.

In the absence of a sufficient grid voltage the heated cathode emits electrons which are accelerated by the anode voltage, such that they collide with the gas atoms producing ions and electrons, resulting in a column of ionised gas. This results in a low voltage [~50 to 100V] across the discharge which will allow a wide range of currents depending in the external circuitry. During conduction, a sheath of ions forms around the grid preventing any voltage applied to it from penetrating the main body of the discharge, and hence keeping the grid from losing control. To return the tube to a non-conducting state the anode voltage has to be removed, or reversed, for a time sufficient to allow the charge density to decay to a low value. After this has occured, the grid re-establishes its control, and does not allow conduction to take place when the anode voltage is re-applied.

2.6.2 The EEV CX-1573 Deuterium Tetrode Thyratron

For certain applications, of which this laser is one, the variation in firing time may need to be reduced still further than that obtained with the triode thyratron. The development of the tetrode thyratron has improved on the switching characteristics.

The tetrode thyratron differs from the conventional triode in that it has an extra grid. This allows a variety of ways for driving the pair of grids. The fast switching method is applicable in this system, and it is recommended that grid-1 should be DC primed and grid-2 be driven by a fast rise, low impedance, high amplitude pulse. Grid-1 performs the function of ionising the gas between itself and the cathode, whilst grid-2 performs the gating function when pulse driven above its negative DC bias level. The negative bias on grid-2 is essential for tube control, since it prevents the priming current on grid-1 from causing a continuous state of conduction. Cathode damage caused by prefire is prevented by the DC drive to grid-1. The grid-2 bias and grid-1 DC excitation circuit is shown in Fig. 2.16. Here, a separate cathode and reservoir heater transformer is used, such that the rectifier transformer can be mains fed instead of from the heater supply. This avoids increasing the rating of the transformer supplying the heaters and the use of two transformers in cascade.

2.7 COMPARISON OF SPARK-GAP AND THYRATRON TECHNOLOGIES

A comparison was made of the operating characteristics of an in-house constructed spark-gap, and the EEV CX-1573 thyratron for switching pulse currents suitable for laser operation. It was already known that the thyratron offered the capability to go to much higher repetition rates while still being capable of handling the same average power (since these devices had primarily been developed a radar modulators). It was therefore decided to look at the dissipation of energy in both devices when operated under the different load conditions of the CO_2 and excimer laser discharges.

2.7.1 Temperature Measurements of a Spark-Gap

The spark-gap was used in the circuit configuration given in Fig. 2.17 with a compact, high prf, CO_2 laser [2.13] available within the M.G.L. group. The spark-gap consisted of two electrode plates mounted between a Delrin spacer block, which had to be capable of withstanding a few atmospheres of N_2 used to hold-off the DC voltage, making the electrode separation 10mm. The profiled electrode caps were made of Elkonite which was more resistant to discharge erosion. The grounded electrode incorporated a Champion spark-plug that was used to trigger the spark-gap once the laser was ready to fire.

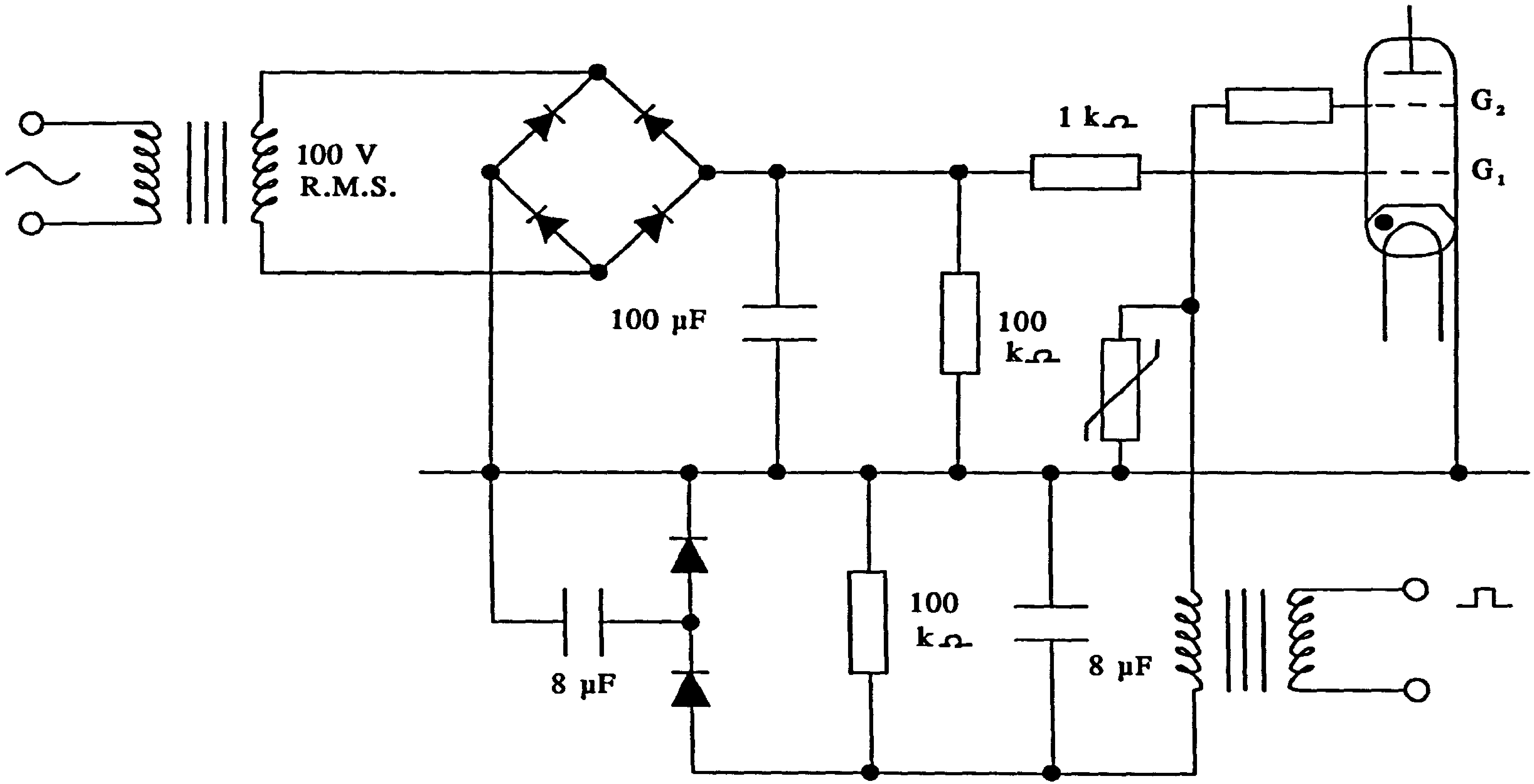

Fig. 2.16 Thyratron driver circuit: grid-1 DC excitation and grid-2 bias

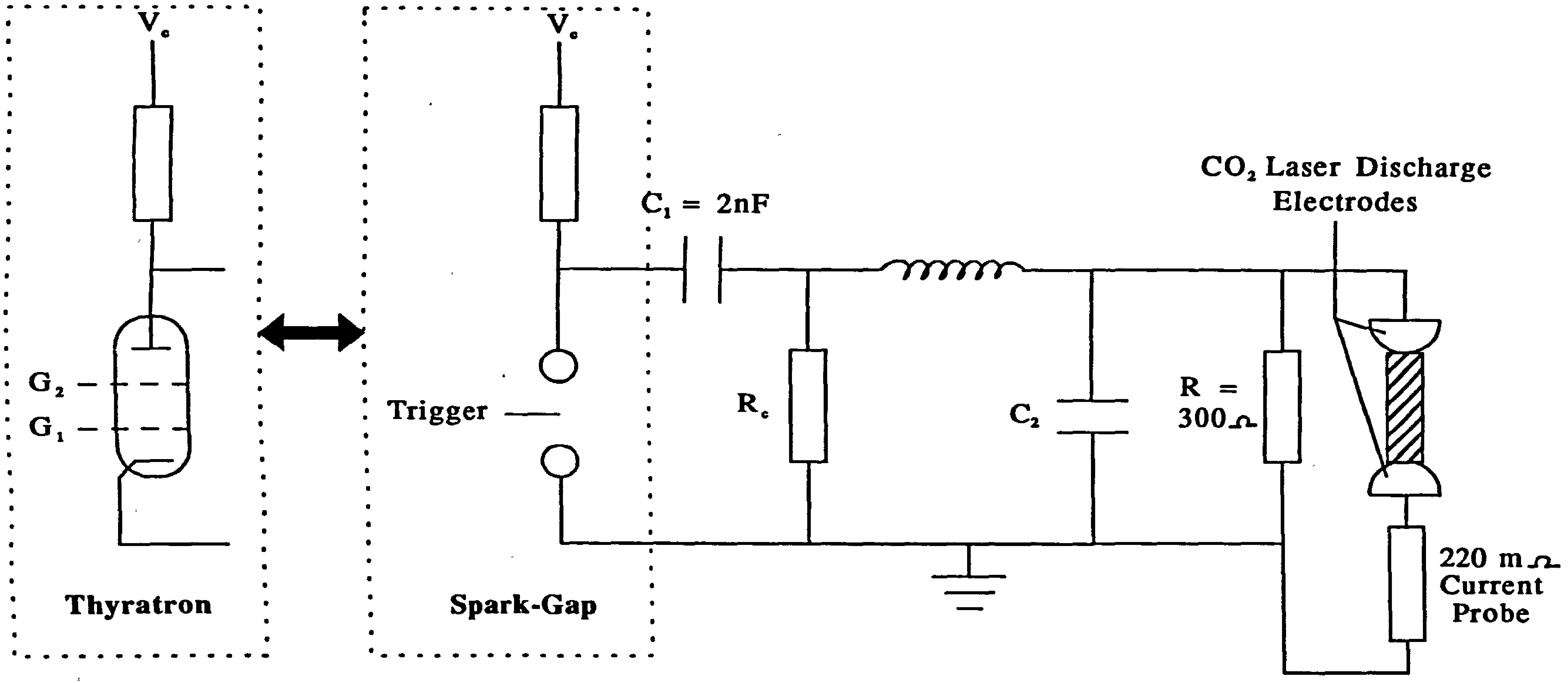

Fig. 2.17 Circuit diagram for comparison of spark-gap and thyratron technologies

Thermocouple temperature probes were mounted to both top and bottom electrodes, and the temperature monitored as a function of time (Fig. 2.18) whilst the discharge fired at a repetition rate of 60Hz. For a main discharge capacitor of 2nF charged to 25.2kV, a power of 38W was switched through the spark-gap. The temperature was monitored until thermal equilibrium was reached (~80 minutes) at which time the discharge was switched off and the spark-gap allowed to cool, once again monitoring the temperature. It can be seen from Fig. 2.18 that typical steady temperature rises of 28°C and 36°C resulted at the anode and cathode.

A resistive heating element was then placed inside the spark-gap, between the electrodes, to measure just how much power had to be put into the spark-gap to induce a 32°C temperature rise. The first resistive heater put a total of 9.27W into the spark-gap producing the temperature curve shown in Fig. 2.18. Assuming that the temperature gradient is linear across the spark-gap, this power input was not quite sufficient to provide the temperature rise. A second heating element, that produced 9.85W, was placed into the spark-gap, and its temperature effect recorded (Fig. 2.18). This produced a curve that lies equidistant between those curves measured for the top and bottom of the spark-gap when the discharge was running. This means that 26% of the 38W being switched by the spark-gap, was being dissipated as heat in the switching process.

2.7.2 Temperature Measurements of a EEV CX-1573 Thyratron

Initial experiments were carried out by replacing the spark-gap with the thyratron in Fig. 2.17. Thermocouple temperature probes were then placed $\frac{1}{3}$ of the way between the anode and grid-2, and also close to the cathode. The thyratron posesses two heaters, one for the cathode (135W) and one for the

Fig. 2.18 Temperature of the spark-gap with the laser running @ 60Hz, or with a resistive heating element.

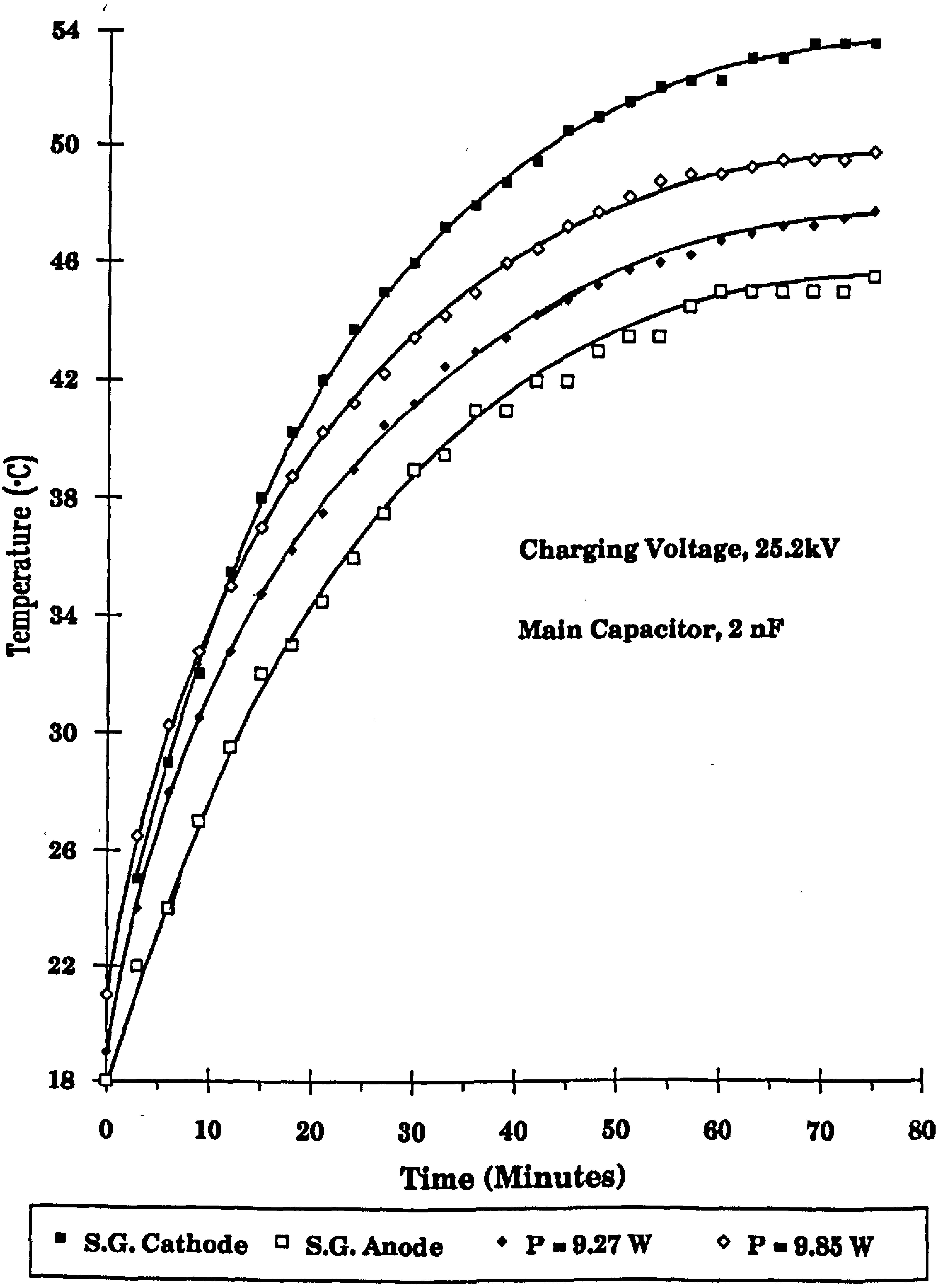

reservoir (35W), delivering a total of 170W. According to the manufacturers specifications the thyratron should be left to warm-up for 15 minutes prior to operation, which allows the thyratron to exceed the minimum thyratron envelope temperature, for operation, of 75°C.

After switching on the thyratron, it was allowed to come into thermal equilibrium ~80 minutes later (Fig. 2.19). The discharge was then run under the same conditions as the spark-gap at 60Hz until the temperature stabilised, once again ~40 minutes later (Fig. 2.19). Based on the input power of 170W, due to the thyratron heaters and corresponding 120°C temperature rise, the power consumed by the thyratron in switching 38W of power was estimated:

$$\frac{120^\circ C}{170W} = \frac{9.25^\circ C}{P_{LOST}} \; ; \; P_{LOST} = 13W$$

Therefore, under these conditions 34% of the power being switched by the thyratron was being dissipated as heat and not being transferred to the discharge. At a later date, the same type of measurement was made for the thyratron running an excimer discharge (Fig. 2.20). The main discharge capacitor, in this case, was 15nF with the charging voltage set to 25kV, resulting in 280W being switched at 60Hz. Performing the same calculation as for the CO_2 case, it is found that the power consumed by the thyratron in its switching process is 75W or 27% of the input power.

2.7.3 Thyratron/Spark-Gap Comparison Conclusions

In conclusion, there does not seem be any major benefit to operating at low repetition rates with a thyratron, other than convenience in that it does not require additional gas sources for its operation. The spark-gap had marginally

Fig. 2.19 Temperature of the thyratron envelope during warm-up, and with the laser running @ 60Hz and with 38W being switched.

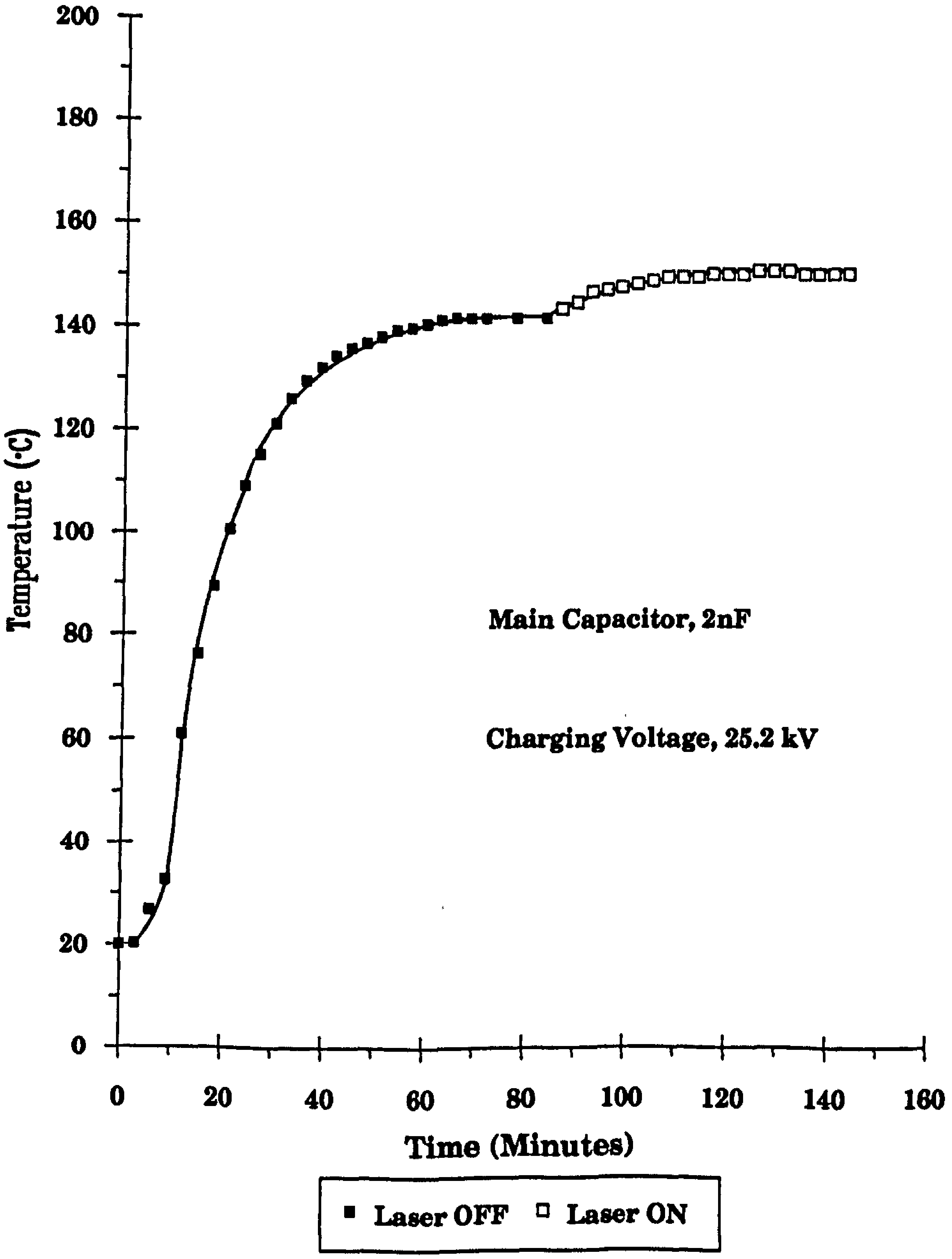

Fig. 2.20 Temperature of the thyratron envelope during warm-up and operation as a function of time.

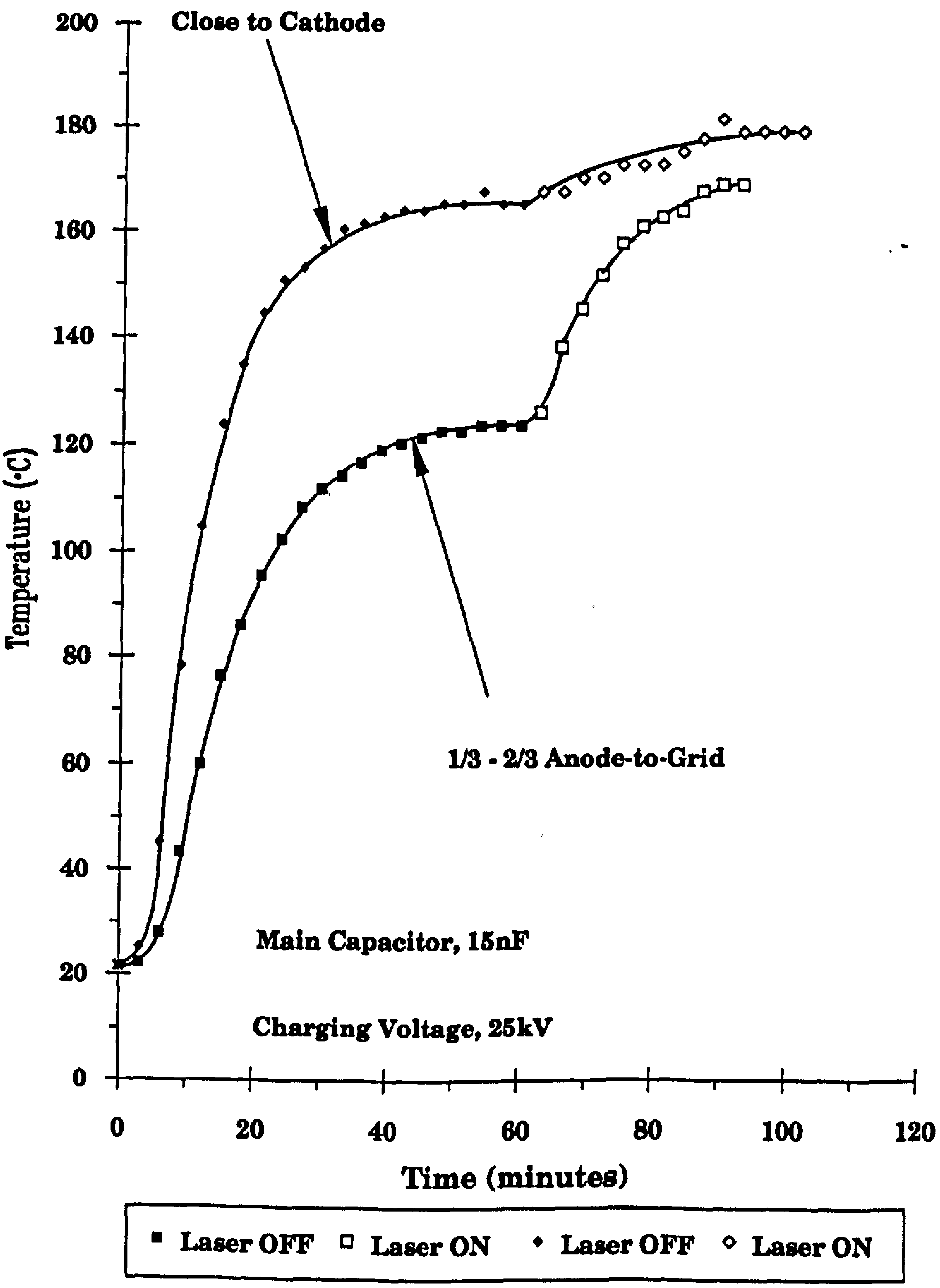

lower power consumption in the switching mode, but at higher powers and with a well conditioned thyratron this difference dropped to zero. Lifetimes of thyratrons are significantly better than spark-gaps, but to anybody operating at low prf's this is not really an issue. Also, the initial price of the spark-gap is significantly lower than that of the thyratron. Where the thyratron comes into its own is in the switching of high prf (> few hundred Hz) devices. Here the spark-gap is unable to compete in operation, or in terms of longevity.

2.8 THE ELECTRICAL CIRCUIT

In the design of any laser system, consideration must be given to both electrical and physical layouts of the pulse power circuit. In an excimer discharge pumped laser circuit, a number of special issues must be taken into account:

(a) the discharge impedance of the discharge drops to $<1\Omega$ during breakdown of the electrode gap, and it is therefore difficult to match the circuit impedence to that of the discharge;

(b) the laser pulse is typically over in <20ns in a discharge pumped device, and therefore care must be taken to minimise the rate of rise of both the current and voltage pulses;

(c) negative going high current pulses (~a few kA) tend to occur in such devices except under well damped conditions, this can lead to excessive wear in the pulse power and laser discharge components;

(d) efficiences of discharge pumped devices are, at best, only a few percent;

(e) operation will be in the 15→40kV region;

Additionally, in the present application, the power being switched was ~3000W at repetition rates of ~1000Hz.

These factors dictate the component specifications. The main discharge capacitor must be of the low impedance type to meet the fast switching characteristics required, and to be capable of operating at high powers and high prf's. The high voltage switch, or thyratron in this case, must be able to be switched in the region of a ns; operate at voltages in excess of 35kV; handle the power and prf requirements; and also be relatively robust, to withstand the negative going high current pulses that can, and will, occur.

In order to gain an appreciation of the physical relevancy of some of the issues, the completed laser chamber was set up to investigate and determine the circuit configuration that would be most applicable once the rest of the ductwork was completed.

2.8.1 Initial Studies

An outline of the circuit configuration used for this laser is shown in Fig. 2.21. As has previously been described, an English Electric Valve Co. CX-1573 tetrode thyratron was selected for the switch since, having no experience of thyratron selection, it offered the voltage and switching speed criteria already laid out at the beginning of this section. The main discharge capacitor selected was made by Maxwell Laboratories Inc. with a single ended connection, which reduced the effective inductance of the capacitor. The capacitor was also capable of operation at high prf's, ~500Hz. This type of laminated capacitor is very rugged in construction, lending itself very well to this application.

Initially, the whole circuit was mounted on a grounded base-plate adjacent to the main laser head, without the ducting, and with the voltage fed by two high voltage co-axial cables into the laser head. The cavity configuration,

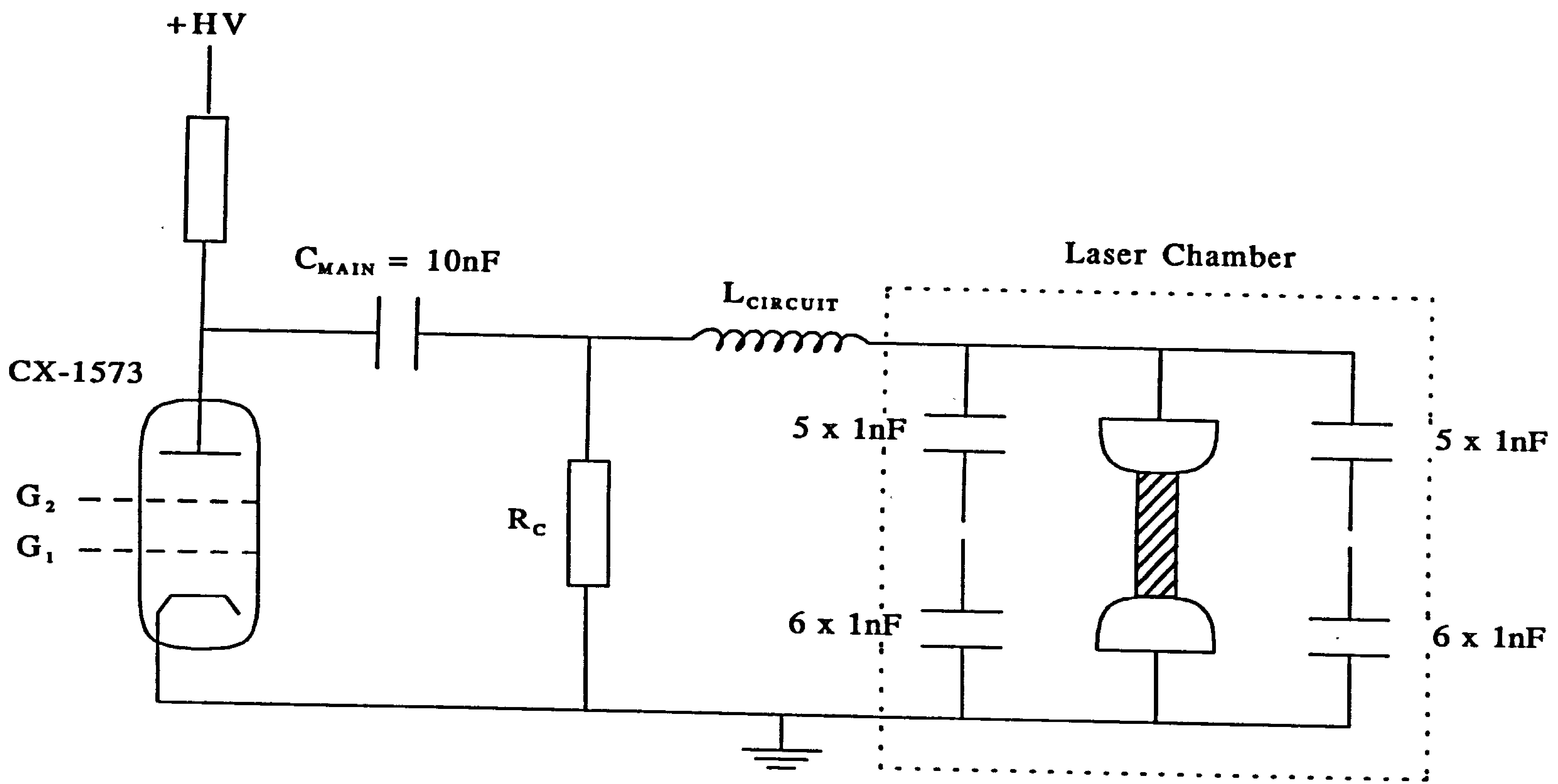

Fig. 2.21 Initial high repetition rate laser circuit configuration

used in this case, consisted of a pair of fused silica windows on the end of the chamber and an external mirror.

The electode gantry (Fig. 2.21), used in these initial studies, consisted of a pair of nickel Chang profile electrodes along with a "doorknob" capacitor spark array to provide the uv preionisation. A more detailed discussion of the design can be found later in this thesis in Section 3.3.1.

The gas mix for XeCl operation was chosen to be similar to that used in a slightly larger device (*viz.* 2210 torr He: 60 torr Xe : 10 torr HCl) but with this, only weak lasing occured. Initially, it was thought that the gas mixture may have been incorrect and was changed. The overall pressure in the chamber was raised to 4 atmospheres (absolute) with a 2963 torr He : 60 torr Xe : 17 torr HCl mix. Again, however, lasing barely occured. The pressure was reduced to 3 atmospheres, but lasing only increased to a few mJ. Since these experiments proved inconclusive, it was felt that a reduction of the circuit inductance should be tried next.

2.8.2 Final Configuration of the Electrical Circuit

The "speeding-up" of the circuit was achieved by mounting the capacitors and thyratron very close to the high voltage feedthroughs, Fig. 2.22. The Maxwell capacitor was mounted vertically above the two feedthroughs, being connected on one side by a copper stripline. A second copper stripline on the other side of the capacitor was connected to the anode cup of the thyratron, which was mounted horizontally. The use of the closely coupled striplines obviated the need for the two high voltage co-axial cables, and significantly reduced the inductance of the circuit. The circuit inductance was calculated to be ~220nH (Appendix-3).

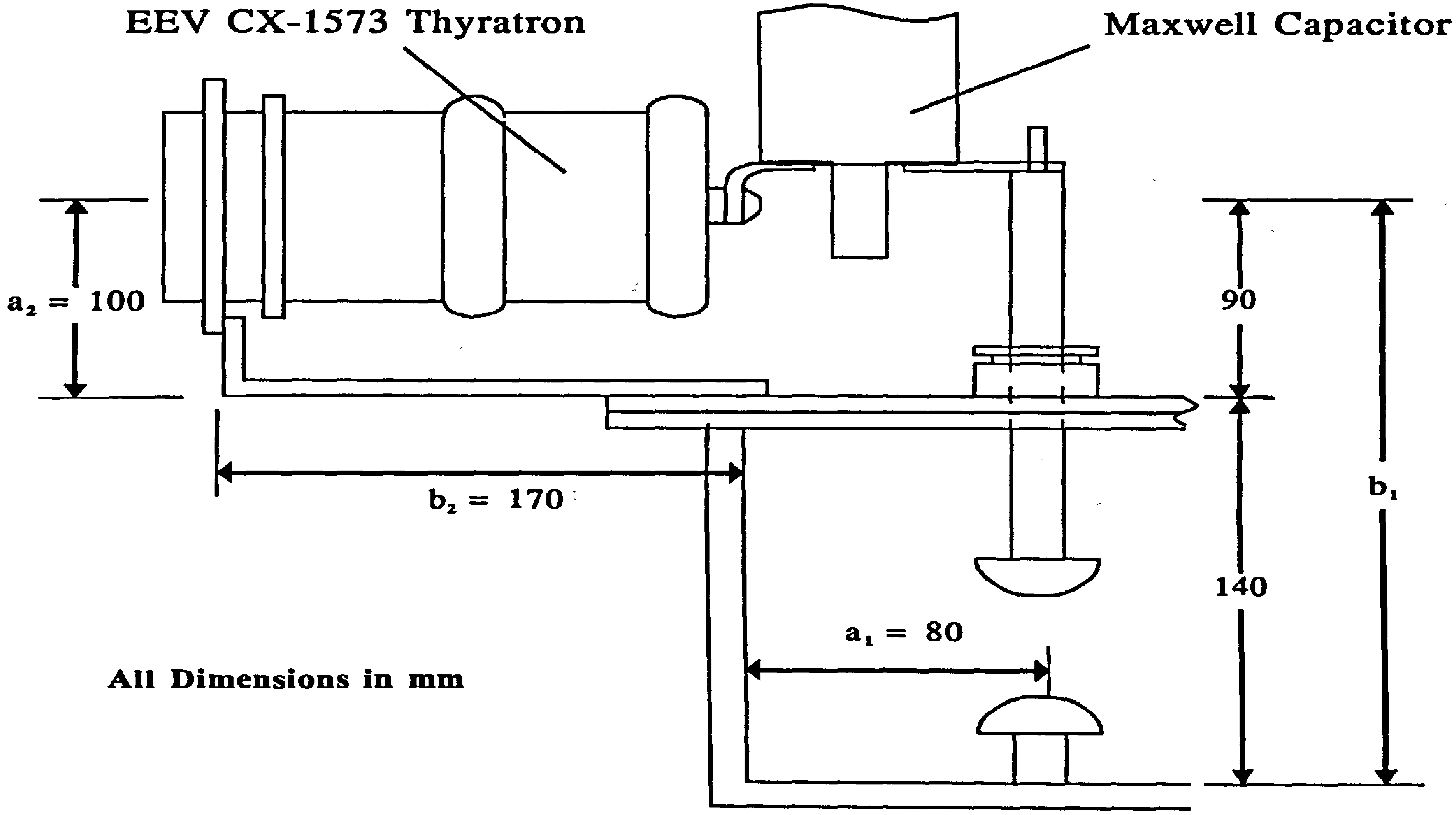

Fig. 2.22 Schematic of the high speed circuit design including the parameters used for the inductance calculation in Appendix-3

With this circuit, and the same gas mix as in the previous section, lasing occured but was still erratic, so the pressure was dropped producing a slightly more stable discharge and ~2→4mJ output. It was at this time that reflections were noticed coming off the electrodes. As a consequence the laser resonator was realigned. The overall pressure in the laser chamber was then raised to 4 atmospheres such that the gas mixture was:

2978 torr He : 48 torr Xe : 14 torr HCl

Output laser energies from this configuration were ~10→18mJ. This mix was then left in the chamber overnight to condition the system and when tested seemed to produce a more steady output. The fluctuations, however, were still ~10→20mJ.

The circuit at this time was deemed to be operating satisfactorily, and work was then carried out on the optimisation of the gas mixtures (see Chapter 3) for more information on these results). Minor modifications occured at various stages of the rest of the program, but this circuit design was primarily used with the completed tunnel design. The introduction of the ALE 302L power supply later in the program, brought with it its own set of problems, mainly related to protection of the device. Other changes such as replacing the Maxwell capacitor with discrete ceramic capacitors, or varying the charging resistor so that the circuit could be tuned, will be discussed also in Chapter 3.

REFERENCES

[2.1] R.TENNANT, LA-UR-81:559, Los Alamos National Laboratory, NM, (1981)
R.TENNANT, Laser Focus, 17, 65 (1981)

[2.2] R.TENNANT & N.PETERSON,
LA-UR-82:2268, Los Alamos National Laboratory, NM, (1982)

[2.3] P.E.CASSADY, G.MULLANEY & S.R.BYRON, SPIE, 279, 18 (1981)

[2.4] J.L.MILLER, J.DICKIE, J.DAVIN, J.SWINGLE & T.KAN,
Appl. Phys. Lett., 35, 912 (1979)

[2.5] R.C.SZE & P.B.SCOTT, SPIE, 190, 305 (1979)

[2.6] T.S.FAHLEN, IEEE J. Quant. Elec., 16, 1260 (1980)

[2.7] R.C.SZE & E.SEEGMILLER, IEEE J. Quant. Elec., 17, 81 (1981)

[2.8] K.RAJ & C.REISER, Laser Focus, 15, 56 (1979)

[2.9] Private Communications,
Mechanical Engineering Department, University of Hull

[2.10] GENERAL ELECTRIC CO., "Fluid Flow Data Book" (1977)

[2.11] ASME, "Boiler and Pressure Vessel Code" (1971)

[2.12] R.C.PANKHURST & D.W.HOLDER,
"Wind Tunnel Techniques", Pitman (1952)

[2.13] P.E.DYER & B.L.TAIT, Appl. Phys. Lett., 37, 356 (1980)

3. LASER DISCHARGE AND PERFORMANCE STUDIES

During the studies carried out of the laser discharge and the relative performance of this laser, several design iterations took place. Initial studies at low repetition rates, ~1Hz, took place with an electrode gantry design based on the capacitively coupled preionisation scheme developed for the pulsed CO_2 laser by Burnett and Offenburger [3.1]. An extension of this design, into one that included a venturi flume to increase the gas flow velocity between the electrodes, eventually resulted in the finished tunnel design being capable of repetition rates exceeding 1kHz. Other preionisation schemes were also investigated, including resistively-ballasted uv preionisation based on the work by Alcock *et al* [3.2], and also, a coronal preionisation scheme from the work by Marchetti *et al* [3.3].

3.1 GAS MIXTURE OPTIMISATION

Gas mixture optimisation in any laser system is not straight forward, since it is dependent on a number of factors such as charging capacitance, electrode configuration, charging voltage, overall pressure and choice of buffer gas. This is further complicated in a high repetition rate device which is capable of operation at sub-1Hz and up to levels exceeding 1kHz, because different gas mixtures are required to cover the range of operation. In tests carried out, optimisation for this laser was restricted to two categories:

(i) Firstly, the case where no ducting or no flow is present, that is to say the single-shot mode.

(ii) Secondly, with flow, when the laser is operated in a low (>50Hz) to high pulse repetition frequency mode.

Similarities in the results can be seen; although there is no hard and fast relationship, some general trends can be discerned. Gas optimisation in this section was carried out using the capacitively coupled preionisation scheme that will be discussed in Section 3.3.1 of this chapter.

3.1.1 Single-Shot Mode

In this case, there was no ducting attached to the laser head, and hence no flow, limiting the prf to less than 5Hz. Starting with a rich Xe gas mixture (e.g. 80torr) and a known concentration of HCl, the energy was monitored as the overall pressure was increased from 1 to 4 atmospheres absolute with, at first, helium being used as the buffer gas. This gas mixture was then pumped down and re-buffered with helium according to a preset scheme, in order to extract the maximum amount of information i.e. the effect of a change in the gas composition on laser energy. At each pressure point, the voltage was varied between 25 & 39kV to measure its effect on the output energy. This procedure is then repeated, but with either a different procedure for the pumping down and re-buffering and/or a different gas composition.

Fig. 3.1 & 3.2 show results for 30torr & 80torr Xe mixtures with HCl concentrations from 0→16torr and for overall pressures in the range 2→4 atmospheres. Clearly, there is a distinct difference in the characteristics of the two graphs, in that for the 30torr Xe mixture the optimum pressure is at 4 atmospheres whereas in the 80torr case it is 3 atmospheres. Also the peak of the HCl concentration shifts to a slightly lower value for the 30torr Xe mixture. In order to conserve the very expensive xenon (~£6.60/litre, early 1984) it was decided to carry out further investigations with the optimum (30Xe:3HCl) torr ratio of gases added to the buffer gas under test.

For the helium buffered gas mixture, the energy was again monitored as a function of pressure, but this time with the charging voltage being varied

Fig. 3.1 Output energy as a function of HCl concentration: Xe=30 torr, 29 kV @ 1Hz

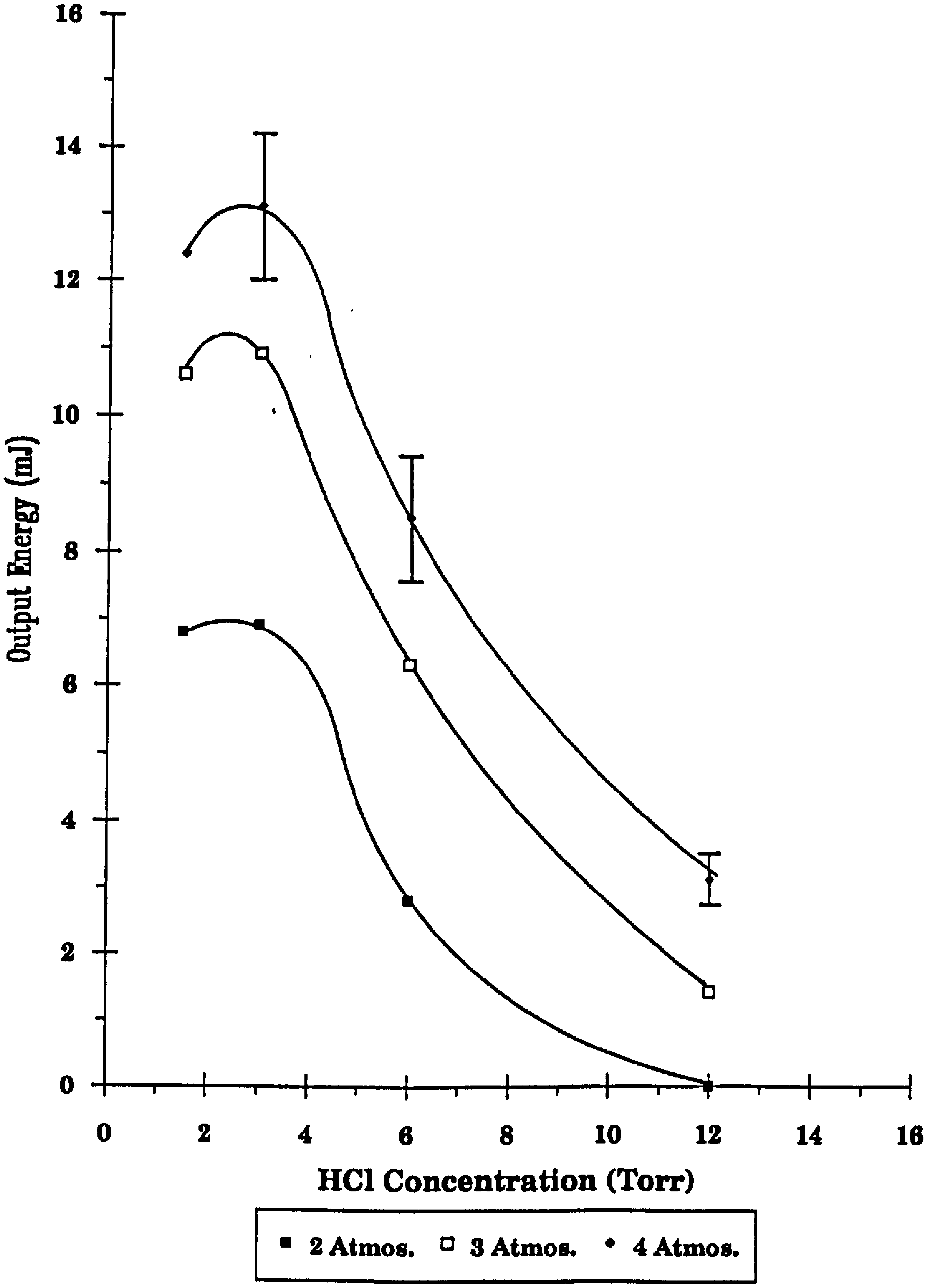

Fig. 3.2 Output energy as a function of HCl concentration: Xe=80 torr, 29 kV @ 1Hz

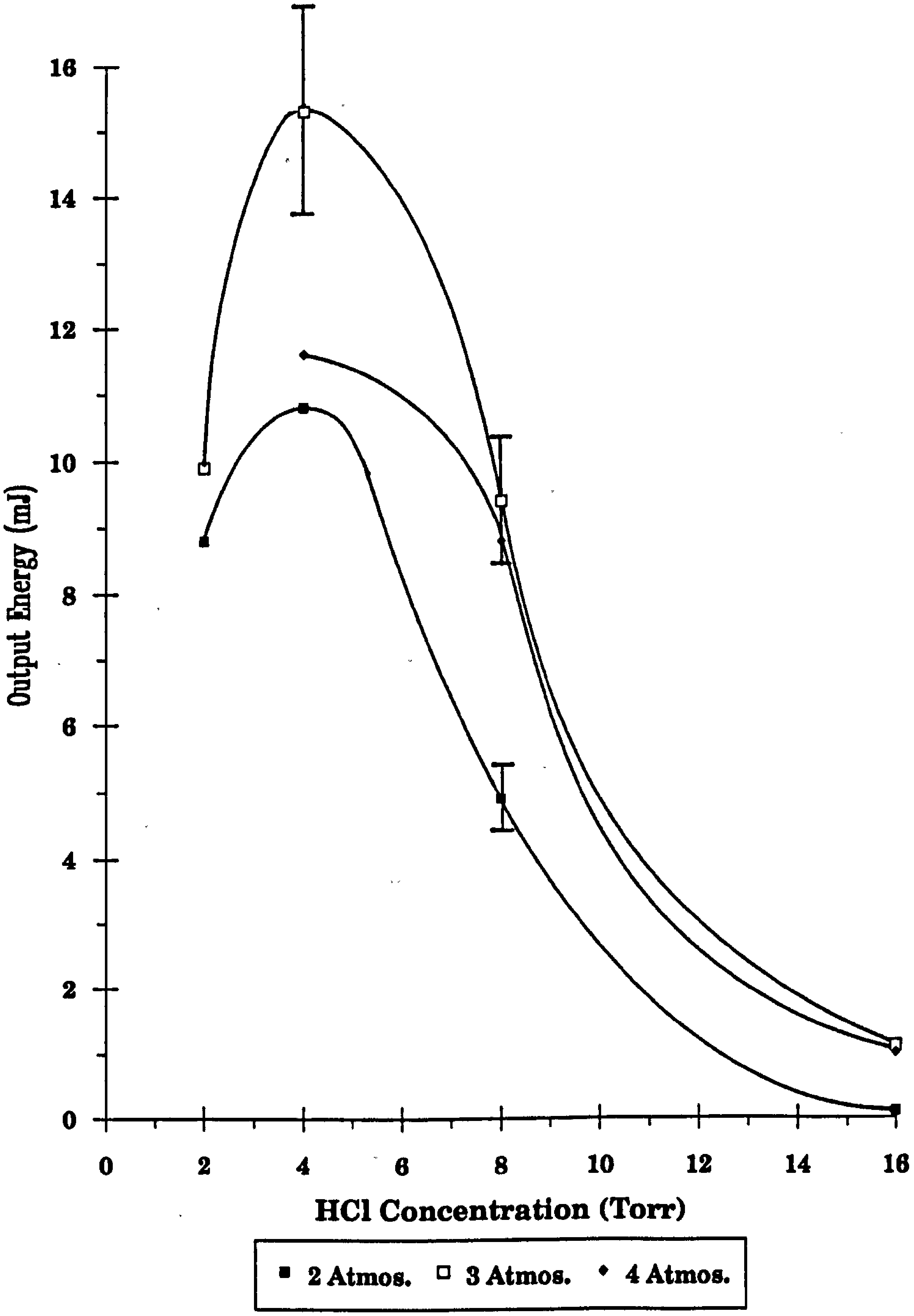

from 25→33kV. The results, shown in Fig. 3.3, indicate that at higher pressures the mixture requires the higher charging voltage to maintain the linear increase in energy. However, as the pressure is dropped, the dependence on the higher voltage diminishes, such that at 2 atmospheres it is beneficial to drop the voltage to at least 29kV because of the improvement in the efficiency. This procedure was then repeated for argon and neon buffered mixes using the same 30Xe:3HCl ratio.

In the case of argon buffered mixtures (Fig. 3.4) optimum operating pressures occured between 1.5 and 2 atmospheres depending on the charging voltage. The discharge was observed to be more striated due to streamer growth than for helium and neon buffered mixes. Operation above 2.5 atmospheres was hampered by the onset of arcing, and hence suffered from an erratic output. This mixture was much more dependent on the charging voltage over the whole pressure range, with the best energy recorded for 33kV operation at a pressure of 2 atmospheres.

For neon buffered mixtures (Fig. 3.5) the voltage dependency was once again weak, as for helium, but this time over the whole operating pressure range. Also, unlike both helium and argon, no optimum overall pressure, for all charging voltages, was obtained up to the pressure limit of the device (i.e. 4 atmospheres).

Figs. 3.6→3.8 represent the results, as discussed above, for the three buffer gases as a function of voltage. Clearly at lower voltages, neon is the preferred buffer gas at higher pressure with argon winning out at sub-1.5 atmospheres pressure. At higher voltages, the helium buffered gas mixture takes over from neon at high pressures, with argon's domain extending to pressures up to 2 atmospheres.

Fig. 3.3 Output energy as a function of operating pressure for helium buffered gas mixtures

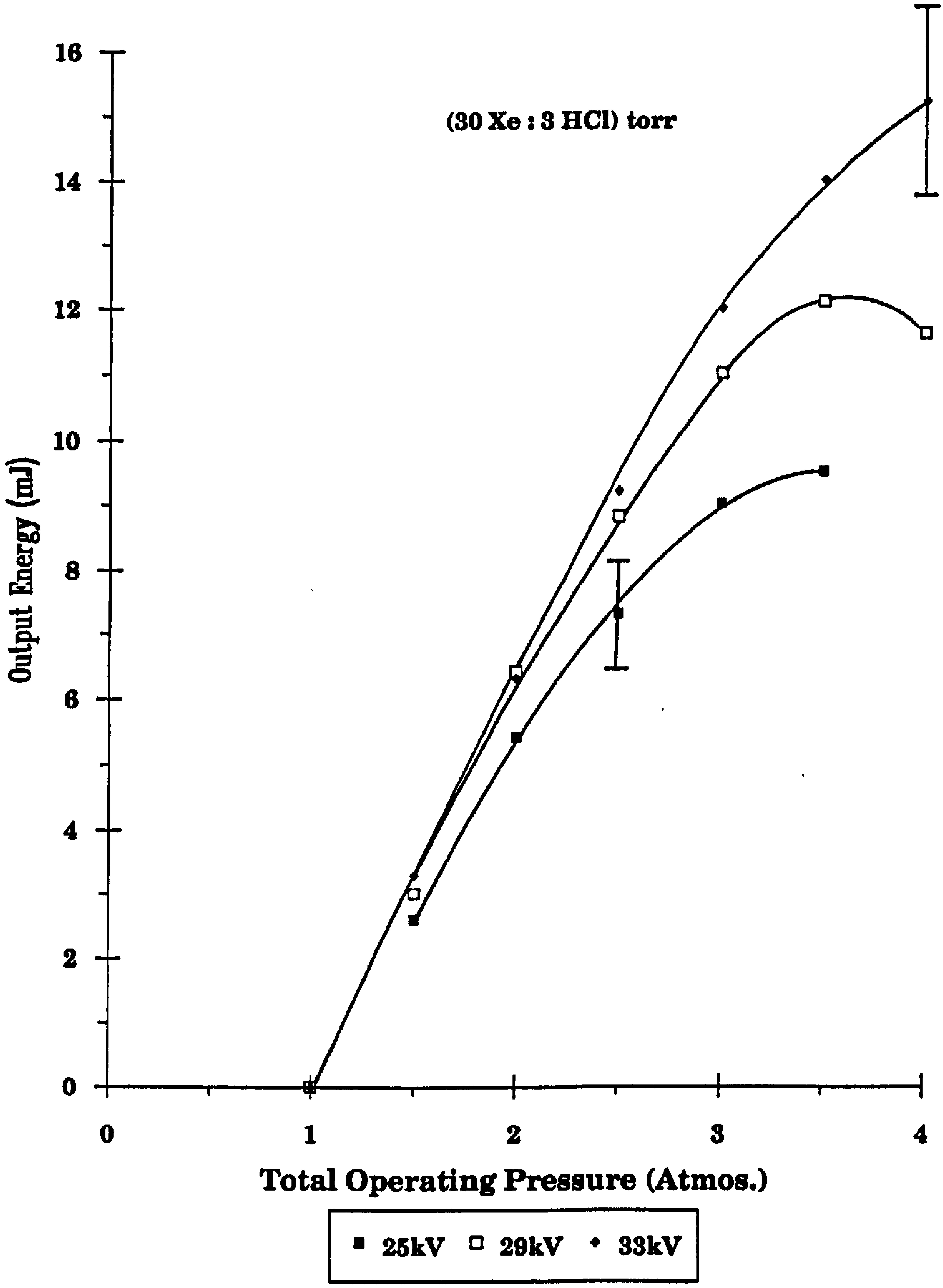

Fig. 3.4 Output energy as a function of operating pressure for argon buffered gas mixtures

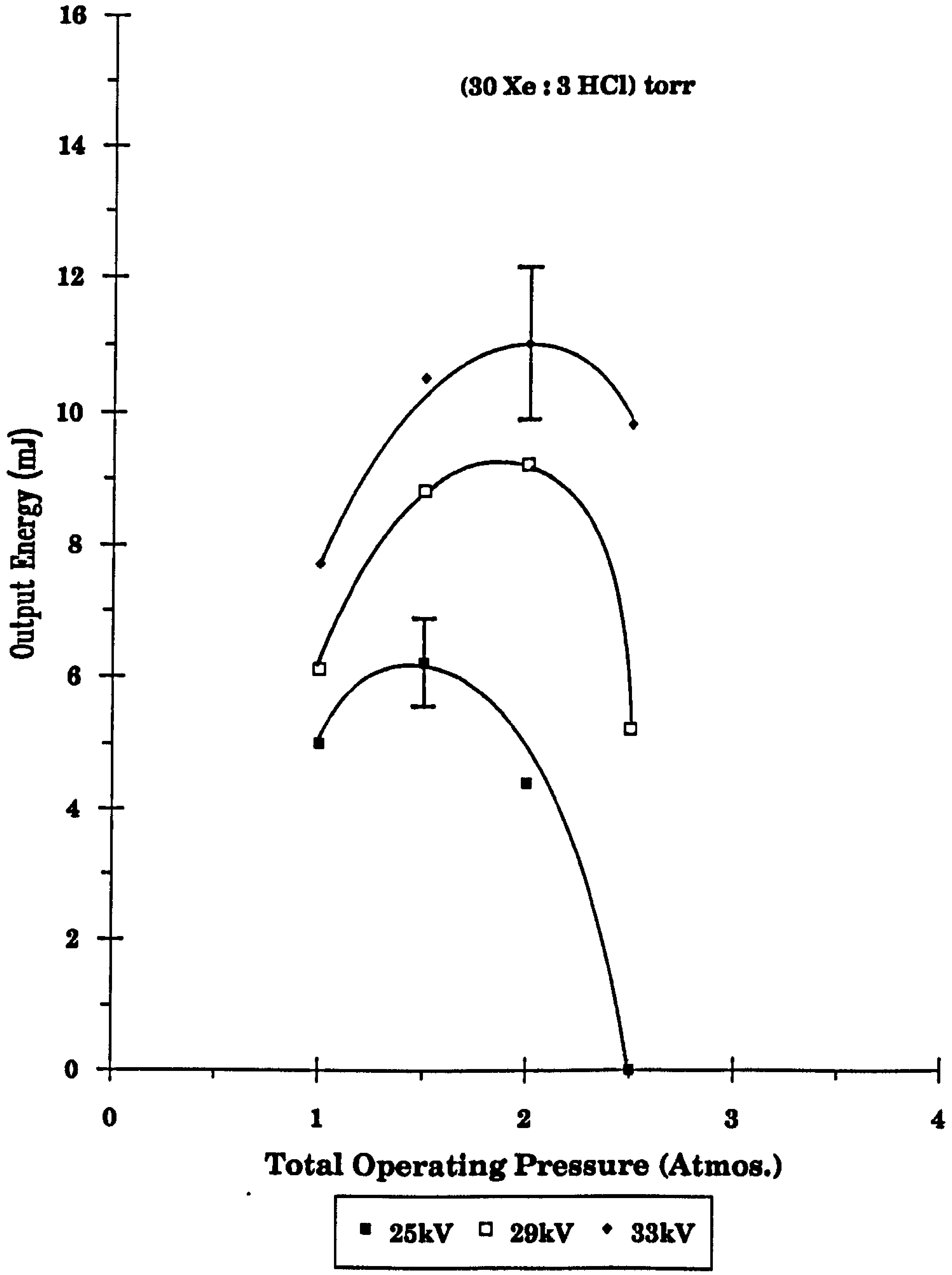

Fig. 3.5 Output energy as a function of operating pressure for neon buffered gas mixtures

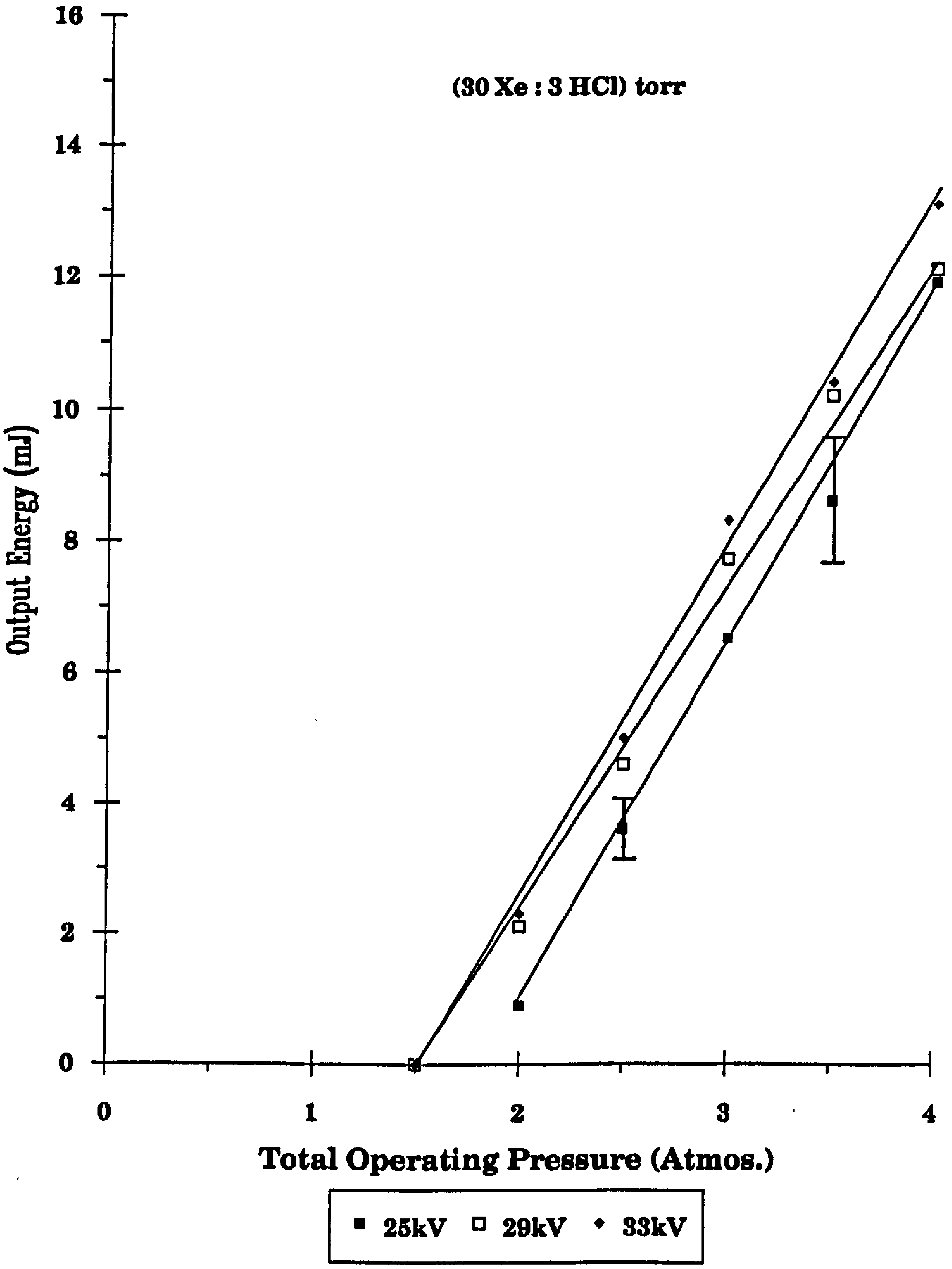

Fig. 3.6 Output energy as a function of operating pressure @ 25 kV

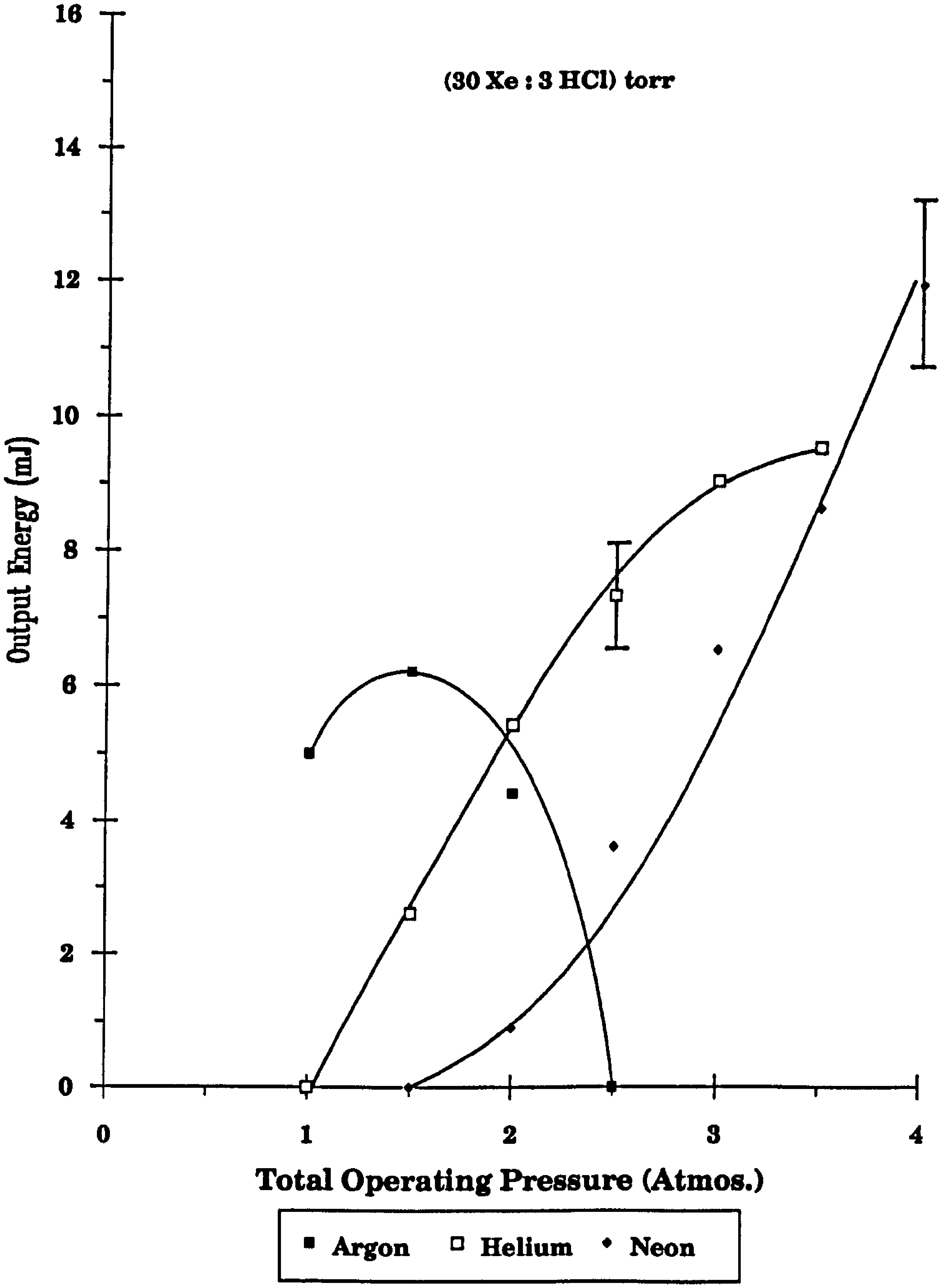

Fig. 3.7 Output energy as a function of operating pressure @ 29 kV

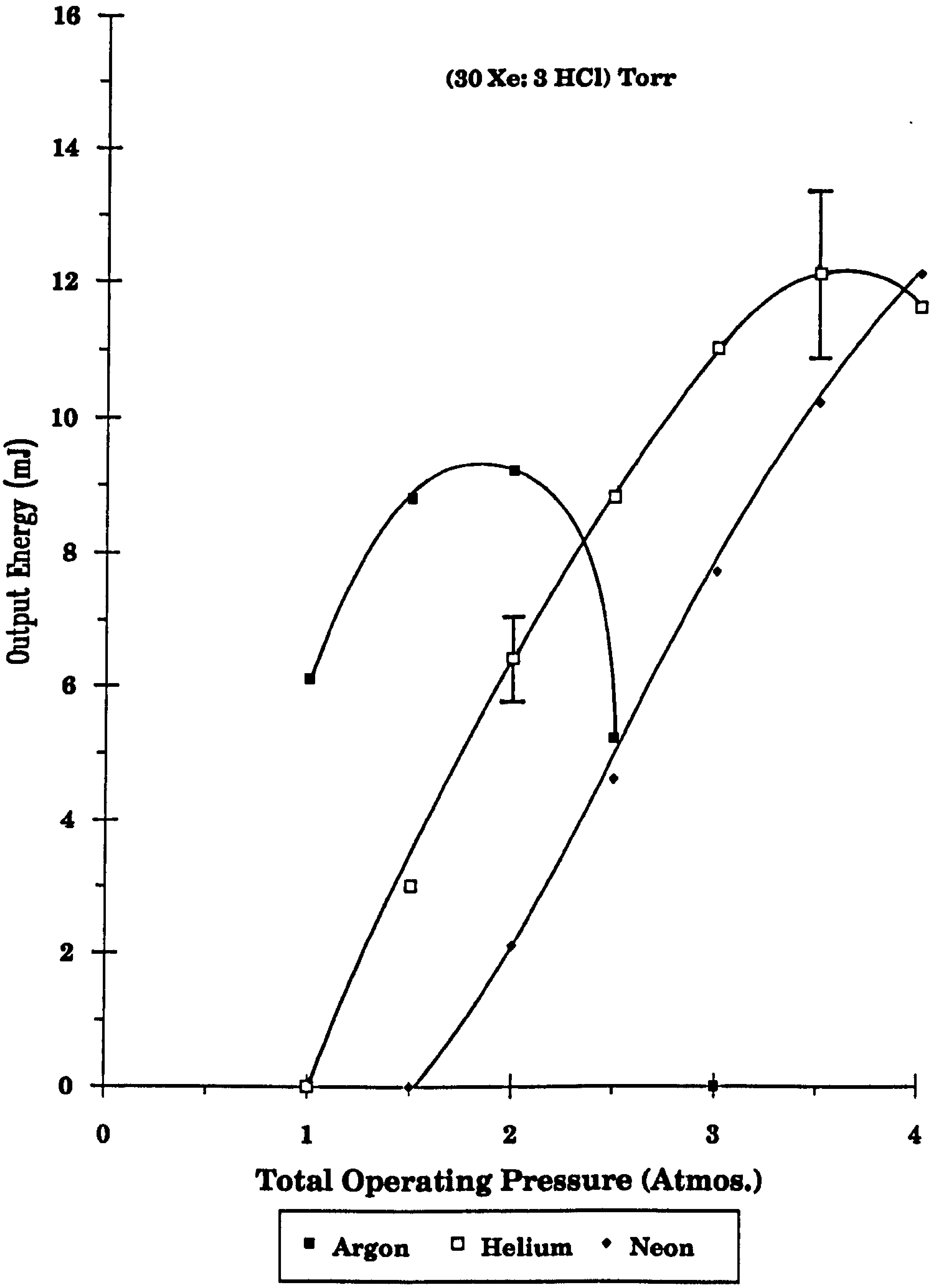

Fig. 3.8 Output energy as a function of operating pressure @ 33 kV

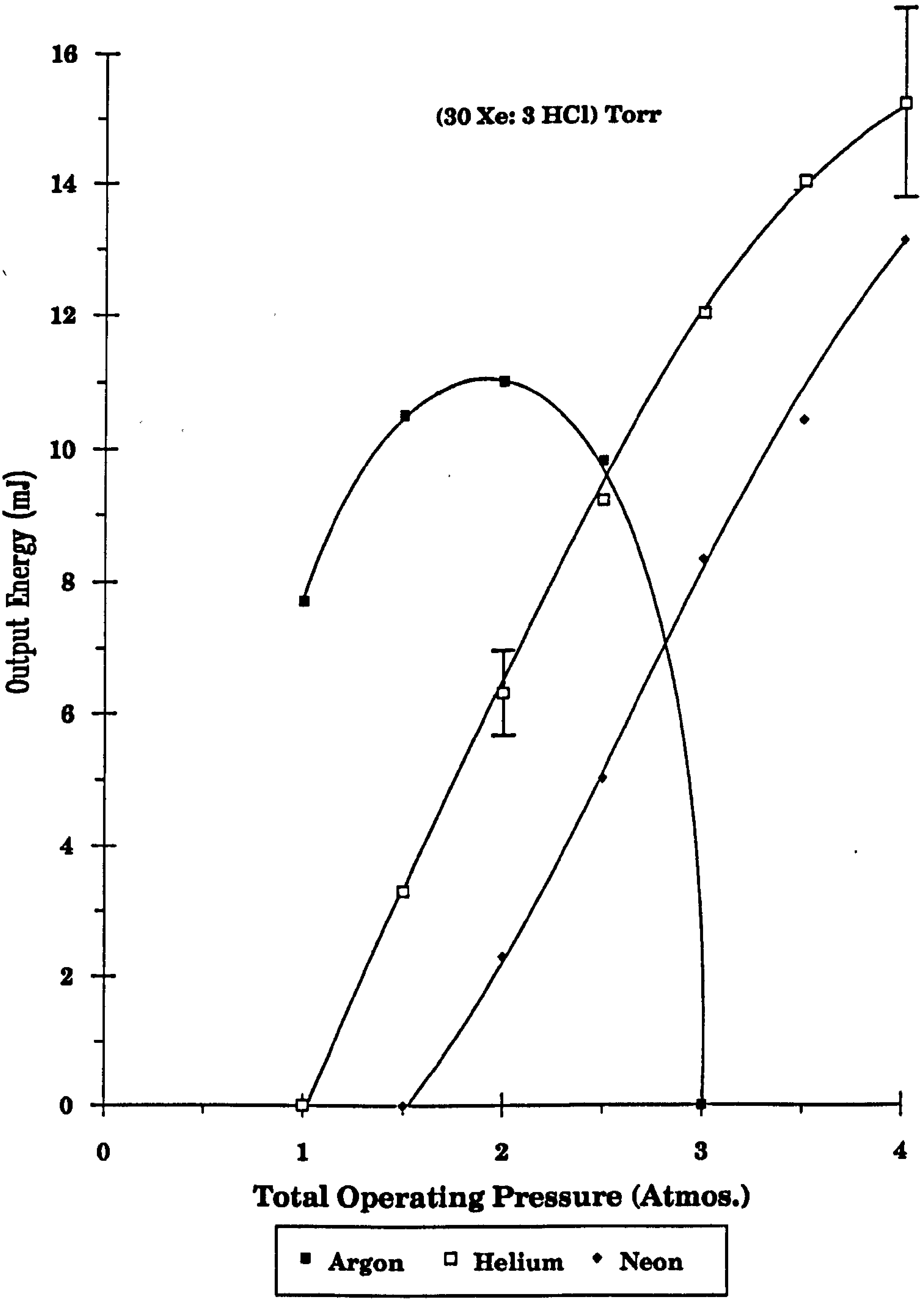

3.1.2 High-Repetition-Rate Mode

Upon completion of the duct sections, gas mixture optimisation was extended to slightly higher repetition rates (~50Hz): the procedure outlined in Section 3.1.1 was used, but this time varying the HCl concentration (Fig. 3.9) and then the voltage (Fig. 3.10) as a function of Xenon concentration. Irrespective of the rest of the gas composition, it is clearly seen in both cases that a saturation point for the partial pressure of the HCl concentration of ~2mbar is reached, and an optimal charging voltage of ~27kV for peak efficiency. These results will be echoed later in the sections on high repetition rate operation and investigations of different uv preionisation techniques. In those sections, it will be shown that for reliable kHz level operation, neon is the preferred buffer gas since lower voltages have to be used due to power supply limitations.

3.2 GAS LIFETIME STUDIES INVOLVING AN ELECTROSTATIC PRECIPITATOR [3.4]

An electrostatic precipitator is used for the collection of fumes, and fine solid particles, or dust, suspended in a gas stream by means of a high voltage, DC, electric field. In any transversely excited pulse discharge laser, where high peak currents are switched between a pair of electrodes, material is removed from the electrodes. This debris either collects under the force of gravity at the base of the the laser chamber, or, in the case of lasers with a gas recirculation system, will circulate the gas back through the discharge time and time again. In the later case, i.e. that of high repetition rate lasers, the debris generated is detrimental to the stability of the discharge, leading to the formation of streamers and eventually arcs, loss of gain, and dirtying of the optics. This in turn will result in a further increase in the material

Fig. 3.9 Output power, @ 50 Hz, as a function of HCl concentration for various xenon partial pressures.

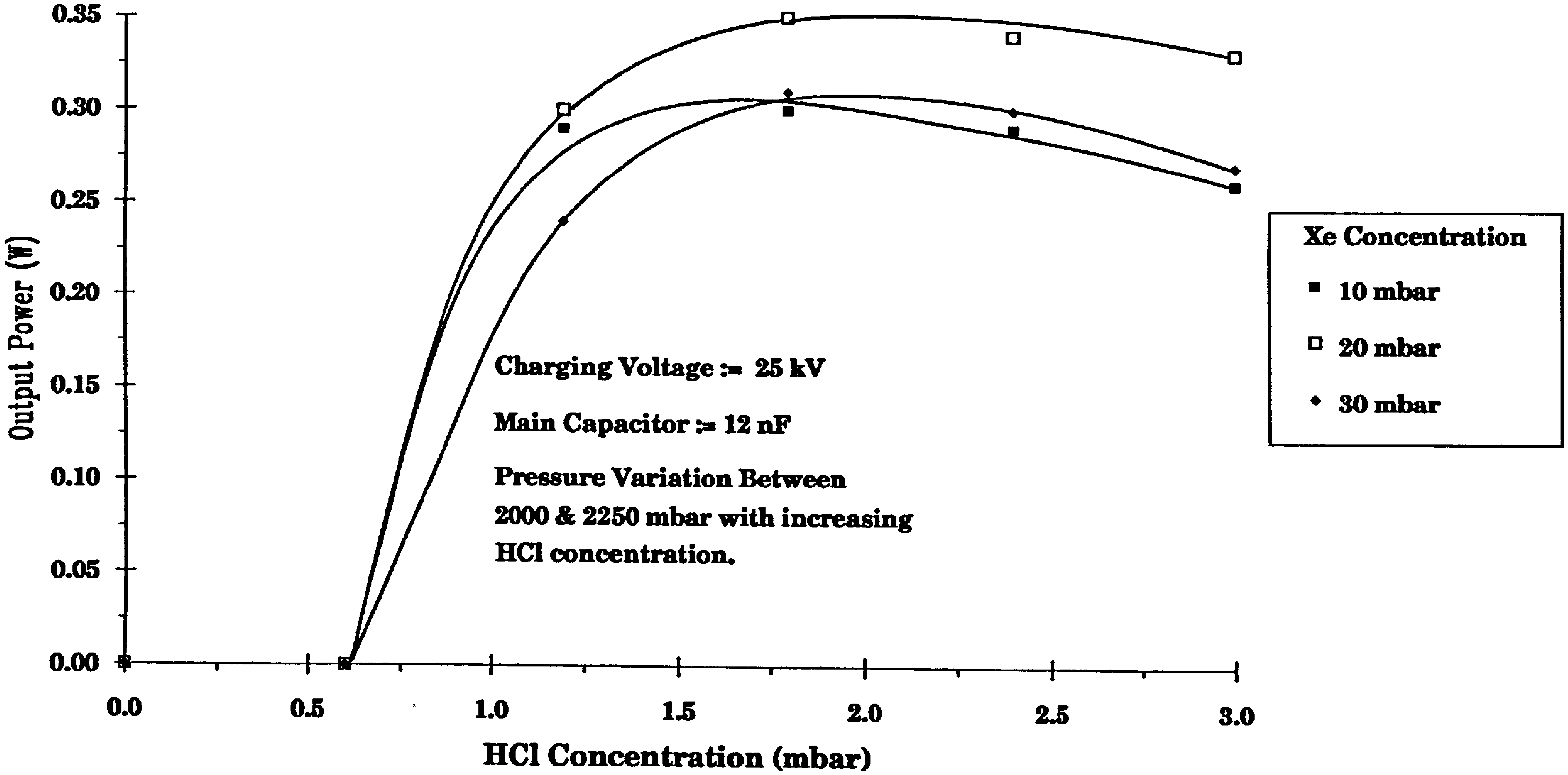

Fig. 3.10 Output power, @ 50 Hz, as a function of charging voltage for various xenon concentrations

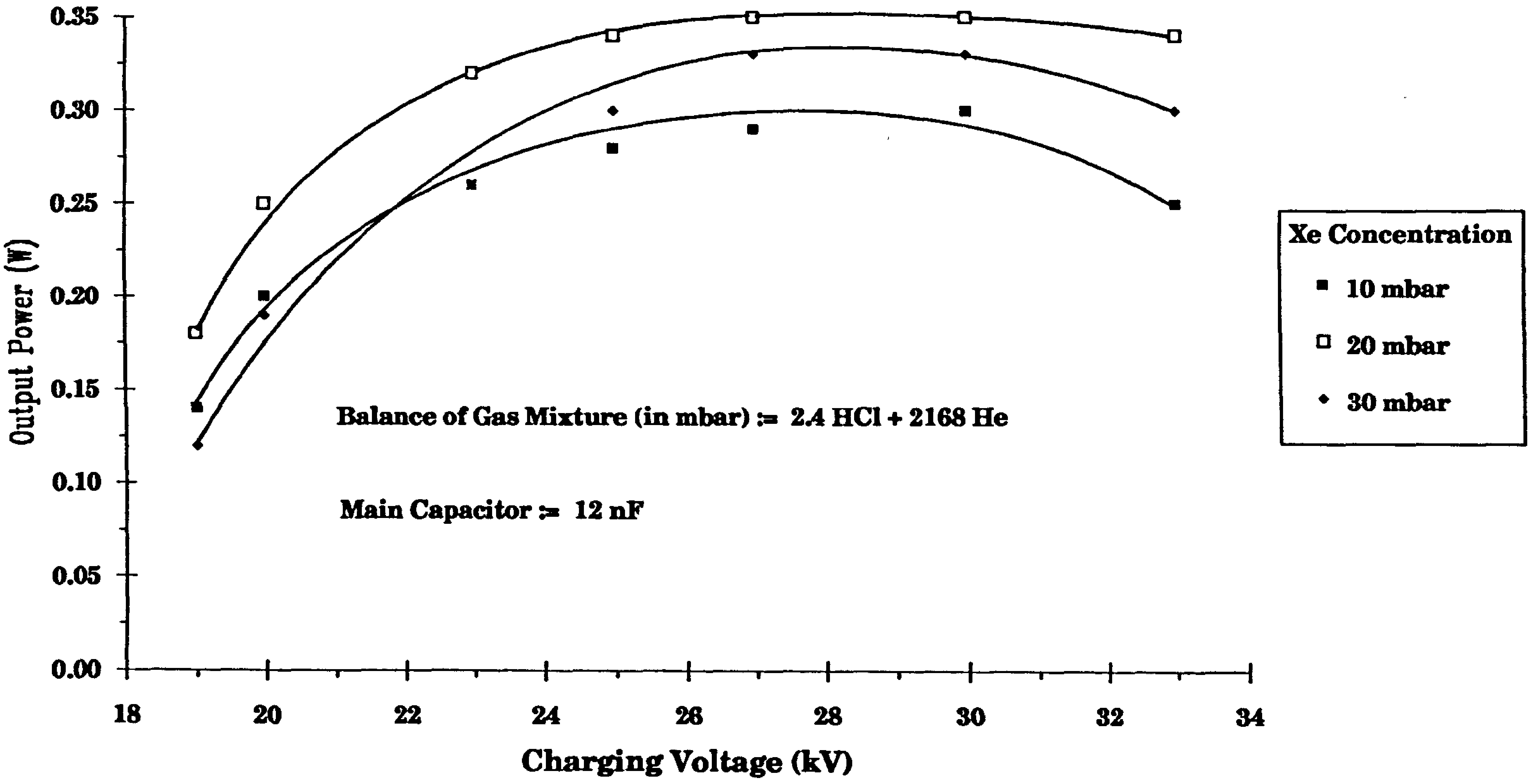

removal rate due to an increase in current density where high intensity discharges form. The rate at which material is removed by the precipitator is dependent upon a number of parameters including the peak current, the material removal rate (measured in $mg.C^{-1}$) which is material dependent, and the type of preionisation scheme used. In the case of excimer lasers, the conditions are quite extreme, leading to high material removal rates because of the very high peak currents, approximately several kA. It would, therefore, be beneficial to the operation of the laser to remove this dust, using an electrostatic precipitator.

3.2.1 Principles of Operation

The electrostatic precipitator is composed of a discharge electrode and collecting electrode. The coronal current, generated by applying a high voltage to the discharge electrode, flows to the collector plate where the ionised particles build-up in a dense layer. The mechanism by which the ionised particles move to the collector surface is by the intensity of the electric field. Precipitators are commonly built in one of three basic forms:

(i) a high-potential point (as the corona producing electrode) opposite a grounded plane (as the collecting electrode) with the gap between the two electrodes being large compared to the radius of the smaller electrode.

(ii) a grounded cylinder with a coaxial, high-potential, wire as the corona discharge electrode.

(iii) two grounded parallel plates, together with an array of parallel discharge wires mounted in a plane midway between the plates.

Gas with suspended solid or liquid particluates is then passed through either the tube, or between the plates. If a sufficient difference of potential exists between the discharge and collecting electrodes a corona discharge will form between them. The migration of ions across the intra-electrode space, due to the effect of the electric field, results in the ions attaching themselves to the particulates in the gas stream. These charged particles are then attracted to the collecting surface and hence extracted from the gas.

The initiation of the coronal discharge requires the availability of free electrons in the gas, in the region of the intense electric field surrounding the discharge electrode. As the potential difference between the electrodes is raised, the gas near the more sharply curved electrode breaks down, at a voltage less than the spark-breakdown value for the gap length in question. This incomplete breakdown is called *corona* and appears as a highly active region of glow, extending into the gas a short distance beyond the discharge electrode surface. The polarity of the discharge electrode determines the direction of the potential gradient, and the flow of the charged particles. Hence, the phenomena that develop will depend on the polarity of this electrode. The opposite electrode will be considered to be planar in geometry and be potentially grounded.

It is generally recognised [3.5] that negative (or cathode) corona, rather than positive (or anode) corona, is better operationally since it is inherently more stable. Hence, only cathode coronas will be discussed here.

3.2.2 Mechanisms of Negative Corona Formation (Static Fields)

When the negative voltage, applied across a point-to-plane gap, is gradually increased, a current is measured in the order of 10^{-14}A. No ionisation occurs, and in this case, the current is the *saturation current*, i.e. the first steady current to be observed without the onset of pulses. At a certain voltage, an abrupt current increase signals the development of an ionisation form that produces regular current pulses. These pulses were first studied in 1938 by Trichel, and hence are often refered to as *trichel pulses.* The voltage at the onset of corona does not vary much in magnitude with the point-to-plane separation, but is comparable with the onset of *streamers* (the equivalent in the anode corona case). Raising the voltage does not result in a change of the corona mode for a considerable voltage range (typically $10^{-6} < I < 10^{-4}$A). However, this region of existence of the trichel, transient, pulse is much larger than that for the streamer case. Eventually, a new mode of corona arises in which a steady current flows, and a glow is observed on the cathode. The onset of this glow is by no means well defined, but above this value the steady, glow corona continues to persist until spark breakdown occurs. In very large separation devices, yet another type of corona is observed between the glow and the spark, this being the negative feather (or streamer).

Trichel Pulses. Trichel pulses are extremely regular in both magnitude and their repetition frequency, also, the shape of the current pulse hardly changes. At the onset, the frequency is typically 2000 pulses per second (pps) which increases rapidly, but gradually with voltage, and eventually attains a maximum of a few $\times 10^6$ pps just before the onset of the steady glow. It never drops like the frequency of the streamers at the anodes [3.4].

Cathode Glow. When the voltage is increased beyond the critical frequency of the trichel pulses, a transition to a steady current flow suddenly, but not irrevocably, occurs. No large change in the average current accompanies this transition, with increases or decreases of 5% having been reported. The transition, from a trichel pulse corona mode to the pulseless mode, occurs when the *critical* trichel pulse frequency has been reached ($\sim 10^6$pps). The suppression of the trichel pulses and the early transition to glow has been observed to depend on the amount of electronegative constituents in the gas under observation. The glow mode of cathode corona differs from the trichel pulse mode, in that it is continuous rather than intermittent. The physical structure of the ionisation process is, however, the same for both modes.

Negative Feathers and the Transition to Spark Breakdown. The mode of cathode corona known as "negative streamers" (feathers) appears only at very nonuniform field configurations, and can thus be observed only at large electrode spacings and very high voltages. Feather-like traces emerge from the point in 3-dimensional space from the negative glow portion of the cathode glow, with their intensity decreasing gradually. The positive column shrinks to form the feather stem that extends towards the anode with very little or even no branching. The current, produced by the feathers, is composed of a steady component with superimposed regular pulses. The maximum range of these feathers is a function of the voltage and is rather independent of the inter-electrode separation in the vincinity of the cathode. The transition to spark, or to full breakdown, occurs in a similar fashion to that of the space-charge-free gap.

In general, the feathers increase slowly at first, then more rapidly as the voltage is raised and the feathers approach the grounded plane. When negative feathers approach the anode, positive "retrograde" streamers start to propagate toward them from the positive plane. The advance toward the negative feathers, results in the eventual transition to a fully ionised channel that constitutes a spark. Since positive streamers do not have a high conductivity channel, this stage does not necessarily constitute the completed breakdown. When two simultaneously propagating ionisation waves meet, that have tracks sufficiently high in concentration of ionised particles, a channel is completed with a conductivity high enough to cause instability in the current. This instability increases up to a point determined by the parameters of the outer circuit, until a highly ionised plasma channel, the spark, has materialised.

Negative feathers start at slightly higher voltages than their positive counterparts (streamers), and propagate much less in radial and axial directions. Therefore, at the same voltage the feathers are much smaller than streamers and hence more dificult to detect. Feather channels are wider than those of streamers, but the number of negative feathers never exceeds 8→10, whereas positive streamers can reach as many as 300→400 individual branches.

3.2.3 Performance Studies of an Electrostatic Precipitator

An electrostatic precipitator was designed to replace one of the copper cooling tubes that had been made redundant with the inclusion of the venturi flume. The device designed, mirrored the point-plane geometry mentioned earlier. A PTFE bar, 1" in diameter & ~12" in length, was bored down the centre to within an inch of the end, and a $^3/_8$" diameter copper bar was forced into the hole. The copper bar at the outlet end had been drilled to accept a banana-plug connection. A series of nickel pins were then forced, in a line, through the PTFE into the bar (Fig. 3.11). This provided point sources, with the corresponding water cooler below providing the grounded plane. The bar was then sealed into the duct work using an "o"-ring compression seal of the same type used for the coolers.

In the following discussion, it should be remembered that in no way are *totally pure* gases being referred to, since any commercially purified gas usually contains small amounts of impurities. Therefore any 'pure' gas in

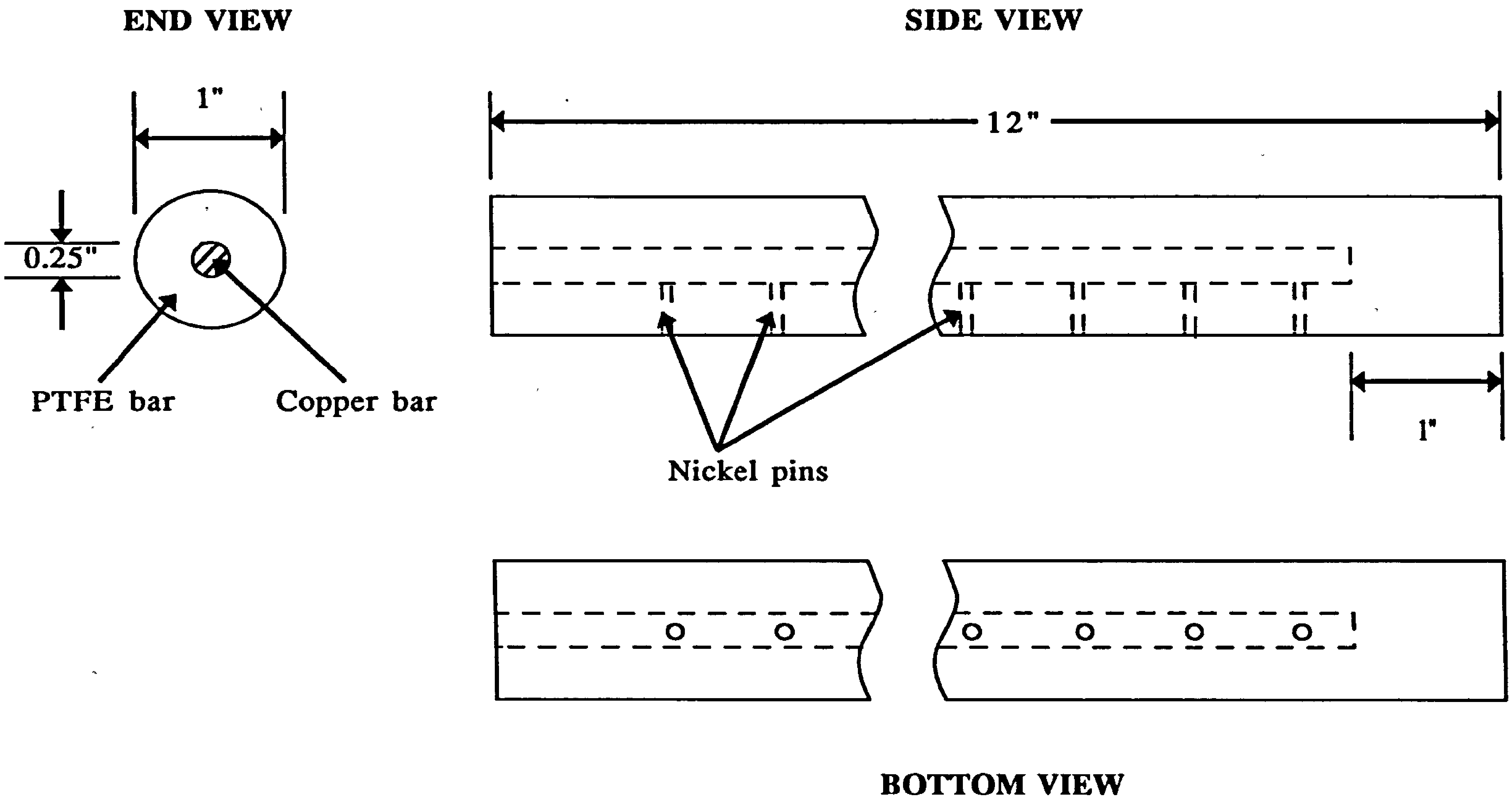

Fig. 3.11 Schematic of the electrostatic precipitator

usually <99.999% pure and it is impossible to rule out the effect of the impurities in the results.

The electrical circuit consisted of a 0→6kV power supply, that could supply either polarity, connected to the copper bar of the precipitator (Fig. 3.12) using a banana-plug lead; an AVO ammeter connected to the water cooler; and a Comark μ-voltmeter conected across a 330Ω dropping resistor. In order to determine where to operate the device in terms of voltage, it was decided to investigate the affect of different gas compositions on the operation of the precipitator. The results for helium in Fig. 3.13 clearly show the transition to cathode glow mode, described earlier in this chapter, since there is a sharp rise in the current. As the pressure is increased, however, the voltage hold-off increases, and the transition to cathode glow mode occurs at much higher voltages. Figs. 3.14 & 3.15 show the results for helium buffered mixes containing 5mbar HCl and 5mbar HCl+50mbar Xe respectively. Here, the expanded graphs show the small rate of rise of current prior to switching to the cathode glow mode.

In Fig. 3.16, a new pure helium discharge was run for 90×10^3 pulses before repeating the measurements previously made. Clearly, it can be seen from Figs. 3.13 & 3.16 that there has been a shift toward lower applied voltages to produce the switch to cathode glow mode, presumably due to the added ionising radiation of the discharge. Measurements were also made for other buffer gases such as neon and argon, but in these cases breakdown of the gas did not occur within the range of the of the small 6kV power supply.

In order to confirm the assumptions that, what was being seen, was the transition to cathode glow, it was decided to look for the generation of trichel pulses using a Telequipment D83 oscilloscope. Trichel pulses were

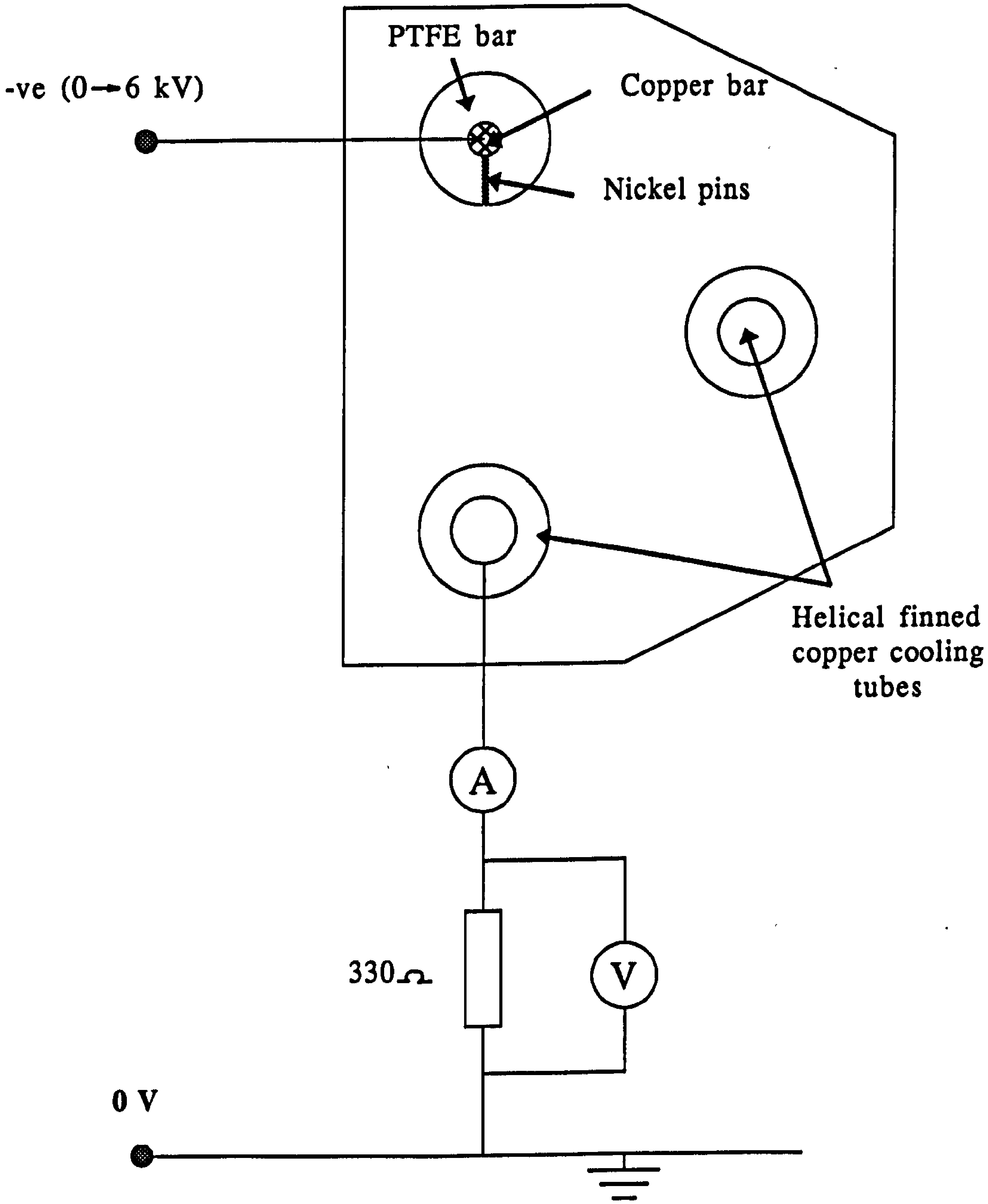

Fig. 3.12 Circuit diagram for the electrostatic precipitator

Fig. 3.13 Precipitator discharge current as a function of applied voltage in a helium atmosphere for different operating pressures

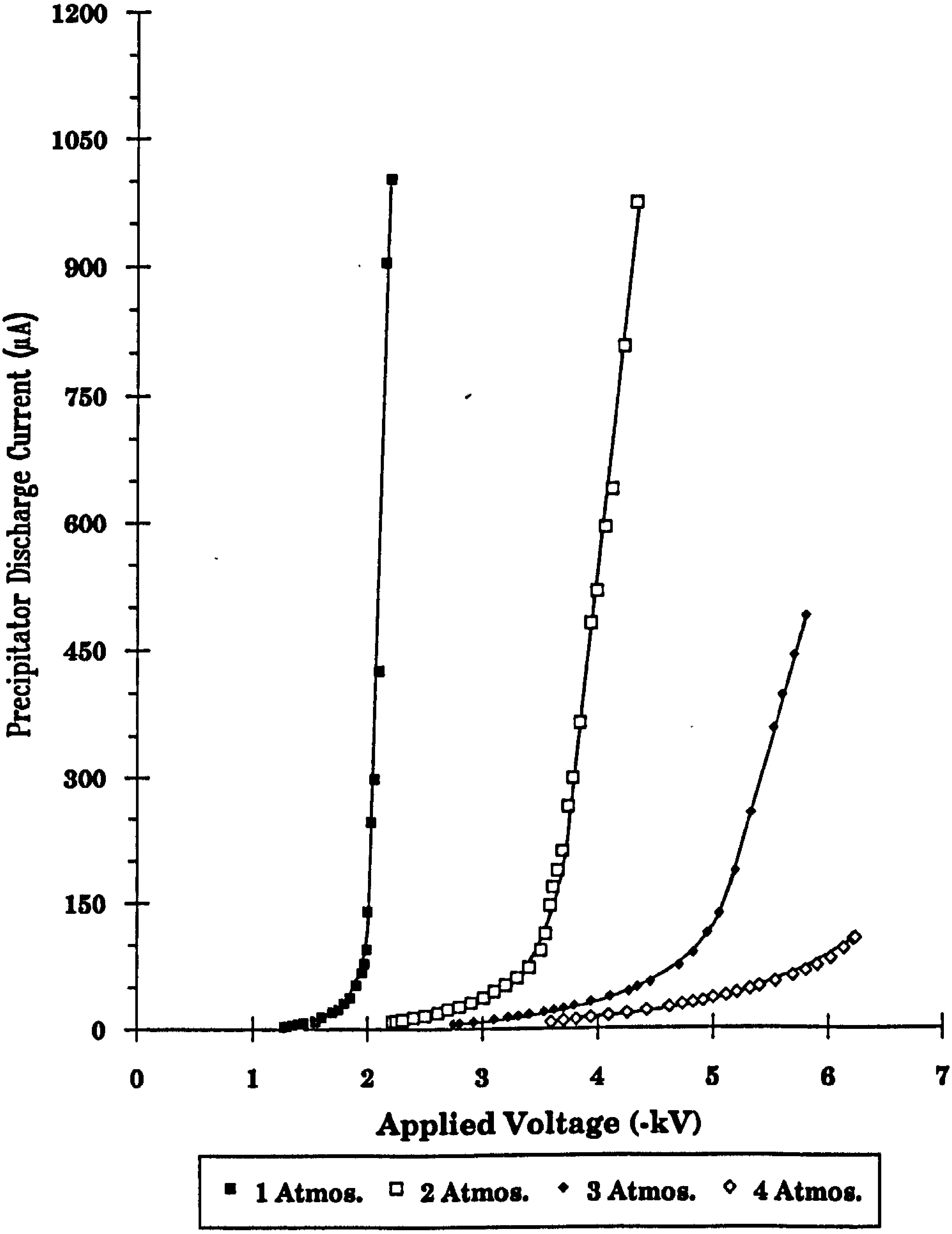

Fig. 3.14 Precipitator discharge current as a function of applied voltage in a He + 5 mbar HCl atmosphere for different operating pressures

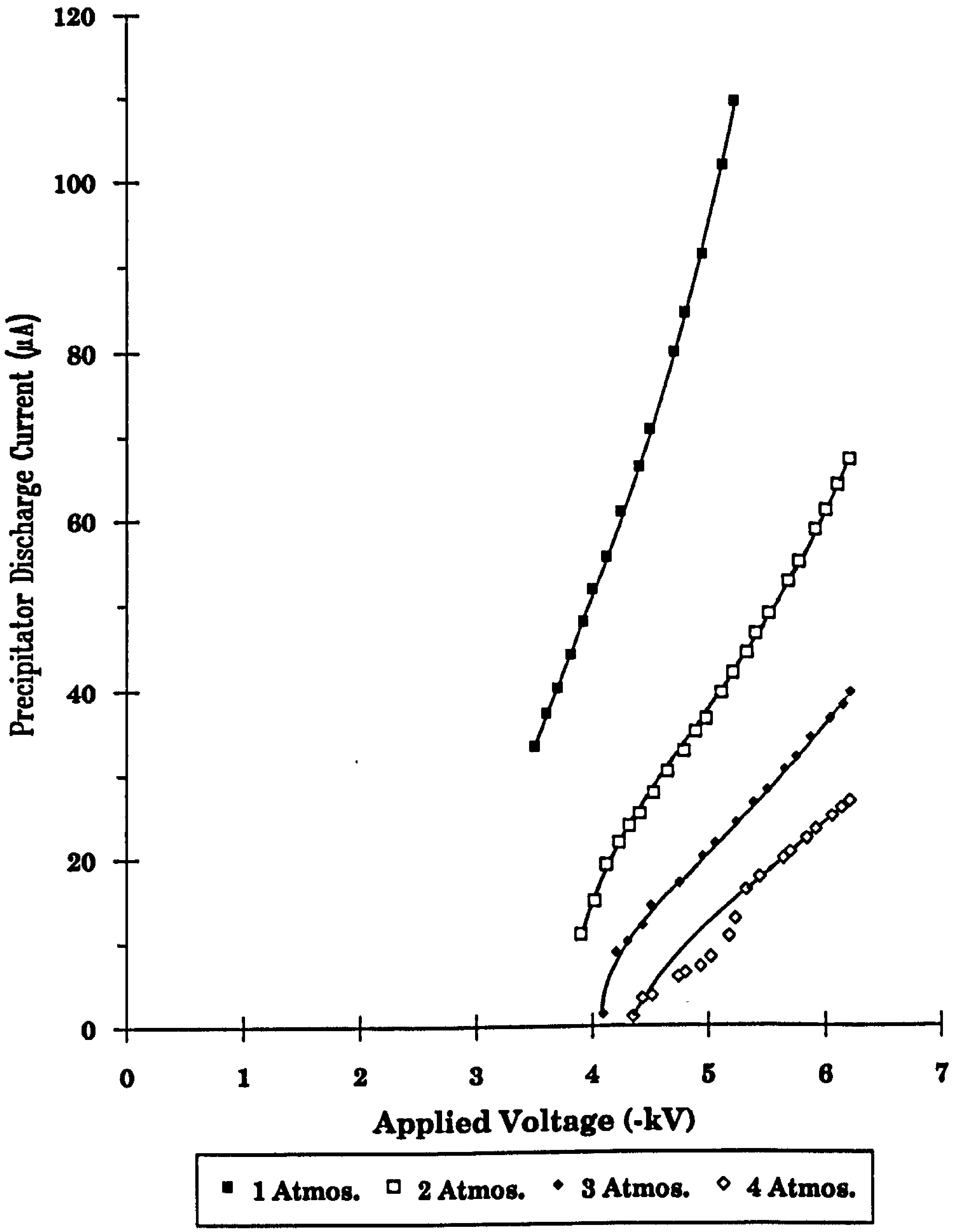

Fig. 3.15 Precipitator discharge current as a function of applied voltage in a He + 5 mbar HCl + 50 mbar Xe atmosphere for different operating pressures

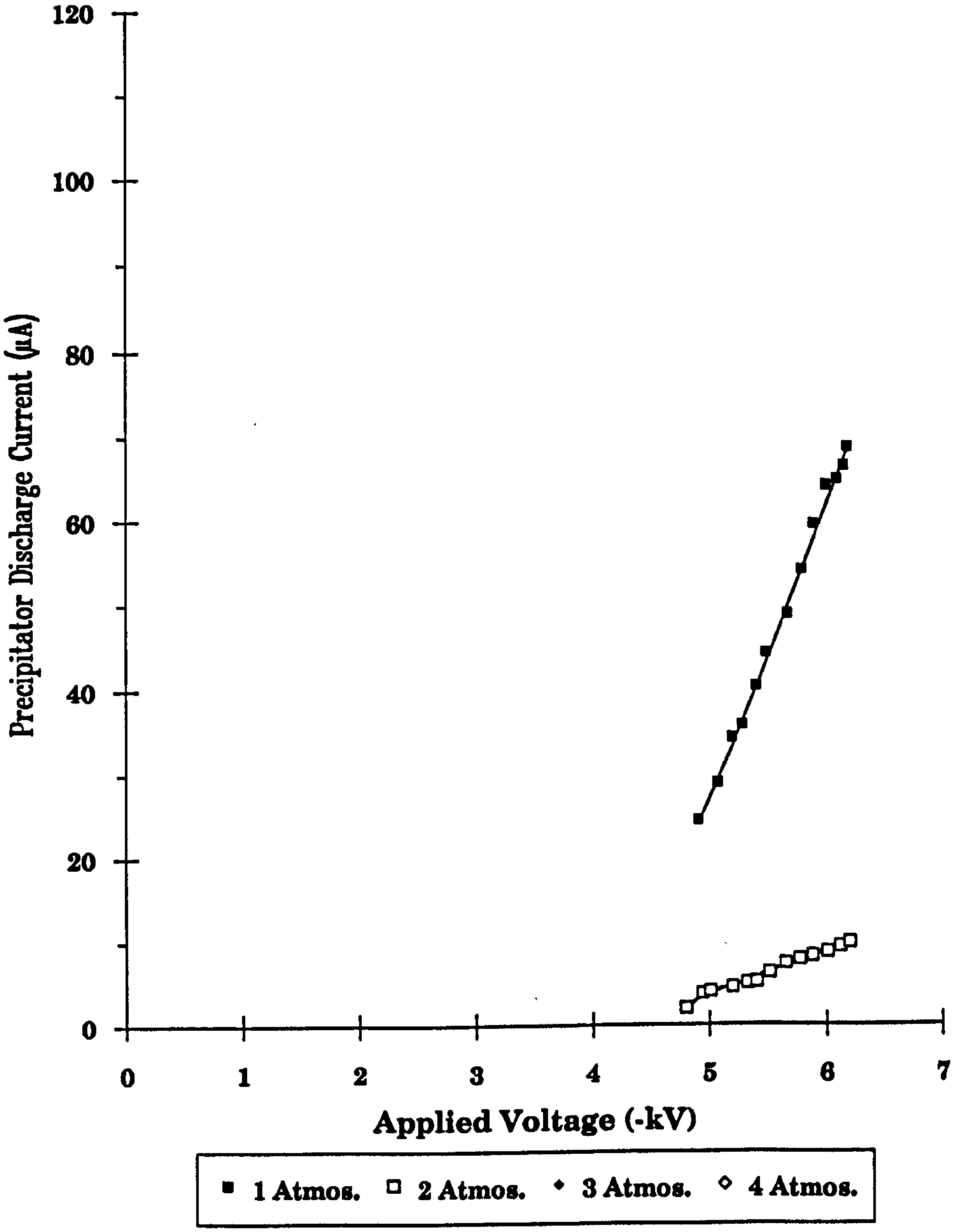

Fig. 3.16 Precipitator discharge current as a function of applied voltage in a helium atmosphere for different operating pressures, after 90,000 pulses

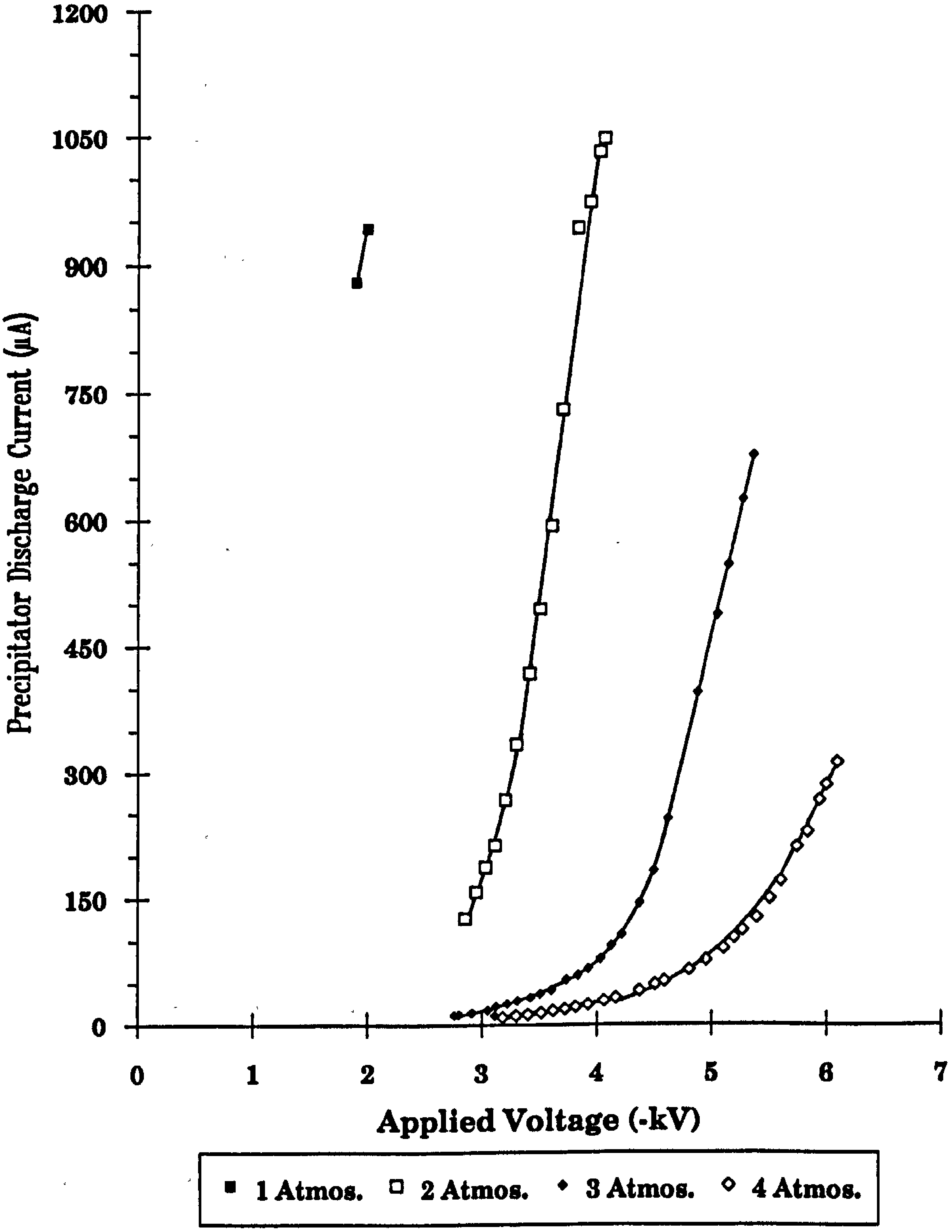

observed at approximately -0.8kV and were dependent on gas composition. They appeared regular in nature (Fig. 3.17a)) and of the order of 2kHz in frequency as long as the pressure remained low (~0.5bar). As the applied voltage was increased, the frequency decreased. However, as the pressure of the medium was increased to ~1.0bar and greater, much higher voltages were required >-1.0kV. This resulted in more erratic behaviour of the pulses in amplitude, but at much higher pulse frequencies ~3.5kHz @ 1bar and ~6kHz @ 4bar for Figs. 3.17b) & c) respectively. This change in frequency is ascribed to the much higher mobility of the negative ions at lower pressures [3.4]. Fig. 3.17d) shows the effect of the addition of an electronegative gas such as hydrogen chloride. Here, the onset voltage rises from -1.6kV for helium at 1bar, to -3.8kV for the case where 5mbar of HCl is added to the helium for a total pressure of 1bar.

In conclusion, it can be seen that the onset voltage decreases with decreasing pressure, but increases with the amount of electronegative gas added. When helium is exchanged for heavier gases, a noticeable increase in the onset voltage for the precipitator has been observed. Even additions of small quantites of Xe & HCl make a significant difference to the onset voltage.

3.2.4 Gas Lifetime Enhancement Using and Electrostatic Precipitator

To investigate the clean-up benefits of the precipitator, a He:Ne laser was aimed directly into the laser chamber upstream and parallel to the discharge. The discharge was then run for several minutes at high repetition rate, during which there was an increase in scattering of the He:Ne beam by the particulates being generated by the discharge. Eventually, a solid pencil of light could be observed running the full length of the laser discharge chamber. At this time, the electrostatic precipitator was switched on, and in

a) P = 0.5 bar
t = 0.5 ms/div

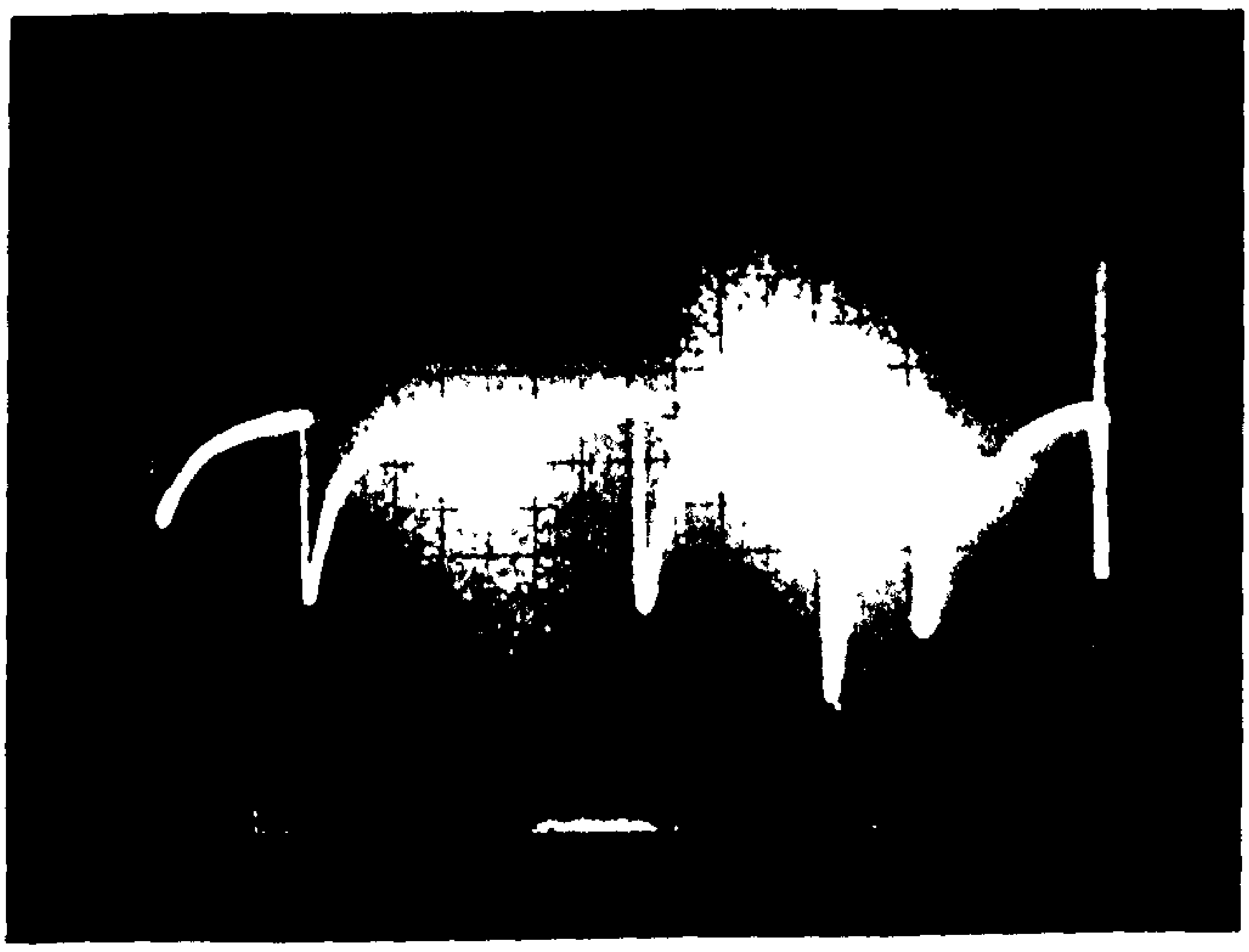

b) P = 1.0 bar
t = 0.2 ms/div

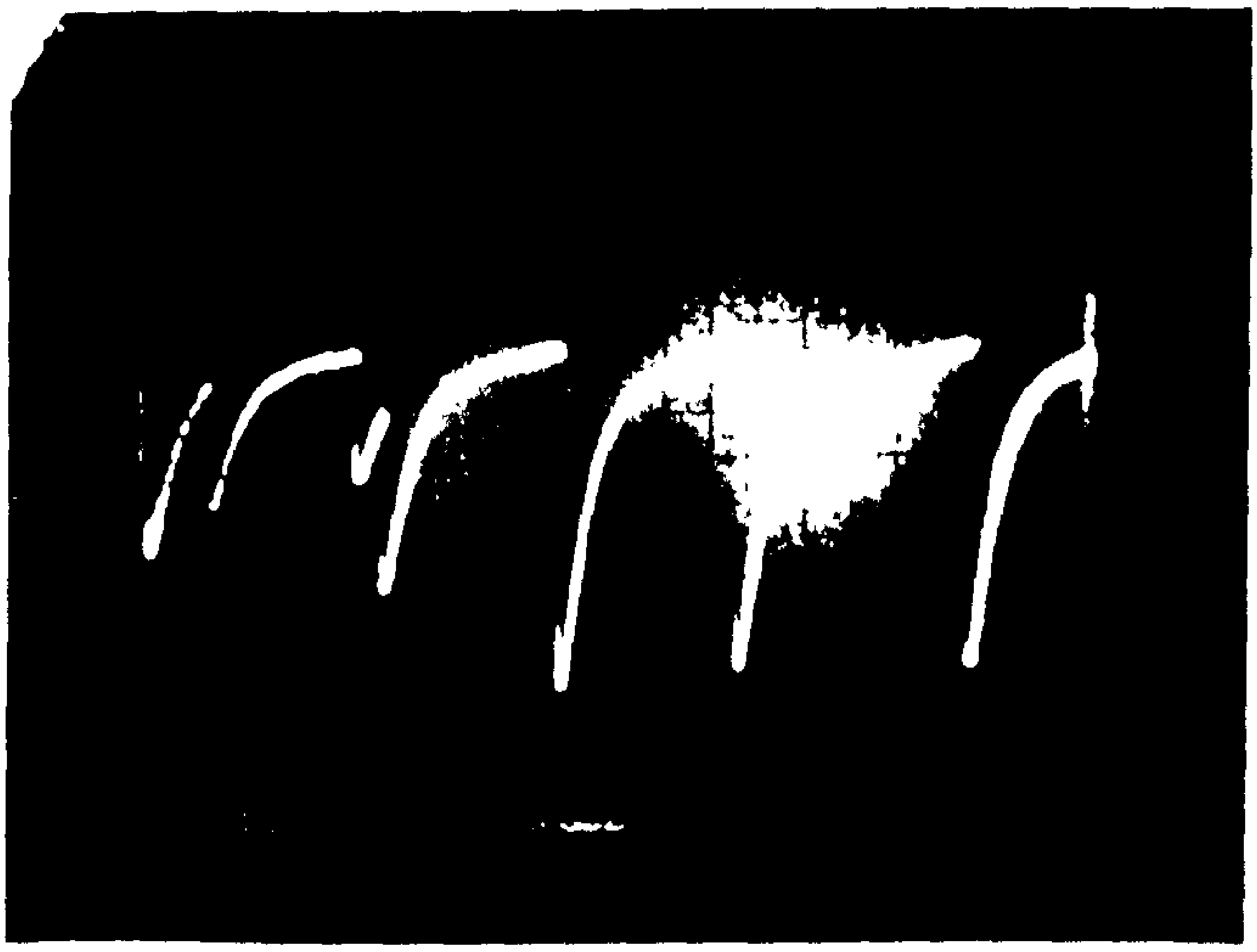

Fig 3.17 Trichel pulse observations made for:
a) 0.5 bar & b) 1.0 bar helium atmospheres

c) P = 4.0 bar
t = 0.1 ms/div

d) P = 1.0 bar
t = 0.2 ms/div

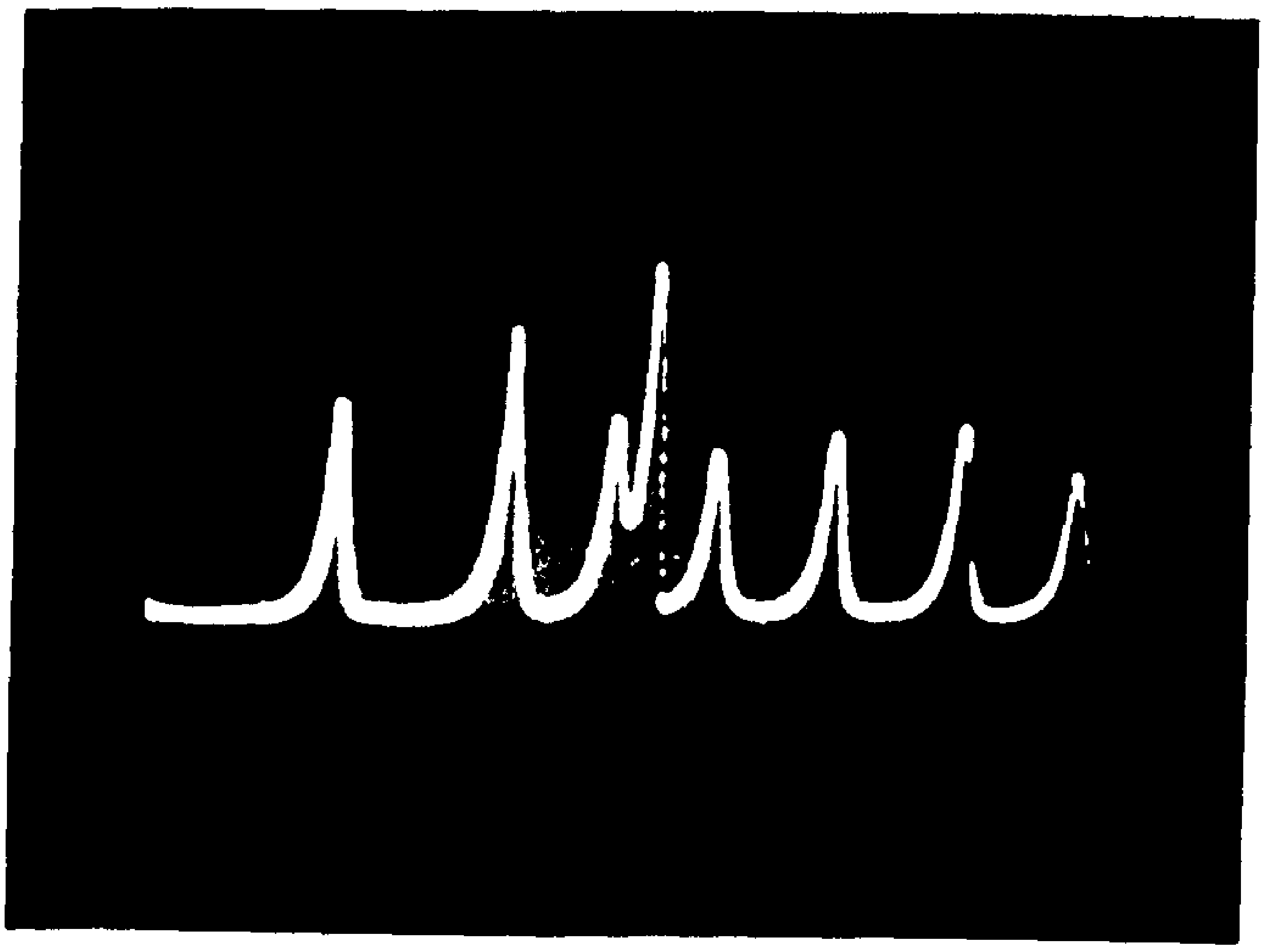

Fig 3.17 Trichel pulse observations made for: c) a 4.0 bar helium & d) 5mbar HCl in 1 bar helium atmospheres

less than a minute the pencil of light (caused by the scattered He:Ne beam) vanished, leading to the conclusion that the precipitator was behaving as expected, and that dust removal was being achieved.

The next step was to investigate the benefits of the precipitator on the lifetime of a laser gas mixture as a function of laser output power. The gas mixture used for this experiment was as follows:

4 HCl : 50 Xe : 3946 He (all units in mbar)

The laser output power was monitored at the start of the run, with the end point being taken at the half-power point. This particular gas mixture lasted just over 100×10^3 pulses to half power with no precipitator in operation (Fig. 3.18). The mixture was then replaced with a fresh fill and the precipitator switched on. The run was then started, and the initial output power recorded. As can be seen from Fig. 3.18 this particular fill lasted just over 400×10^3 pulses giving a factor of four increase in the gas lifetime with the electrostatic precipitator. These results were also borne out with other gas mixtures to be reported later in this thesis.

3.3 A STUDY OF VARIOUS UV PREIONISATION TECHNIQUES

It is well known that transverse discharge lasers have a tendency to form arcs, and this condition is more prevalent in excimer lasers because of the high electronegativity of the halogen donor gas. To obtain an arc free, uniform glow discharge, it is necessary to preionise the gas mixture using uv radiation. Transverse discharge lasers utilising uv preionisation schemes offer many advantages over systems which are pumped or preionised using electron beam or x-ray techniques. These advantages include, for example, simplicity, lower cost, and ease of scaling in pulse repetition rate. Several schemes have been proposed for preionising TEA CO_2 lasers [3.1→3.3 & 3.6→3.10]. For

Fig. 3.18 Normalised output power as a function of gas lifetime with and without an electrostatic precipitator

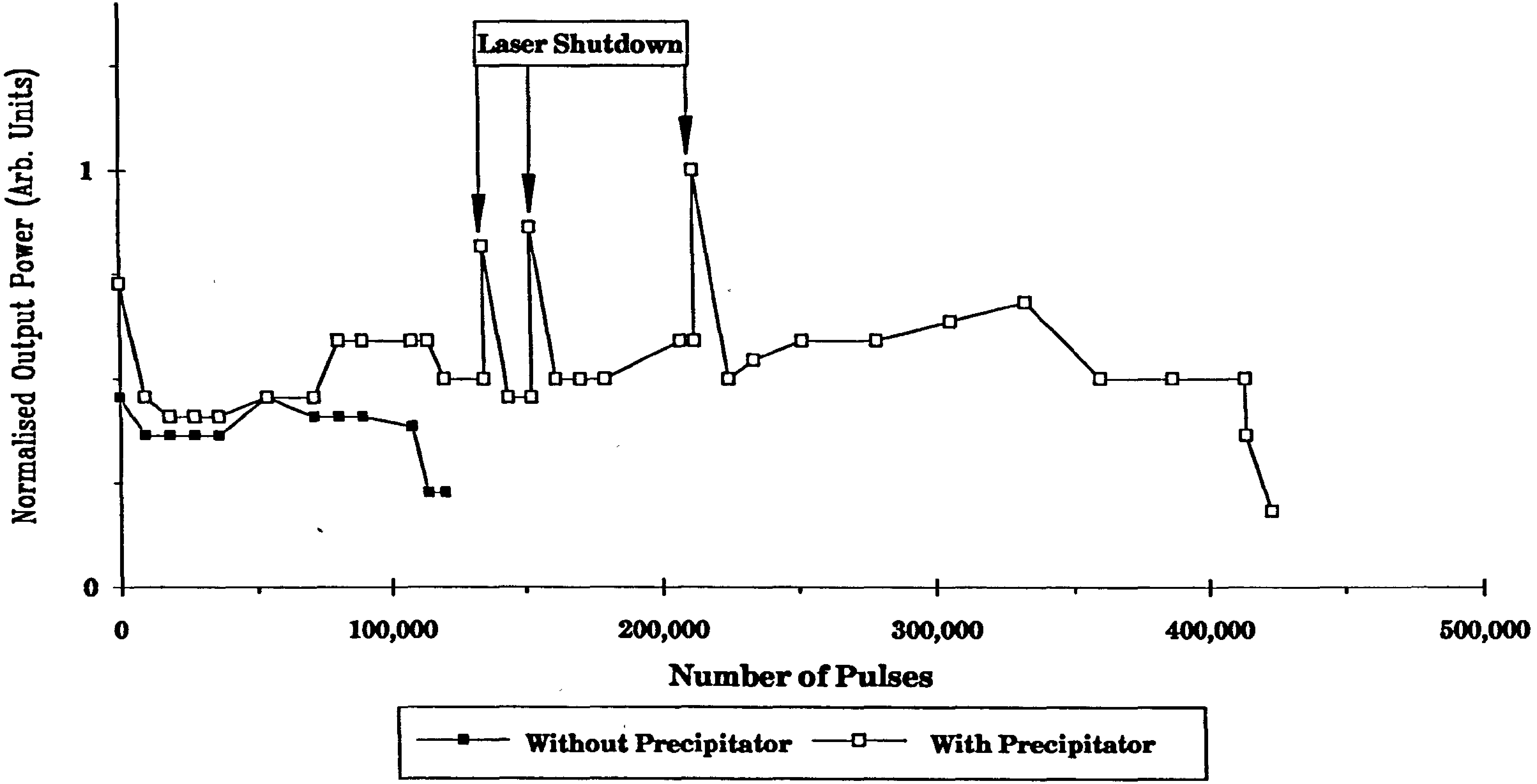

excimer lasers, the predominant discharge circuit, in use today, is based on the work by Burnett & Offenburger [3.1].

3.3.1 Capacitively Loaded UV Sparks

The uv preionisation scheme reported by Burnett & Offenburger [3.1] lends itself very well to excimer laser discharge technology, since it allows the construction of a self-synchronised, fast (low inductance) discharge loop to produce the high peak currents necessary for excimer laser operation.

In the original design configuration, a pair of 18cm gain length nickel electrodes, with a Chang [3.11] cross-sectional profile and semi-circular ends, were spaced 12.1mm apart by an electrode gantry. This gantry also housed a series of "doorknob" capacitors, 5 along the top and 6 along the bottom on each side of the electrodes (Fig. 3.19), and were connected electrically in parallel with the main discharge electrodes. Attached to these capacitors were doubled preionisation pins, which provided 11 uv preionisation spark discharges along each side of the main discharge electrodes. The separation of the pins was set at 2mm in this configuration. This preionisation scheme produced a 32mJ initial maximum output, using a 4HCl:40Xe:2956He (torr) mixture, but this was fluctuating, and the energy eventually settled back to ~8mJ. It was also at this time that problems with the Ferrofluidic seal leaking (mentioned in Chapter 2) were being investigated. With the design where the duct surrounds the electrode gantry, this preionisation scheme produced a maximum power of 1.3W @ 340Hz, and reached a maximum prf of 760Hz at which point lasing was still being observed, but with little output power.

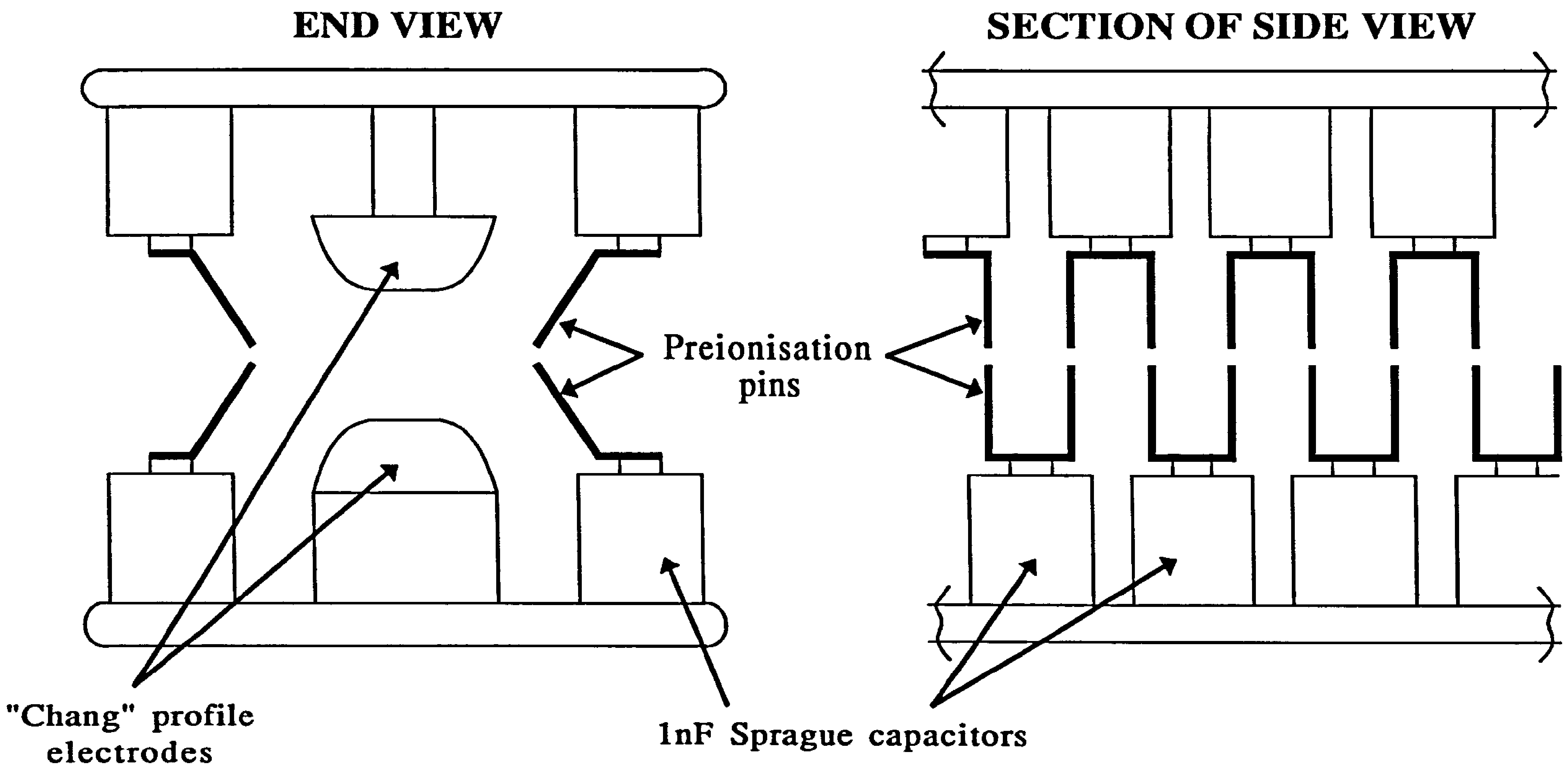

Fig. 3.19 Schematic diagram of the initial "Chang" profile electrode gantry

It was then decided to change the buffer gas from helium to argon. In order to carry this out, the main discharge capacitance was optimised (Fig. 3.20), and the flow velocity measured as a function of the fan motor voltage (Fig. 3.21) for pure argon at atmospheric pressure. For V_c=15nF, a mixture of 4HCl:76He:60Xe:1110Ar (torr), and an electrode separation of 12.1mm a maximum pulse energy of 17mJ was achieved at 29.8kV. It was then decided to increase the gap from 12.1 to 17.2mm since, according to Andrew *et al* [3.12], the gain in a excimer laser increases linearly with length and as the square with electrode separation. This increase in the electrode separation produced no lasing under the same operating conditions as that of the 12.1mm gap. The gas mixture was then optimised to produce a maximum of 8.5±12%mJ at 2.5bar total pressure. The preionisation pin gap was then increased to 5mm, from the previously set 2mm gap, but this resulted in an erratic discharge. The gap was then reduced to approximately 1.25mm resulting in a more stable discharge and a pulse energy of 14.5±12%mJ.

From these measurements, and those of other laser systems within the MGL group, it was concluded that in order to use "Chang" profile electrodes in an excimer discharge, the maximum electrode separation should not exceed 1.7x the gap used in the profile calculations. That is to say for the 7mm gap profile used in these experiments, the separation must not exceed ~12mm.

After these results, a special set of electrodes were made based on the in-house developed "Monk" profile, which consisted of a piece of circular bar stock, in this case brass, machined equally on two sides to make the desired electrode thickness. Then a 1mm flat was produced in the centre of one side by machining two 2° angles on either side of the centre. This basic profile was then blended by hand, with the ends of the electrodes forming an elliptical profile. The effective gain length of the electrode pair was 22cm.

Fig. 3.20 Pulse energy as a function of the main discharge capacitor for an argon buffered gas mixture

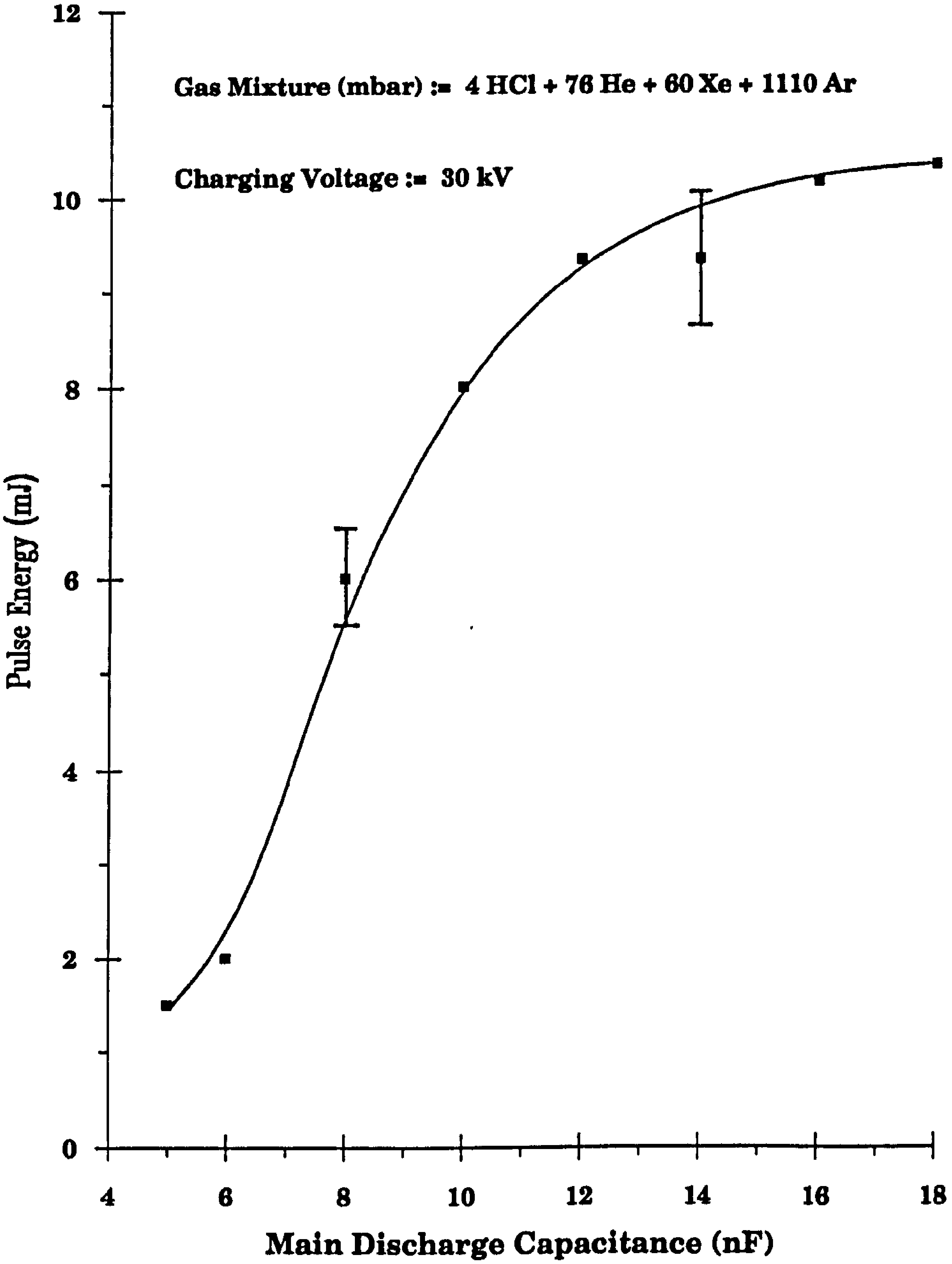

Fig. 3.21 Flow velocity through the discharge region as a function of fan motor voltage for an argon buffered gas mixture.

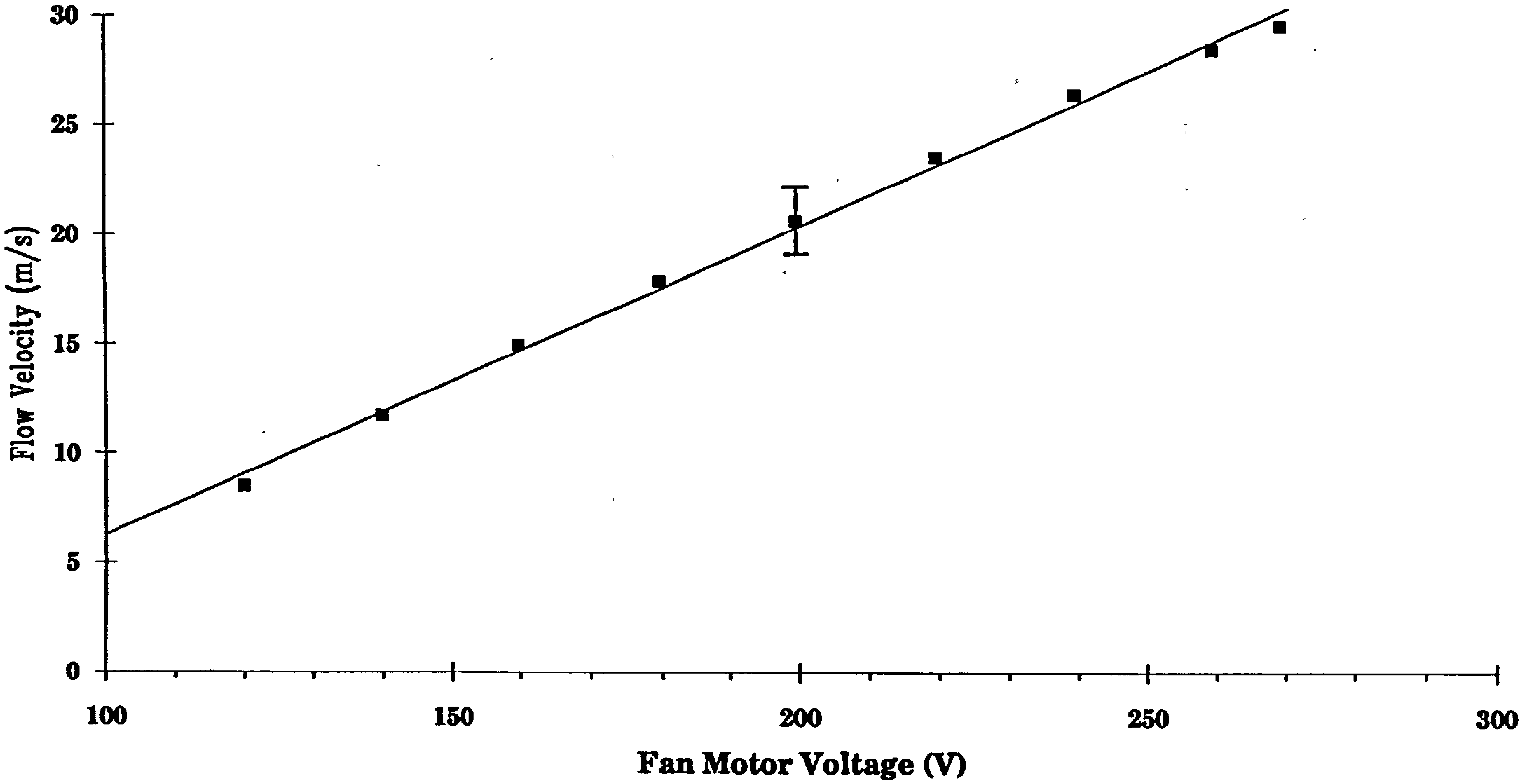

This electrode set was then gapped to 15.85mm separation. For a 10HCl:60Xe:2930He (mbar) gas mixture this electrode profile produced 19±6%mJ output energy. With an argon buffered gas mixture a maximum of 11±10%mJ was produced. For the helium buffered gas mixture (mentioned earlier in this section) the output energy reached a maximum of 24mJ, but the discharge became more erratic; also the output stability did not improve with several partial pump-outs and refills. It was then decided to investigate the effect of preionisation on the discharge characteristics by varying their position relative to the centre of the discharge.

Several preionisation positions relative to the centre of the electrodes were tried, and the effect on the discharge monitored by observing the discharge markings on the electrodes. With 5 sparks, staggered down each side of the electrodes and 3cm from the centre of the electrodes, the discharge was observed to be "pulled" closer to the side where the preionisation pins were sparking. This resulted in the discharge "snaking" its way down the length of the electrodes, with the discharge heaviest opposite each preionisation pin (Fig. 3.22a)). The next experiment increased the number of preionisation sparks to 11 down each side, but not staggered this time (Fig. 3.22b)) and still 3cm from the centre of the electrodes. Here, more intense regions of the discharge were produced opposite each preionisation spark, with a more diffuse discharge in between. This preionisation arrangement, producing the maximum number of sparks possible in this particular gantry configuration, was then moved back until the distance to the centre of the electrodes was 4cm. This produced a discharge that was almost as intense as that seen for the bunched discharge found at 3cm separation, with the exception that there was almost complete overlap of the intense regions, producing an quasi-uniform excitation down the whole gain length. Moving the preionisation sparks further back to 6cm from centre of the electrodes,

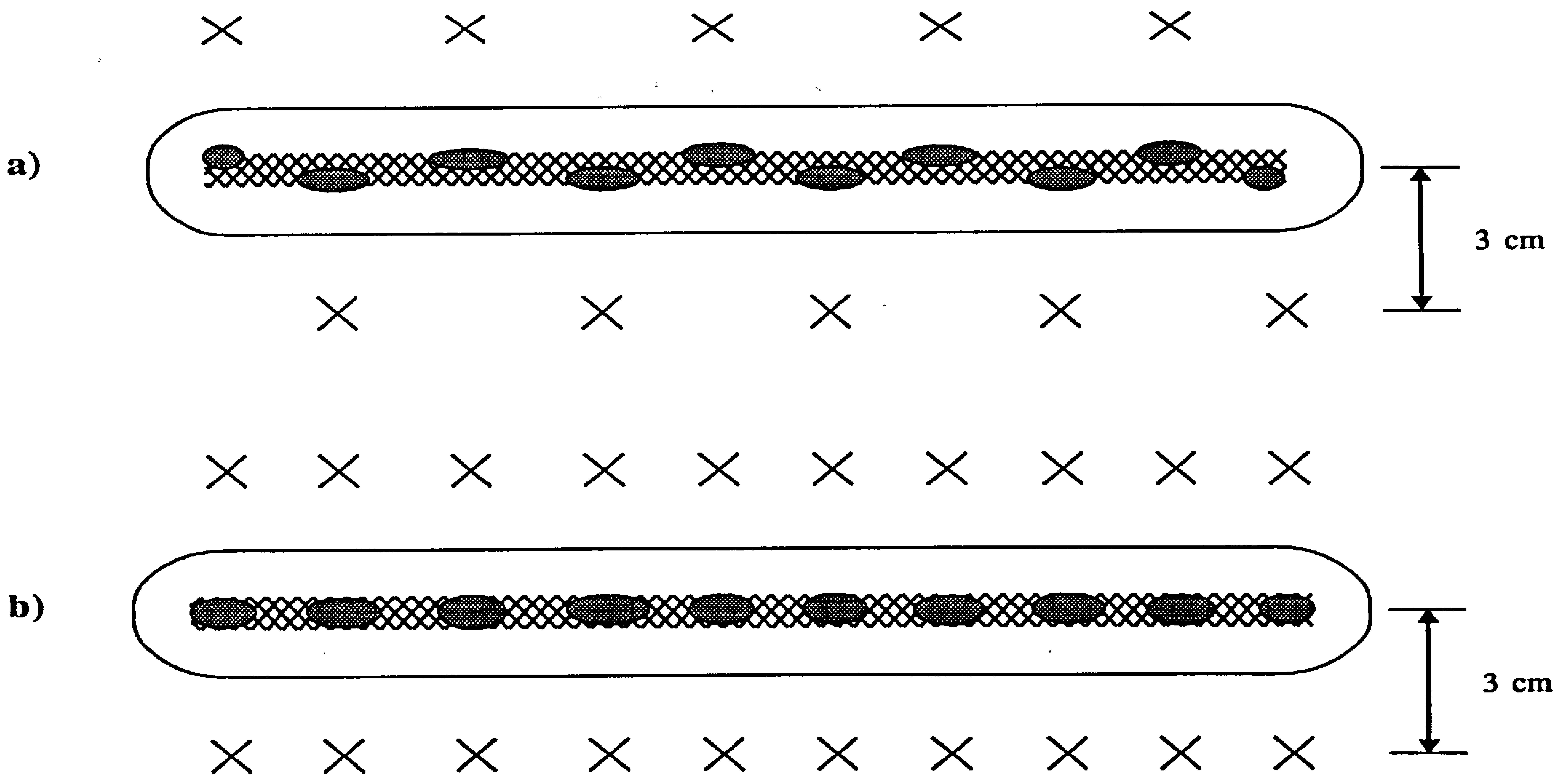

Fig. 3.22 Schematic diagrams of the preionisation spark positions relative to the centre of the discharge

resulted in a very uniform, and very stable, discharge that was light in intensity. One interesting supplementary measurement, made with an argon buffered gas mixture and the preionisation pins at 6cm, showed the output to be abysmal and erratic. It was assumed, that the uv from the sparks was being absorbed by the gas, before the uv could penetrate the discharge region and preionising it well enough for stable operation.

The preionisation pins were then set back to the optimal position of 4cm from the centre of the electrodes, and the performance optimised at high prf's (>400Hz) for different values of capacitance (Fig. 3.23). The best result was achieved for C_{main}=12nF producing 8W @ 550Hz and 33.5kV. Using the 12nF capacitor it was decided to try the higher Xe concentration gas mixture used by MSNW [3.13] 1.5H_2 : 9HCl : 120Xe : 700He : 2170Ne (mbar). This mixture produced very good pulse energy, 32mJ @ 50Hz, but fell to ~25mJ after 5 minutes of operation. The maximum power achieved with this mix was 5.7W @ 350Hz, with the maximum prf being 460Hz, at which 4W was measured but the discharge was noticeably starting to break-up, i.e. the flow limit had been reached. This lower limit on prf compared to that previously attained, was attributed to the high xenon concentration, which had previously been seen to affect the flow velocity of the gas because of its great mass.

In an excimer discharge, it is very difficult to match the impedance of the circuit to that of the discharge, since the impedance drops to a fraction of an ohm when the discharge strikes. It was therefore decided to look at the variation of the charging resistor, R_c, (Fig. 2.21) on the output of the laser. A range of charging resistors from 10→130Ω were used, and the results of these measurements plotted in Fig. 3.24. At lower impedance values, <25Ω, the output drops off quite sharply. In the range 50→100Ω there is little

Fig. 3.23 Maximum ouput power as a function of frequency @ 400 Hz & 33 kV for various capacitances

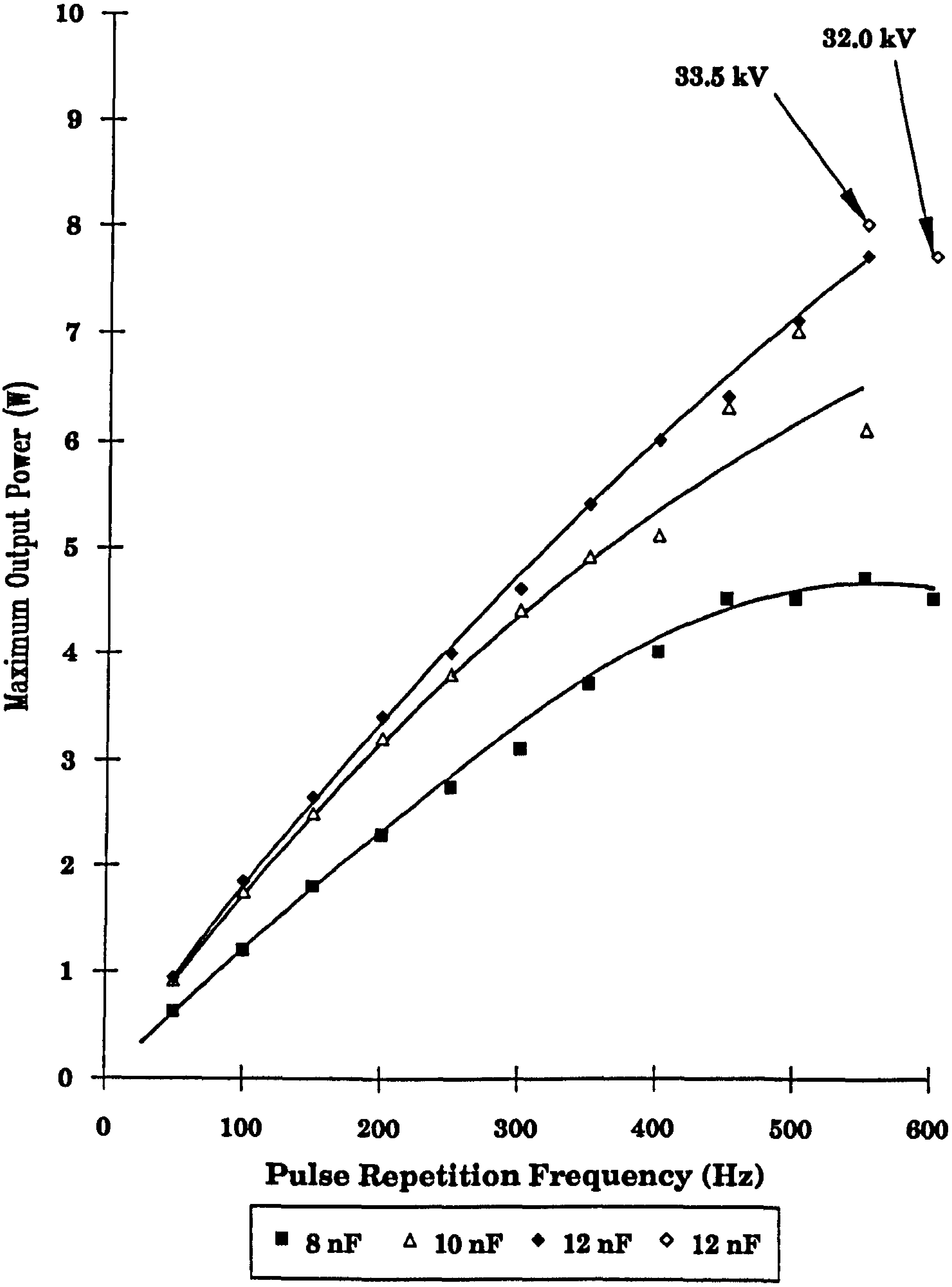

Fig. 3.24 Laser output power as a function of charging resistor value @ 450 Hz

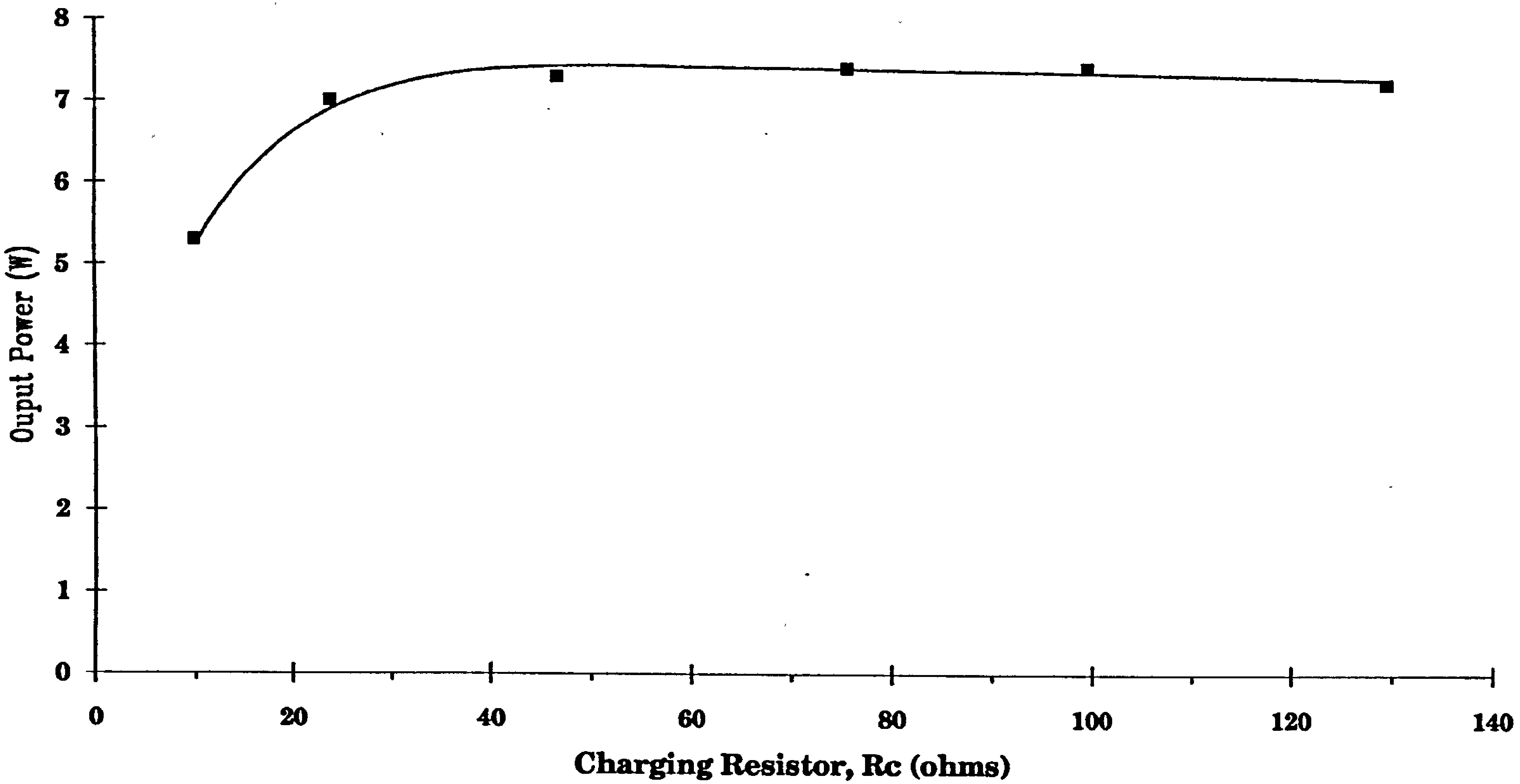

change in the output, with a gradual drop-off in power occuring above 100Ω. Comparing the 24 and 47Ω resistors as a function of prf (Fig. 3.25), both result in linear increases in output power with pulse frequency, but there is a steeper slope for the 47Ω case. Based on these results, it was decided to standardise the circuit with the 47Ω resistor.

It was at this time that new high voltage feedthroughs were installed, along with a new, thicker, lid for the laser chamber. The new feedthroughs were felt necessary since there were preliminary signs of tracking on the old design. Because of the tracking, the new design was made from 1" PTFE bar, machined with anti-tracking grooves to increase the tracking distance to the lid of the laser chamber. The lid of the laser chamber was also replaced with a thicker, $\frac{1}{2}$" stainless-steel plate, since the previous version tended to bow under pressure. With the new lid and feedthroughs in place a maximum power of ~10W @ 550Hz was achieved. However, there was some difficulty in repeating these measurements after the laser was run at high repetition rate. It was felt that some of the internal capacitors had possibly been damaged by tracking, so it was decided to remove the electrode gantry and test the capacitors with a high voltage ohmmeter. None of the capacitors seemed to be faulty, but the electrode gantry had developed a sticky coating on its surface, presumably some hygroscopic metal chloride film. The electrode gantry was completely stripped, cleaned, and rebuilt, and then placed back into the laser chamber which was then leak checked and filled with a static passivation HCl:He gas mixture to be left overnight. This, unfortunately, did not enable us to repeat the measurements made before. Although the reason for this is unknown, one might speculate that other surfaces inside the laser enclosure also had this sticky coating which could have affected laser performance. Extensive running to heat the enclosure and dry the walls may have assisted, but time was a limited.

Fig. 3.25 Maximum laser output power as a function of pulse repetition frequency for different charging resistors

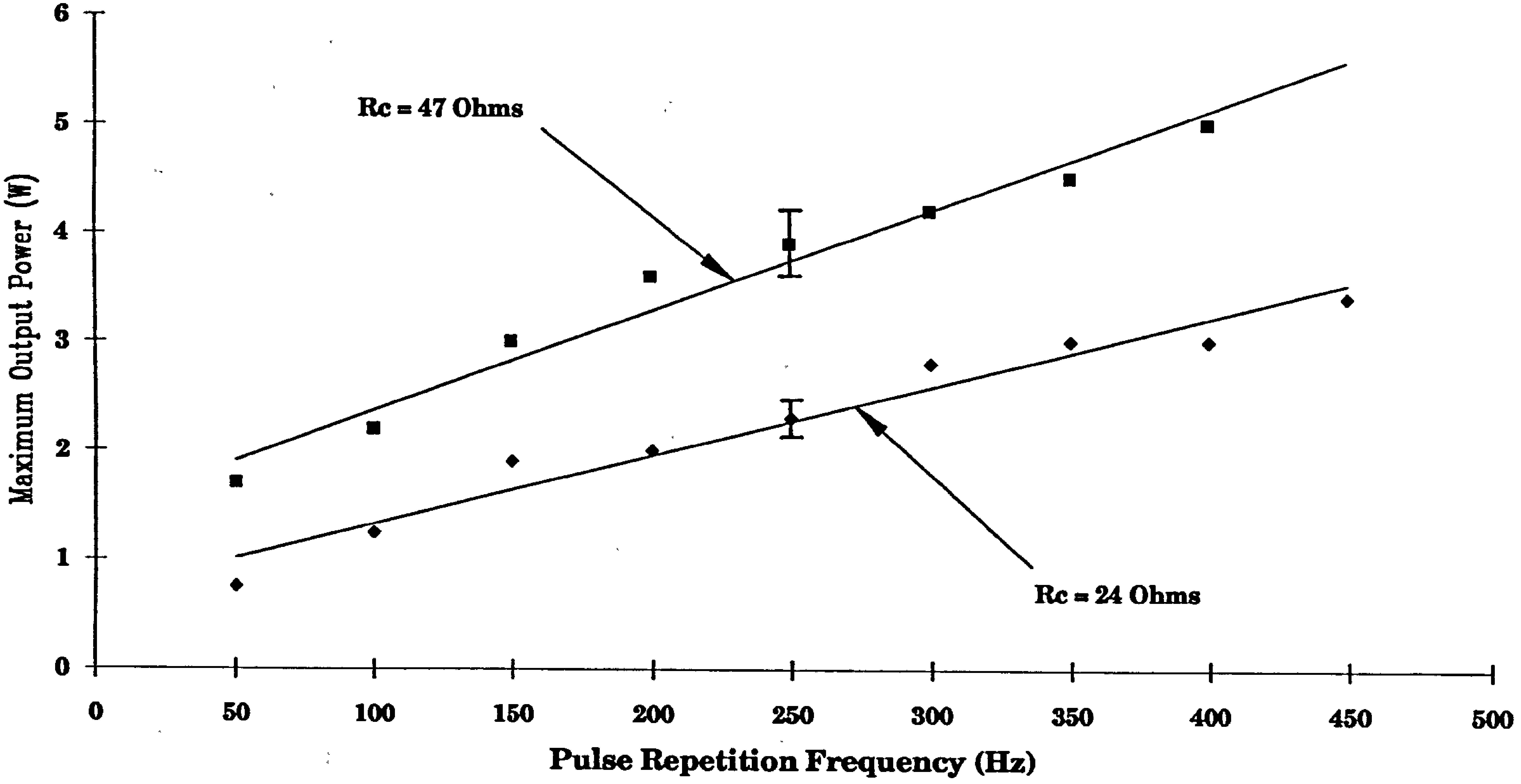

The preionisation pins were then moved closer to the discharge, 3cm from the centre of the electrodes. This resulted in a repeat of the previous maximum power of 10W this time at 500Hz, and also achieving an efficiency of 0.4% at 400Hz, a result which had only previously been attainable at low repetition rates. Further investigation of the preionisation effects on the discharge were carried out using preionisation pins only on the downstream side of the discharge; powers were produced of 4.1W @ 500Hz, less than half that with both sets of preionisation pins in position.

From the knowledge gained from these results, and those of the flow measurements and material compatibility issues, a new electrode gantry based around the original frame was constructed using the "Monk" profile electrodes as the starting point. Sixty custom built 180nF Steatite & Porcelain ceramic capacitors, without epoxy encapsulation, were used as the preionisation capacitors producing an effective capacitance of 2.7nF internally. This increased the number of preionisation sparks down each side of the electrodes, from eleven to fifteen, with the aim of increasing the preionisation uniformity. These capacitor proved to be quite successful with only one known failure to-date. This can probably be attributed to the distributed high voltage across the capacitor pairs, thereby minimising the possibility of surface flash over. The side benefit of having no epoxy encapsulation is that contamination of the gas mixture is reduced. With this new design, flow through the discharge region was considerably enhanced making operation beyond 1kHz possible.

One or two single-ended 5nF Maxwell capacitors were used for the main discharge capacitor. Using a 5nF external capacitor 6.7W @ 1kHz and 31kV was achieved with a gas mixture of 3HCl:30Xe:2467He (mbar), and a maximum prf of 1300Hz was attained. The move to a neon buffered mixture of 3HCl:30Xe:3067Ne (mbar) did not increase the maximum output power (initially 5.5W @ 1kHz and 27kV), but did improve the stability of the discharge, and enabled operation out to 1600Hz where 3.8W was achieved. Operation at 2kHz was tried, but was unsuccessful due to the power supply not being able to supply sufficient voltage, at that repetition rate, to maintain lasing action. With 10nF external capacitance, 9.8W @ 700Hz and 30kV was achieved. Eventually after a month of operation the laser with a new fill produced 20W @ 700Hz and 16W @ 1000Hz (Fig. 3.26), both at 27kV with a 10nF discharge capacitor.

3.3.2 Resistively Ballasted UV Sparks

In this scheme, preionisation was supplied by a resitively ballasted spark array (Fig. 3.27), constructed with a series of 10kΩ, 25kV Allan-Bradley RJ153-15300 resistors. A secondary preionisation capacitor was used to control the amount of energy being deposited through the uv spark array (Fig. 3.28). In the initial experiment, the spark-array was only used on the downstream side of the discharge with the aim that it would minimised the time taken for the debris from the sparks to clear the discharge region. Using 8nF for the main discharge capacitor, the preionisation capacitor was varied between 0.34 & 2nF, to determine the optimum capacitance. This was found to be 0.68nF. The main discharge capacitor was then increased in order to maximise the output power of the laser. The optimum capacitance in this case was found to be 12nF, increasing the output from 0.30W @ 50Hz with 8nF, to 0.99W @ 50Hz with 12nF of capacitance. Upon increasing the repetition rate, a maximum output of 5.2W was achieved at 450Hz. Putting a new gas mix in the laser increased the low repetition rate pulse energy to 22mJ @ 50Hz , but did nothing for the average power at high prf's.

Fig. 3.26 Laser output power as a function of pulse repetition frequency for a neon buffered gas mixture & a 10 nF main discharge capacitor

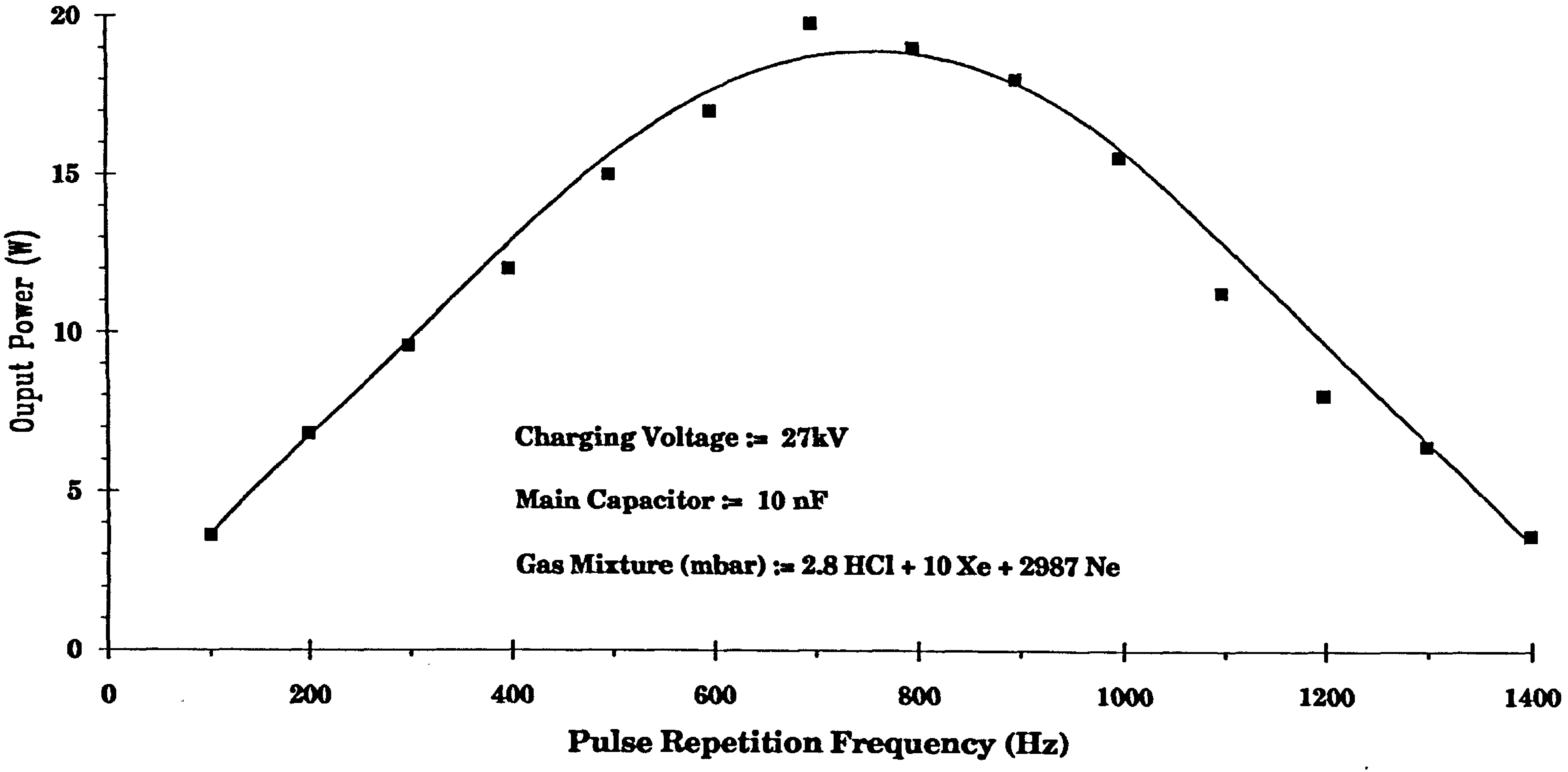

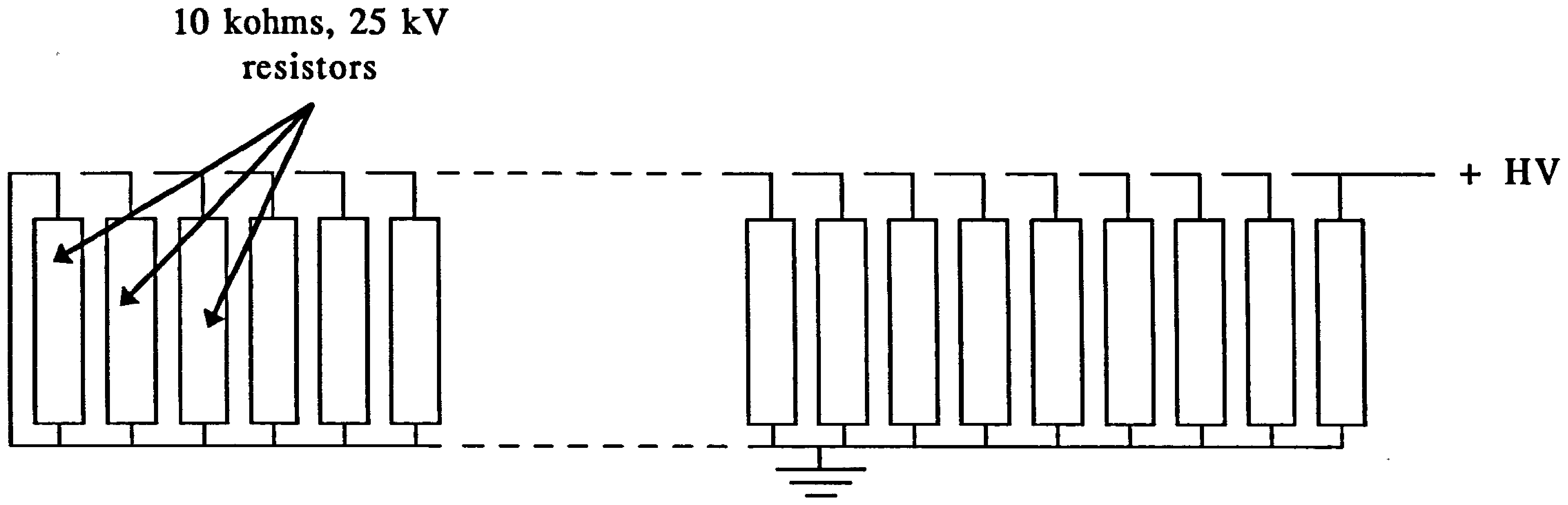

Fig. 3.27 Schematic diagram of a resistively-ballasted preionisation pin array using Allan-Bradley RJ153 resistors

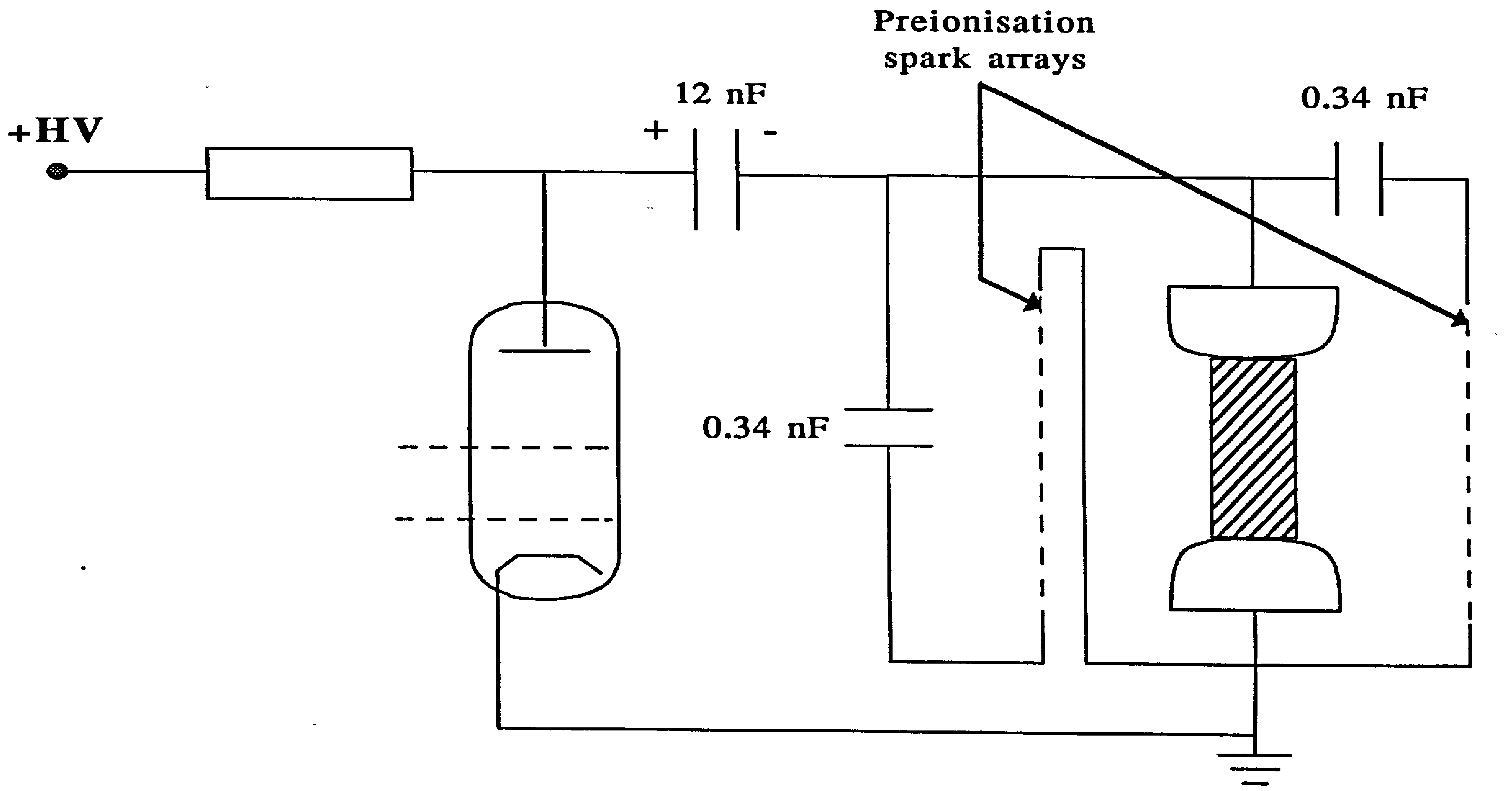

Fig. 3.28 Electrical circuit for resistively-ballasted uv preionisation

A second resistively ballasted array was built for incorporation into the system. The first array had been postioned some 3.5cm from the centre of the laser discharge, the second, due to confines of space, was positioned 4.6cm upstream of the centre of the discharge. The 0.68nF preionisation capacitor bank was split evenly between the two arrays. With a 12nF main discharge capacitor, charged to 33kV, 1.3W @ 50Hz and 5.0W @ 450Hz was obtained. Variation of the preionisation capacitance did not result in any significant changes in the output power.

The ability to fire only one preionisation array in this configuration made it possible to investigate the effects of upstream versus downstream preionisation, and whether or not flow had a great role to play in the low repetition rate (~1Hz) disharge stability. The results of this investigation have been tabulated in Table 3.1. In the case of only the upstream preionisation array firing, with no flow, the output was mostly zero. It should be noted that with both arrays firing, 0.34nF feeding each array, the pulse energy came up to 22mJ and the discharge was steady.

To resolve if the reduced output of the upstream preionisation was due to positioning, or from the debris caused by the preionising sparks, it was decided to bring both sides a little closer to the laser discharge, this time a distance of 33mm from the centre. To do this, one resistor had to be removed from each end of the array to enable the arrays to fit between the stand-off's of the electrode set. Table 3.2 shows the results obtained, with flow, at 50Hz using single-sided (upstream or downstream) and double-sided preionisation. In the case of the double-sided preionisation, tests were made of the two arrays fed by one, or two individual, storage capacitors. Based on the findings, it can be seen that irrespective of the preionisation scheme used, the same output power was achieved. Thus, it can be concluded that

Preionisation Position	Pulse Energy (mJ)	
	No Flow	With Flow
Upstream - 4.6 cm (0.34 nF)	0 → 3 (very erratic)	0 → 5 (erratic)
Downstream - 3.5 cm (0.34 nF)	16 → 19 (fairly stable)	17 → 20 (stable)

Table 3.1 Effect of upstream or downstream resistively ballasted pre-ionisation arrays on the pulse energy of the laser with and without flow.

Preionisation Position	Power @ 50 Hz (Watts)
Single-sided upstream (0.68 nF)	0.66
Single-sided downstream (0.68 nF)	0.66
Double-sided (Single feed, 1 x 0.68 nF)	0.64
Double-sided (Double feed, 2 x 0.34 nF)	0.64
Double-sided (Single-feed, 1 x 0.34 nF)	0.64

Table 3.2 Effect of either upstream, downstream or the combination of both resistively ballasted pre-ionisation arrays on the pulse power of the laser.

the drive capacitor for the preionisation has been optimised at 0.68nF, and that the position of the preionisation relative to the centre of the discharge is critical to achieve optimum performance and discharge stability. This reinforces the conclusion made in the case of the capacitively ballasted preionisation schemes.

3.3.3 Corona Preionisation

Corona preionisation is high on the list of schemes that could be used in high-repetition-rate laser designs, since it lends itself very well to incorporation into duct designs. In a suitable geometry (e.g. behind a mesh electrode), it will also directly preionise across the width of the discharge, ensuring a good uniform glow.

The coronal electrode design in this scheme was based around the work of Marchetti *et al* [3.3], and consisted of a ceramic sheathed HV conductor (~0.25" diameter) placed into a groove of a profiled electrode with nickel mesh stretched tight over the electrode (Fig. 3.29). This electrode was placed opposite a standard electrode at a separation of 1.46cm, with an effective discharge length of nominally 22.5cm producing a discharge width of 0.8cm. The overall discharge volume was 26.3cm^3. Initially, the corona preionisation bar was charged positively with respect to the mesh (Fig. 3.30). In this configuration, the main discharge capacitor was once again 12nF, the 0.68nF & 5nF capacitors acted as a voltage divider, giving over voltage protection to the corona bar, and the 5nF capacitor also acted as a peaking capacitor for the main discharge.

Initial experimental investigation of this scheme ran into trouble because flash-over occured inside the laser head. Lasing was eventually achieved at

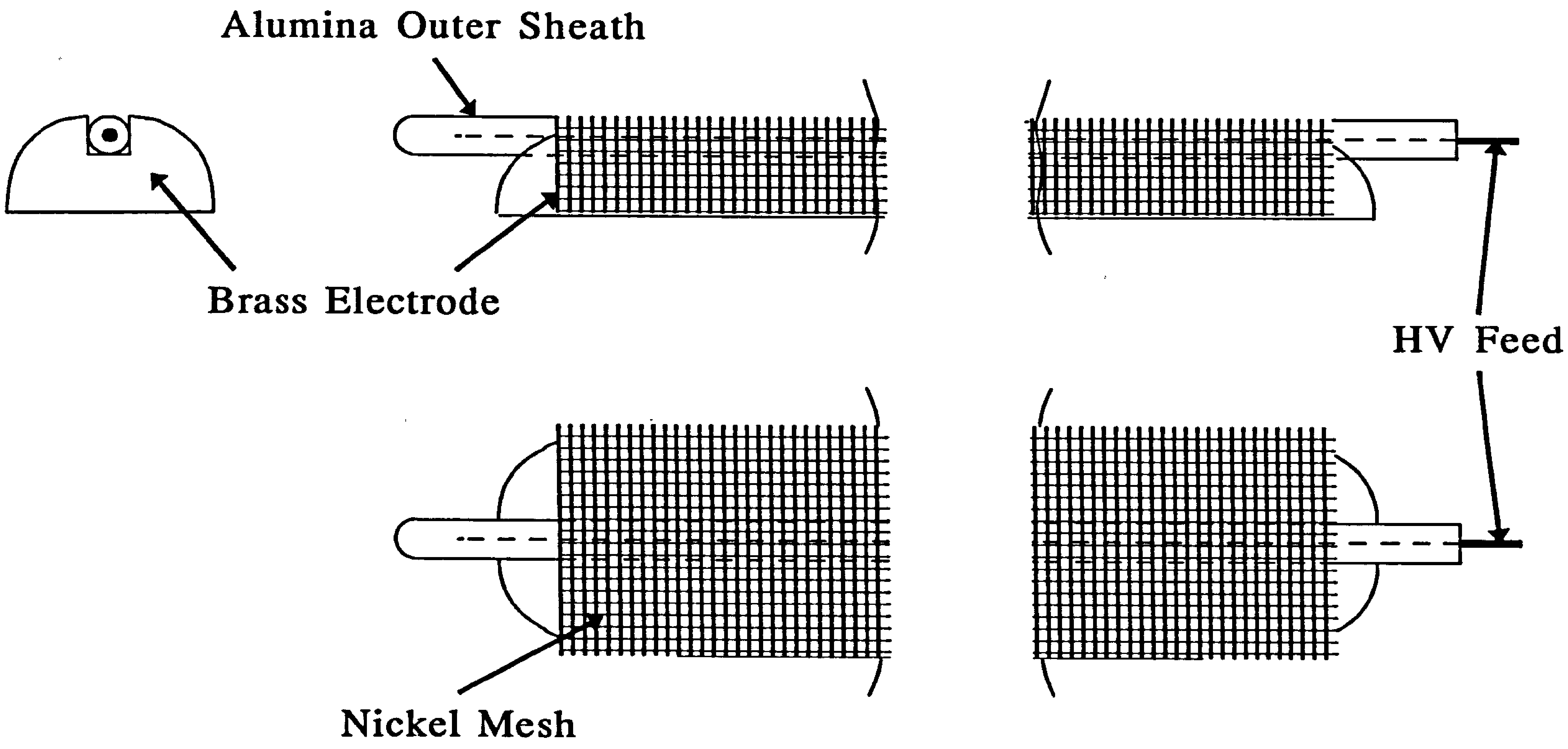

Fig. 3.29 Schematic diagram of the construction of the corona preionisation electrode

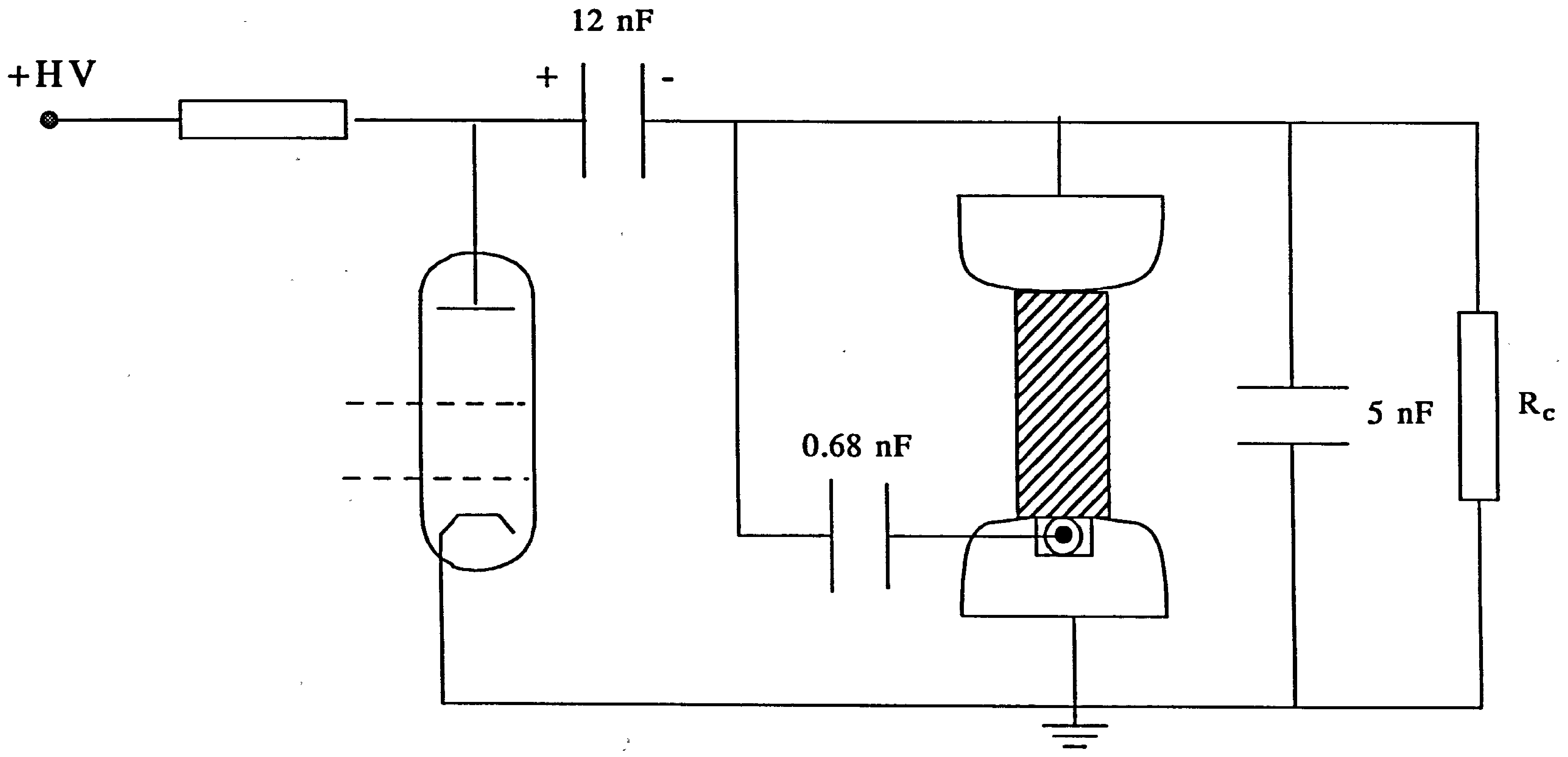

Fig. 3.30 Electrical circuit for positive feed corona preionisation

low pressure (<2 atmospheres absolute), but with very little output (~0.1W @ 50Hz). This was not unexpected, as a large amount of the discharge energy was being diverted by flash-over occuring between the corona preionisation bar and the edge of the hole of the optic port. Tracking was also found to occur between the peaking capacitor and the corona electrode.

Having eliminated these problems, investigation of the effects of pressure on the disharge suggested that coronal preionisation was very poor at pressures >2500mbar, leading to an erratic discharge. Fig. 3.31 shows beam burns taken on Dylux paper at 3000, 2500 & 2000mbar total pressure. These clearly show an improvement in the beam uniformity as the pressure is reduced. The output energy also improved to 5→6mJ at 2000mbar, and became more stable. Optimisation of the pressure and realignment of the resonator optics increased the pulse energy to 7→8mJ, with an output power of 0.3W @ 50Hz being achieved.

It was then decided to investigate reversing the polarity of the corona circuit, such that the mesh was now negatively charged with respect to the corona preionisation bar (Fig. 3.32). The corona bar was capacitively coupled by a 0.34nF capacitor to ground. This configuration produced a much more stable discharge compared to that of the positively charged corona scheme [3.5].

Since this circuit configuration was operationally different, the gas mixture was optimised once again. Fig. 3.33 shows the variation of output energy with voltage for gas mixtures varying in Xe concentration from 10→30mbar for optimised HCl and final gas mixture pressures using He as the buffer gas. Although the best energy at 50Hz was achieved with a mixture containing 20mbar Xe, the best power output at high repetition rates occured with the 30mbar Xe mix reaching a power of 4.6W @ 750Hz. It was also noticed at

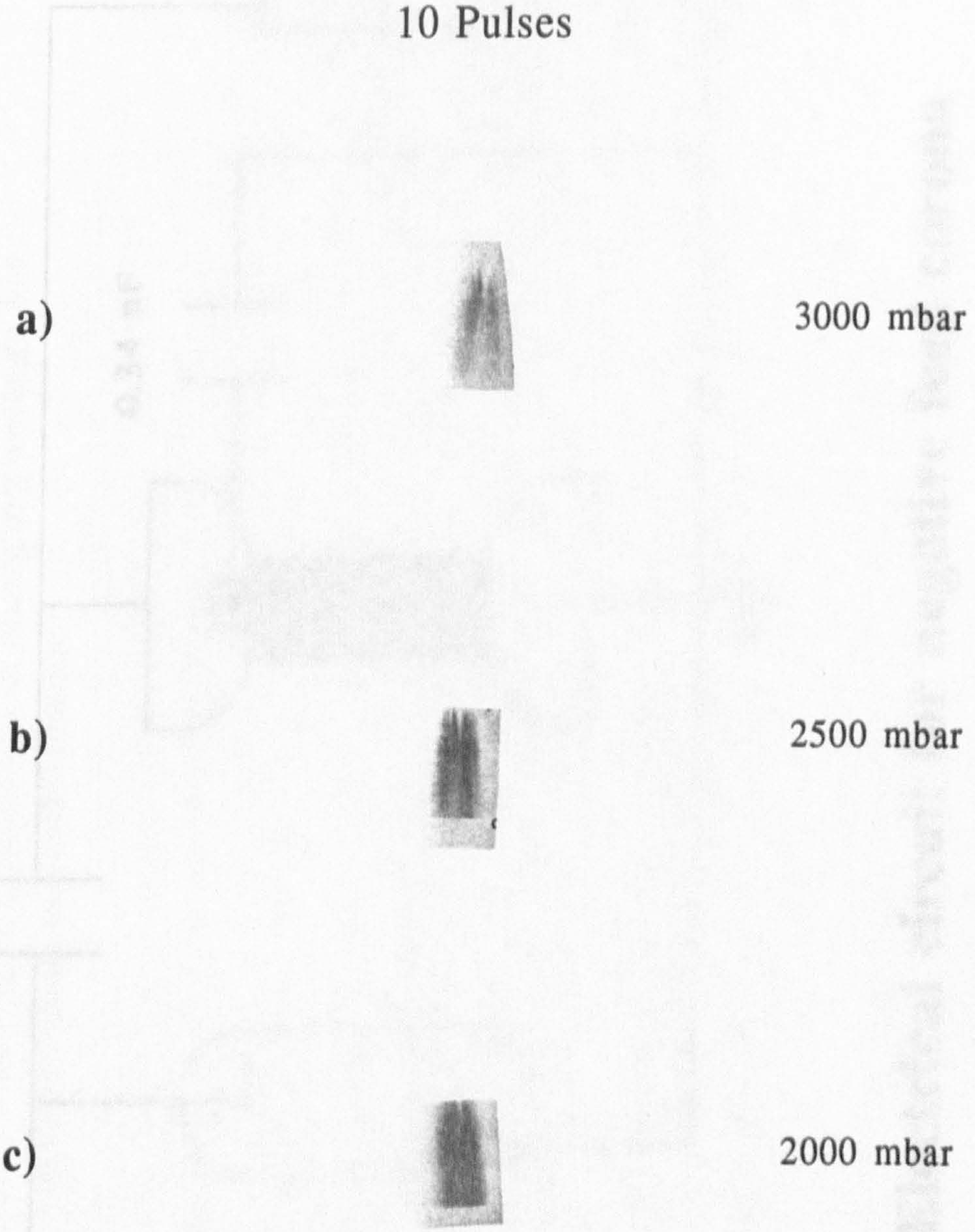

Fig. 3.31 Laser burn patterns, taken on Dylux paper, at various operating pressures

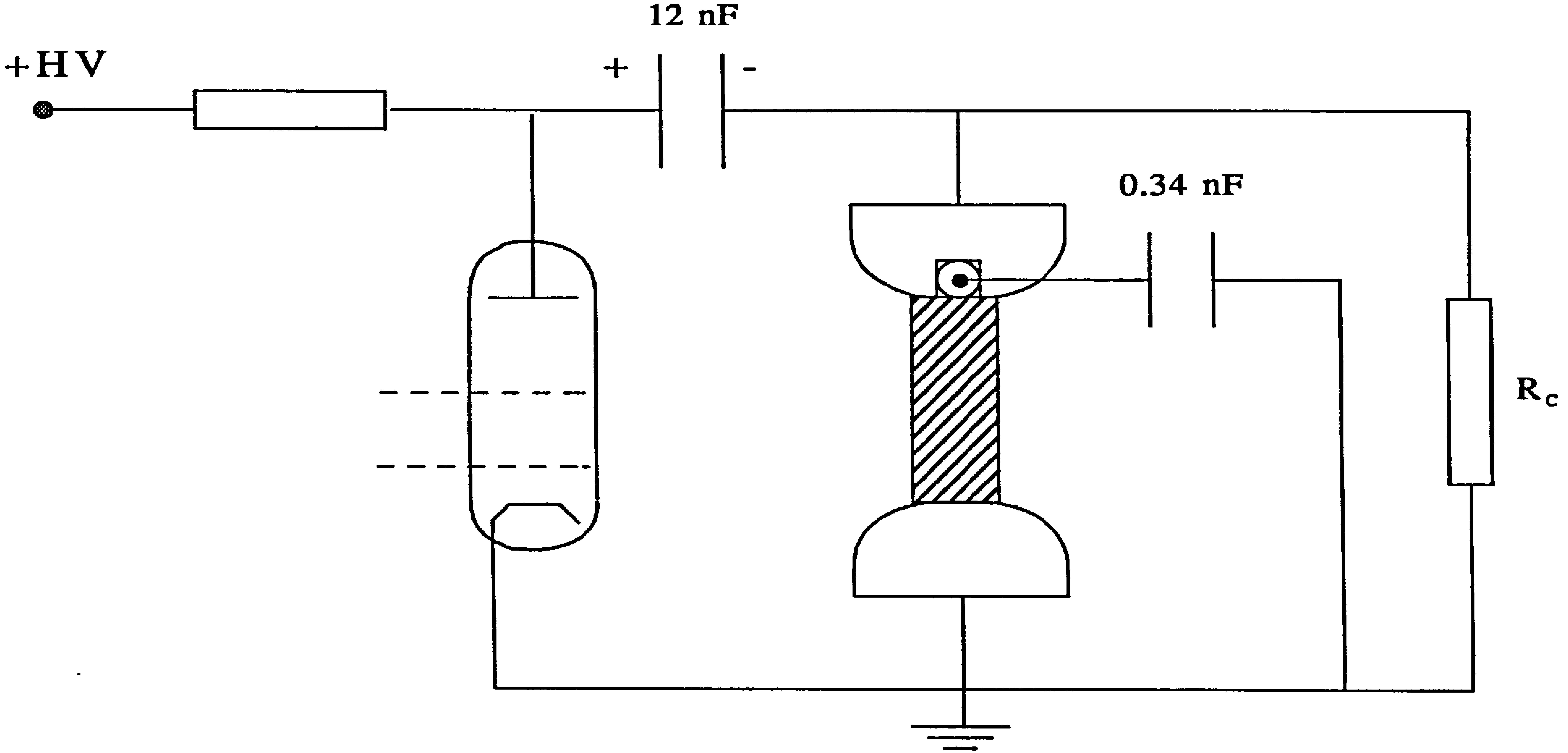

Fig. 3.32 Electrical circuit for negative feed corona preionisation

Fig. 3.33 Output power, @ 50 Hz, as a function of charging voltage for various xenon concentrations

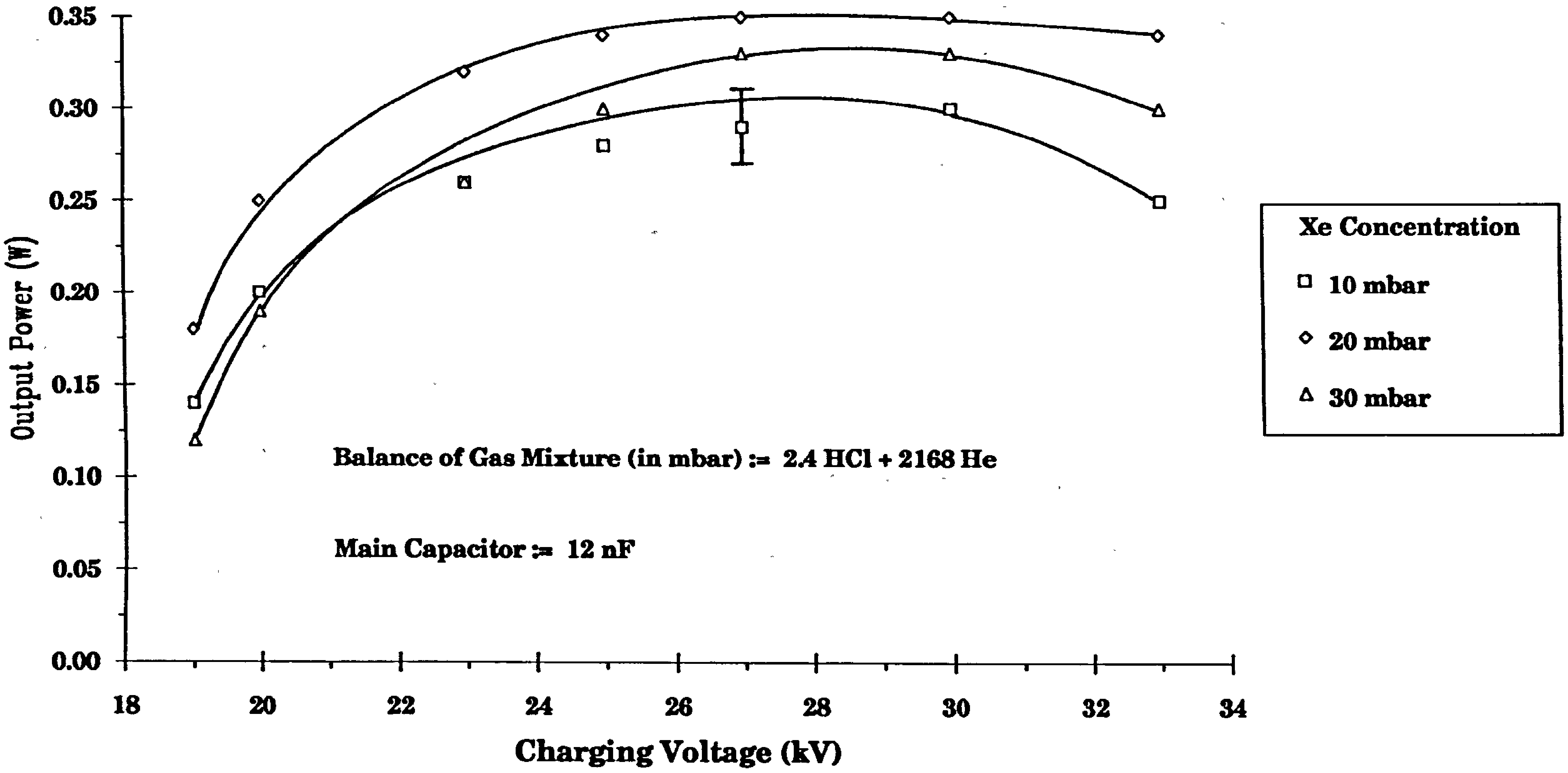

this time that the motor voltage setting required to obtain 400Hz operation was now down to 140V from that of the 160V required for the more conventional capacitively-coupled preionisation.

At this time, it was found that one of the Murata capacitors being used in the main 12nF capacitor bank had failed. As had happened previously, it was the capacitor placed opposite the thyratron connection that failed, presumably due to thermal effects from the high envelope temperature of the thyratron†. Once this capacitor was replaced, the effects of coupling capacitance to ground, for the corona preionisation bar, were investigated. Fig. 3.34 shows that as the coupling capacitance increases, so does the output power. At the low end, stray capacitance provided an estimated few pF's, a ~0.5m length of cable (100pF.m^{-1}) provided ~50pF capacitance, and at the high end, the corona preionisation bar was shorted out simulating "infinite" capacitance. It was decided to continue with the 0.34nF coupling capacitance, since there was no benefit in going higher and this served to protect the insulating ceramic from excessive currents in the event of a breakdown. The effects of inductance were also looked at, but with no measureable change in the output power.

Several lifetime runs with the corona preionisation scheme were made (Fig. 3.35) for helium and neon buffered gas mixtures optimised for maximum

---

† It should be noted that the epoxy encapsulation used in the "door knob" capacitors goes through a phase change, typically around 150°C, resulting in a glass like material being formed. This transition will result in the eventual failure of the capacitor. Therefore, since the thyratron envelope exceeds 140°C it is likely that this transition is taking place, and hence the capacitor eventually fails.

Fig. 3.34 Laser output power, @ 50 Hz, as a function of corona preionisation coupling capacitance

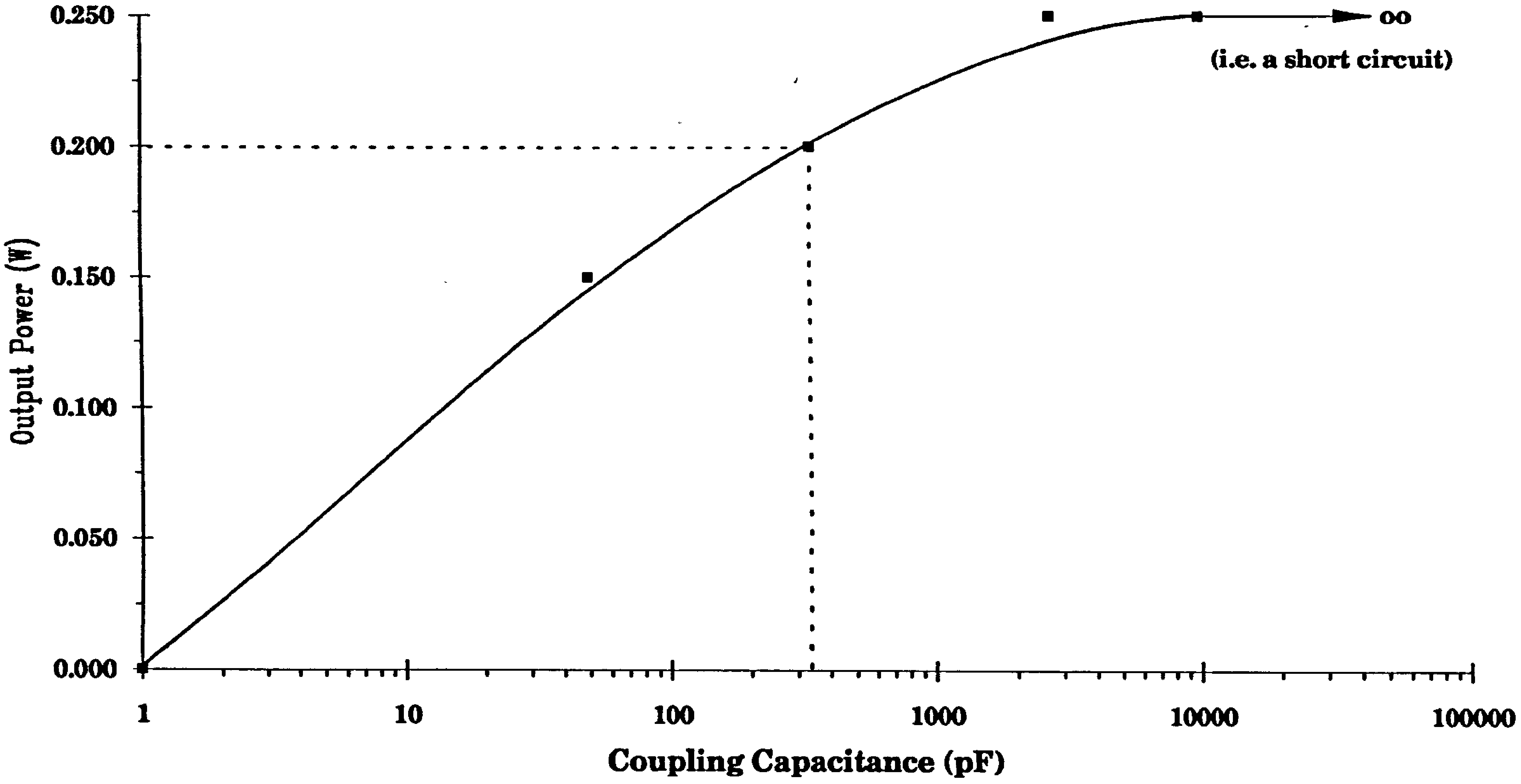

Fig. 3.35 Comparison of lifetimes for He & Ne buffered gas mixtures using the modified corona preionisation scheme

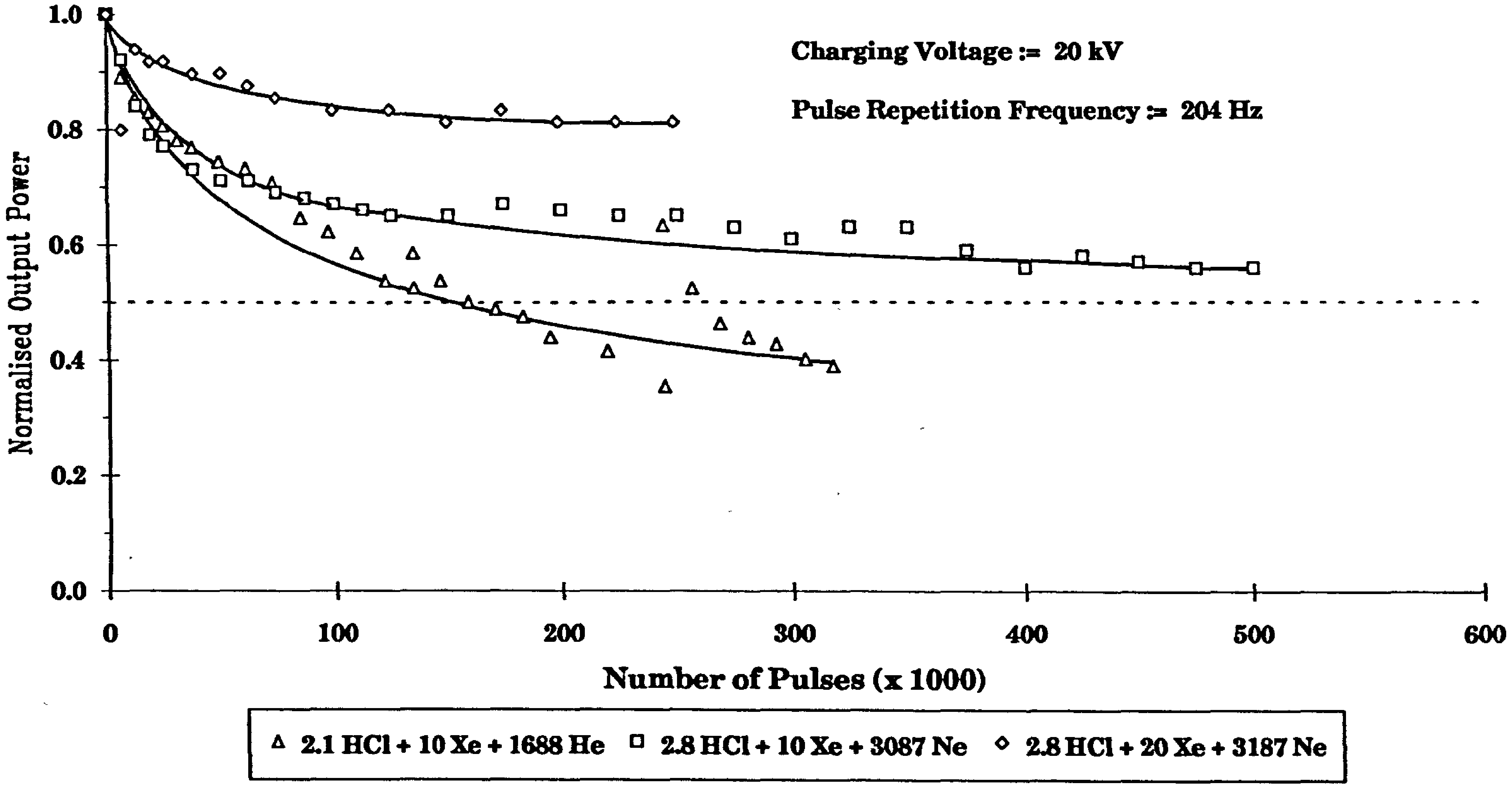

power output. Significant lifetime extension was made, ~2.5x, by changing the buffer gas from helium to neon, with a further uncompleted run with 20mbar Xe (rather than the 10mbar used on the previous runs) showing a lot of promise for lifetimes of the order of 10^6 pulses to half power. The effects of output coupler reflectivity on the output power at 700Hz were also investigated (Fig. 3.36), showing once again that a reflectivity of 36% was optimal. This, in keeping with the results for capacitively-coupled preionisation, indicates that in order to extract maximum efficiency from this size gain medium, operating at high-repetition-rate, higher cavity reflectivities are needed compared to high pulse energy devices which exhibit higher gain.

3.3.4 Conclusions

In conclusion, it was found that for efficient operation of the small gain length system constructed, particular attention in the design and layout of preionisation configurations was required. This is further borne out in the next section dealing with axial x-ray preionisation.

Of the preionisation techniques investigated, probably the best for discharge uniformity, and hence the ability to produce stable, homogeneous output pulses, was that of the negative feed corona preionisation scheme. However, the low output energy generated with this scheme was probably attributable to the non-optimal time delay between the preioniser emission and the main discharge pulse; resulting in a weakly preionised discharge. This situation may have been corrected if it had been possible to optimise the time delay between the preioniser and main discharge pulses. The capacitively coupled preionisation scheme produced a more intense preionising spark resulting in higher efficiences approaching 1%. However, because of the discrete nature of

Fig. 3.36 Laser output power @ 700 Hz as a function of output coupler reflectivity for a coronal preionisation scheme

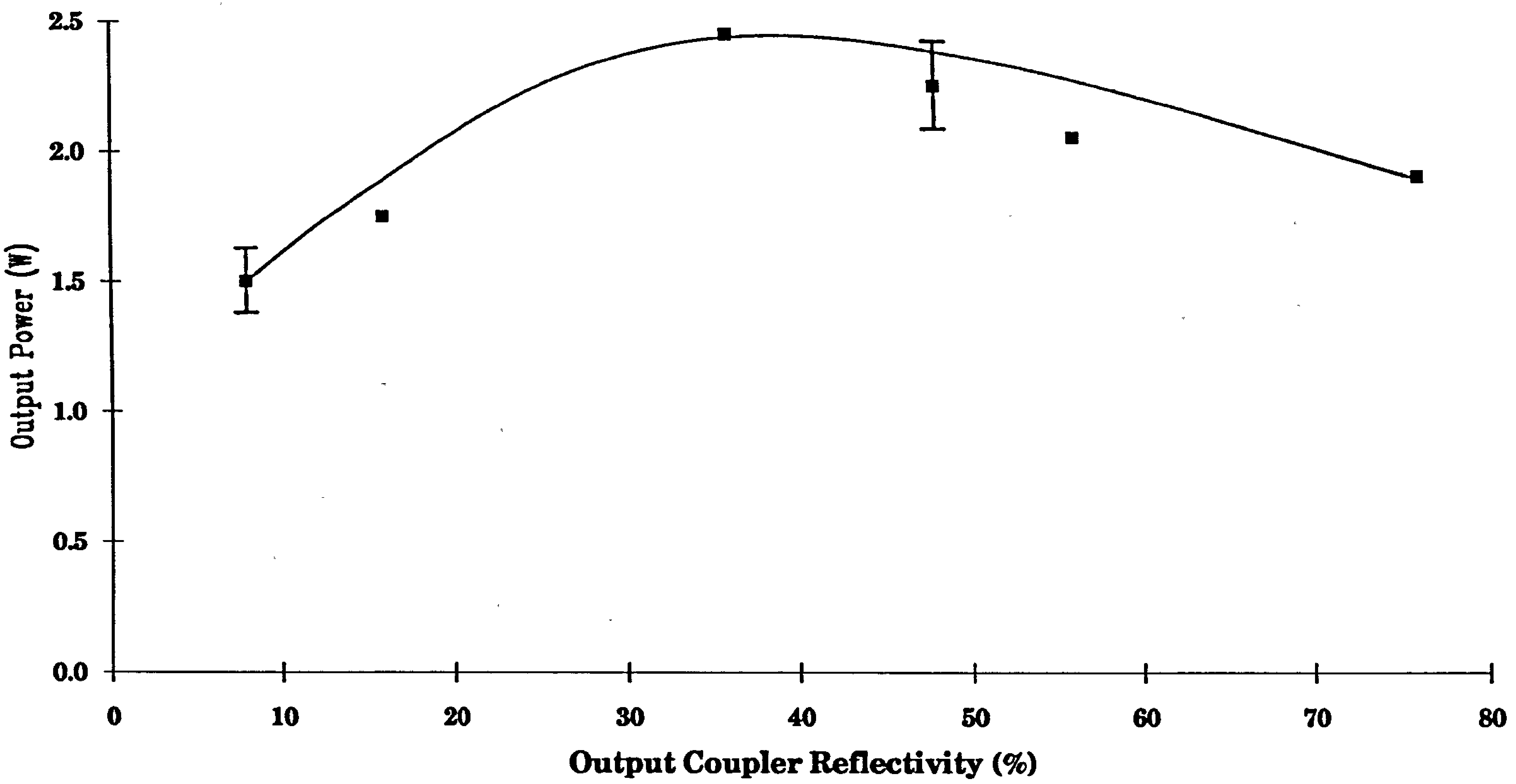

the sparks, it is a lot harder to achieve uniform discharges without compromising preionisation density, and hence pulse energy.

The poor results with the resistively-ballasted preionisation scheme were, like the corona preionisation scheme, probably attributable to the inadequate time delay between the preioniser emission and the main discharge pulse, and also the time taken for all the spark gaps to breakdown. This resulted in a poorly preionised discharge and reduced laser output. Once again this situation may have been corrected if it had been possible to optimise the time delay between the preioniser and main discharge pulses. Although the resistively-ballasted preionisation scheme proved inconclusive for excimer discharges, it was highly successful for the slower CO_2 laser operation where the time delay was more appropriate.

3.4 AXIAL X-RAY PREIONISED XeCl LASER

In this section, the use of an x-ray pulse generator to axially preionise this XeCl laser is described, and the results compared with the more conventional uv-preionisation technique. The axial x-ray source was initially developed for preionisation of a high pressure (>10 atmosphere) CO_2 laser [3.14]. The advantage of a small area x-ray source, to axially preionise a fast pumped 308nm XeCl laser, over transverse x-ray illumination [3.15 & 3.16], is that a very simple source is employed, with the preionising radiation entering the discharge chamber through one of the laser mirrors; it thus avoided the need for a slot window in the high pressure vessel. By this approach, x-ray preionisation can readily be incorporated into an existing laser system [3.17] and, as described below, allows a direct and meaningful comparison to be made between x-ray and uv preionisation. It is shown that the relative performance of the axial x-ray preionised and the optimised uv preionised

XeCl laser, in terms of output energy and efficiency, is dependent on the Xe concentration in the mixture, with up to 50% enhancement in the output energy being obtained for high Xe concentrations in the x-ray scheme. The combined use of uv and x-ray preionisation was found to be unattractive, since the laser performance, in most cases, mirrors that attained with the poorer of the two sources (i.e. uv preionisation).

Prior to starting any experimentation, calculations were made, for various likely materials to be used, of the mass absorption coefficient, μ (cm^2g^{-1}); the linear absorption coefficient, $\bar{\mu}$ (cm^{-1}); and hence the x-ray transmission coefficient, $\bar{T}$. These calculations were necessary to determine the window material for the laser resonator as well as that for the x-ray gun. Also, it was necessary to ensure the safety of the personnel involved in this experiment by shielding them from the stray radiation hazard. Calculations were also made for the gas mixture, to ensure that sufficient penetration of the x-rays would occur to uniformly preionise the length of the discharge region.

3.4.1 Calculation of $\bar{T}$ for Various Materials

The following calculations were carried out for HCl/Xe/Ne gas mixtures consisting of 4mbar HCl, 20→80mbar Xe, and total pressures in the range 1500→3000mbar using Ne as the buffer gas. Calculations for specific x-ray wavelengths of 0.178Å (69.5keV), 0.42Å (29.3keV) and 1.02Å (12.1keV) were made; 0.178Å & 1.02Å corresponding to the K & L_I absorption edges respectively of the tungsten target used in the x-ray diode, and 0.42Å corresponds to the peak of the x-ray spectrum for the tungsten target at an excitation potential of 90keV [3.18].

The mass absorption coefficient, μ, as a function of wavelength was obtained for each element [3.19]. μ was then calculated for HCl using,

$$\mu_{A_1A_2\ldots A_i} = \sum_{i=1}^{N} [A_i\%]\,\mu_{A_1A_2\ldots A_i} \qquad \ldots (3.1)$$

where μ_{A_i} is the mass absorption coefficient of an element (or molecule), and $A_i\%$ is the percentage by weight of the element (or molecule) in the mixture denoted by $A_1A_2 \ldots A_i$. A_i is the mass weight of one of the components calculated from the product of the number of moles, n_i, and the molecular weight, M_i, of each gas, i, and by applying the equation of state for an ideal gas:

$$P_iV = n_iRT \qquad \ldots (3.2)$$

$$A_i = n_iM_i \qquad \ldots (3.3)$$

where P_i is the pressure of the i^{th} gas, V is the volume, R the universal gas constant and T the temperature of the gas. Table 3.3 summarises the mass absorption coefficient data as a function of x-ray wavelength.

From the product of $\mu_{A_1A_2\ldots A_i}$ and the total density $\rho_{A_1A_2\ldots A_i}$, the linear absorption coefficient $\bar{\mu}_{A_1A_2\ldots A_i}$ can be obtained:

$$\bar{\mu}_{A_1A_2\ldots A_i} = \mu_{A_1A_2\ldots A_i} \cdot \rho_{A_1A_2\ldots A_i} \qquad \ldots (3.4)$$

where

$$\rho_{A_1A_2\ldots A_i} = \sum_{i=1}^{N} \rho_{A_i} \qquad \ldots (3.5)$$

Mass Absorption Coefficient, μ (cm^2g^{-1})	X-ray Energy (keV)		
	12.1	29.3	69.5
μ_{Ne} ($A_{Ne} = 20.183$)	7.165	0.540	0.191
μ_{HCl} ($A_H + A_{Cl} = 36.46$)	33.193	2.727	0.361
μ_{Xe} ($A_{Xe} = 131.30$)	110.750	9.810	5.724

Table 3.3 Mass absorption coefficients for Ne, HCl and Xe for various x-ray energies. [3.19]

Xenon Partial Pressure (mbar)	Linear Absorption Coefficient, $\bar{\mu}$(cm^{-1})		
	X-ray Energy (keV)		
	12.1	29.3	69.5
20	1.92×10^{-2}	1.53×10^{-3}	5.4×10^{-4}
40	2.18×10^{-2}	1.74×10^{-3}	6.44×10^{-4}
60	2.44×10^{-2}	1.95×10^{-3}	7.5×10^{-4}
80	2.71×10^{-2}	2.17×10^{-3}	8.5×10^{-4}

Table 3.4 Linear absorption coefficient for HCl:Xe:Ne gas mixture for various concentrations of Xe and x-ray energies using 4 mbar HCl and balance Neon to 3000 mbar.

and

$$\rho_{A_i} = \frac{M_i}{RT} P_{A_i} \qquad \ldots (3.6)$$

The latter equation is obtained by substitution of Eqs. (3.2) & (3.3) into $\rho_{A_i} = {}^{A_i}/_{V}$. Table 3.4 shows the linear absorption coefficient, $\bar{\mu}$, for various concentrations of Xe and x-ray wavelengths. From this data it is clear that Xe, despite its low concentration, plays a dominant role in the gas mixture in determining how well the x-rays will penetrate; this is because of its high atomic number (Z=54) and mass absorption coefficient. This domination does, however, reduce on moving to higher x-ray energies.

The transmission coefficient, $\bar{T}$, of the x-rays passing through the gas is given by [3.19]

$$\bar{T} = \frac{I_r}{I_o} = e^{(-\bar{\mu}_{mix}.r)} \qquad \ldots (3.7).$$

where I_o is the x-ray intensity at r=0 and I_r is the intensity after passing a distance r through the gas mixture. Fig. 3.37 shows the transmission, $\bar{T}$, as a function of r for Xe partial pressure in the range 20→80mbar and x-ray energies of 69.5, 29.3 & 12.1keV. As one would expect, based on the data presented in Table 3.4, $\bar{T}$ decreases with increasing Xe concentration as a function of distance. Also, $\bar{T}$ decreases with decreasing x-ray energy, indicating that the lower energy component of the broad-band source will be rapidly attenuated on propagating into the gaseous medium.

Fig. 3.38 shows the mass penetration depth, ${}^{1}/_{\bar{\mu}}$, as a function of Xe concentration for different x-ray energies. ${}^{1}/_{\bar{\mu}}$ decreases as a function of Xe concentration, such that, for 69.5keV x-rays, the penetration depth drops

Fig. 3.37 Transmission coefficient, $\overline{T}$, as a function of x-ray penetration depth, r, for various Xe concentrations and x-ray energies

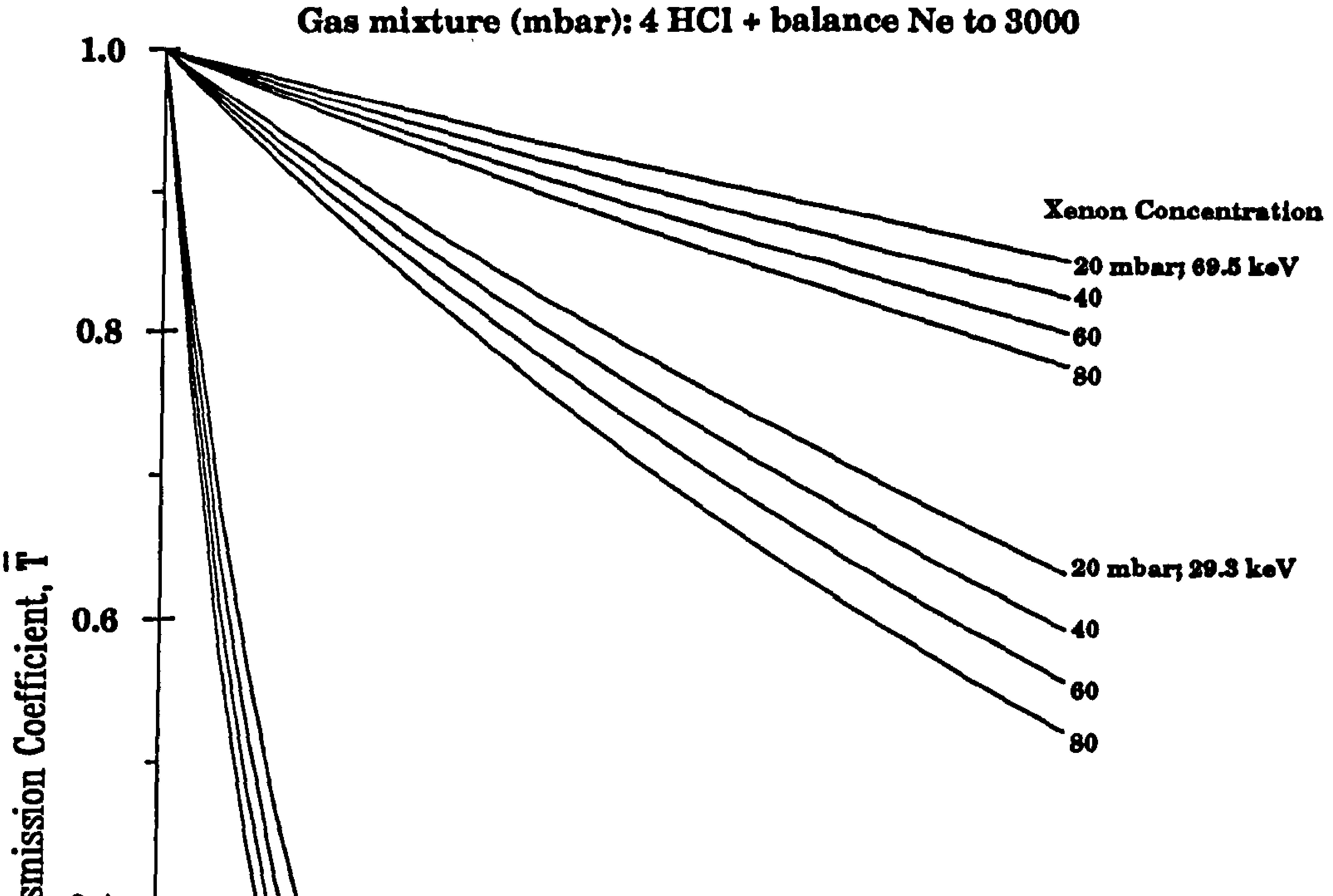

Fig. 3.38 Mass penetration depth, 1/$\bar{\mu}$, as a function of Xe partial pressure for different x-ray energies

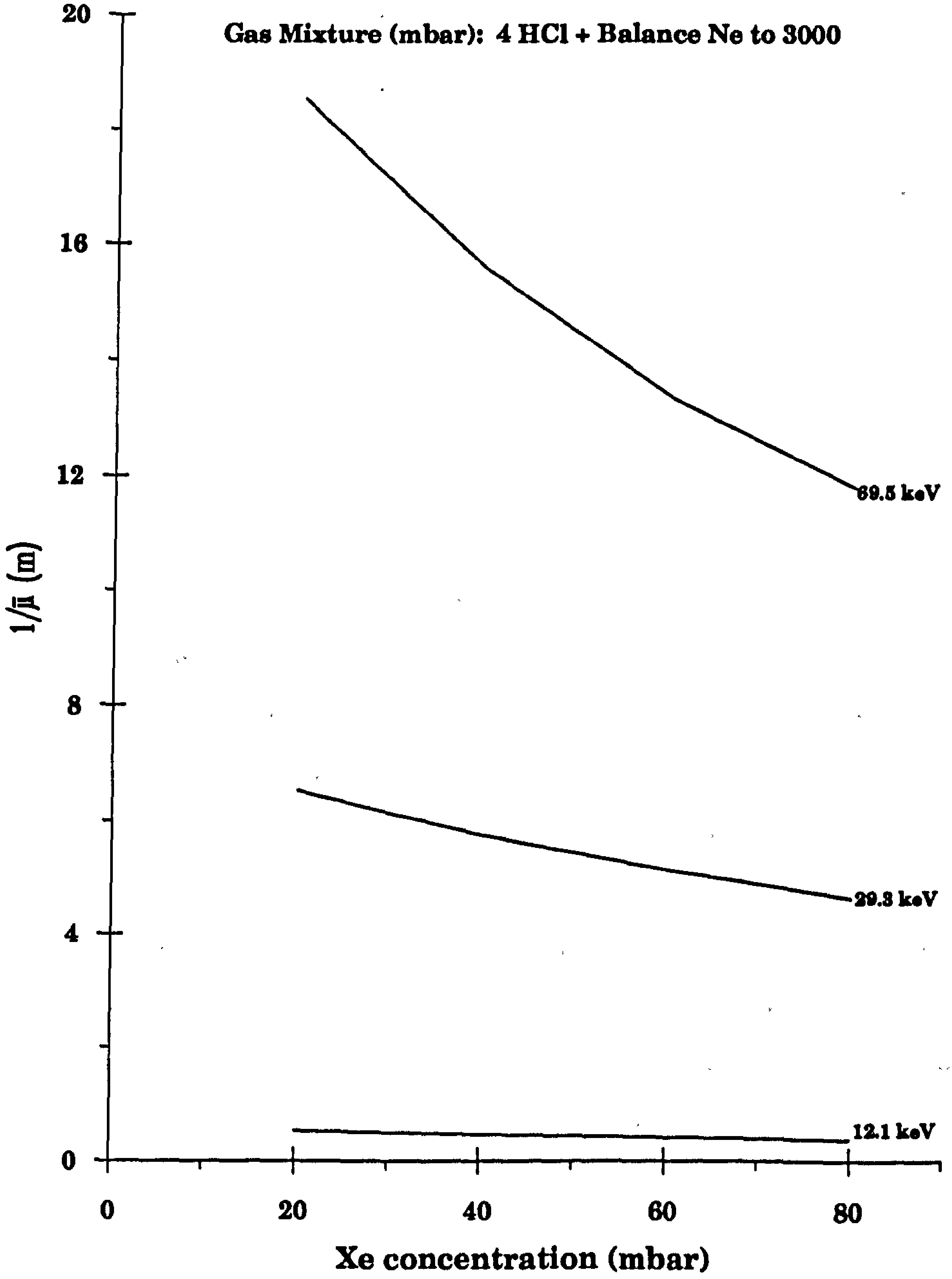

from 18.4 to 11.7m for Xe concentrations between 20 and 80mbar repectively. $^1/_{\bar{\mu}}$ for 12keV x-rays is essentially constant around 0.4m irrespective of the Xe concentration.

Calculations were also performed for a variety of materials pertinent to the experiment in terms of windows for the x-ray gun and for the laser, as well as other materials relating to safety requirements [3.19]. Table 3.5 gives the linear absorption and transmission data for materials such as fused silica (SiO_2), used as the substrate for the rear reflector of the laser resonator, and perspex ($C_5H_8O_2$) which was used for the window of the x-ray diode because of its low density (1.19g.cm^{-2}).

3.4.2 Description of the Experimental Arrangement

High voltage breakdown between point-plane tungsten electrodes at a pressure $<10^{-4}$ torr was used to form a small area x-ray source as shown in Fig. 3.39. The anode was fabricated from mallory metal (copper-tungsten alloy) with a 5mm diameter tungsten insert which acted as the main target. The anode angle of 70° was chosen to maximise emission in the direction of the 2.4mm thick perspex window of the x-ray tube. A two-stage Marx generator, charged at $50 < V < 57.5$kV and having an erected capacitance of 600pF, was used to power the x-ray source (Fig. 3.40). At the maximum charging voltage, the dose measured at the outer surface of the perspex window was ~35mr/shot; the x-ray pulse duration was dependent on the charging voltage, but typically was 30→80ns (FWHM) as measured using a high-speed scintillator (NE 104)-photomultiplier (EMI 9813) combination. A more detailed description of the experimental arrangement and performance of the x-ray source can be found elsewhere [3.14].

Material	Depth (cm)	Linear Absorption Coefficient $\bar{\mu}$(cm^{-1})	Transmission, $\bar{T}$		
			X-ray Energy (keV)		
			12.1	29.3	69.5
Pb	0.2	37.4			5.64×10^{-4}
		362.88		3.02×10^{-32}	
	0.4	37.4			3.18×10^{-7}
		362.88		9.15×10^{-64}	
Fe	0.63	6.76			1.41×10^{-2}
		63.7		3.73×10^{-18}	
Perspex ($C_5H_8O_2$)	0.2	0.21			0.96
		0.35		0.93	
		2.3	0.63		
Fused Silica (SiO_2)	0.1	0.56			0.95
		2.12		0.81	
		27.93	6.12×10^{-2}		
	1.0	0.56			0.57
		2.12		0.12	
		27.93	7.42×10^{-13}		
Perspex & Fused Silica	0.3	0.71			0.81
		1.75		0.59	
		18.44	3.96×10^{-2}		

Table 3.5 Linear absorption coefficient, μ, and transmission coefficient, T, for various materials used in the system.

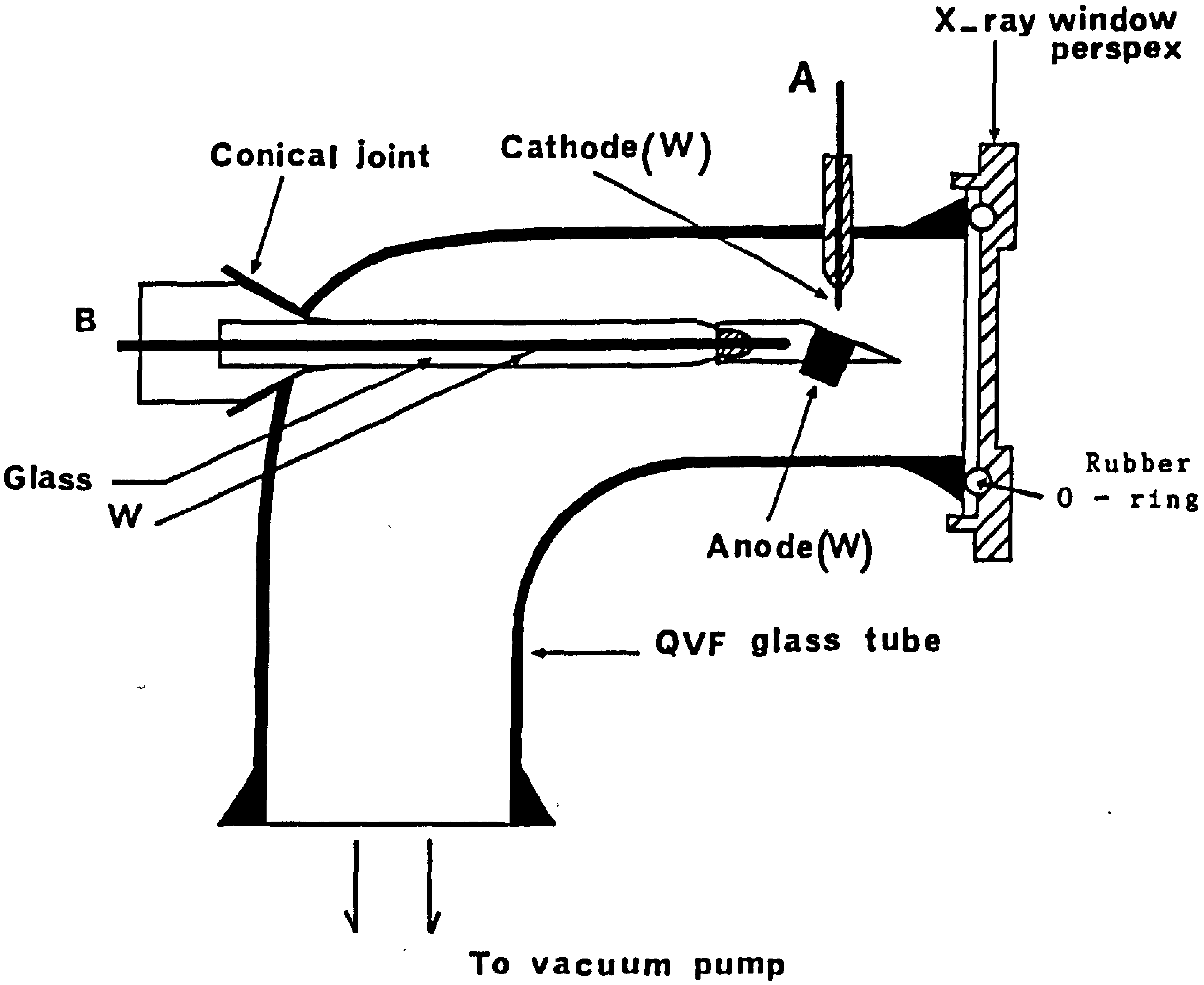

Fig. 3.39 Schematic diagram of the x-ray generator, showing the point-plane (W) geometry

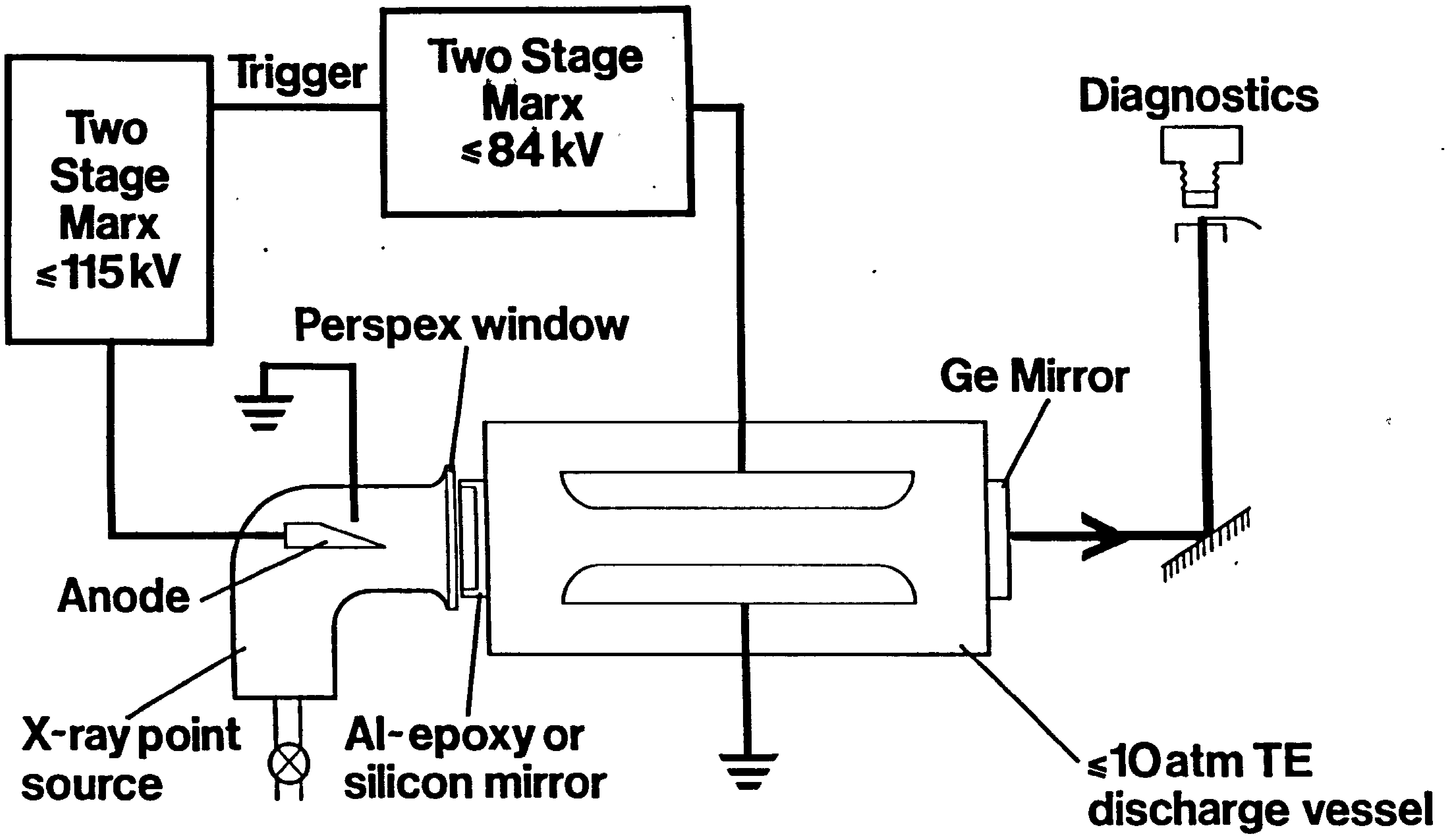

Fig. 3.40 Schematic diagram showing the experimental set-up of the two-stage Marx generator, used to power the x-ray source and detector arrangement

Visual observation of the anode, following multishot breakdown, showed that a relatively bright, clean area, was formed extending to slightly beyond the boundary of the tungsten insert, with a surrounding, approximatley circular, darkened zone extending the full width (10mm) of the anode. X-ray pinhole photographs of the source using a 0.5mm diameter pinhole in the lead sheet and a magnification of unity were obtained viewing the source normal to the x-ray window. These revealed that the most intense emission occured from a zone of 5mm diameter, corresponding to the tungsten insert with a weaker diffuse emission spreading over the anode to a diameter 10mm. At the viewing angle of 70° the source appeared elliptical with a width to height ratio of ~3:1. The peak current density estimated on the basis of the full emission area was $\sim 6\text{A.mm}^{-2}$.

Preionisation x-rays entered the laser chamber through the fully reflecting mirror at one end of the laser, as shown in Fig. 3.41. Initially, in order to maximise the transmitted dose, a thin perspex disc was used to seal the pressure vessel. Furthermore an internally mounted 1mm thick fused silica substrate, aluminised on its rear surface, was employed as the fully reflecting mirror. However, subsequent experiments showed adequate preionisation could be obtained using a 10mm thick rear-surface aluminised silica flat, which also acted as the pressure seal, and this was used for all experiments because of its better optical quality and dimensional stability. The partial reflector was formed by an aligned silica flat, which sealed the pressure vessel, and a ~28% reflectivity mirror mounted externally to the discharge head.

For this preionsation comparison, the XeCl laser discharge was formed between the uniform field "Monk" profile electrodes described in Section 3.3.1. This arrangement used a capacitively-coupled uv spark array, consisting

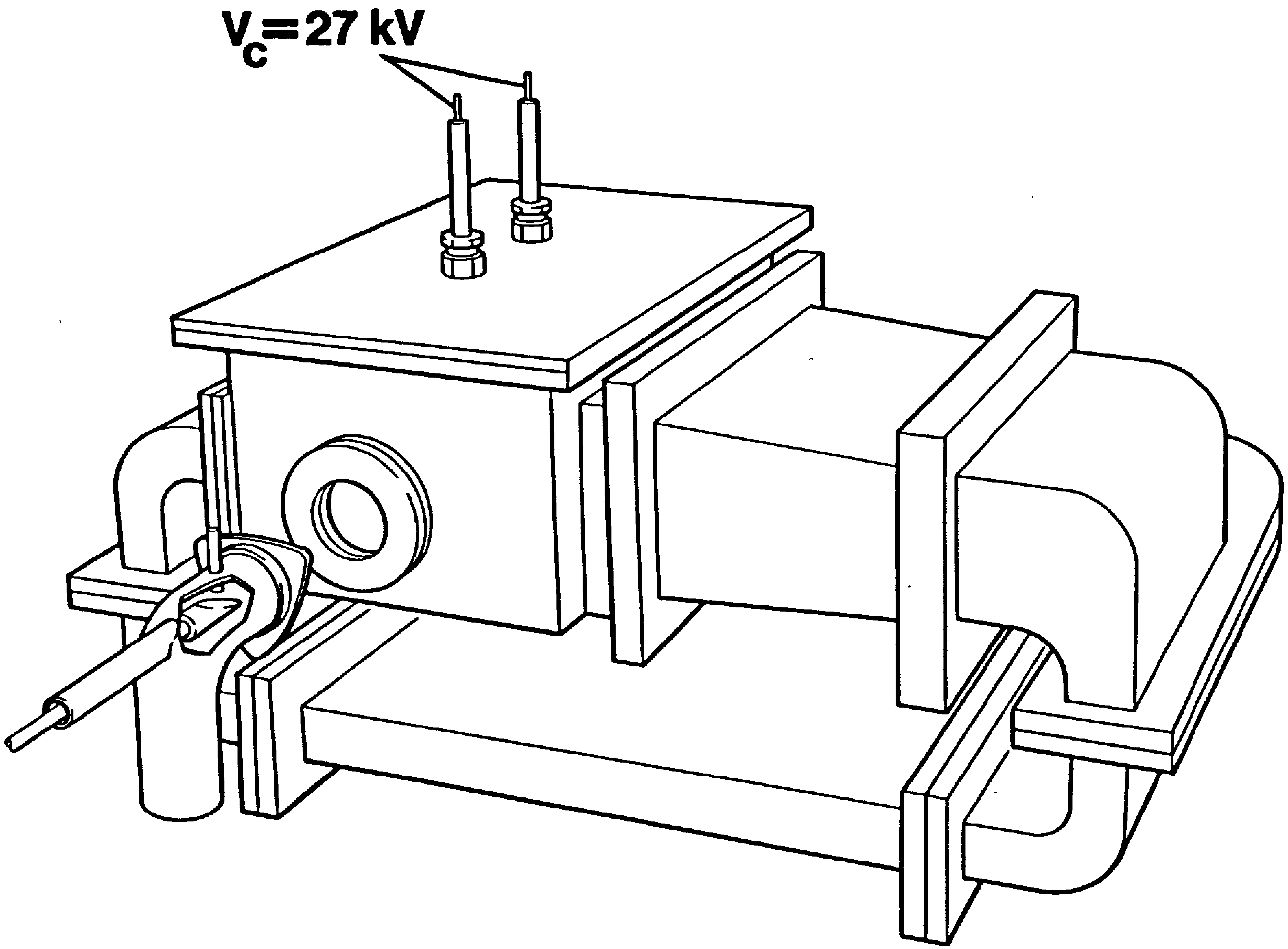

Fig. 3.41 High PRF laser chamber incorporating an axial x-ray preionisation system

of 15 sparks down each side of the discharge, and produced the maximum output energy and best illumination uniformity. For the axial x-ray preionisation studies, the internal spark gaps were either, short circuited using wire links, or covered using polyvinylidene fluoride (PVDF) tubes (Fig. 3.42). The PVDF covering completely attenuated the uv preionising radiation, but did not prevent the spark gaps from closing, or short circuited using wire links. Removal of the tubes or links allowed operation in the uv preionised mode without altering in any way the electrical circuit characteristics of the device. In some experiments, dual x-ray and uv preionisation were investigated; in the absence of uv and x-ray preionisation no laser output was observed.

The main discharge was excited using a 10 nF capacitor, charged at 16→35 kV, and switched using a thyratron. In the uv preionised mode, the delay between spark initiation and the appearance of the XeCl laser pulse was estimated from the time resolved voltage measurements to be 100 ns. With x-ray preionisation, the delay between the peak of the x-ray emission pulse and the rise of the voltage on the main laser electrodes was fixed at 140 ns, giving close to the optimum value required for effective lasing [3.20].

3.4.3 Performance Studies of UV and X-ray Preionisation

In all experiments great care was taken to adequately passivate the stainless steel pressure vessel which housed the discharge structure, in order to obtain reliable and reproducible lasing.

Performance studies were carried out with HCl/Xe/Ne mixtures at total pressures 1500→3000 mbar and Xe contents of 20, 40, 60 and 80 mbar. Using x-ray, uv, and combined sources as preionisers (Figs. 4.43→4.46), the laser

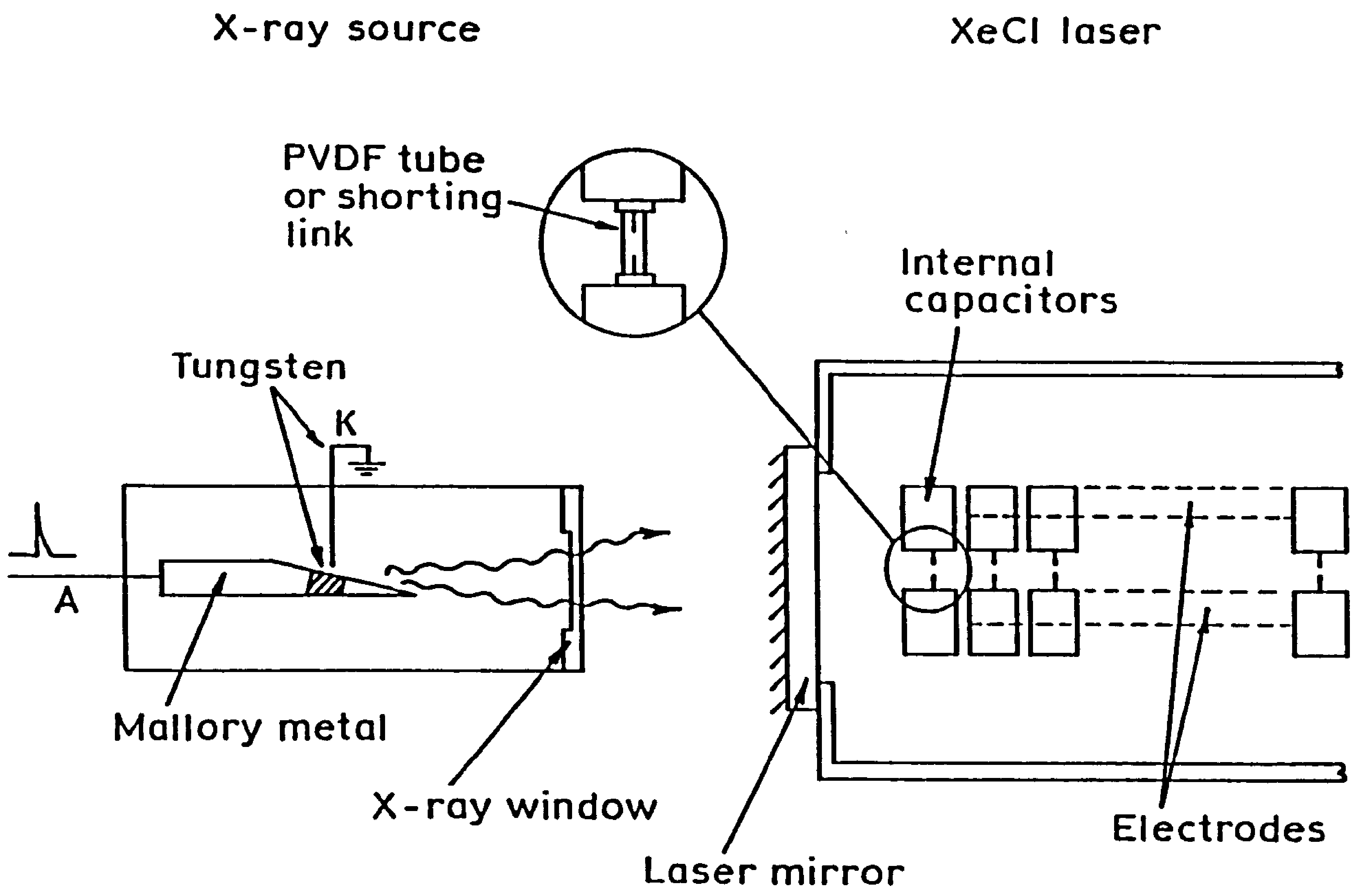

Fig. 3.42 Experimental arrangement used to study the effect of uv and axial x-ray preionisation

Fig. 3.43 Laser output energy as a function of laser charging voltage, for a Xe concentration of 20 mbar, with either uv or x-ray preionisation at various operating pressures

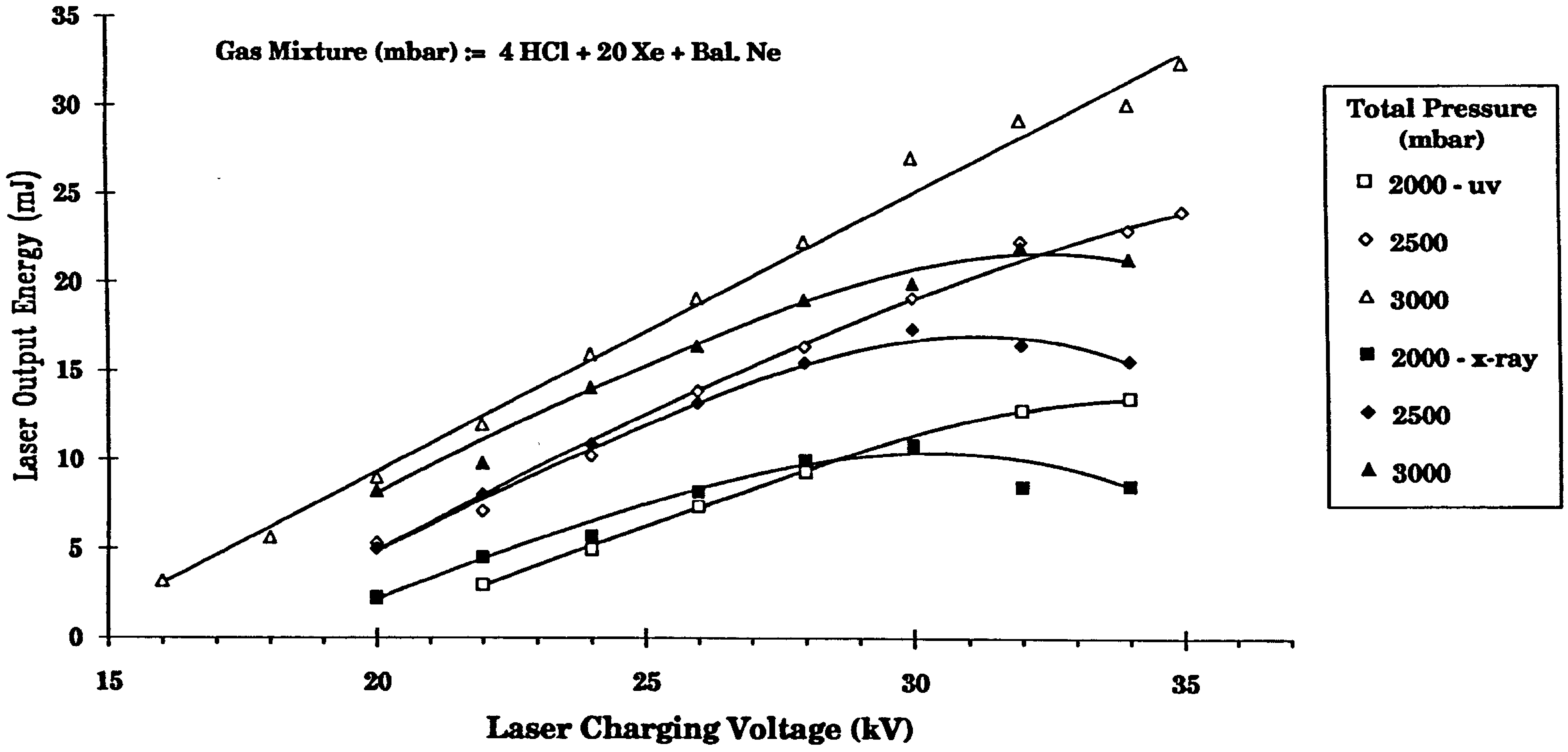

Fig. 3.44 Laser output energy as a function of laser charging voltage for a Xe concentration of 40 mbar with either uv or x-ray preionisation at various operating pressures

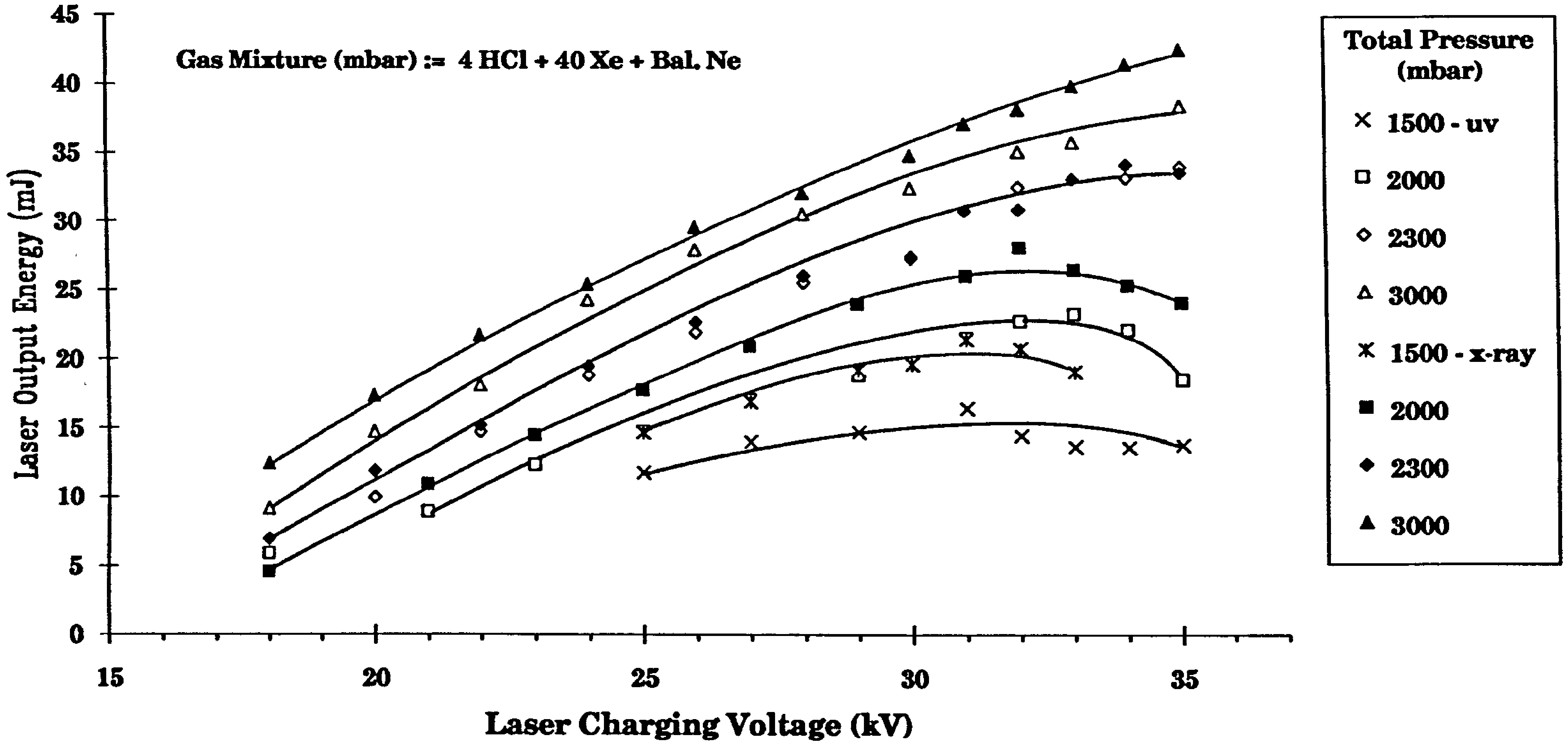

Fig. 3.45 Laser output energy as a function of laser charging voltage, for a Xe concentration of 60 mbar, with either uv or x-ray preionisation at various operating pressures

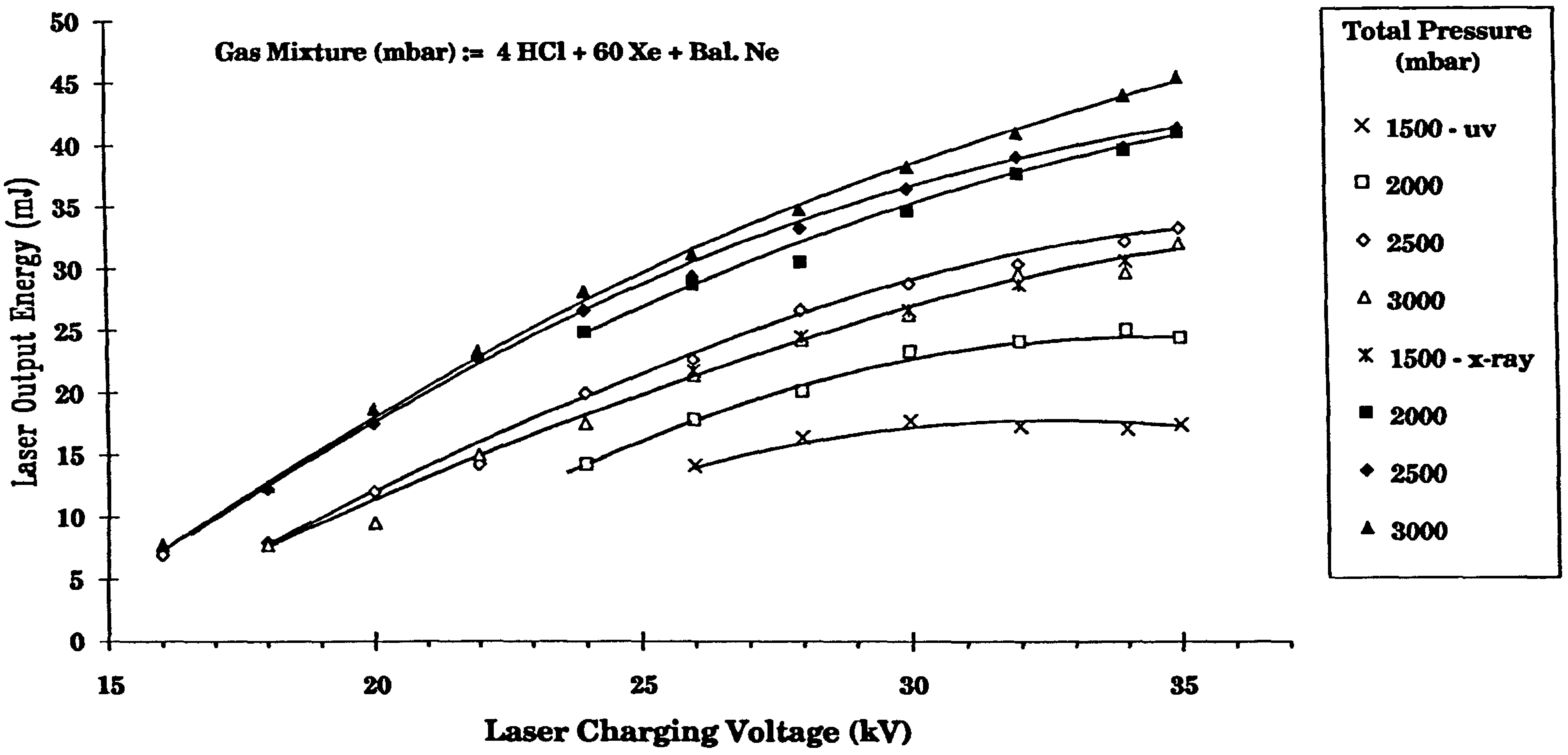

Fig. 3.46 Laser output energy as a function of laser charging voltage, for a Xe concentration of 80 mbar, with either uv or x-ray preionisation at various operating pressures

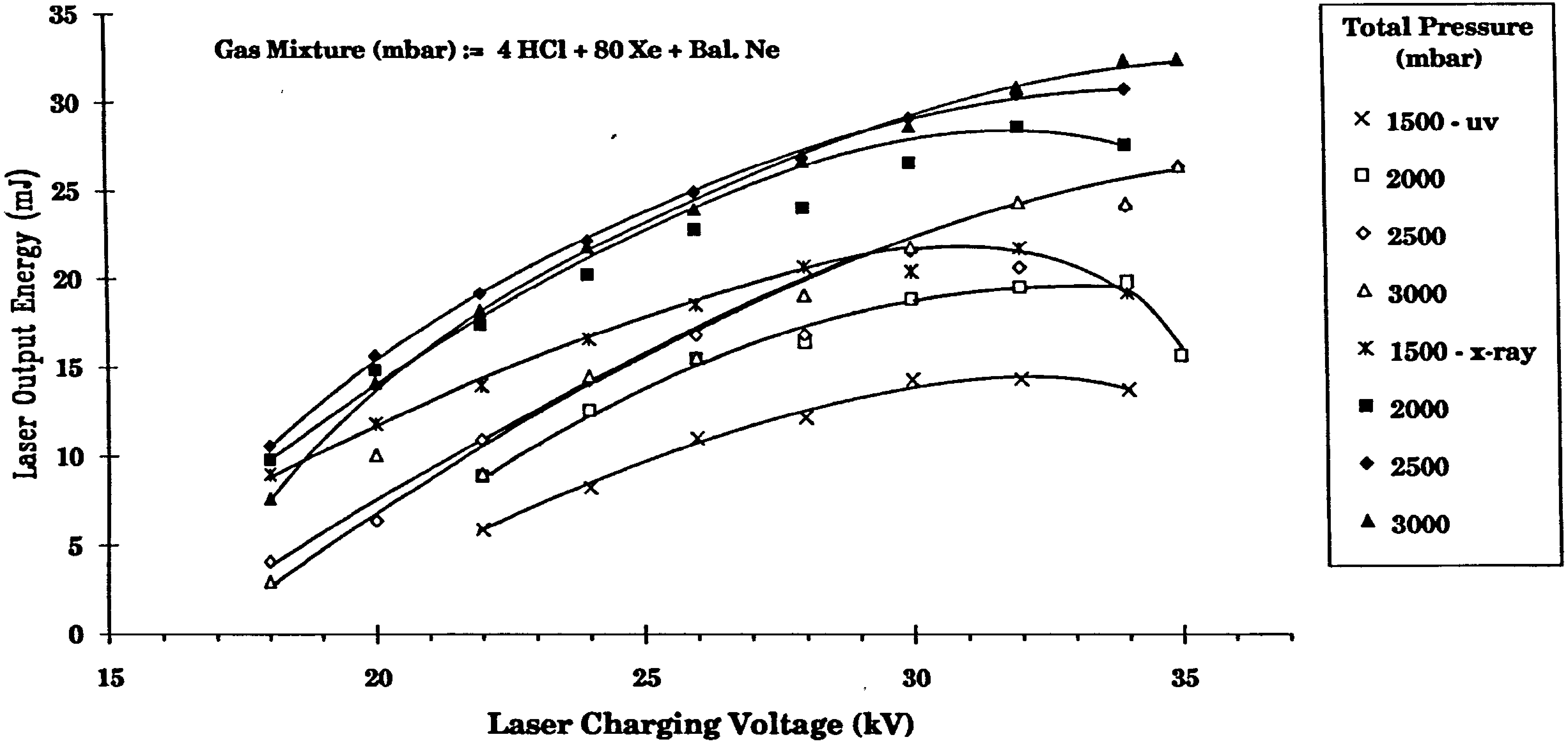

charging voltage was varied for various buffer gas pressures. At a Xe concentration of 60 mbar, the enhancement in energy output with the x-ray source nearly reaches its maximum value and, as can be seen, this gave significantly improved performance over the entire working range. Similar curves for other Xe concentrations were used to derive the enhancement factor (x-ray/uv laser output energy ratio) and results for this, together with the uv and x-ray preionised laser efficiency, are summarised in Fig. 3.47. Here the laser voltage was 24 kV giving, at 3000 mbar, nearly maximum efficiency in both cases. It can be seen from Fig. 3.48, that the enhancement factor is dependent on the Xe concentration, with x-ray preionisation leading to a marginally poorer performance for Xe = 20 mbar, but giving ~1.5 times improvement in energy for Xe > 60 mbar. The laser efficiency at Xe ~ 40 → 60 mbar shows a corresponding improvement with the x-ray system, attaining a value of nearly 1%. Shot-to-shot reproducibility with x-ray preionisation was considerably better (< 3%) than with the uv preionisation array (5 → 9%). For both sources, the laser pulse consisted of an initial fast-rising spike, followed by a broad tail with oscillatory structure having a full basewidth of ~60 ns (Fig. 3.49).

Results for the combined x-ray an uv sources are shown in Fig. 3.50. It was found that the performance under these conditions was nearly identical to that obtained using the uv preioniser alone. This behaviour was also noted for Xe=20 mbar and 40 mbar. Only for Xe = 80 mbar did the combined sources produce an improvement over the uv system, although the output energy still did not match that of the x-ray preioniser alone under these conditions. These results suggest that the local non-uniformities in preionisation, produced by the discrete nature of the uv array, dominate device performance, rather than a lack of sufficient preionisation density to effectively condition the discharge.

Fig. 3.47 Laser efficiency as a function of Xe concentration with either uv or x-ray preionisation

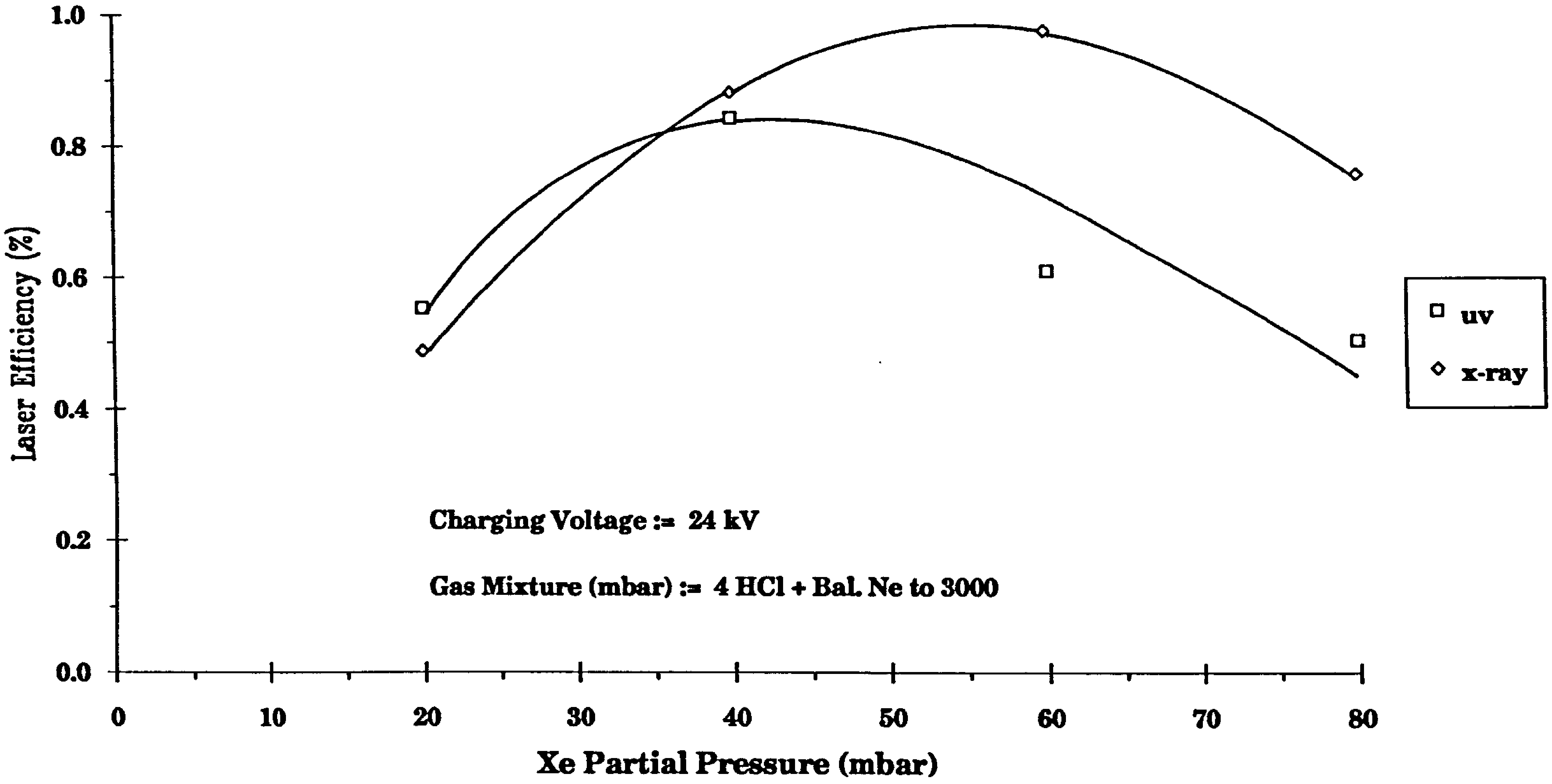

Fig. 3.48 X-ray/uv enhancement factor as a function of Xe partial pressure

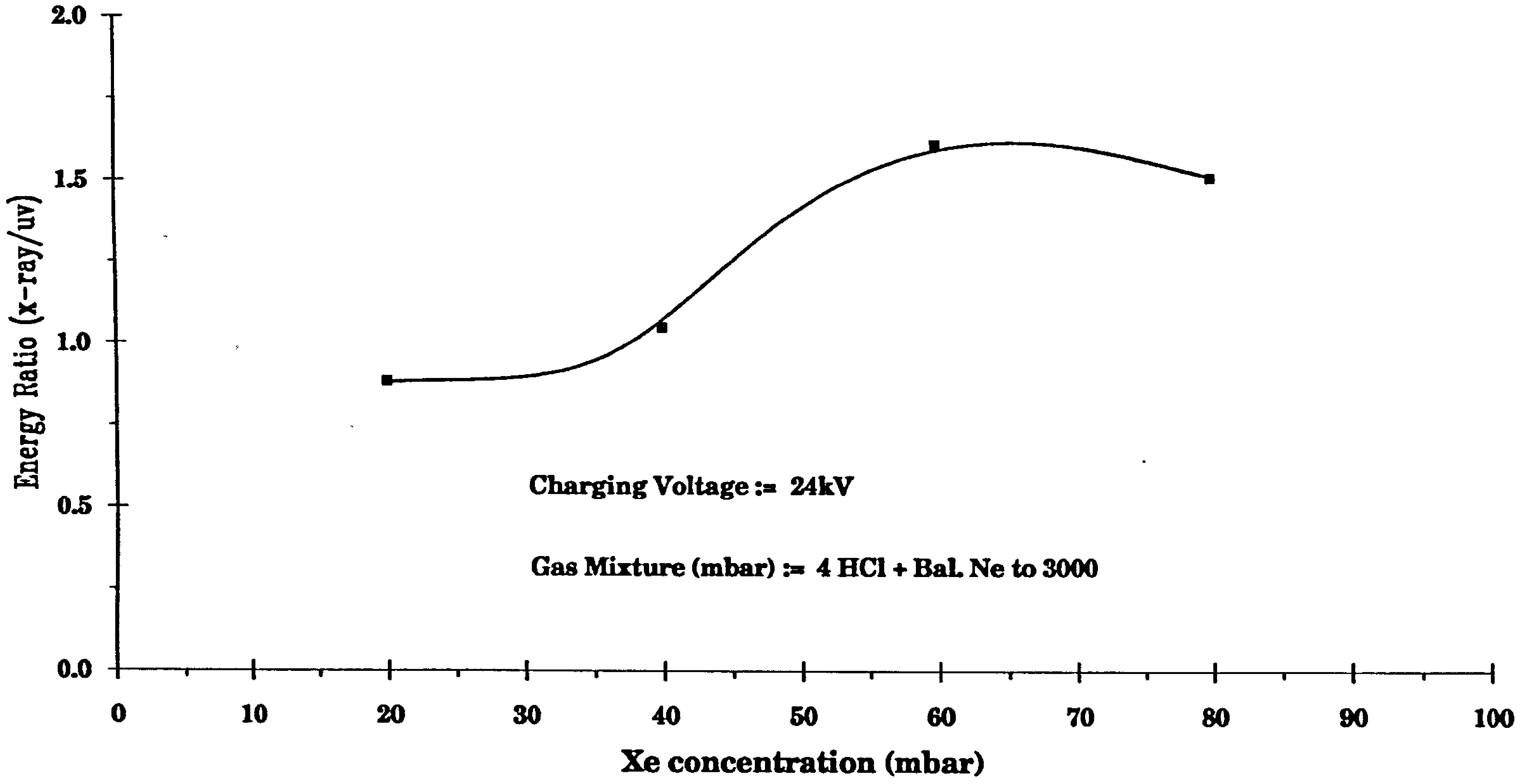

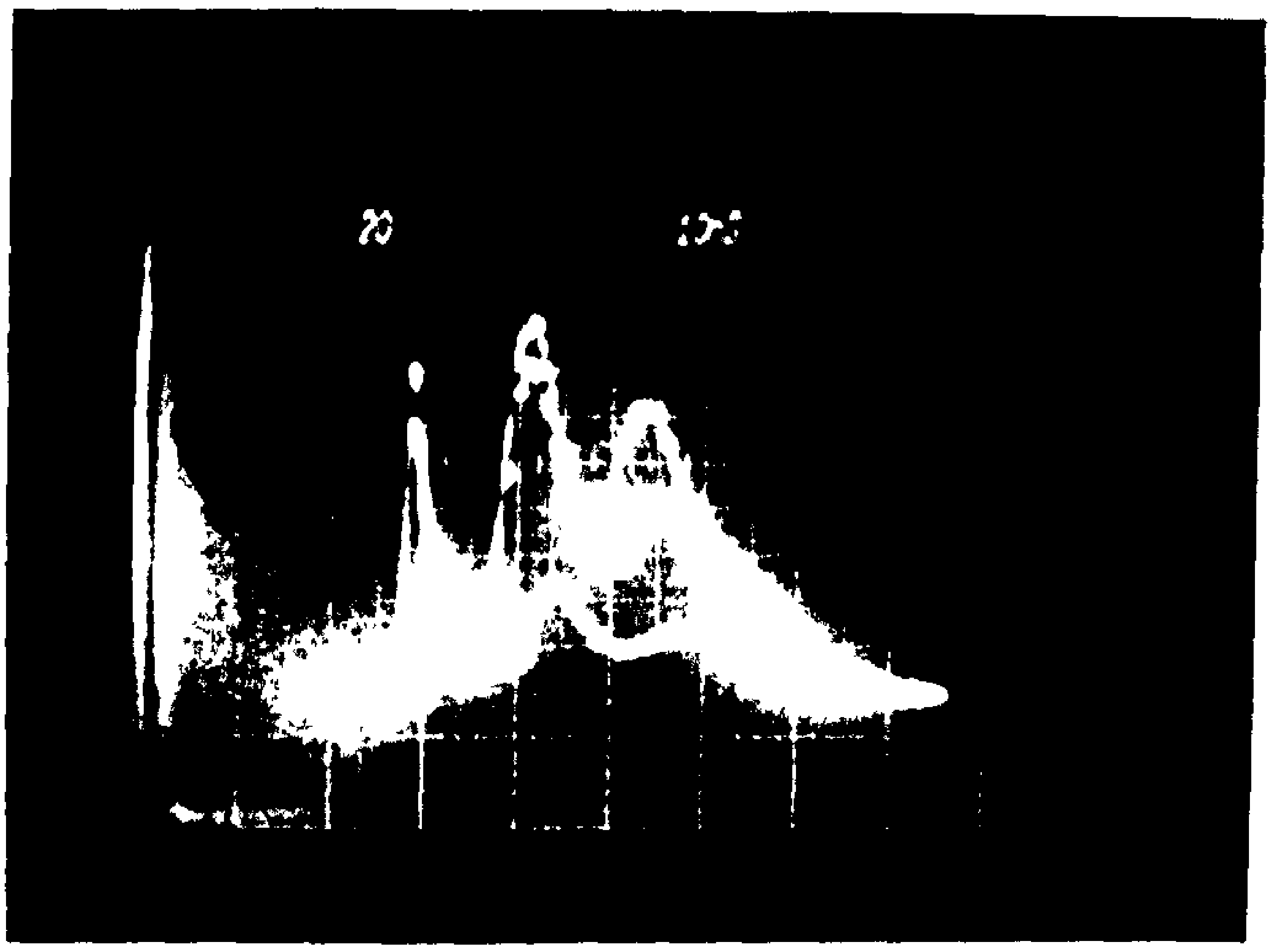

t = 10 ns/div

Fig. 3.49 XeCl laser pulse shape for a 4 mbar HCl + 80 mbar Xe + balance Ne to 3000 mbar gas mixture for various charging voltages

Fig. 3.50 Laser output energy as a function of laser charging voltage for various Xe concentrations and either uv or uv/x-ray preionisation

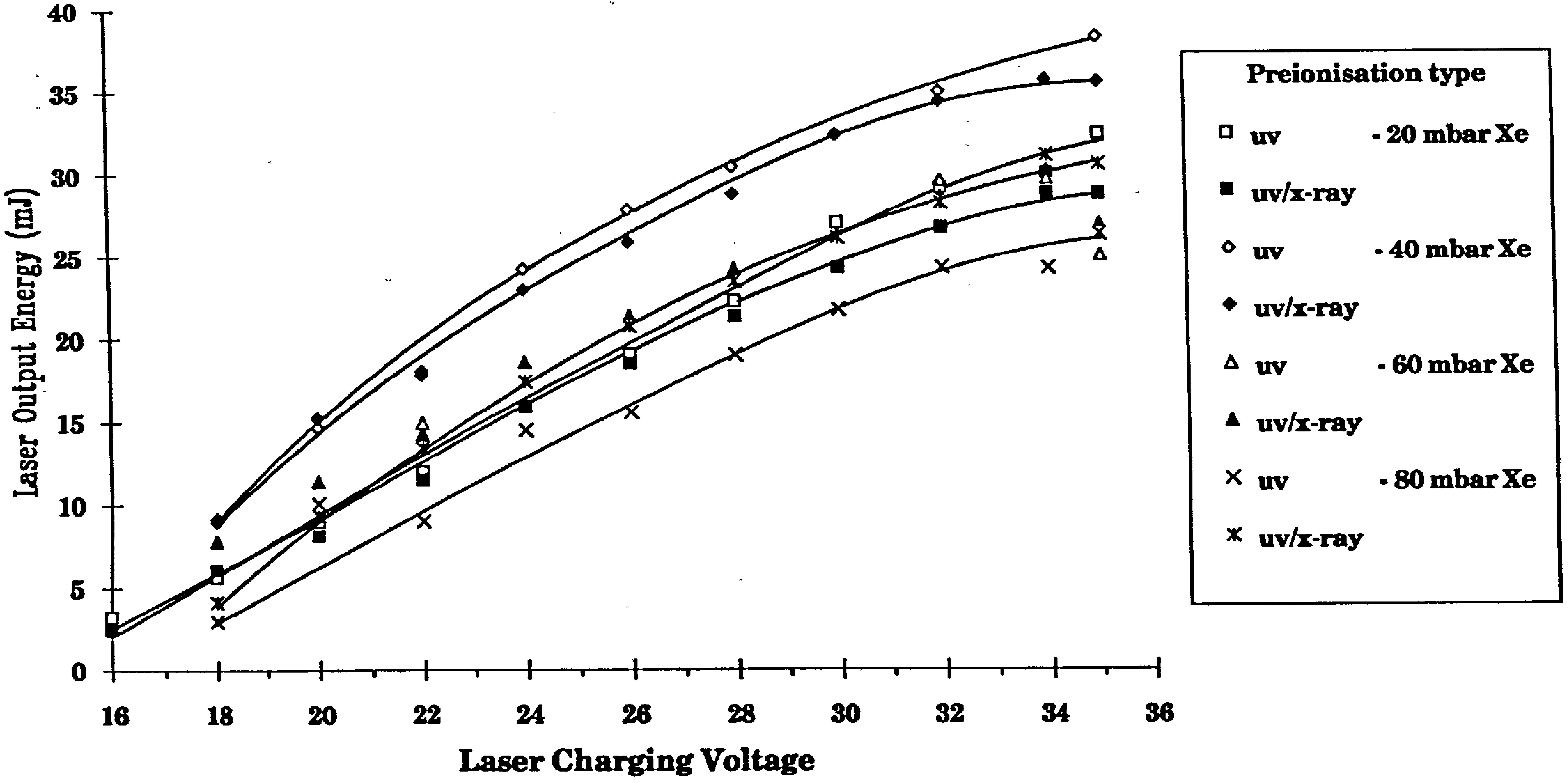

Consideration of the x-ray source characteristics [3.18], and filtering effects of the source window and laser mirror, indicates that the ionising radiation entering the discharge cell will be restricted to energies of $30 < E < 115\,keV$ for which, with Xe = 80 mbar in a 3000 mbar Ne buffered mixture, the corresponding range is > 200 cm. Thus, for the short gain length device, divergence of the x-ray from the near-point source, rather than absorption, will dictate the axial preionisation uniformity. Based on the source location, and an approximately inverse square intensity fall-off, the preionisation density can be estimated to vary by a factor of ~5 along the full length of the electrodes. In contrast, the preionisation uniformity across the aperture of the discharge is expected to be excellent. Using the measured x-ray transmission coefficient of the laser mirror (~12%), and the close proximity of the x-ray source to the mirror, the x-ray exposure at the far end of the electrodes was estimated to be 0.16 mrad; this exceeded the minimum value reported [3.21] being necessary for effective discharge conditioning. The corresponding electron density is calculated to be $7 \times 10^{8}\,cm^{-3}$, based on the absorption properties of the gas, although this may be an over-estimate because of fluorescence re-radiation [3.20]. Since Xe begins to dominate the x-ray absorption (and hence preionisation density) for pressures > 20 mbar, the improvements in output energy at high Xe concentrations (Fig. 3.47) can probably be attributed to the higher preionisation density achieved. It is interesting, that even with a substantial axial non-uniformity, this simple x-ray scheme gives improvement factors over uv techniques similar to those reported [3.22] for a transverse x-ray illumination scheme.

3.4.4 Conclusion

This work has shown that a simple and compact x-ray source is suitable for preionising a fast pumped XeCl laser, in an axial illumination scheme.

Although a significant axial intensity non-uniformity is present, because of divergence from the near-point source, a considerable enhancement in laser energy over that with an optimised transverse uv array is obtained. Some further improvements should be possible, using uv laser mirrors designed to provide a higher x-ray transmission than the value of ~12% attained in the present experiments. The axial preionisation technique can readily be incorporated in existing lasers, and should prove useful for improving the performance of, for example, compact high pulse rate devices albeit with the penalty of increased system complexity over uv preionisation.

REFERENCES

[3.1] N.H.BURNETT & A.A.OFFENBURGER, J. Appl. Phys., **44**, 3617 (1973)

[3.2] A.J.ALCOCK, K.LEOPOLD & M.C.RICHARDSON, Appl. Phys. Lett., **23**, 562 (1973)

[3.3] R.MARCHETTI, E.PENCO & G.SALVETTI, J. Appl. Phys., **56**, 3163 (1984)

[3.4] E.NASSER, "Fundamentals of Gaseous Ionisation and Plasma Electronics", Wiley (1971)

[3.5] A.OGAWA, "Separation of Particles from Air and Gases" (Volume II), CRC Press (1984)

[3.6] A.K.LAFLAMME, Rev. Sci. Inst., **41**, 1578 (1970)

[3.7] H.M LAMBERTON & P.R.PEARSON, Elect. Lett., **7**, 141 (1971)

[3.8] H.SEGUIN & J.TULIP, Appl. Phys. Lett., **21**, 414 (1972)

[3.9] B.NORRIS & A.L.S.SMITH, J. Phys. E: Sci. Inst., **10**, 551 (1977)

[3.10] K.RICKWOOD, J. Appl. Phys., **53**, 2840 (1982)

[3.11] T.Y.CHANG, Rev. Sci. Inst., **44**, 405 (1973)

[3.12] J.E.ANDREW, P.E.DYER, P.MONK & P.J.ROEBUCK, "Quantum Electronics and Electro-Optics", Wiley (1983)

[3.13] MATHEMATICAL SCIENCES NORTHWEST,

Private Communication (1983)

[3.14] D.N.RAOUF, PhD Thesis, Univ. of Hull (1987)

[3.15] S.LIN & J.I.LEVATTER, Appl. Phys. Lett., **34**, 505 (1979)

[3.16] K.MIDORIKAWA, M.OBARA & T.FUJIOKA,

IEEE J. Quant. Elec., **QE-20**, 198 (1984)

[3.17] D.N.RAOUF & P.E.DYER, Opt. Comm., **53**, 36 (1985)

[3.18] M.EHRLICH, J. Nat. Bureau of Standards, **54**, 107 (1955)

[3.19] E.F.KAELBLE, (Ed.) "Handbook of X-rays", McGraw-Hill, London (1967)

[3.20] H.SHIELDS, A.J.ALCOCK & R.S.TAYLOR, Appl. Phys. B, 31, 27 (1983)

[3.21] C.R.TALLMAN & I.J.BIGIO, Appl. Phys. Lett., **42**, 149 (1983)

[3.22] R.L.SANDSTROM, J.I.LEVATTER & R.P.ATKINS,

WF2, CLEO'83, Baltimore 1983

4. HIGH PRF TE LASER OPERATION

4.1 EFFECTS OF DISCHARGE INSTABILITIES ON LASER PRF

The output characteristics of high repetition rate, discharge pumped, gas lasers are determined by the electrode system efficiency for single pulse operation, and the ability to maintain these parameters under high repetition rate conditions. It has been shown, [4.1], that the time required for the gas flow to clear the inhomogeneities from the electrode region, and hence to permit subsequent arc-free glow discharge pulses, determines the maximum pulse-repetition-frequency (prf) of the device. Outlined in this section are experiments carried out in order to evaluate the absolute maximum repetition frequency of the discharge, given the gas flow velocity available. Based on these findings further experiments were made, this time evaluating the stability of the laser output as a function of the gas flow.

4.1.1 Gas-Dynamic Perturbations Generated by a Gas Discharge

Energy deposition, in a suitable pulse discharge for excimer laser operation, occurs in a short time ($t \sim 10^{-7}s$), which corresponds to high power density loadings (from $10^5 \rightarrow 10^7 W.cm^{-3}$). Dissipation of energy in the discharge gap is generally non-uniform due to spatial inhomogeneities in the preionisation, and the presence of distinct zones in a typical glow discharge (e.g. cathode fall and anode fall zones).

A pulsed, gas laser discharge can be thought of as a one-dimensional heated shock tube [4.2]. If one takes the case of the shock wave propagating in the direction opposite to that of the gas flow, then the gas is accelerated in the direction of the shock wave (i.e. decelerated in the direction of the gas flow). As a consequence of the changing motion of the gas, the shock compresses the fluid causing the pressure, p, temperature, T, and mass density, ρ, to rise.[†]

If a finite entropy increase, Δs, across the shock takes place, then for a given pressure ratio p_2/p_1 (where p_2 and p_1 are the high and low pressure regions either side of the shock front respectively), the temperature rise across the shock will be higher than if the compression taken place reversibly, and hence the density increase will be lower than for $\Delta s \sim 0$. In the limit $p_2/p_1 \rightarrow 1$, the shock wave, rather than being non-linear, becomes an acoustic wave and interacts with the propagation medium, which in turn affects successive wave propagation.

If the gas thermalises in times short compared to the acoustic transit time across the discharge, then one may assume that the volume of the discharge does not change during the heating process. Thus, the temperature rise is given by,

$$T_f - T_i = \frac{W_d}{mC_v} \qquad \text{. . . [4.1]}$$

where T_i and T_f are the initial and final temperatures respectively; W_d the nett thermal energy deposited in the discharge; m the mass of the gas (in the discharge); and C_v the specific heat at constant volume. Assuming a perfect gas, the peak pressure of the discharge is

---

[†] A rise in the gas entropy is a measure of the irreversibility of the compression process. Thus, if Δs is small, then standard isentropic relationships can be used to calculate property changes across the shock.

$$P_i = \frac{T_i}{T_f} P_f \qquad \ldots [4.2]$$

where P_i and P_f are the initial and final pressures respectively. Thus, there is a resulting discontinuity in pressure between the discharge and the unheated gas surrounding it. Therefore, as previously described, the outermost disturbance (at some time after the discharge) will consist of shock waves propagating away from the discharge at a velocity

$$v_S = v_a M_S \pm v_F$$

where v_S is the velocity of the shock; v_a the sound speed of the unperturbed gas; M_S the shock Mach number; and v_F the flow velocity of the undisturbed gas.

The time of formation of a shock wave [4.3] is given by the expression

$$\tau_S \sim \frac{\Delta x}{\frac{\Delta P_S}{P_i} \cdot \frac{v_a}{\gamma}} \qquad \ldots [4.4]$$

where Δx is the characteristic size of the initial pressure gradient, determined by the vibrational-translational (V-T) relaxation rate and energy deposition gradient; ΔP_S the initial amplitude of the wave; and γ the ratio of specific heats.

As the wave propagates, energy dissipation occurs in the shock wave, which results in heating of the gas. The increase in the gas temperature, ΔT, after the passage of the wave is determined by the following relationship [4.3]:

$$\frac{\Delta T}{T_1} = \frac{2}{3} \frac{\gamma - 1}{(\gamma + 1)^2} \frac{(M_S^2 - 1)^3}{M_S^2} \qquad \ldots [4.5]$$

The Mach number of the shock wave generated by the discharge, can be determined from the relation for a shock tube with a pressure differential at the diaphragm corresponding to $P_f - P_1$.

Consider the example of a shock tube with initially uniform temperature throughout. When the diaphragm bursts, an expansion wave propagates into the high pressure region resulting in a decrease in temperature of the gas, whilst a shock wave propagates into the low pressure region heating the gas. Thus, a region of thermal discontinuity occurs between the low and high temperature regions; it is known as the *contact surface,* and originates at the intersection of the shock and the expansion waves. In the gas discharge 'driven' case, this corresponds to the boundary between the intially 'discharged' gas and the ambient gas.

The shock wave Mach number depends on the gas properties; the instantaneous pressure and temperature in the discharge region; and the pressure and temperature of the undisturbed gas. It can be shown [4.2] that M_S lies in the range:

$$1 < M_S < \frac{v_S}{v_1} \frac{\gamma + 1}{\gamma - 1} \qquad \ldots [4.6]$$

with v_1 being the local sound speed in the heated discharge gas.

Once the Mach number is known, properties across the shock can be calculated using the 1-dimensional shock relationships (e.g. the acceleration of the undisturbed gas). Since the velocity and pressure are equal on either side of the contact surface, and the pressure and temperature are known from the constant volume heating process, then the temperature between the shock and the contact surface will give access to the thermodynamic properties and gas velocities for the entire flow field.

4.1.2 Expansion of the Heated Gas Slug

Propagation of shock waves up- and down-stream of the discharge result in heating the gas over which it passes: conversely, there also occurs an expansion of the heated gas slug which has the opposite effect of cooling the gas. The discontinuity between the heated and cooled regions of the gas is known as the *contact surface* and moves at the expansion wave velocity. Since the expansion wave propagates at the local sound speed, and the wave becomes thicker as it propagates (i.e. the leading edge of the wave will propagate at the sound speed which is proportional to $\sqrt{T}$), the trailing edge of the wave will propagate at the lower speed because the wave has reduced the temperature to $T_1 - \Delta T$ at that point. An expansion wave is considered to be isentropic such that the fluid is cooled to the minimum possible temperature for a given pressure ratio across the wave. Since the time taken for the deposition of energy in a laser is short compared to the expansion time of the slug, then the parameters associated with this process can be assumed to be adiabatic. Under these conditions [4.3],

$$\frac{W_g}{W_d} = \frac{\left(1 + \frac{W_d}{U}\right)^{\frac{1}{\gamma}} - 1}{\frac{W_d}{U}} \qquad \ldots [4.7]$$

$$\frac{W_S}{W_d} = 1 - \frac{W_g}{W_d} \qquad \ldots [4.8]$$

$$\frac{b}{b_i} = \left(1 + \frac{W_d}{U}\right)^{\frac{1}{\gamma}} \qquad \ldots [4.9]$$

where U is the initial internal energy of the gas; W_d the energy deposited in the discharge; W_g the energy remaining in the gas plug in the form of heat; W_S the energy transferred by the waves and dissipated outside the discharge region; and b is the size of the region occupied by the hot gas after adiabatic expansion.

The strongest gas density perturbation, occuring in the afterglow period following the discharge, is the heated gas slug which gradually expands and is carried by the flow out of the dicharge region. During the first, rapid, stage the slug size grows linearly with time. The duration of this stage corresponds to the time it takes for the gas pressure to level out, and hence is determined by the adiabatic expansion of the heated gas. The second, slower stage, is governed by the heat conduction. The gas pressure variations near the discharge region and the propagation of almost isentropic waves is shown schematically in Fig. 4.1. For simplicity, it is assumed that the discharge across the flow is rectangular in cross-section.

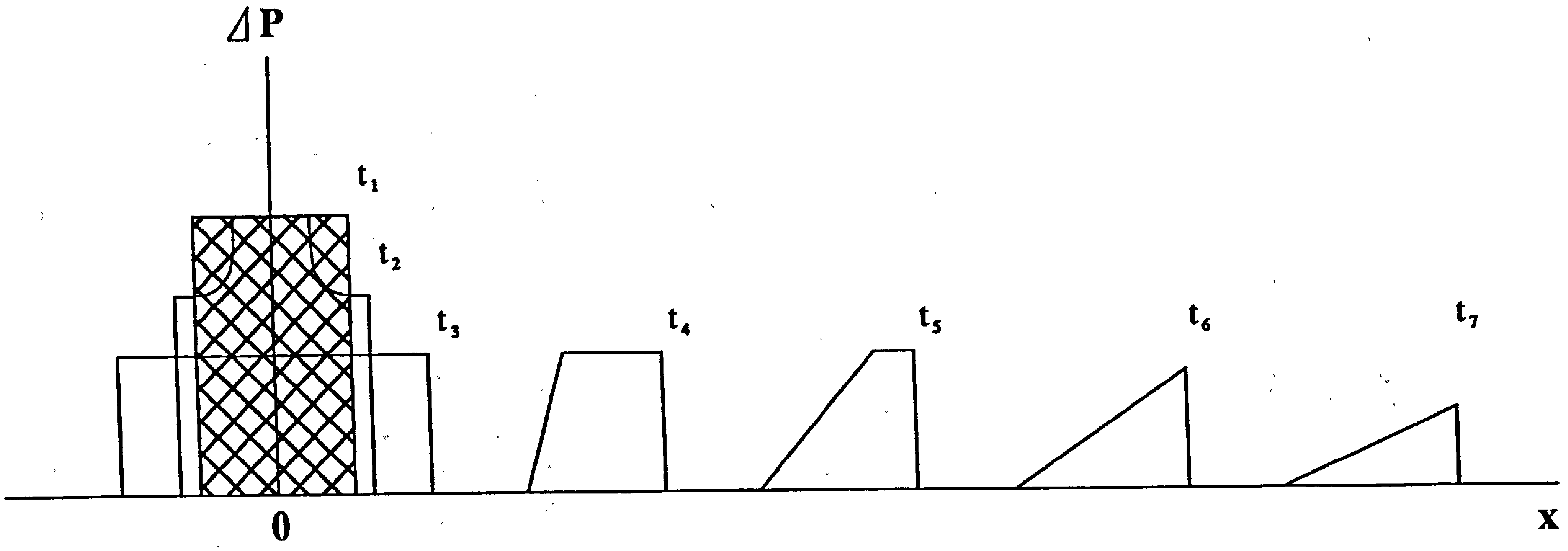

Fig. 4.1 Schematic diagram of the temporal behaviour of the gas pressure in the discharge region and the the shock wave shape

4.1.3 Experimental Arrangement[†]

Several investigators [4.4→4.6] have used interferometric techniques, such as those based on the Mach-Zehnder device, to gain information about density non-uniformities generated by pulsed discharges. Unfortunately, the system under study was very susceptible to environmental vibrations, and hence the optics for such an arrangement would have needed to be supported on a high quality vibration isolation table which was not available during the development period.

It was noticed that the return beam from a HeNe alignment laser, which was some two metres from the output coupler of the high prf laser, suffered a "kick" in its position when the laser discharge pulsed. The kick was caused by density gradients generated by the propagation of a shock wave through the gas. The possibility of exploiting this as a means of measuring wave perturbation effects in the high prf laser was thus taken up as an alternative to Schlieren photography which was under consideration at that time.

The initial experimental arrangement used to investigate this possibility is shown diagramatically in Fig. 4.2. This arrangement consisted of a HeNe laser, mounted on a micrometer adjustable X-Y and tilt translation stage, such that any portion of the discharge could be investigated with repeatable accuracy. The beam was passed through the discharge of the laser, via a beam splitter, and reflected off the back mirror of the resonator to the beam splitter. The beam was then deflected towards a 31cm focal length lens and HeNe (632.8nm) band pass filter, and focussed on to a variable aperture. On

---

[†] These measurements were made using the first electrode gantry and ducting configuration.

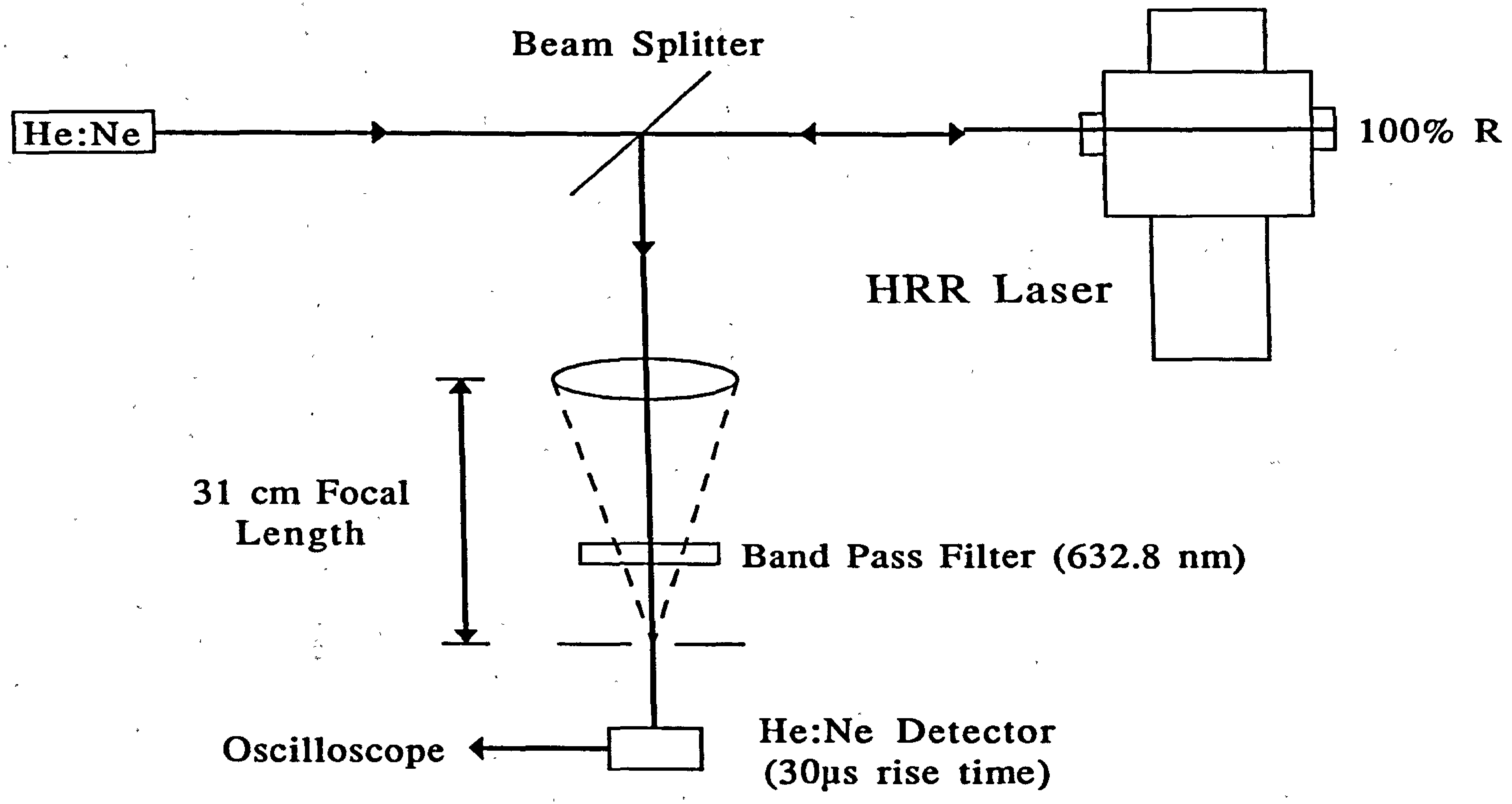

Fig. 4.2 Initial experimental set-up for the beam perturbation studies

exiting the aperture, the beam was arranged to illuminate a ~30μs rise time photodiode with integrated amplifier†. However this arrangement was found to be very susceptible to the effects of pressure waves hitting the back mirror of the resonator. This resulted in the movement of the He:Ne, and consequent modulation of the detected HeNe beam signal.

The experimental arrangement was consequently reconfigured as shown in Fig. 4.3. Here the back mirror of the resonator was replaced with a fused silica substrate, such that the HeNe beam made a single pass through the discharge region. The beam was then steered, at right angles, to the same detector arrangement as used before. This neutralised the effects of the discharge on the beam steering optics. However, the whole system was then found to be extremely sensitive to air movments around the detector and also to the natural resonances of the surrounding media including the laser.

To overcome this problem a sub-nanosecond risetime vacuum photodiode, with an S_{10} cathode, was used in place of the solid state photodiode. This enabled measurements on a sub-nanosecond timescale to be carried out. The final configuration is very similar to that used by Quinn & O'Hare [4.6] in their investigations of a mono-pulse TEA CO_2 laser discharge.

The oscillograph in Fig. 4.4, shows a typical trace of the perturbations generated in the discharge. As indicated, there is a signal corresponding to

---

† A HeNe bandpass filter was used to prevent uv light from the laser reaching the detector and causing an undesired response prior to the medium induced deflection of the probe beam. [It should also be noted that this laser like other quasi-super radiant sources would lase out of both ends of a resonator just consisting of uncoated windows.]

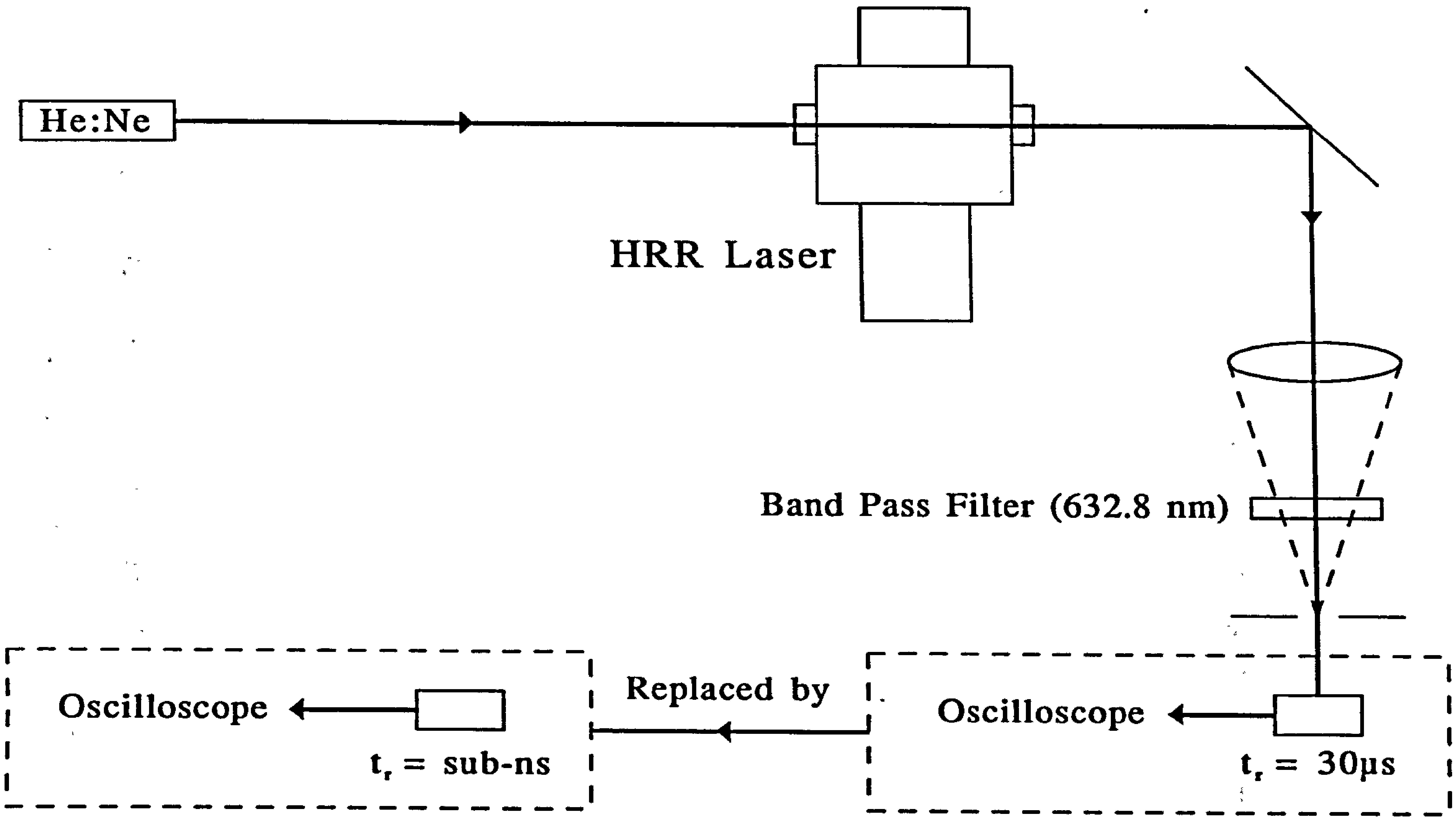

Fig. 4.3 Final experimental set-up for the beam perturbation studies

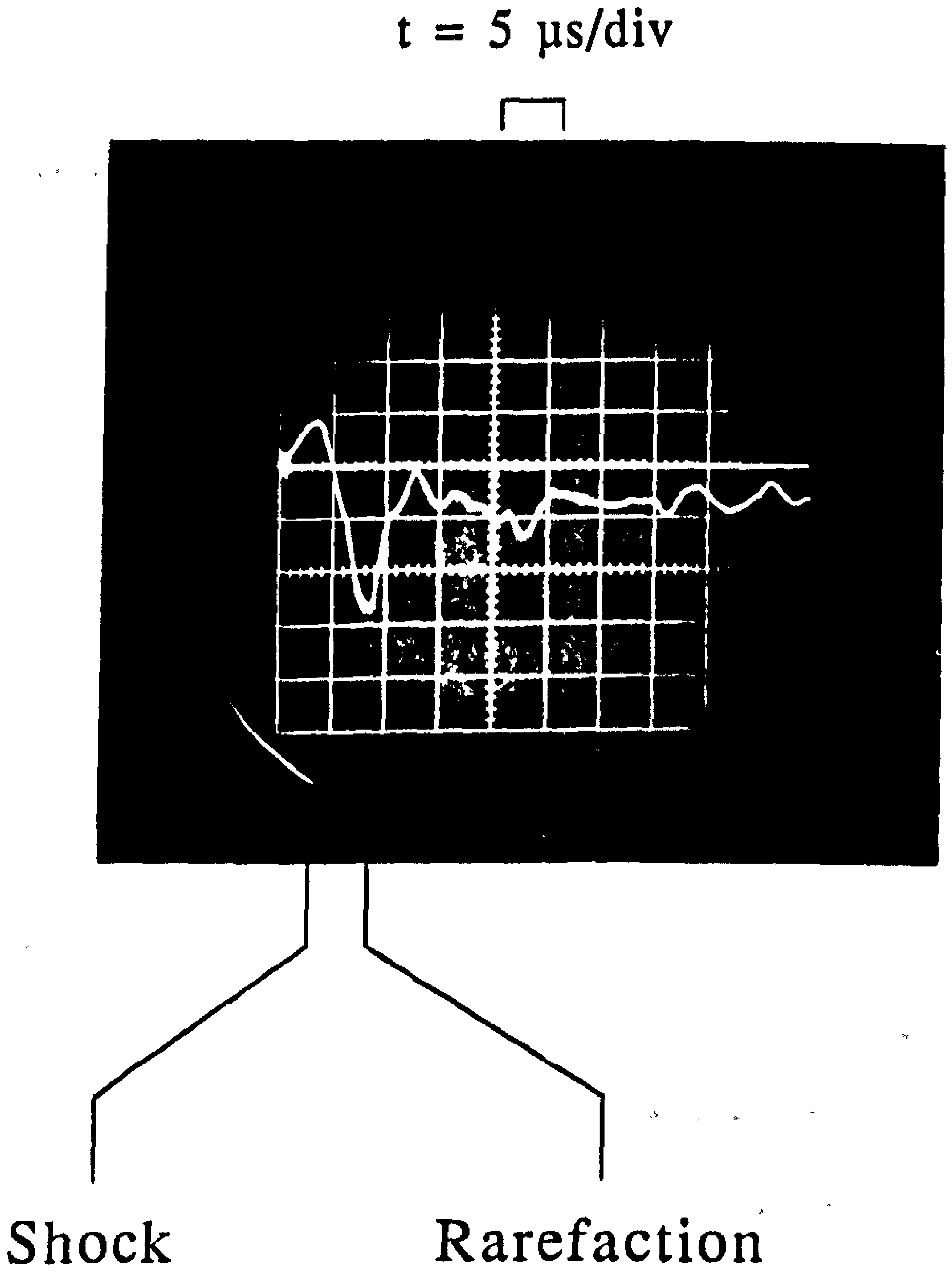

Fig. 4.4 Perturbation of the probe beam caused by the propagation of the shock wave, and followed by a rarefaction

the arrival of the initial shock wave followed by a rarefaction. By measuring the delay in the arrival of the shock pulse, at two different positions upstream of the discharge, it was possible to evaluate the shock propagation velocity.

4.1.4 Measurements of Density Perturbations in the Discharge

Initial experiments were carried out to determine the distance between contact surfaces at t=0 (Fig. 4.5). The detector was set such that in the absence of a discharge, the position of the HeNe beam was just outside the area of the detector element in the horizontal plane. Therefore, with a deflection produced by the discharge, the beam was flicked on to the detector. The HeNe beam was then scanned from the "centre" of the discharge to a point where the first signs of the shock wave produced by density gradients deflecting the beam. By moving slightly back from this position, such that the shock disappeared, located the inital position of the contact surface on one side of the discharge. A typical oscillograph showing the arrival of the initial shock pulse and the subsequent impulses are shown in Fig. 4.6, and can be correlated to the reflections shown in Fig. 4.5. This was then repeated on the other side of the discharge, with the detector repositioned for a deflection in the opposite direction, and by subtracting the two measurements the width of the region between them was determined. The results obtained for both a helium discharge and a standard XeCl laser gas mix are presented in (Table-4.1); measurements of the shock velocity are also shown, calculated from the position of the HeNe probe beam relative to the discharge and the time of arrival of the first perturbation.

Having located the boundary position of the discharge, measurements were made near its centre. Fig. 4.7a) shows the "slow" rise due to non-uniform

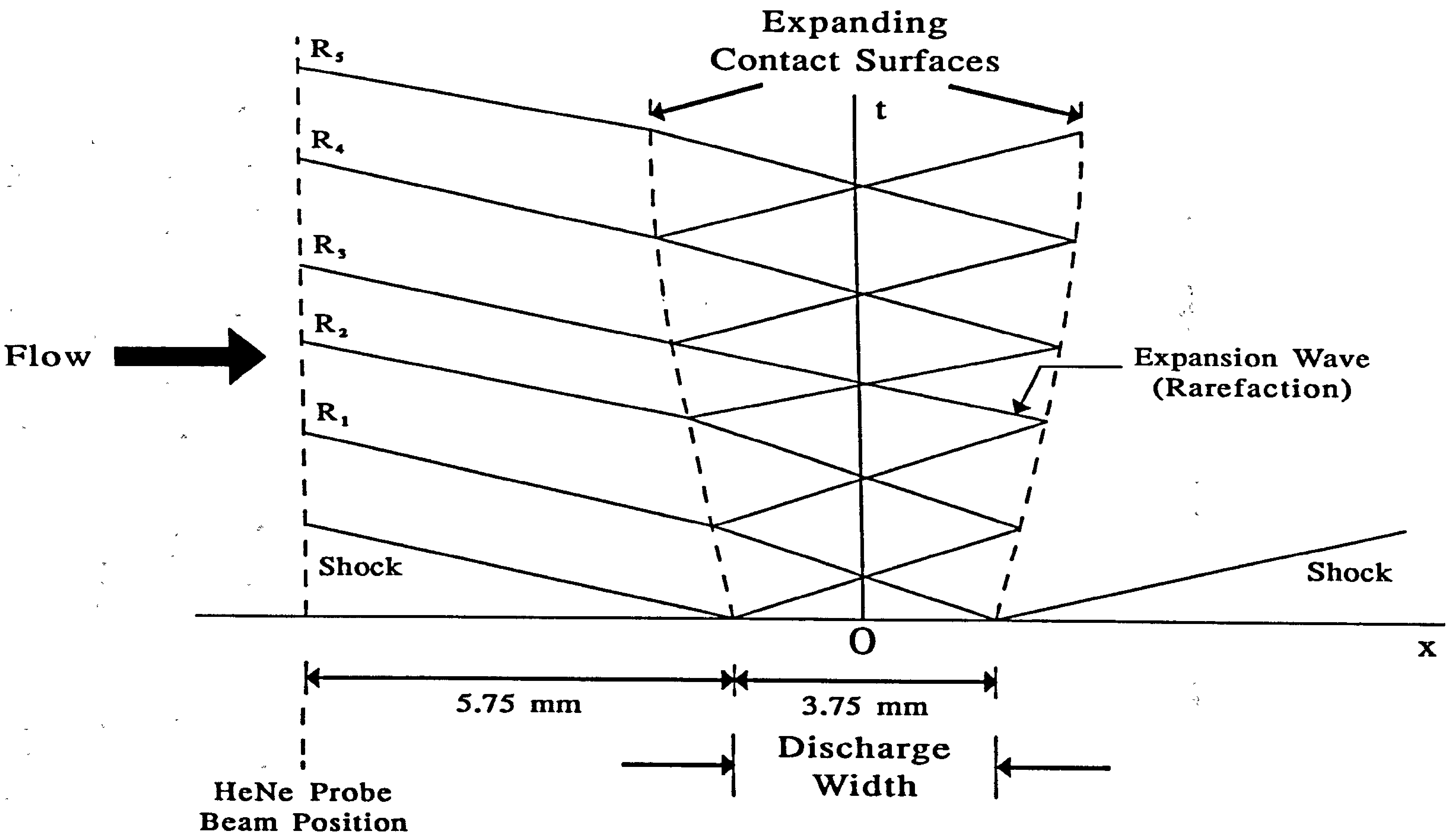

Fig. 4.5 Shock and expansion waves in a pulsed, gas laser discharge

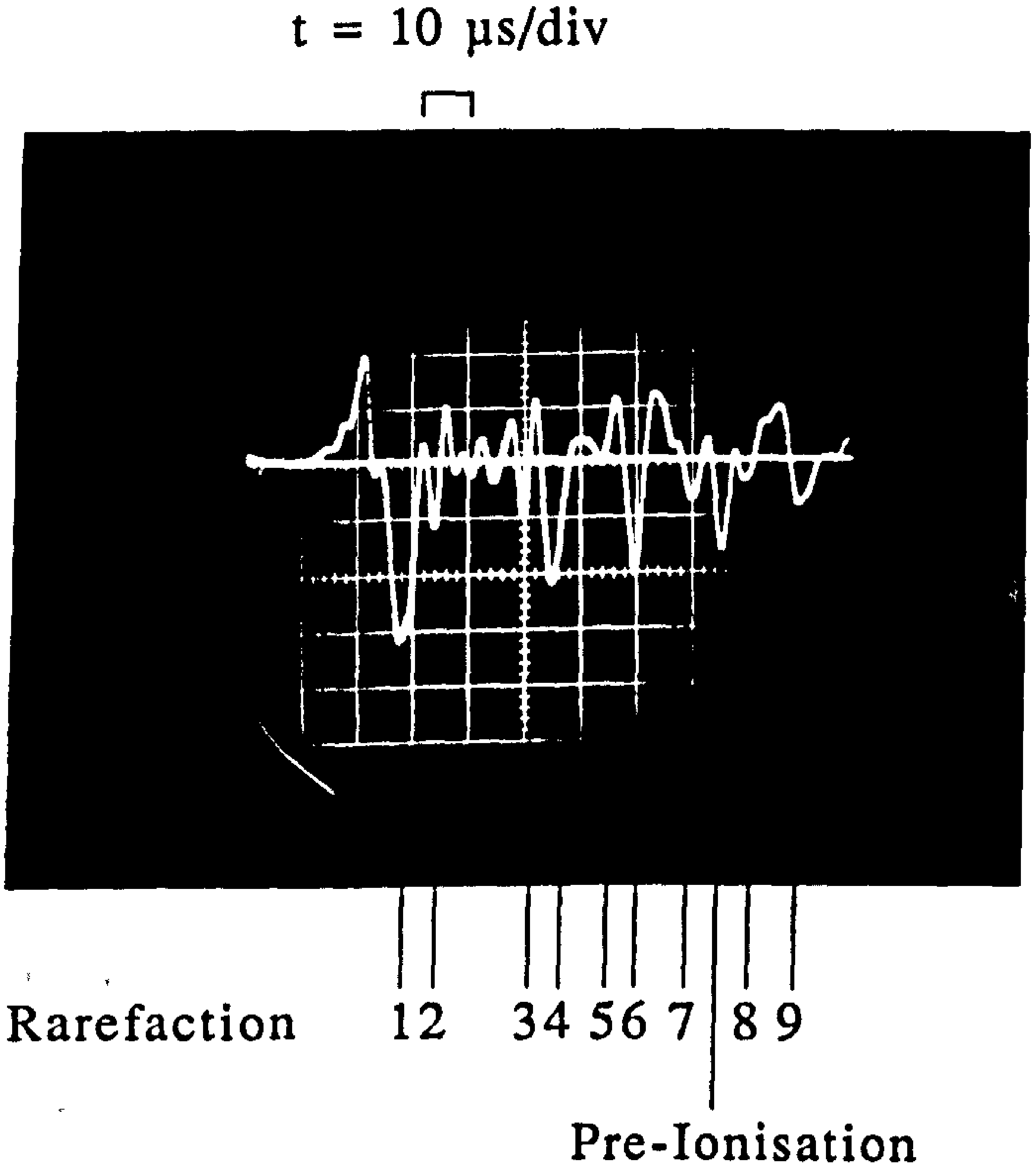

Fig. 4.6 Typical oscillograph of the perturbation of the probe beam due to propagation of the shock wave and rarefactions from the discharge

Gas Pressure (mbar)	Contact Surface Width (mm)	Shock Velocity (m.s^{-1})
He (1000)	8.4 ± 0.1	952 ± 18
He (2000)	—	1042 ± 35
He (3000)	8.9 ± 0.1	1190 ± 46
HCL (3) + Xe (10) + Ne (2987)	4.9 ± 0.1	472 ± 11

Table 4.1 Shock wave velocity measurements for various gases and gas mixtures.

t = 5 μs/div

a) 13 mm downstream from the cathode at the centre of the discharge

with flow

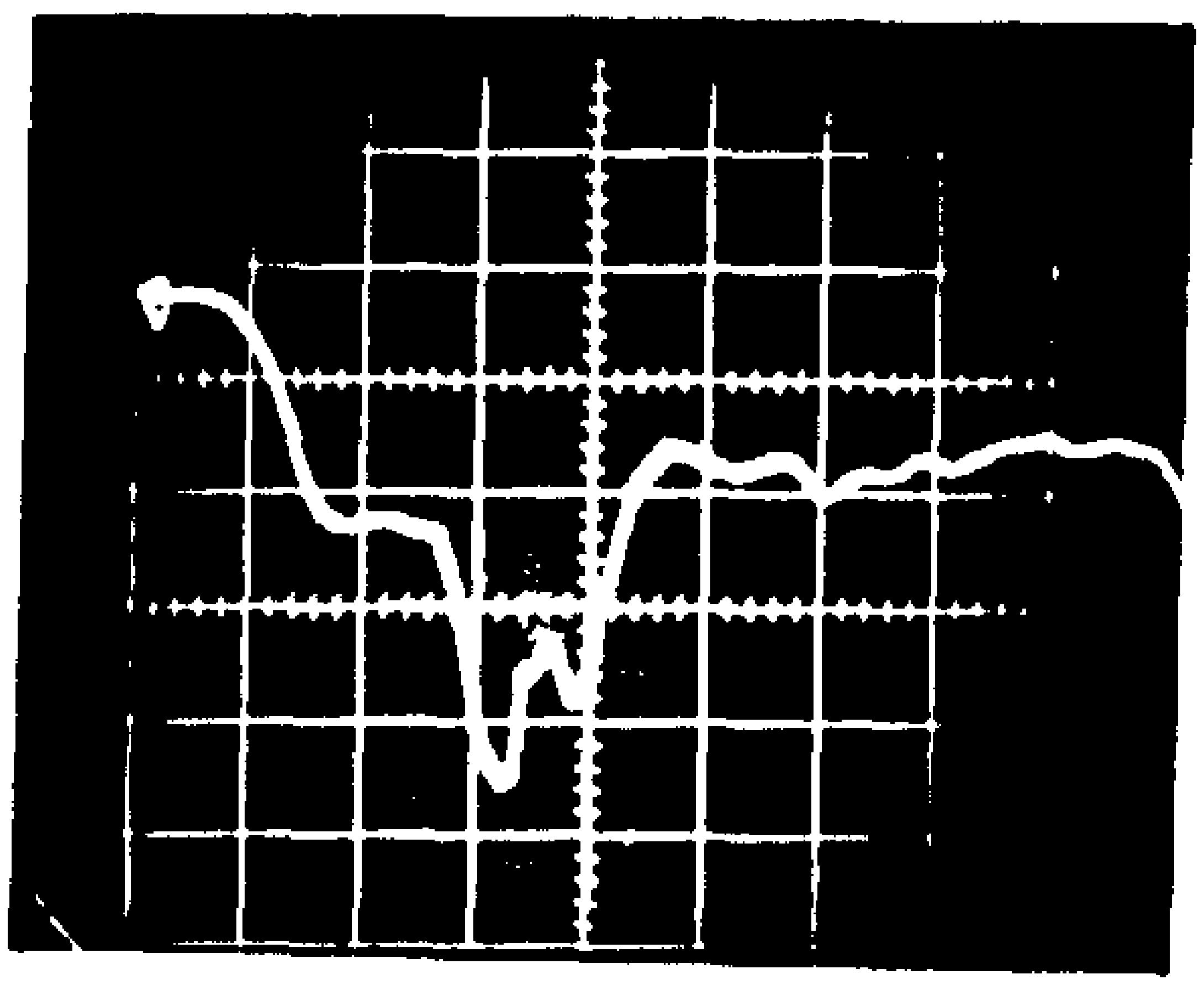

t = 50 ms/div

b) 13 mm downstream from the cathode at the centre of the discharge

no flow

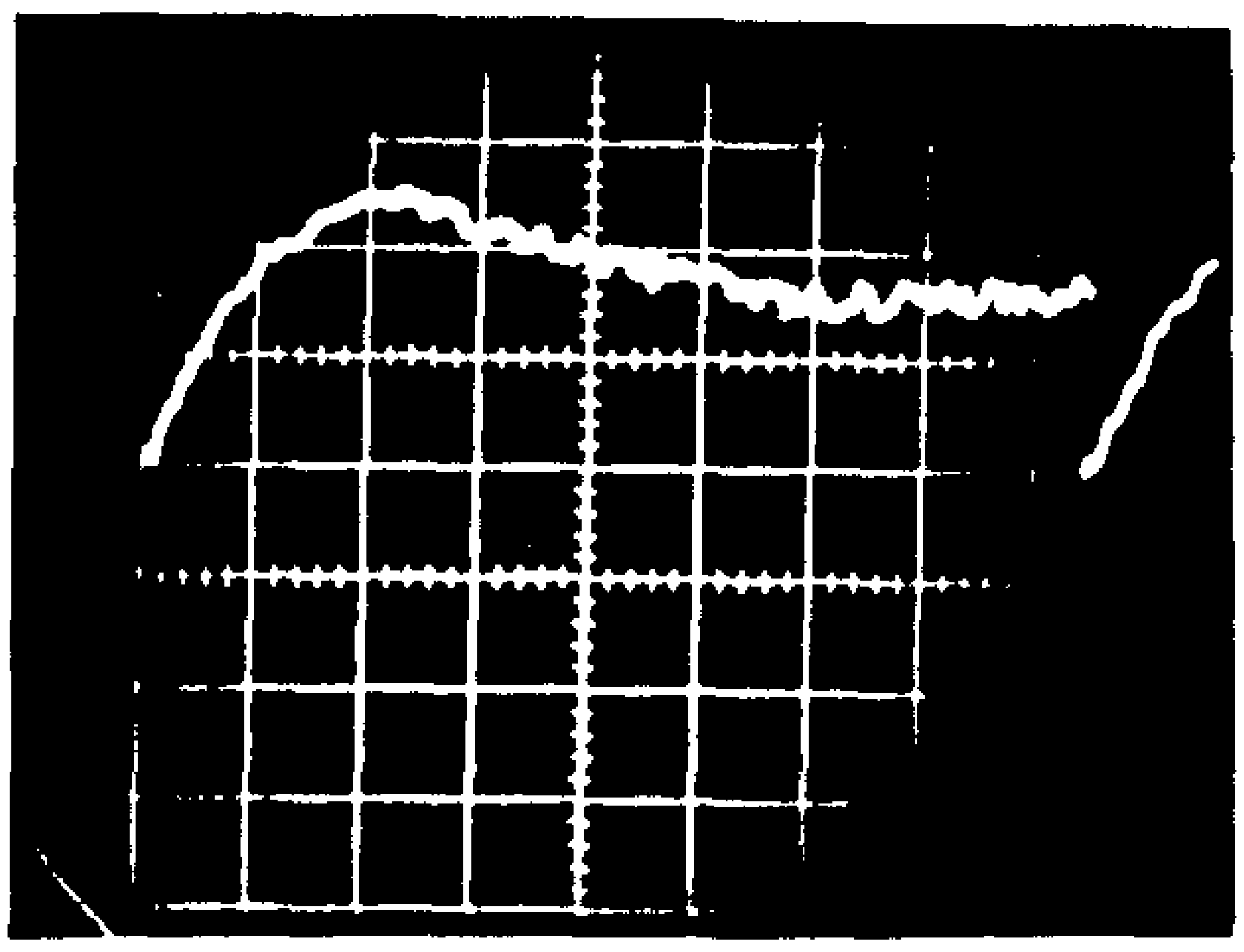

t = 0.5 ms/div

c) 13 mm downstream from the cathode at the centre of the discharge

with flow

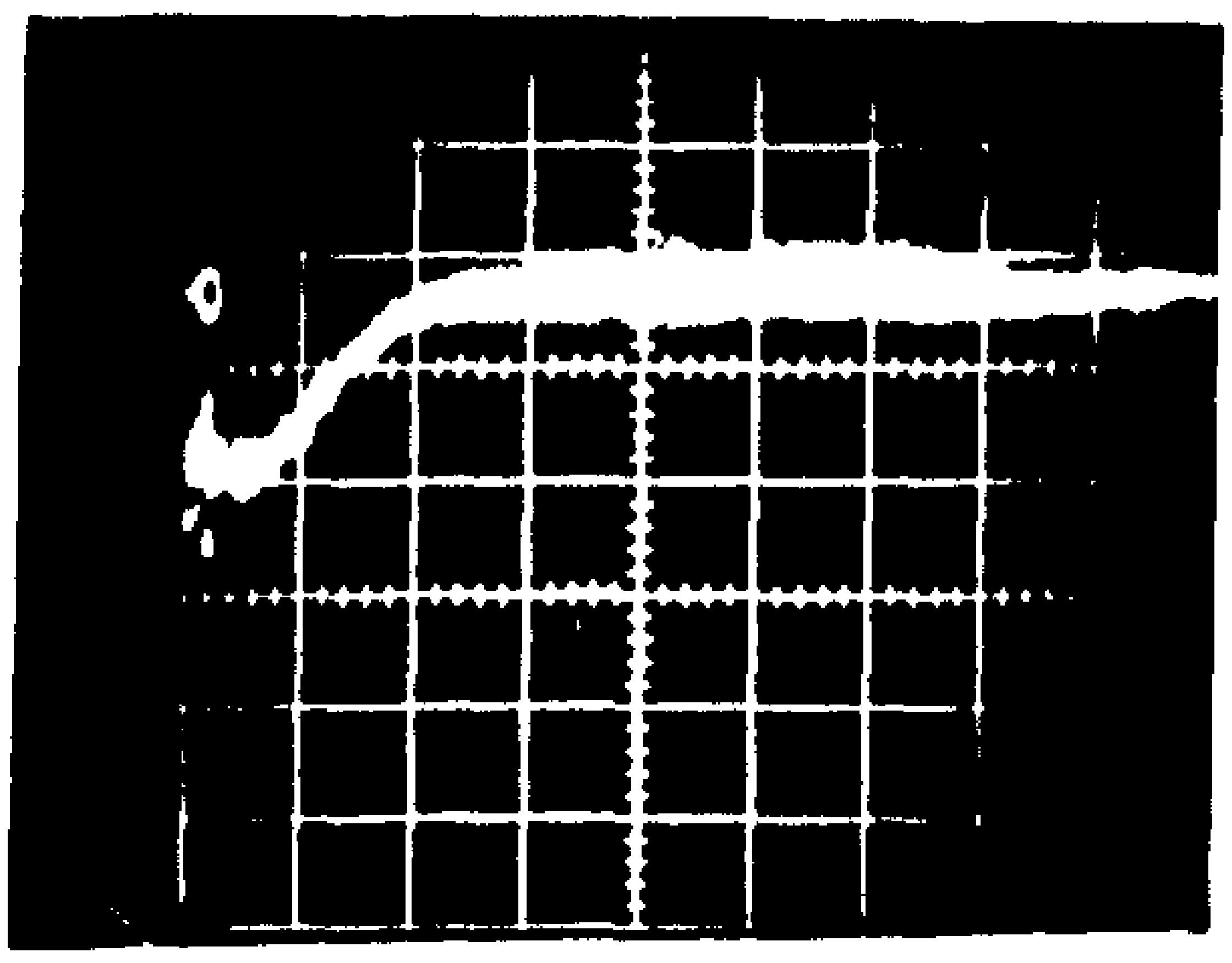

Fig. 4.7 Oscillographs showing the perturbations at the centre of the discharge, close to the anode, due to the heated gas slug

heating of the gas slug. This is followed by the reflection of the cathode shock by the anode, with a delay corresponding to the time taken for the cathode shock to reach the He:Ne beam some 6mm down from the cathode. With no flow in the laser, results obtained on a much longer timescale showed the time taken for the heated gas to clear the centre of the discharge, Fig. 4.7b), to be about 0.3s. This would limit the pulse repetition frequency to ~3Hz. If flow is now added to the system this time is reduced substantially to ~1.9ms (Fig. 4.7c)).

At a distance of 2mm downstream of the centre of the discharge, Fig. 4.8a) shows the non-uniform heating of the gas slug. The rise in the trace after the initial decay can be attributed to the peak of the disturbance being swept across the field of view, of the probe beam, by the fan. Fig. 4.8b) shows an equivalent trace but with no flow, from which it can be seen that the effect of the heated gas slug is much more long-lived.

Taking these last measurements a step further, the fan voltage was varied and the time for the heated gas slug to pass the position of the HeNe beam noted. Initially, the He:Ne laser beam was positioned at the exact centre of the discharge (i.e. the position where deflection of the beam was uniform in each direction), and fractionally above the surface of the anode. With the probe beam in this position, it can be seen from Fig. 4.9a) that, before the fan decoupled, the maximum possible prf is estimated to be ~2.5kHz. However, with the probe beam moved to just beyond the start of the contact surface (downstream of the discharge), this figure falls to ~1.8kHz.

The latter set of results compare very favourably with measurements made of the prf limit, for lasing to occur for a given gas flow velocity (Fig. 4.9b)). Therefore, given the present flow limitations and assuming that the laser t = 0.5 ms/div

a) 2 mm downstream from the cathode at the centre of the discharge

<u>with</u> flow

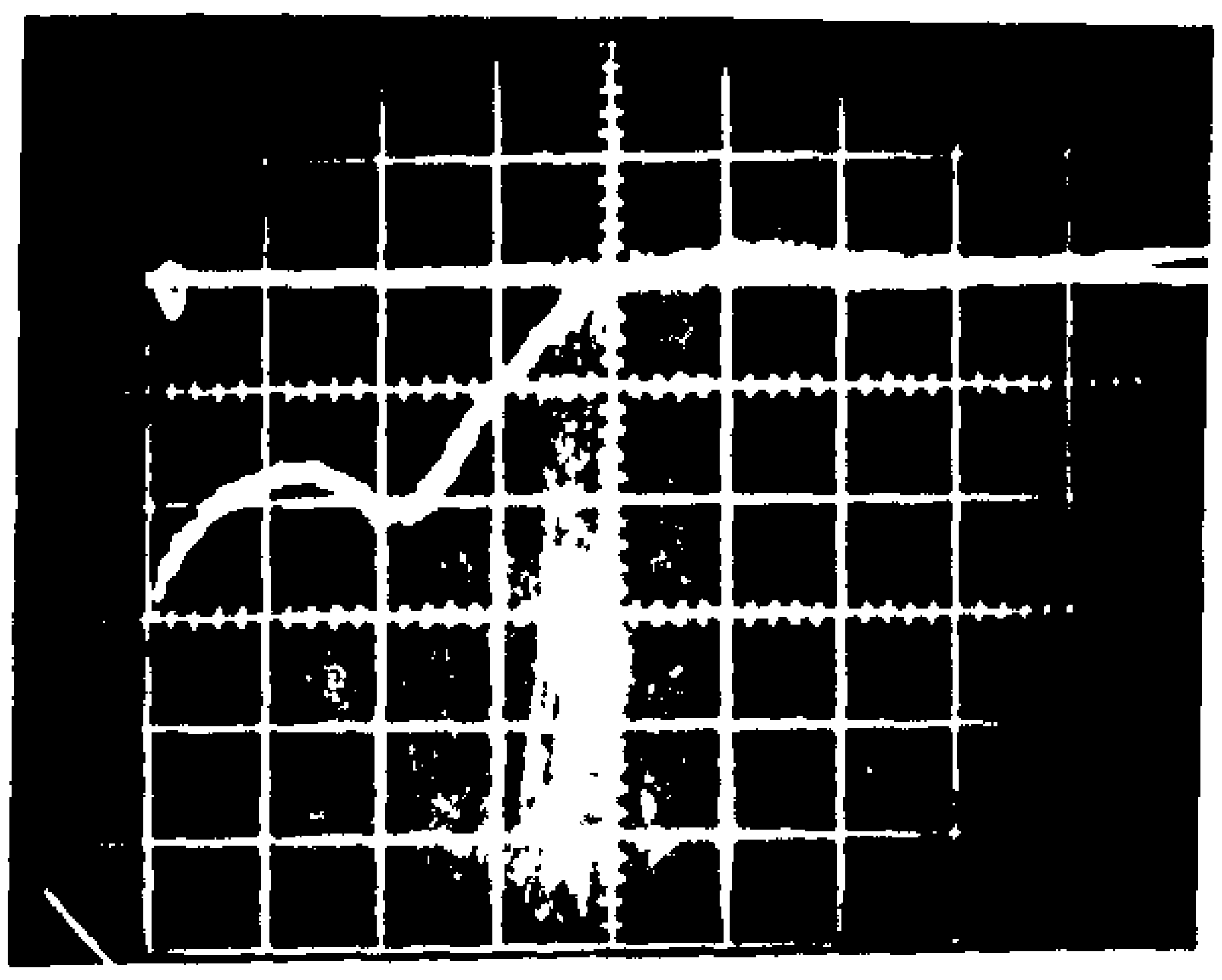

t = 0.5 ms/div

b) 2 mm downstream from the cathode at the centre of the discharge

<u>no</u> flow

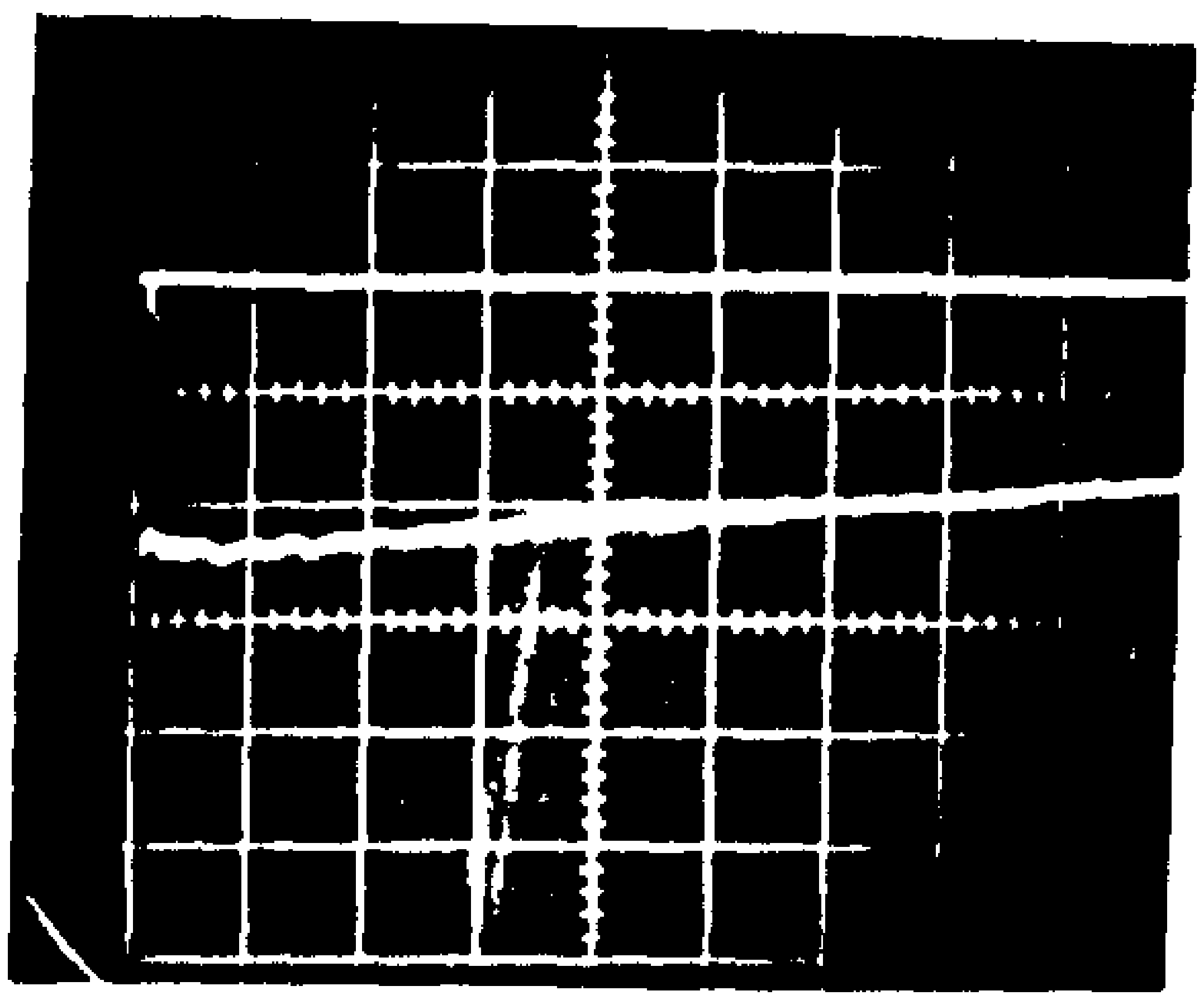

Fig. 4.8 Oscillographs showing the perturbations 2mm from the centre of the discharge, close to the anode, due to the heated gas slug

Fig. 4.9 Measurements made of the absolute maximum prf as a function of the fan motor voltage at: a) the centre of the discharge; and b) the downstream contact surface

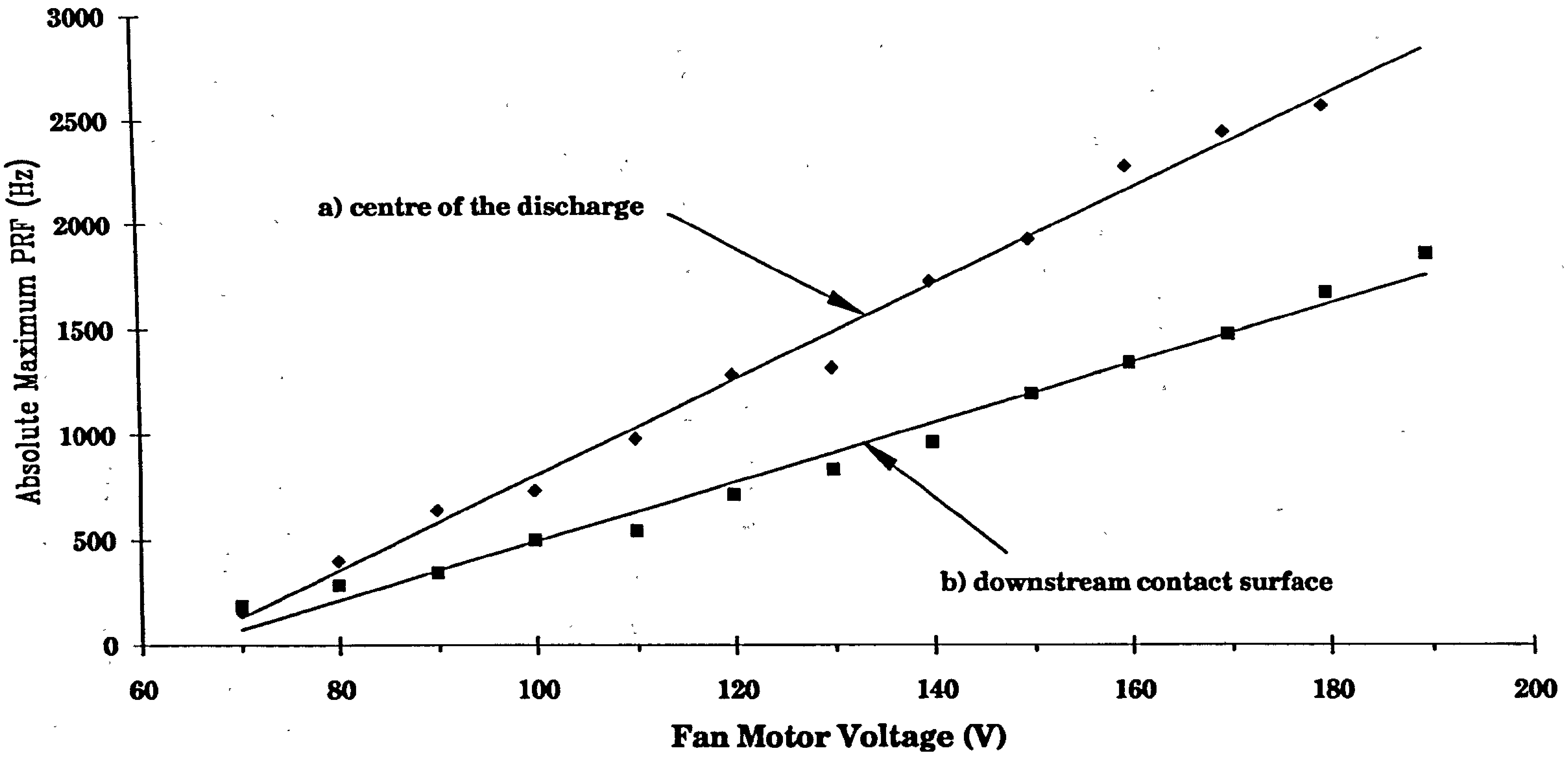

output is not power supply limited, then a maximum prf of ~1.8kHz should be attainable. Under optimum conditions of gas composition, voltage etc. the maximum prf attained was 1.6kHz, resulting in an output power in excess of 4W. A comparison of the predicted maximum repetition rate versus that measured is given in Fig. 4.10. It can be seen for the expected repetition rate limits given by the contact surface, downstream of the discharge, that these is most closely analogous to those made for the high repetition rate power measurements. An investigation of the maximum repetition rate attainable was made whilst still keeping the laser above threshold (Fig. 4.11). This set of measurements corresponded almost exactly to the predictions made by those at the contact surface. Plotting the clearing ratio

$$\mathrm{C.R.} = \left(\frac{{}^{1}/\text{delay time}}{\text{prf}_{\max}}\right)$$

versus fan motor voltage (Fig. 4.12) shows that the clearing ratio starts high, ~3 (as many authors working at low repetition rate have predicted), but decreases to almost unity as the move to high repetition rates is made. Unfortunately, the corresponding measurements were not made under full laser operation, which needed a somewhat higher clearing ratio. Based on the measurements made for this device, a clearing ratio of ~2 would be sufficient to stop any degradation of the beam caused by the lack of flow in the discharge region.

Using the beam probing technique, it was also possible to measure the electrode separation by monitoring the transverse shock wave generated by the discharge striking. The HeNe probe beam was placed at the approximate centre of the discharge. The detector was set such that in the absence of a discharge the HeNe beam was just outside the area of the detector element in the vertical direction. The oscillograph in Fig. 4.13 shows the arrival of the

Fig. 4.10 Comparison of the maximum achievable prf, at optimum output power, as a function of fan motor voltage, and the prf expected from the disturbances measured at: (i) the centre of the discharge; and at (ii) the downstream contact surface

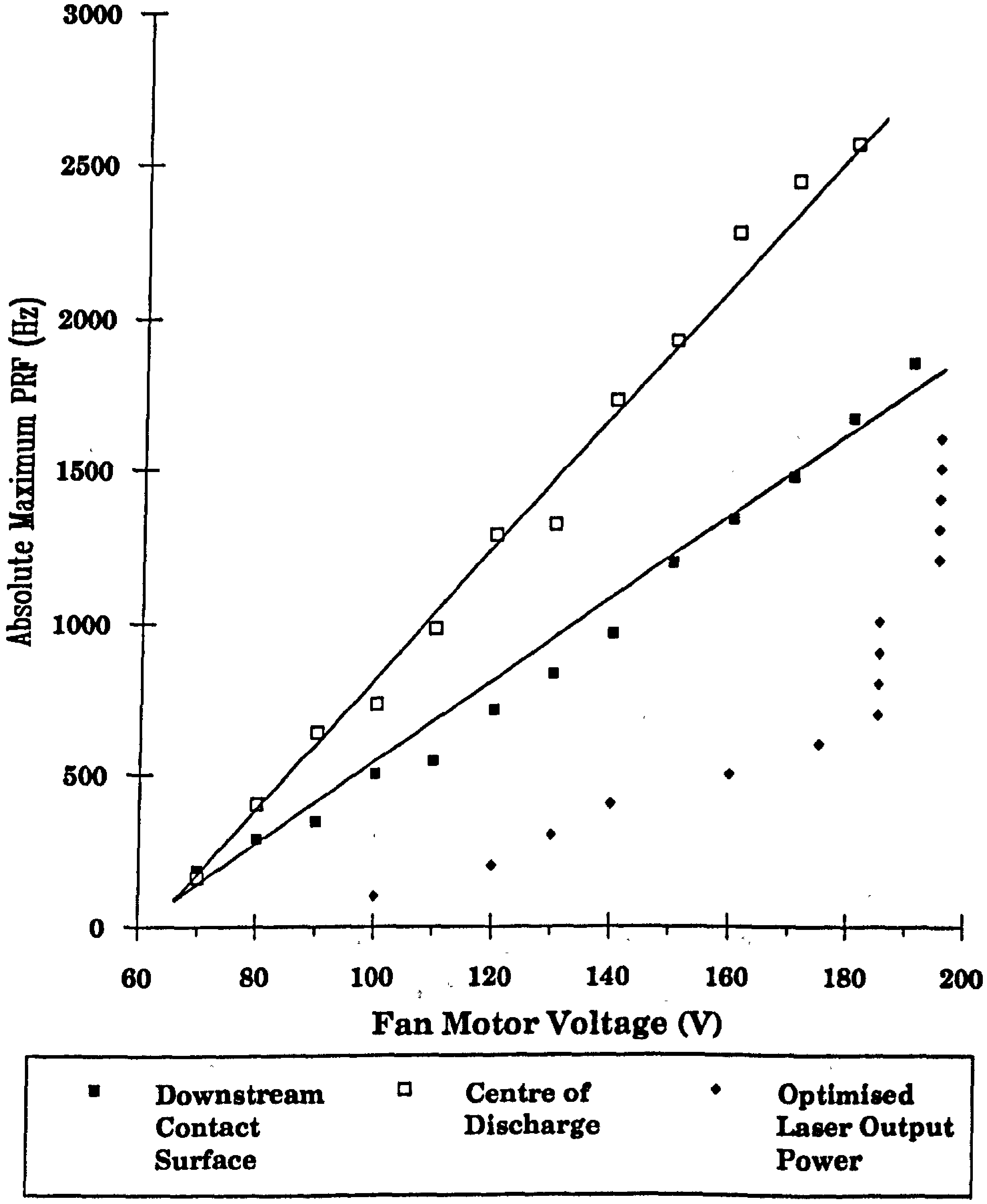

Fig. 4.11 Comparison of the maximum achievable prf, at laser threshold, as a function of fan motor voltage, and the prf expected from the disturbances measured at: (i) the centre of the discharge; and at (ii) the downstream contact surface

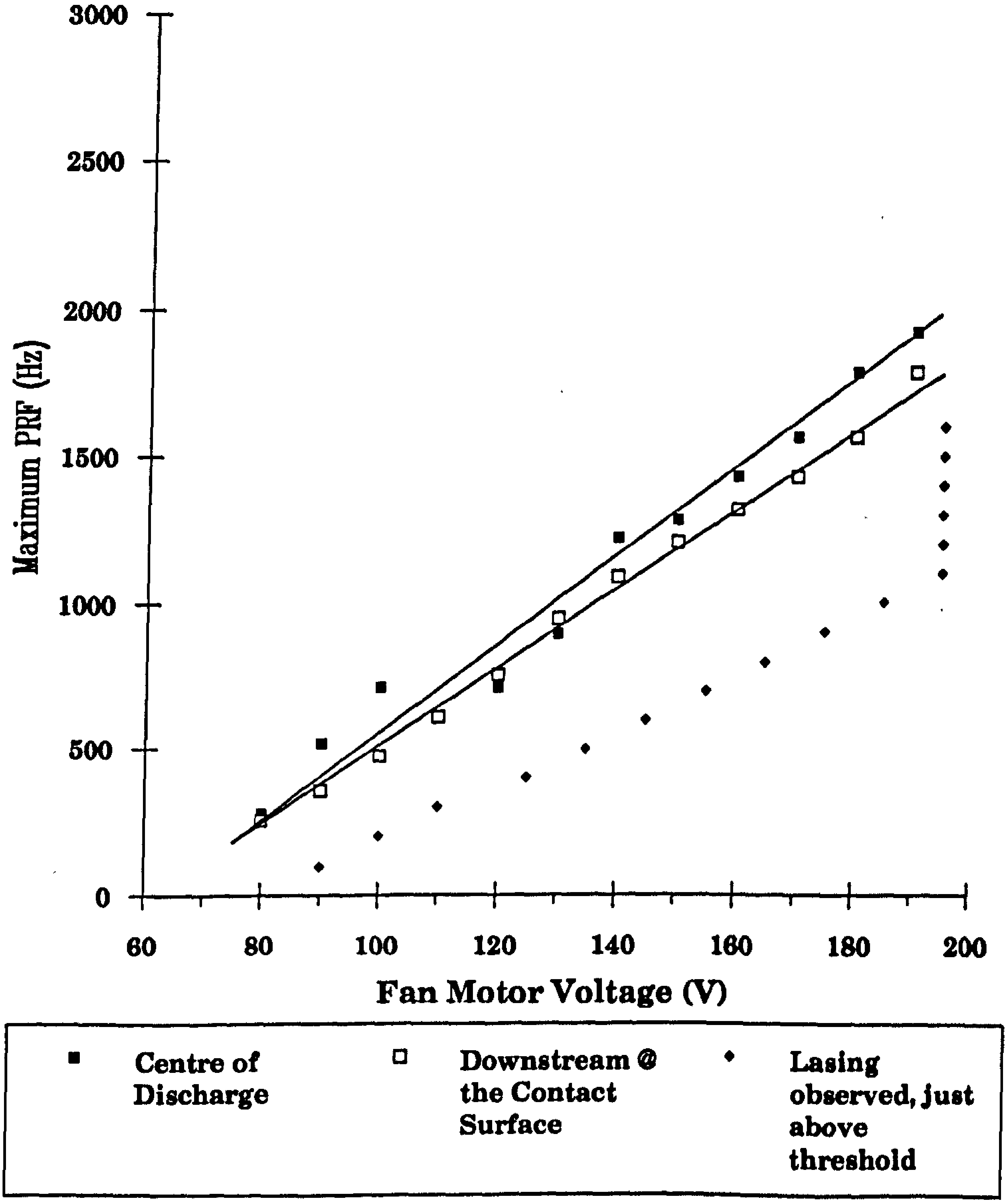

Fig. 4.12 Minimum clearing ratio, with lasing occuring, as a function of fan motor voltage

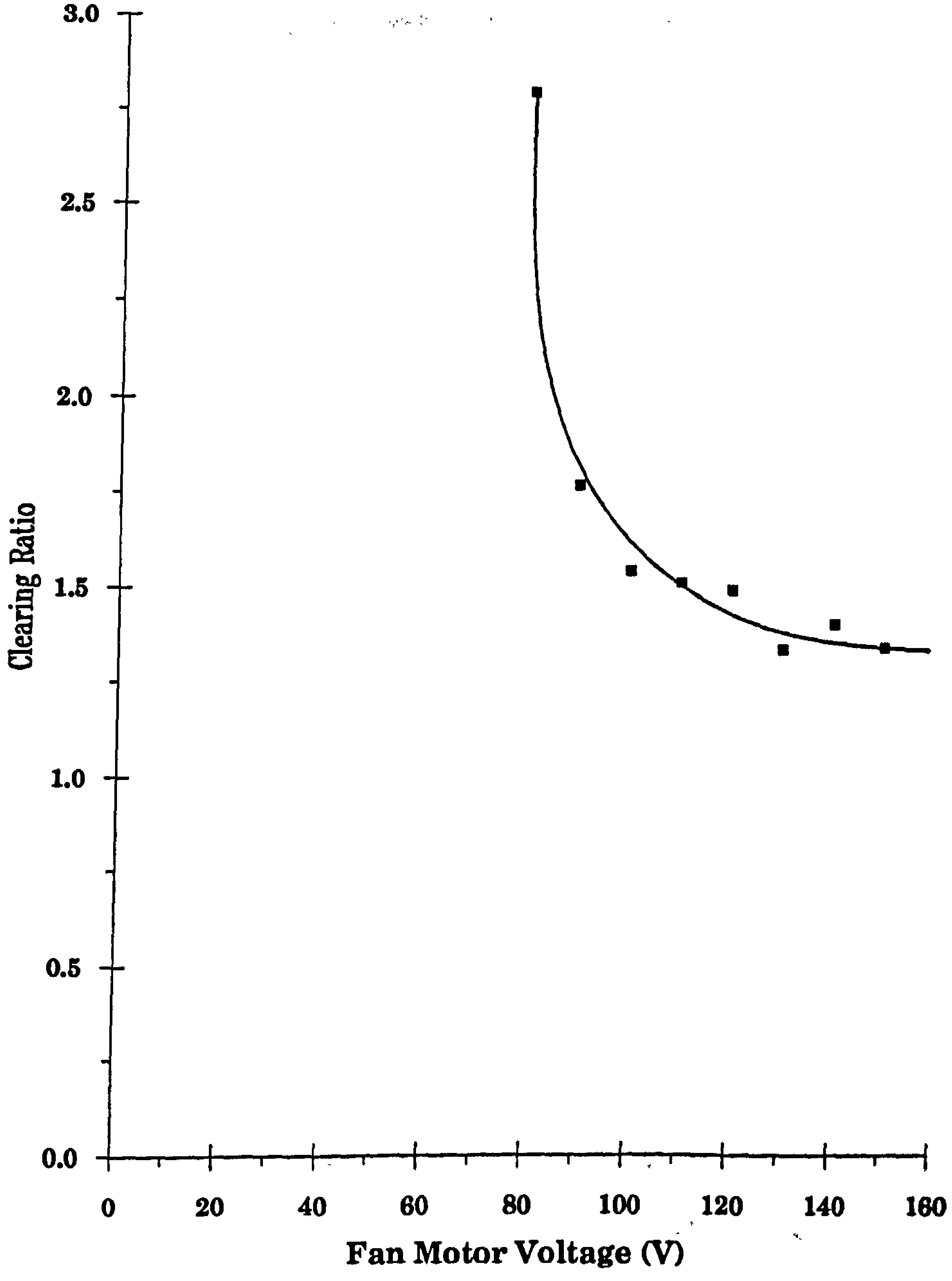

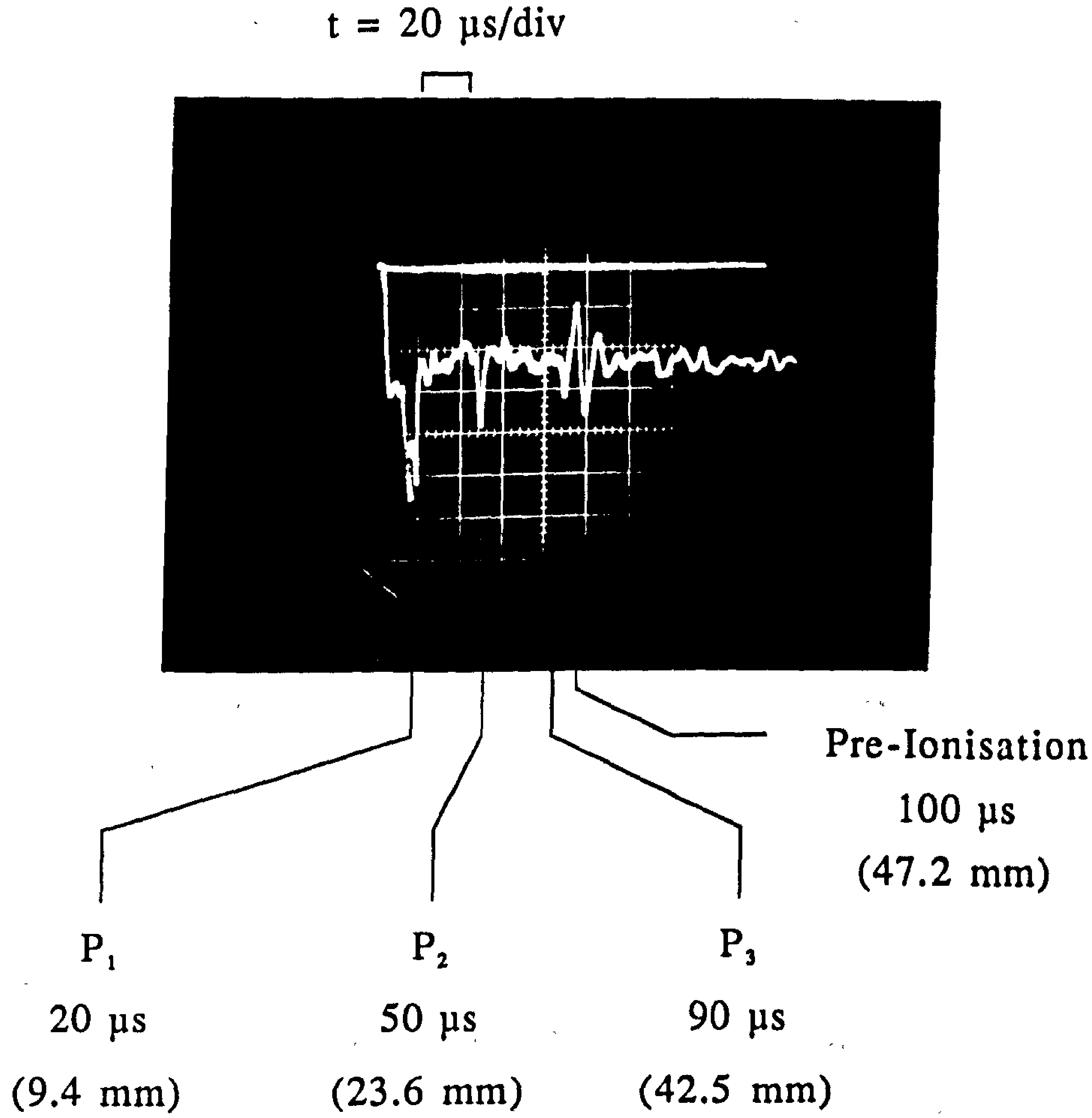

Fig. 4.13 Oscillograph of the probe beam deflection caused by the shock wave between the electrodes

the shock wave from the cathode, then its return after being reflected of the anode, and finally the reflection back off the cathode (Fig. 4.14). From this information, it can be deduced that since one round trip of the electrode separation (i.e. 30.5 mm) took 70 μs, and that the speed of sound in the gas mixture had already been determined to be $472 \pm 11 \text{m.s}^{-1}$ (Table 4.1) then the electrode separation was 16.7mm.

4.2 EFFECT OF WATER COOLING AND GAS ADDITIVES ON LASER GAS LIFETIME

The effect of using an electrostatic precipitator in the gas stream has already been discussed in Chapter 3, but it was also noticed at that time that laser output power stability was also dependent on the temperature and the addition of small amounts of hydrogen [4.7]. In this section, measurements made of the laser power as a function of gas temperature and the effect of the addition of small quantites of hydrogen will be discussed.

4.2.1 Experimental Arrangement

In order to monitor the effects of water cooling on the gas temperature in the laser chamber, it was necessary to place a temperature probe in the gas stream (Fig. 4.15). By adding a "tee" to the 1" vacuum port attached to the laser chamber, it was possible to contruct a leak-tight feedthrough which fed the two signal lines from the temperature probe via banana plug connectors out of the laser. The temperature probe was of the meat thermometer type, bent at 90° to enable it to be put through a hole in the venturi flume upstream of the laser discharge.

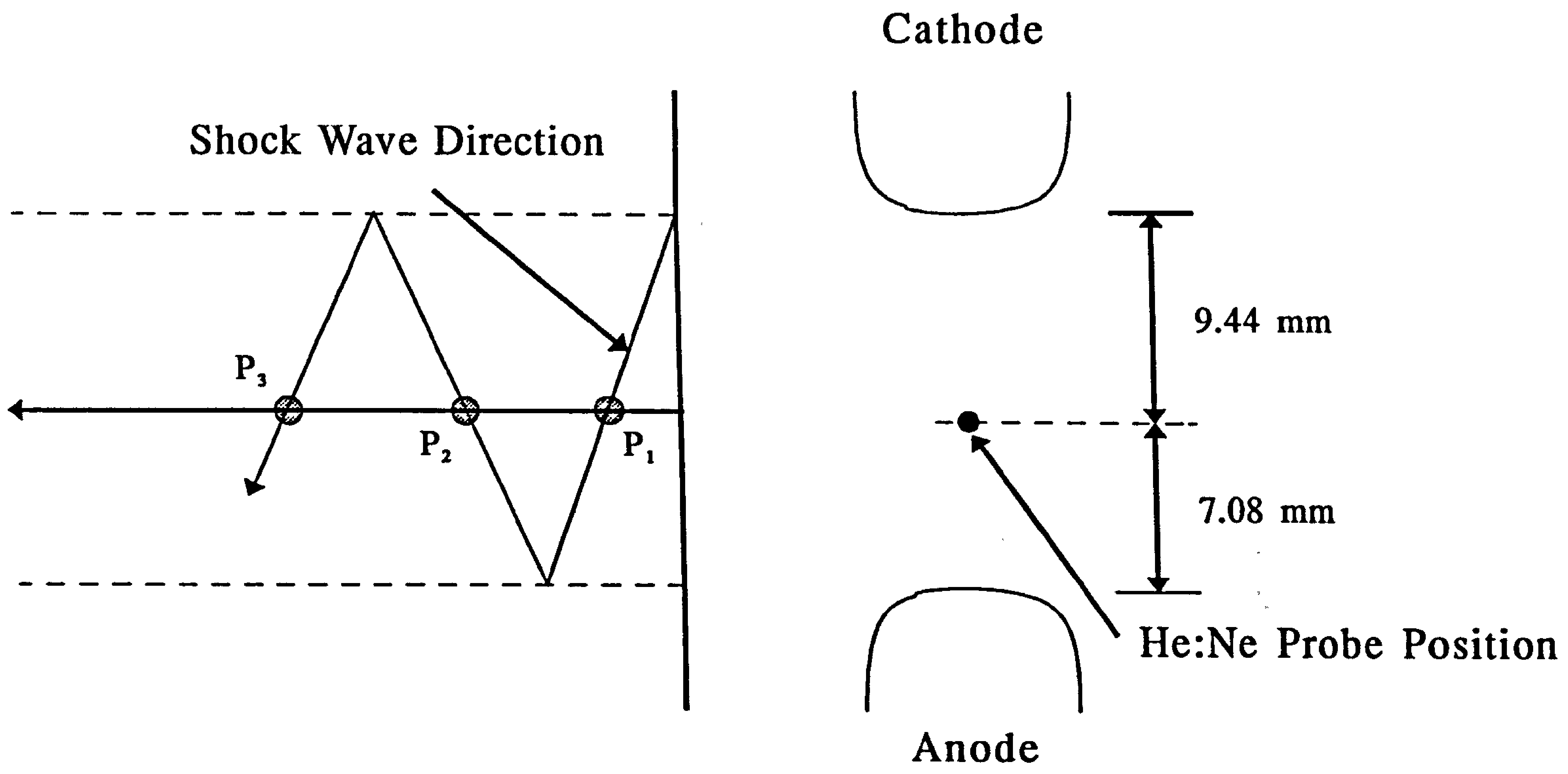

Fig. 4.14 Measurement of the inter-electrode separation using the shock wave occurring between the cathode and the anode

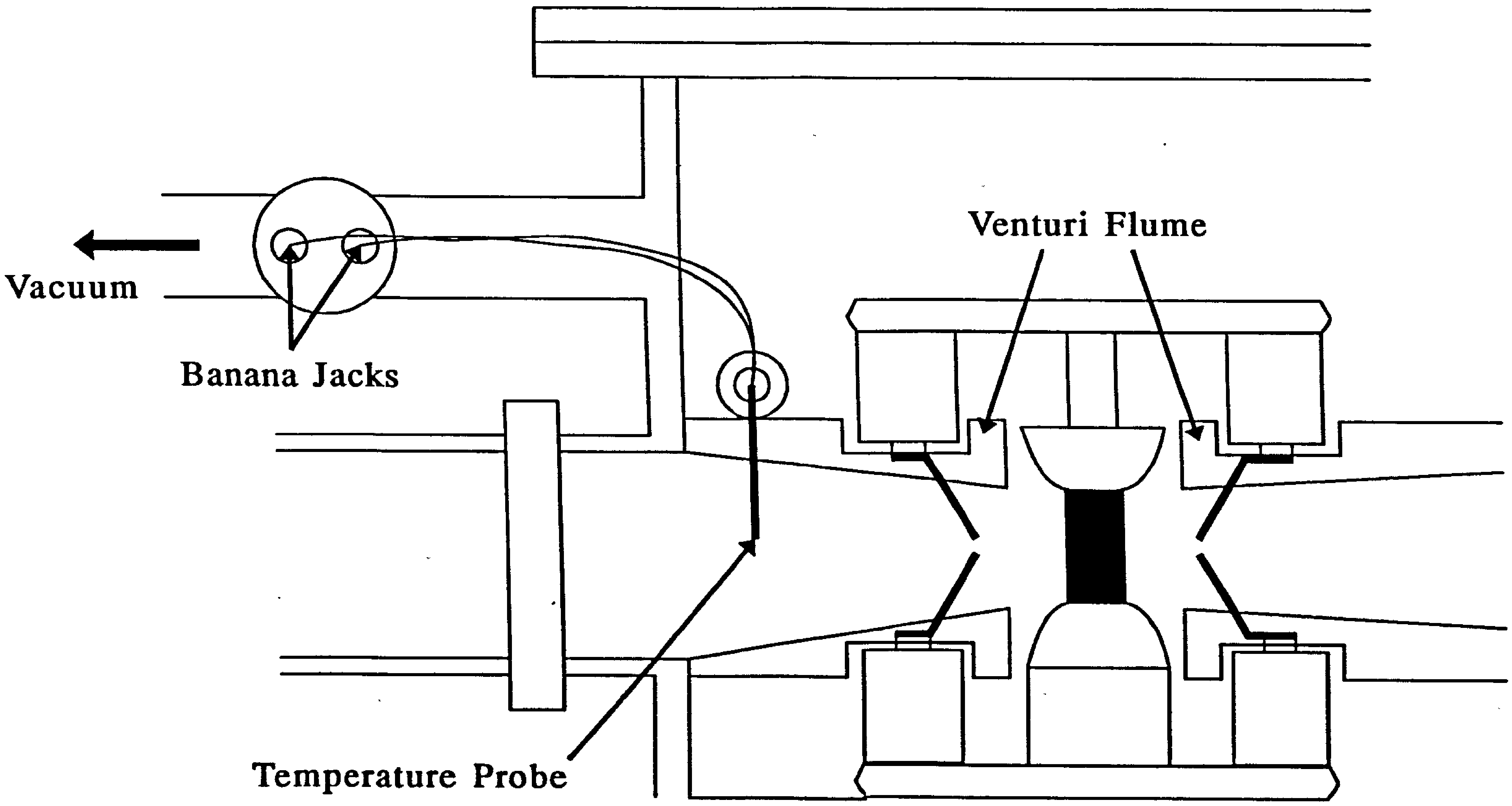

Fig. 4.15 Schematic diagram showing the position of a temperature probe in relation to the discharge region

In this configuration, the gas temperature could be monitored just prior to the recirculated gas entering the discharge region (Fig. 4.15). However, in order to make measurements, it was necessary to turn the laser off since the electro-magnetic interference (emi) produced by the laser and discharge circuitry disrupted the Comark micro-voltmeter used to record the thermocouple output.

4.2.2 Effect of Water Cooling on Gas Lifetime

Initial lifetime runs without water cooling, at 60Hz, produced only a few tens of thousands of pulses before the output power dropped below the 50% (Fig. 4.16). The laser gas temperature in this case increased rapidly over the first couple of minutes from room temperature to ~27°C. The temperature then continued to rise at a somewhat slower but steady rate of increase until a temperature of ~32°C was reach at the end of the run.

The addition of flowing tap water, at ~20°C, produced the same initial fast rate of rise in temperature to ~26°C, Fig. 4.17, and then the temperature proceeded to climb to ~28°C at a slightly slower rate than that described for the no water cooling case. The gas lifetime in this instance showed a noticeable increase, achieving over 10^5 pulses before dropping below the 50% point once again. Maintaining the water temperature to 10°C, Fig. 4.18 (using a Churchill water cooler) made absolutely no difference to the lifetime of the gas mixture, presumably as this only lowered the gas temperature by ~2°C throughout the run.

In conclusion, it has been shown that for a XeCl laser it is important not to allow the gas temperature in the laser to rise above 30°C if gas lifetime is considered important. It can also be concluded that maintaining the

Fig. 4.16 Laser output power as a function of the number of pulses @ 60 Hz

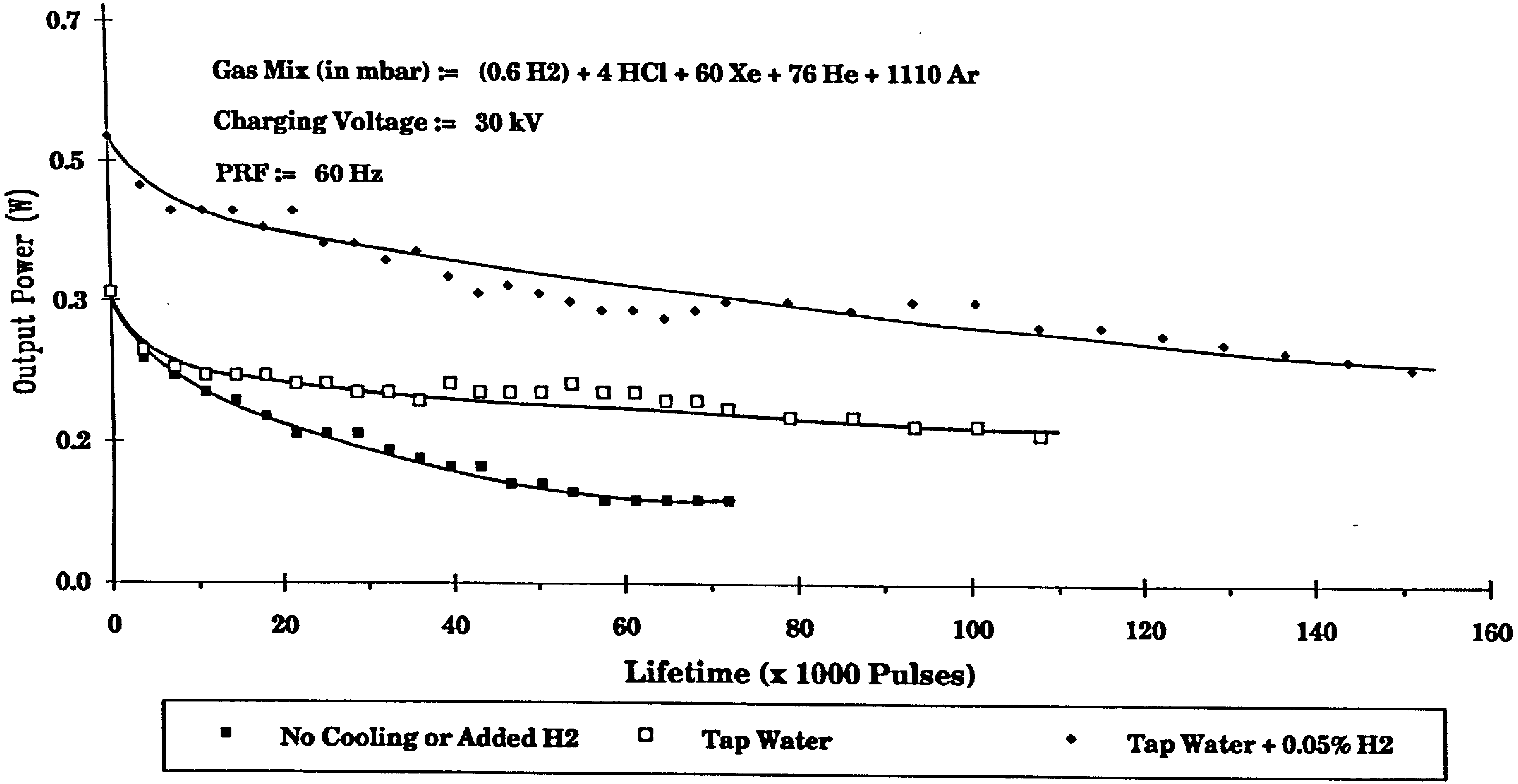

Fig. 4.17 Laser gas temperature, before entering the discharge region, as a function of the number of pulses

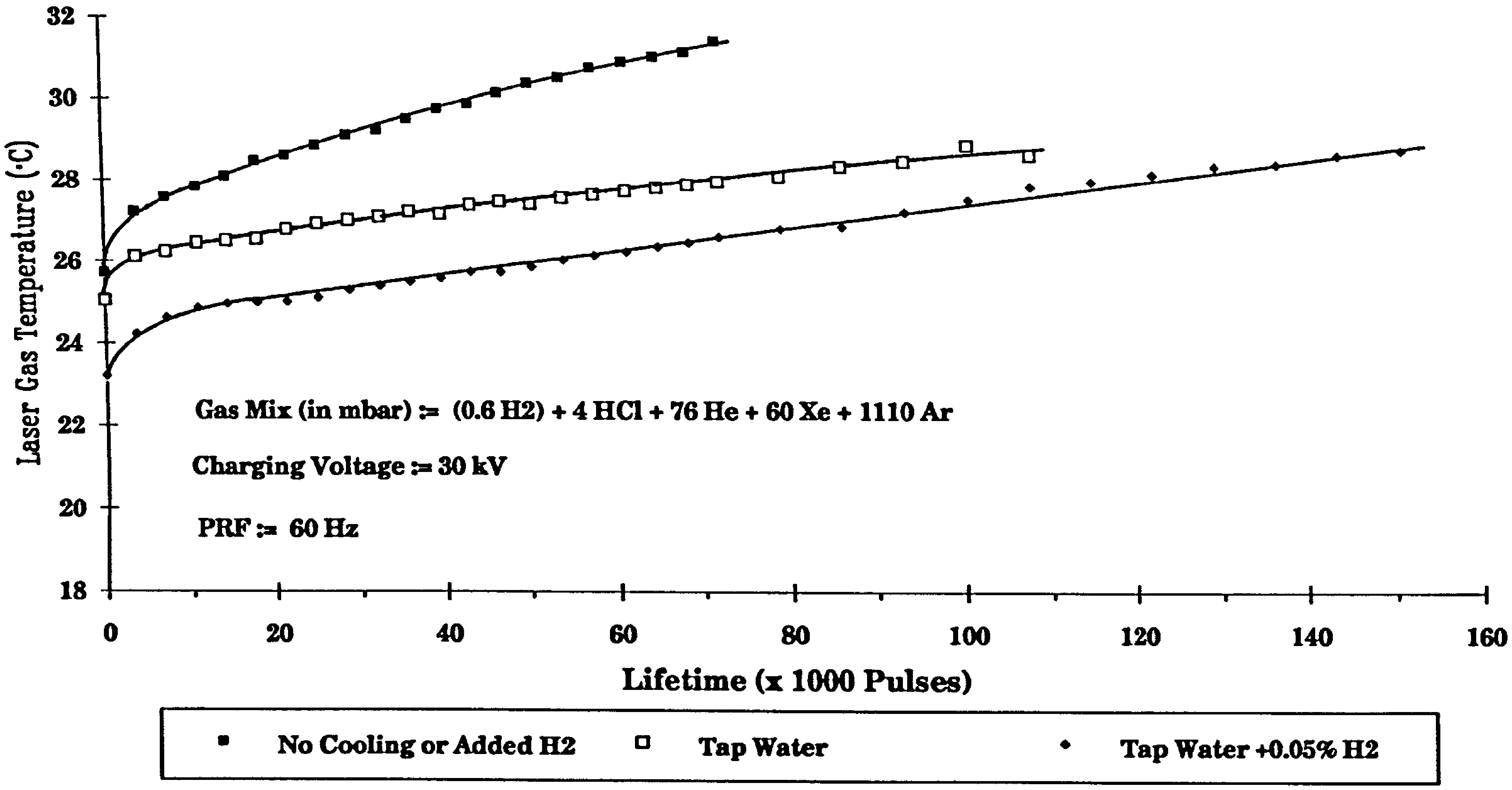

Fig. 4.18 Laser ouput power as a function of the number of pulses
@ 60 Hz

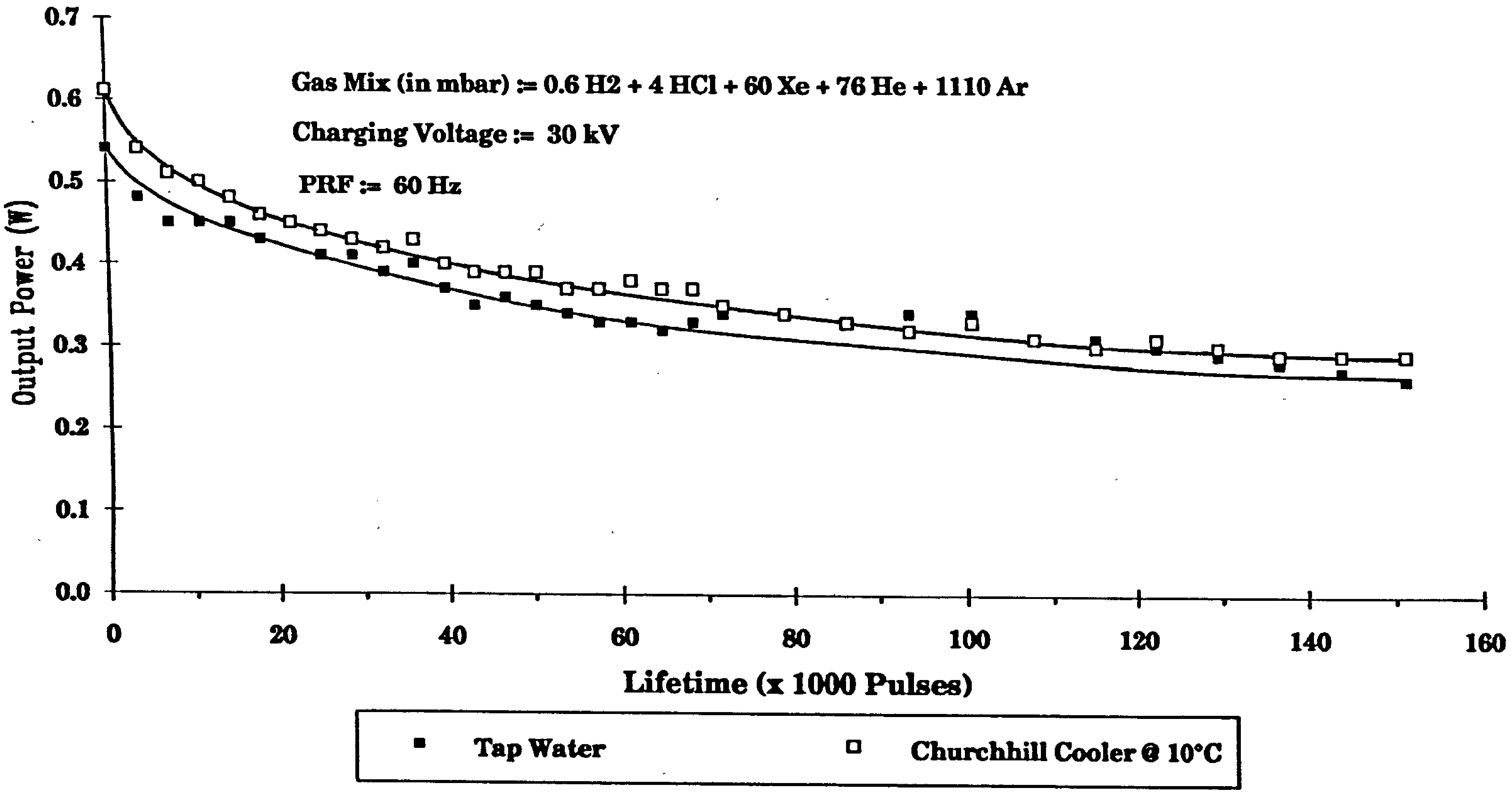

temperature of the gas at, or possibly below, 25°C would produce significant increases in gas lifetime.

4.2.3 Effect of H_2 Additive on the Gas Lifetime

Following on from the work by McKee *et al* [4.13], it was decided to add small quantities of hydrogen to the laser gas mixture. The addition of hydrogen results in the reduction of absorbing species below 230nm: the region where uv preionisation is dominant. This affect is probably attributable to the hydrogen recombining with the chlorine, to form HCl, and thereby reducing the generation of absorbing species.

Using only tap water for cooling, it was found that the power curve exhibited the behaviour found in previous runs. It is interesting to note however, that the final temperature of the gas is the same as that for the case with no hydrogen added (Fig. 4.17), even though the inital starting temperature was a couple of degrees cooler. Power on the other hand, with hydrogen, was higher than before and resulted in a 50% increase in lifetime, i.e. 1.5×10^5 pulses to the 50% power point.

In all cases, the output power curves initially dropped sharply as the temperature in the gas rose rapidly; the output power then decreased at a steady, but slower, rate as the temperature rose more slowly.

4.3 MEDIUM POWER, HIGH PRF XeCl LASER OPERATION

So far in this thesis, the steps that were taken to evaluate different preionisation techniques for high prf operation, and the effects of various parameters relating to the stable operation of the laser have been discussed.

The aim of this section is to pull those results together, and provide a short synopsis of the data leading to the final laser configuration.

4.3.1 Optimisation of the Buffer Gas for High PRF Operation

When looking at the effects of buffer gases on the operation of the laser, it can be concluded that argon for high prf operation is not satifactory due, mainly, to the inherent discharge instability. This is not to say that it does not have its place, but it does tend to lend itself to operation at low prf's in e-beam pumped systems [4.8], where only modest pulse rates are attainable. This then restricts operation of high prf lasers to helium, neon, or combinations of these buffer gases. In this work, the use of combinations of buffer gases never seemed to be more beneficial than use of the pure gas alone.

Helium would be the prefered gas if only monetary aspects were important as it is typically 5 to 8 times less expensive than neon. However, in laser performance terms, the situation tends to change. It has already been shown in Section 3.1.1, that neon offers better performance, over a much wider range of operating voltages, when operating at greater than 2 atmospheres total pressure (where most of todays commercial lasers operate) over a much wider range of operating voltages. Helium typically operates as well as neon when voltages above 30 kV are being used. However, when trying to optimise for operation at higher pressures and voltages less than 30kV (as in the case for high prf devices), then the laser output from a helium buffered discharge tends to peak as you move to higher pressures. This is not the case for neon buffered gas mixtures whose output continues to increase linearly with pressure.

Fig. 4.19 shows the variation of output power with charging voltage for helium and neon buffered gas mixtures, at 2500 and 3100 mbar respectively, optimised for maximum output. In these cases, maximum efficiency occurs when using the 5nF main discharge capacitor, but maximum pulse energy, at 100Hz, occurs with the 10nF capacitor. The effect of the buffer gas, coupled with either a 5 or 10nF capacitor, is shown in Fig. 4.20 where the total gas mixture pressure is optimised for the respective buffer gas and the voltage is kept at 27kV in all cases. It can be seen that in the case of the helium buffered gas mixture, the 10nF capacitor does not result in a major increase in output power, but it does limit the upper pulse frequency that can be obtained. On the other hand, the neon buffered gas mixture does offer significant increases in power using the 10nF capacitor, >50%, over the 5nF capacitor, and the 5nF capacitor offers a >50% increase in prf over the 10nF capacitor.

Using the 10nF capacitor at a charging voltage of 27kV, the best output power and efficiencies measured are shown in Fig. 4.21. Here, it can be seen that efficiences approaching 1% have been achieved at low repetition rates, and >0.7% at 700Hz. These results are the same as presented in Fig. 3.26 except that power measurements made over 700Hz are not displayed since meaningful efficiencies cannot be derived. The explanation for this, is that the A.L.E. power supply delivers only 3kW above 30kV, and below this point the power drops linearly with voltage such that at 27kV the maximum power is ~2700W. From this, it can be concluded that, up to a repetition rate of ~700Hz, can be safely assumed to be constant, but above this will start to drop. Unfortunately when these measurements were made, no accurate measurement of the delivered voltage were taken, and thus calculations of efficiency above ~700Hz are not valid.

Fig. 4.19 Laser output power as a function of charging voltage, for helium and neon buffered gas mixtures, using either 5 or 10nF main discharge capacitors

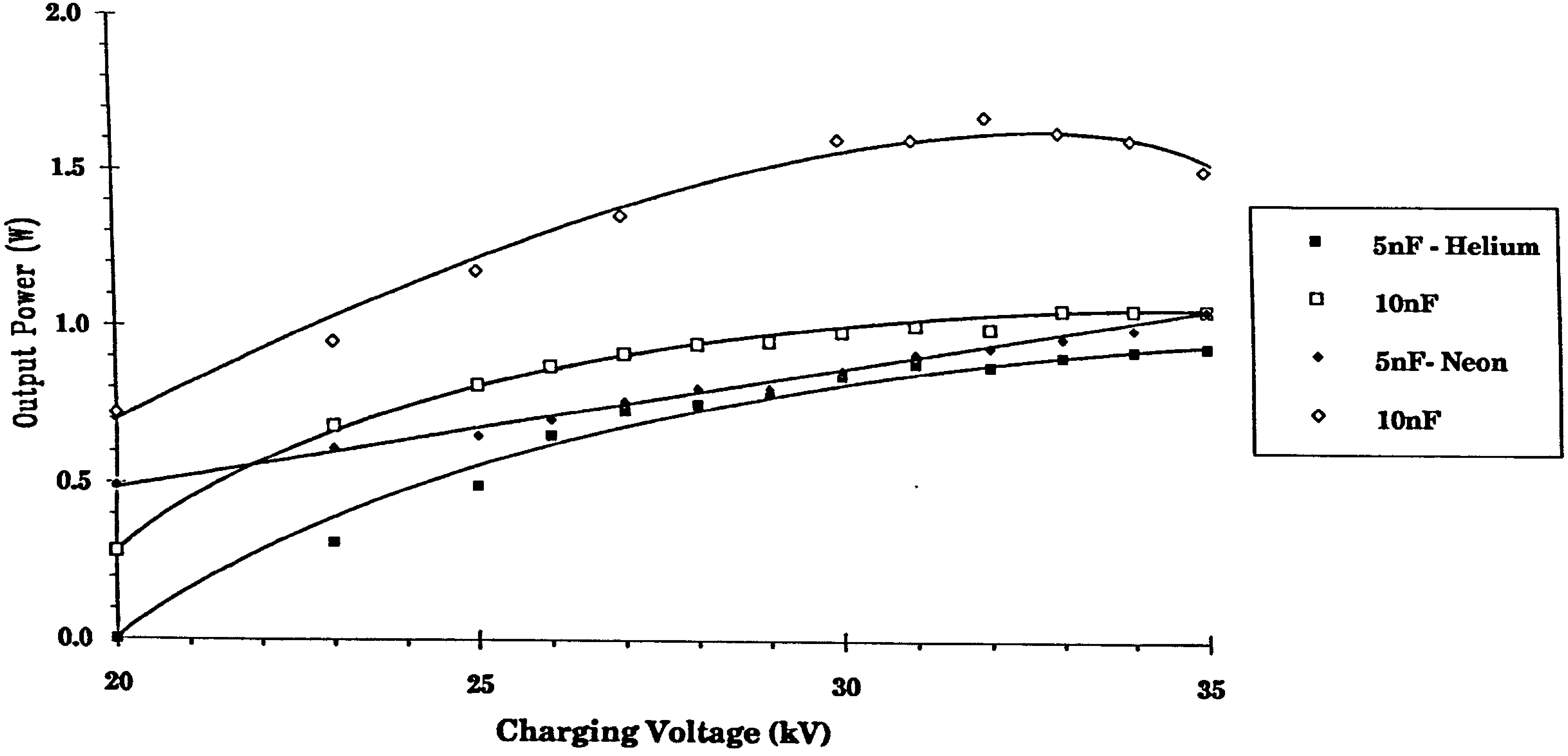

Fig. 4.20 Laser output power as a function of prf, for helium and neon buffered gas mixtures, using either 5 or 10nF main discharge capacitors

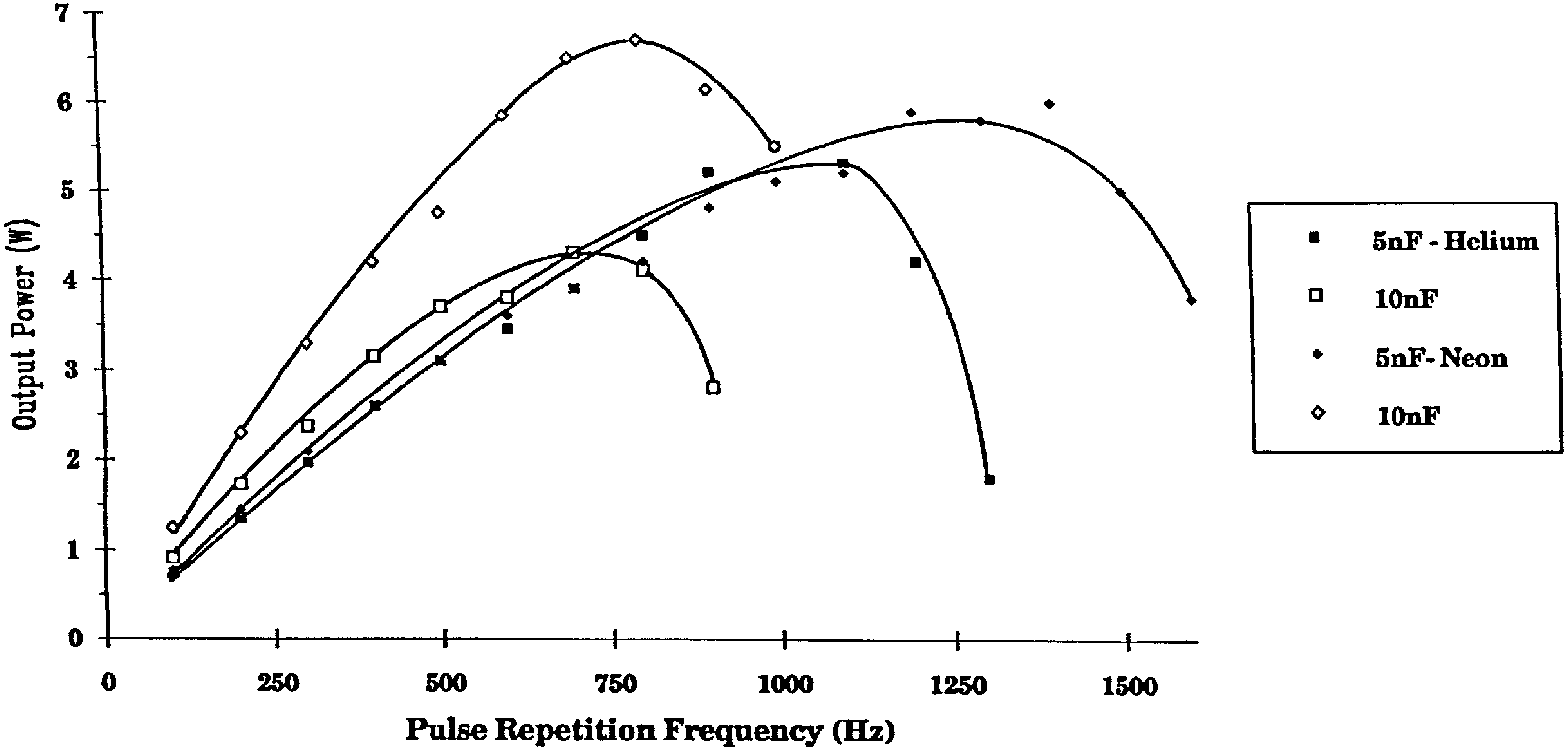

Fig. 4.21 Laser output power & efficiency as a function of pulse repetition frequency, for a neon buffered gas mix, operating at 27kV with a 10nF main discharge capacitor

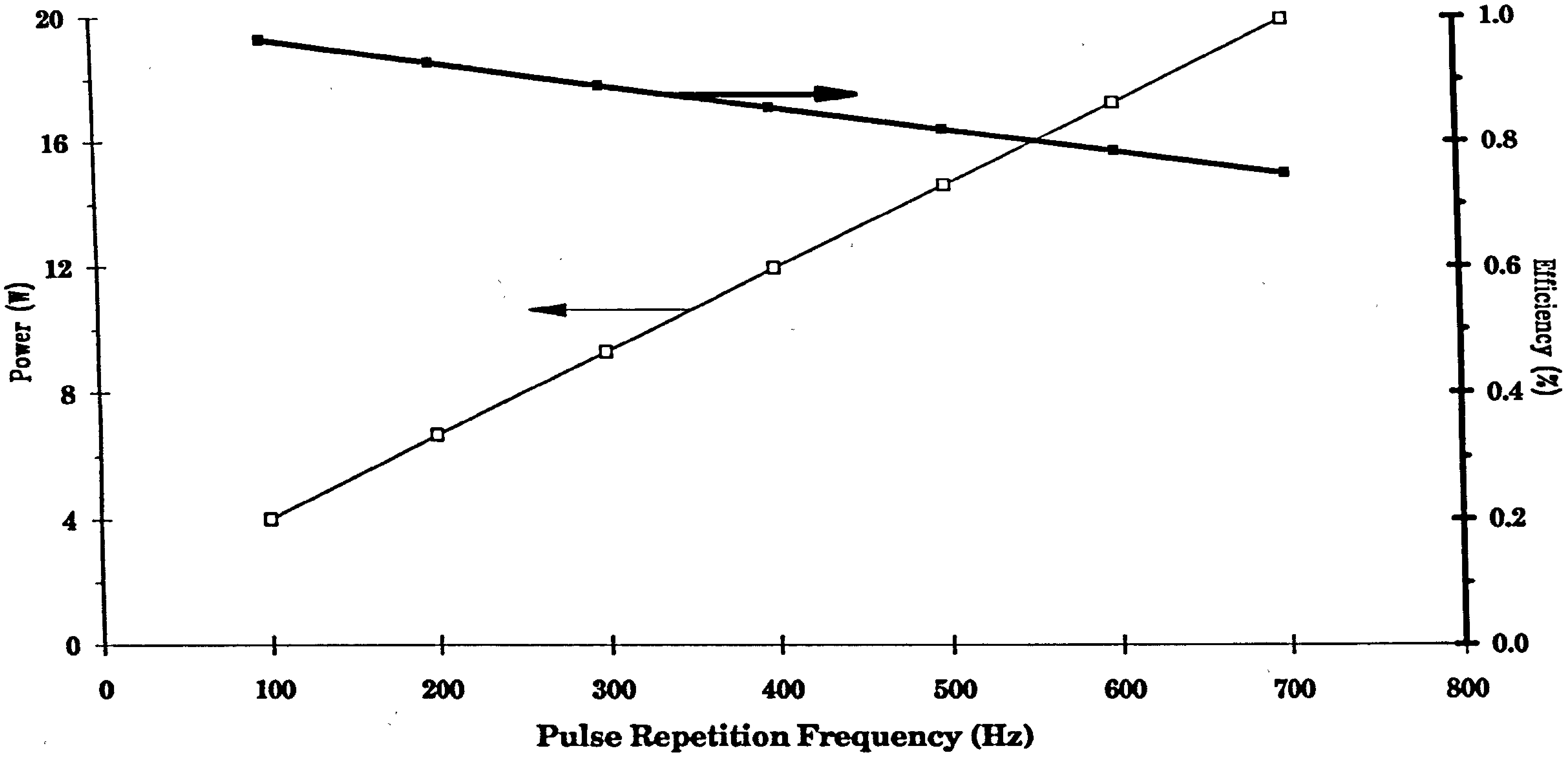

4.3.2 Effects of Output Coupler Reflectivity on Laser Ouput Power and Energy Extraction from the Fluorescence Profile

In a small discharge volume device, having a short gain length, it is necessary to use a suitable optical resonator in order to achieve efficient laser energy extraction. An investigation was therefore carried out to look at the effects of the output coupler reflectivity on the output power of the laser.

For this, several optics were obtained that would, in combination, provide a suitable range of reflectiivities. Fig. 4.22 displays the results measured for both the corona, and capcitively-coupled, preionisation schemes. In both of these cases, a reflectivity of ~36% proved to be optimal. This assumes that there is ~4% reflectance from each uncoated quartz surface, or the reflectance of the coating that was laid on a particular surface. The results presented in Fig. 4.22 proved to be applicable to other discharge configurations.

For the case of the resistively-ballasted preionisation scheme, where very little laser output was obtained, an alternative optical resonator design was tried. In this design, a fused silica rutile prism was used as the rear reflector of the resonator in place of the more conventional aluminium back-surface coated flat (Fig. 4.23). The object of this was to use the prism to fold the beam back on a path parallel to the incoming beam, but shifted about the central axis of the discharge, thereby improving the mixing of the beam, and producing a more homogeneous beam profile. The maximum power generated with this scheme was 1.1W@50Hz which was comparable, if not slightly above, that measured for the conventional resonator configuration. A beam burn on Dylux paper is presented in Fig. 4.24a).

Fig. 4.22 Normalised output power as a function of output coupler reflectivity, for corona and capacitively-coupled preionisation schemes

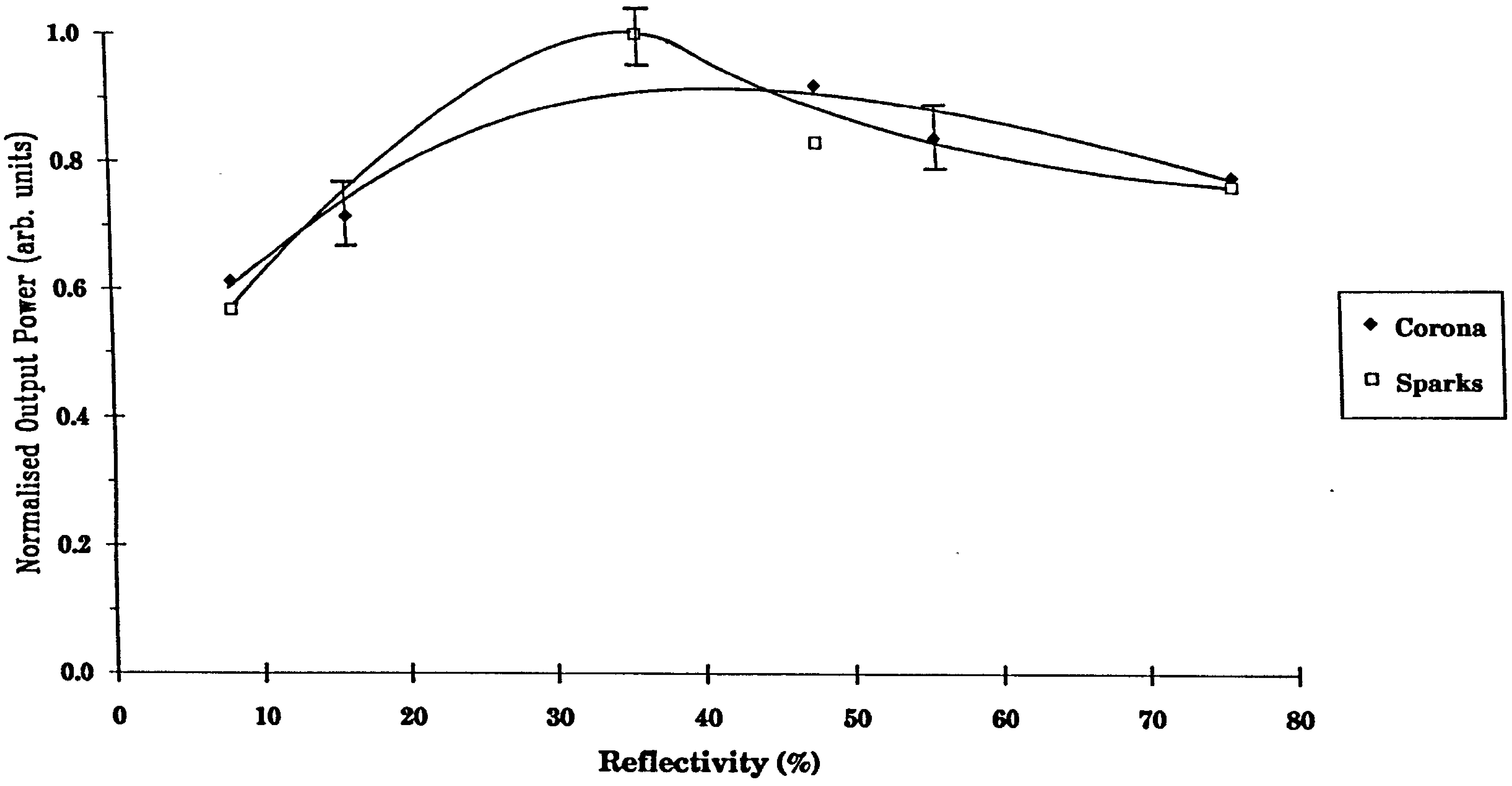

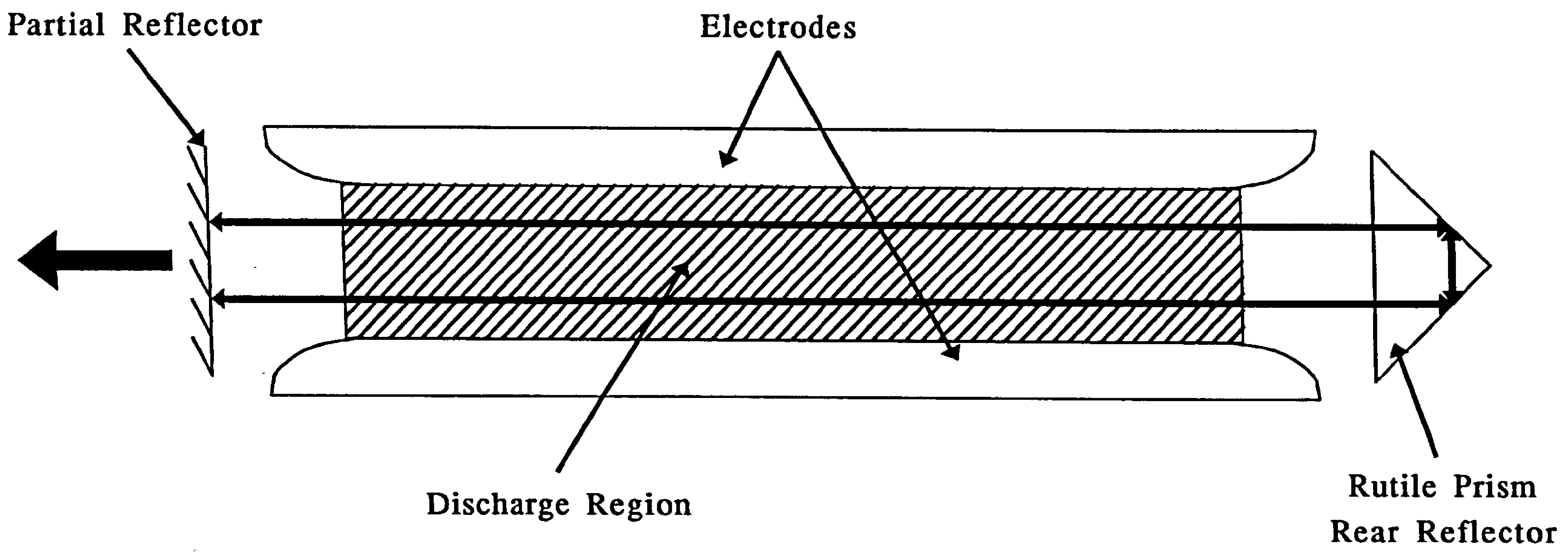

Fig. 4.23 Schematic diagram of the rutile prism in a resonator arrangement used to investigate its total internal reflection properties in improving laser performance and beam homogeneity

a) A beam burn from a resonator configuration using a rutile prism as a rear reflector

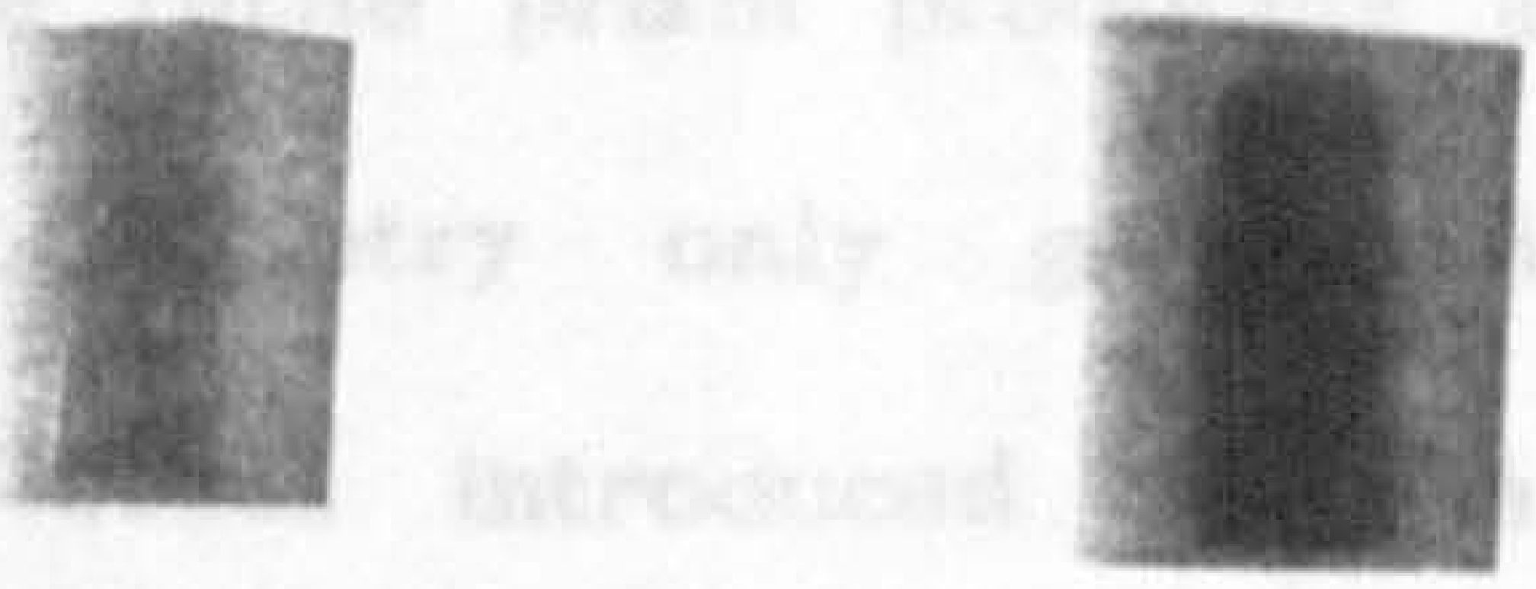

b) A beam burn from a folded-cavity resonator configuration using a rutile prism as a turning mirror

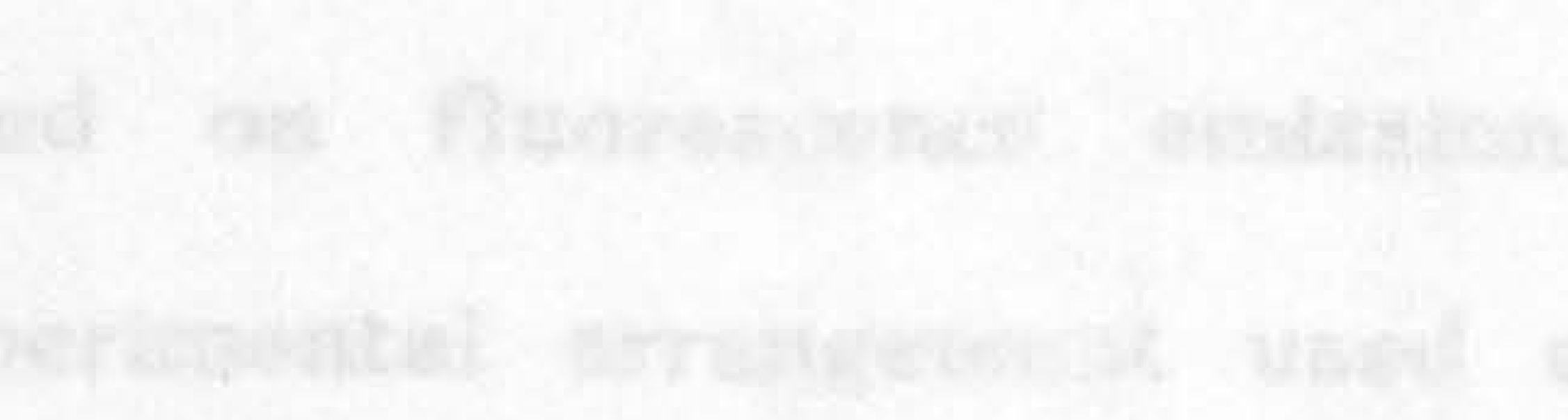

Fig. 4.24 Laser burn patterns, taken on Dylux paper, for two rutile prism resonator configurations

Taking this technique a step further, a folded cavity was constructed around the standard electrode separation configuration. A silvered surface reflector was positioned at the output of the laser perpendicular to, and half way across, the discharge (Fig.4.25). The laser resonator was thus formed between the silvered surface and output coupler, with the rutile prism producing a double pass of the discharge. This cavity geometry only generated 0.7W@50Hz, presumably because of increased losses introduced by the additional components, but the beam burn (Fig. 4.24b)), was fairly square in profile and qualitatively looked reasonably uniform.

Investigation of the output coupler reflectivity on the extraction efficiency were carried out using the technique, based on fluorescence emission, developed by Andrew and Dyer [4.9]. The experimental arrangement used a photomultiplier (EMI 9813) coupled to a monochromator. A spectral profile of the XeCl transition was made using this system (Fig. 4.26) to aid setting the monochromator to the peak of the B→X transition. Fig. 4.26 shows the narrow spectral peak of the B→X and D→X transitions, as well as the broader C→A transition.

The sidelight fluorescence intensity was monitored, without lasing, as a function of output coupler reflectivity for the capacitively-coupled preionisation scheme. Figs. 4.27(a),c),e) & g)) show the fluorescence pulse profiles for this device, with and without lasing, as a function of the output coupler reflectivty. These pulses were overlapped on the oscillograph to indicate the extent of the fluorescence pulse being supressed when lasing took place. From these measurements, it can be seen that at higher reflectivities, depletion of the fluorescence pulse is extended to longer durations and occurs in the tail of the pulse. This is further evident in the

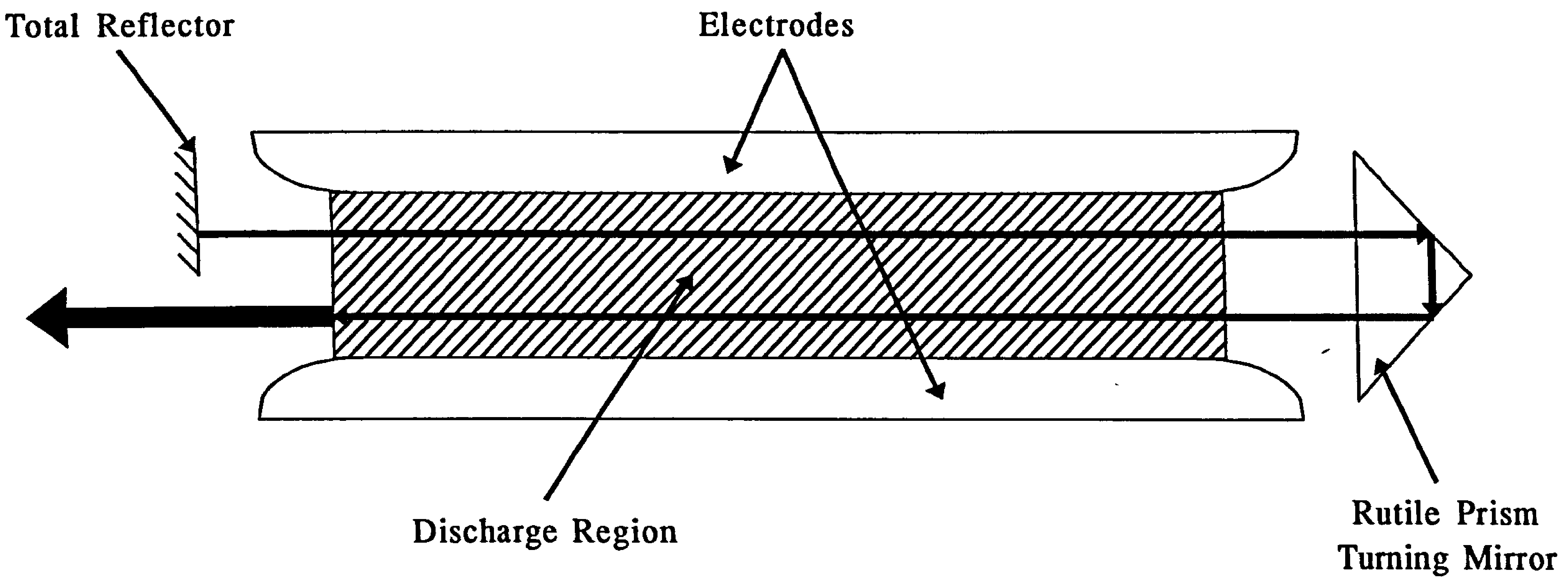

Fig. 4.25 Schematic diagram of the rutile prism arrangement coupled with a total reflector, partially obscuring the discharge, to double the gain length

Fig. 4.26 XeCl fluorescence emission spectrum for this laser device

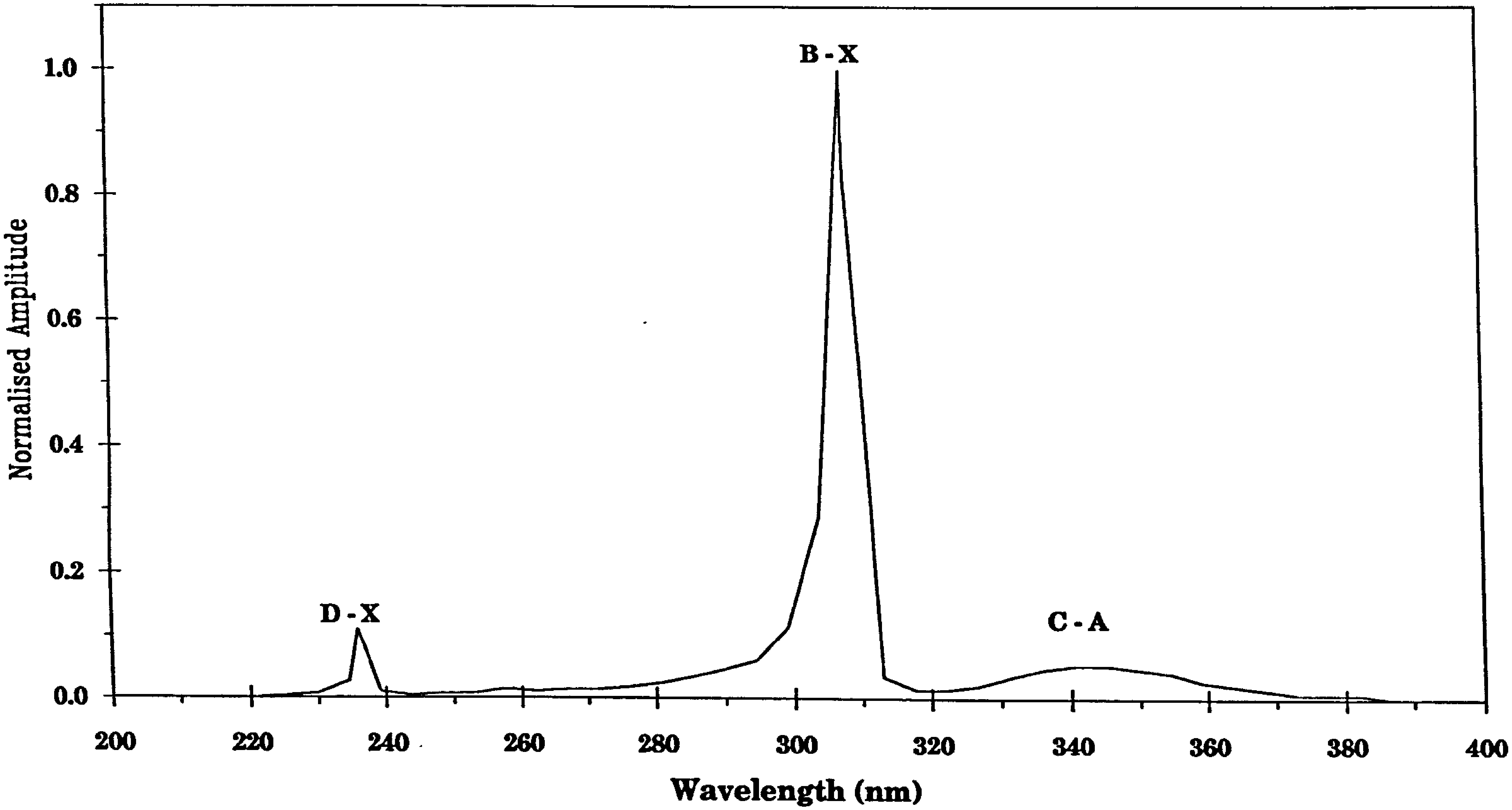

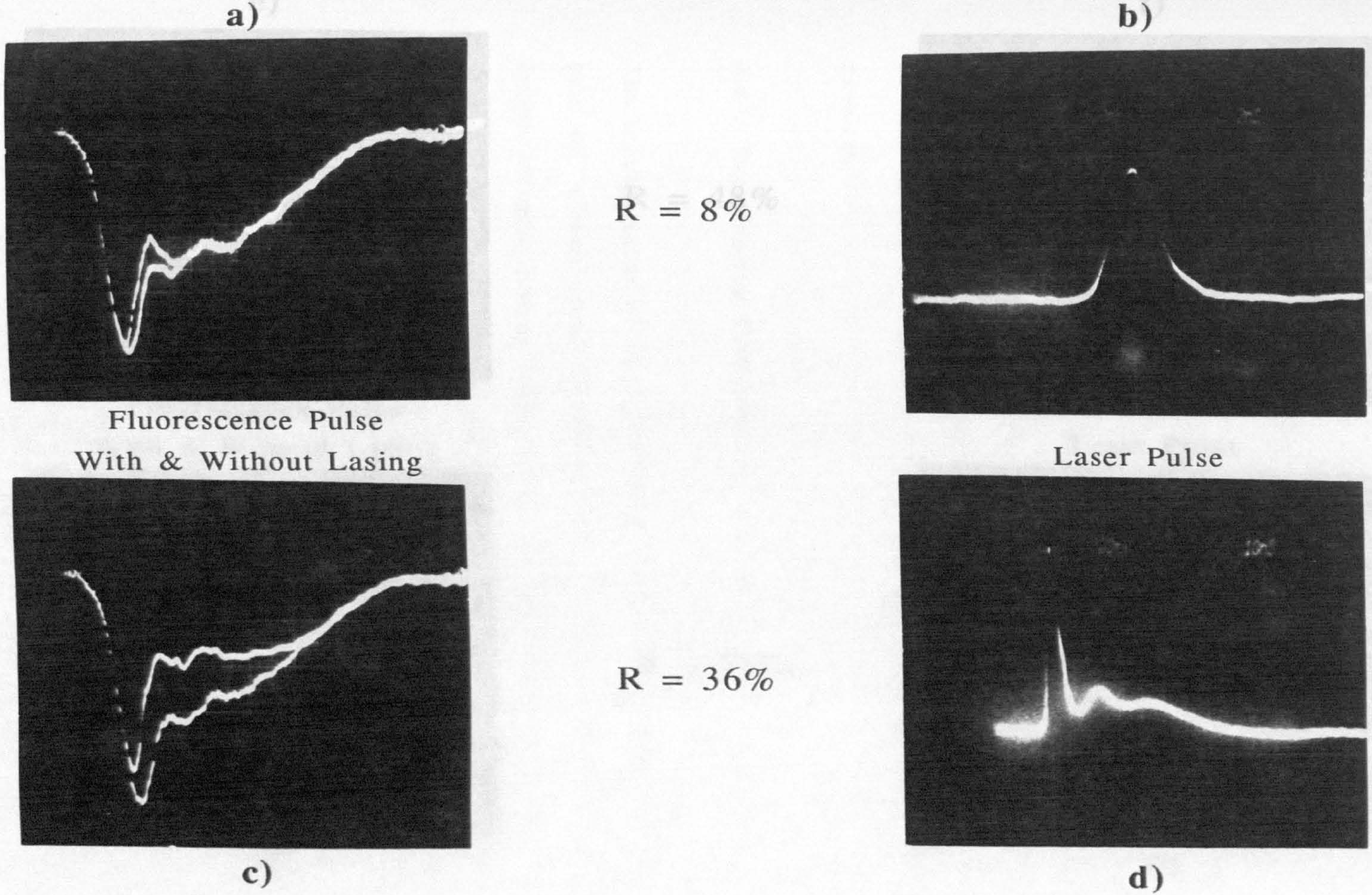

Fig. 4.27 Fluorescence and laser pulse shapes for 8% and 36% reflectivity output couplers

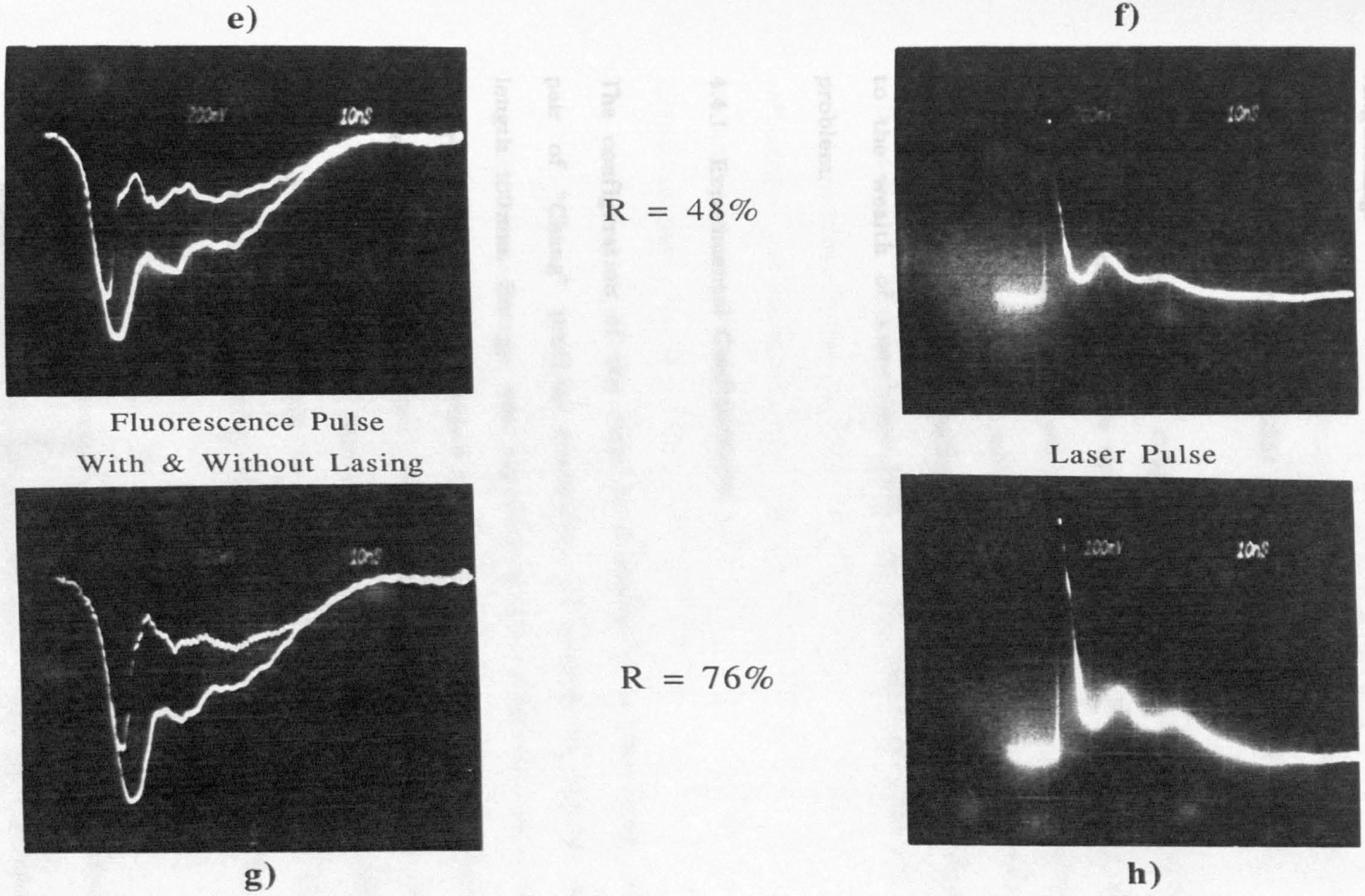

Fig. 4.27 Fluorescence and laser pulse shapes for 48% and 76% reflectivity output couplers

corresponding laser pulse shape Fig. 4.27(b),d),f) & h)) which shows pulse lengthening.

4.4 HIGH POWER, MEDIUM PRF CO_2 LASER OPERATION

The use of a capacitively coupled uv preionisation arrangement, where the sparks were positioned 3cm upstream from the centre of the electrodes, led to very poor lasing at 308nm. In order to determine if the arrangement was either unsuitable for XeCl mixes, or not correctly configured (i.e. electrode misalignment) for lasing discharges to be produced, it was decided to resort to the wealth of knowledge built on CO_2 laser systems to evaluate this problem.

4.4.1 Experimental Configuration

The configuration of the laser head assembly, at that time, consisted of a pair of "Chang" profiled electrodes, of separation 15.8mm and discharge length 180mm. Energy was supplied to the discharge via a 12nF bank of "doorknob" capacitors charged to 33kV. The internal capacitance, set by the single row of preionisation capacitors downstream of the discharge, was 2.5nF. Using a 78%R Ge uncoated output coupler and a 100%R brass 10m radius of curvature reflector for the optical cavity, and a 33% CO_2:17% N_2:50% He gas mixture at 500mbar absolute pressure the following results were obtained,

PRF (Hz)	50	350	500
Power (W)	9	55	78

This proved beyond all reasonable doubt that the preionisation configuration was suitable for CO_2 laser discharges, but the constraints set by the excimer gas mixtures were obviously much greater. It should be noted, however, that the preionisation was not ideal even for CO_2 laser operation.

4.4.2 Gas Mixture and Optical Optimisation

Since the device had been depassivated, it was decided to investigate CO_2 laser performance of the device more thoroughly. Using an identical gas mixture to that used previously, the dependence of output power on the reflectivity of the output coupler was determined as a function of the pulse-repetition-frequency (prf). It can be seen from Fig. 4.28 that as the reflectivity was increased from 56%, an increase in power was brought about producing 116W@550Hz with an output coupler reflectivity of 85%. The output coupler showed no signs of degradation in optical quality even when the laser was run for several minutes at 500Hz.

Limited optimisation of the gas mixture was carried out by firstly increasing the N_2 concentration. An increase in power of 18% (137W@500Hz) was attained in this way. The second, and final, experiment carried out at 10.6μm, involved the addition of 15mbar of H_2 and resulted in a further increase in power to 157W@500Hz (i.e. 4.8% efficiency); it also a highest recorded energy of 410mJ@10Hz. The results of these last two gas mixture alterations can be seen in Fig. 4.29. The limiting factor in all these measurements was not the laser prf but the effect of the maximum power rating of the A.L.E. supply (3000J.s^{-1}).

Fig. 4.28 CO2 laser output power as a function of prf for different reflectivity germanium output couplers

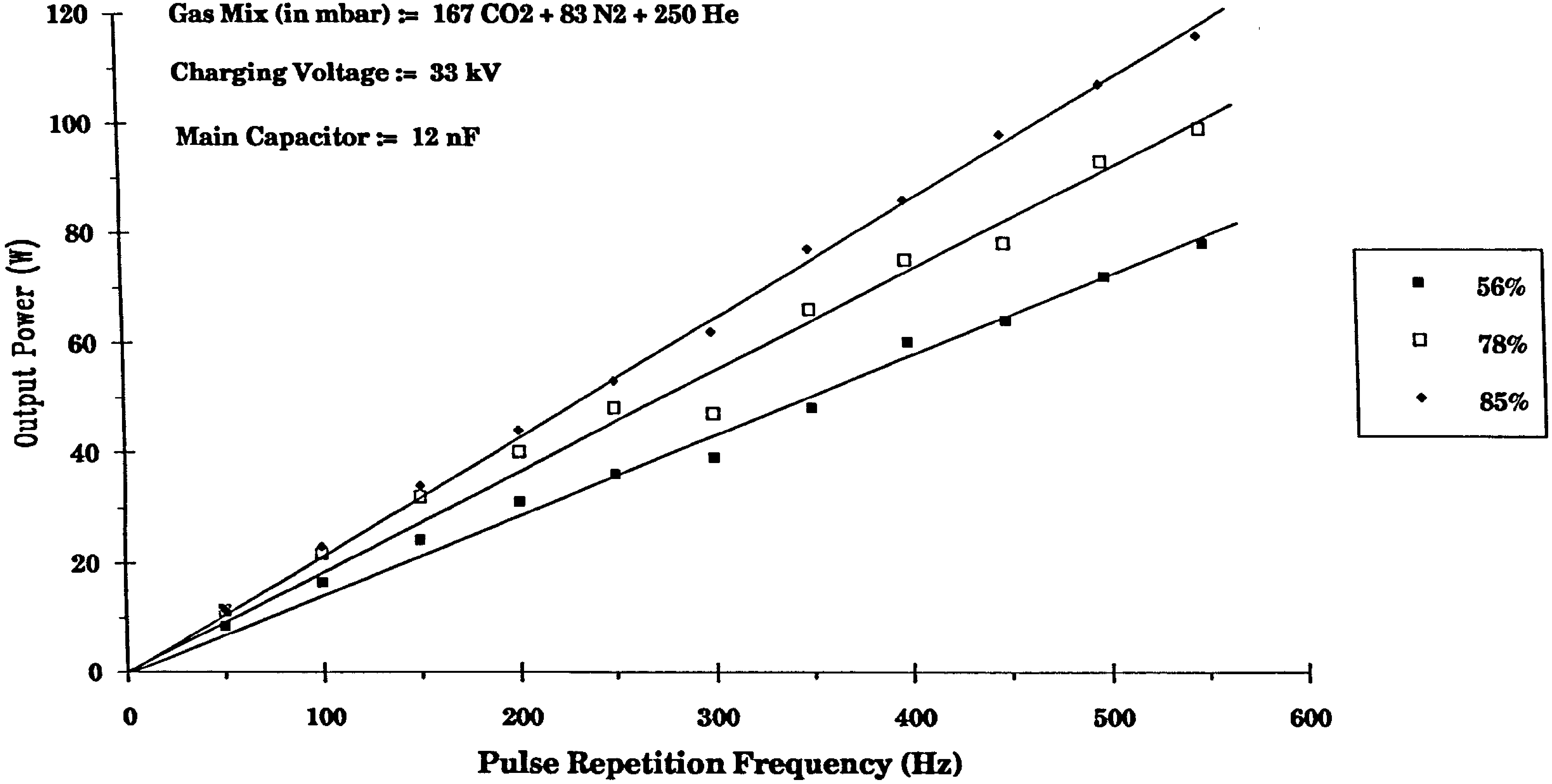

Fig. 4.29 CO2 laser ouput power as a function of prf for different gas mixtures

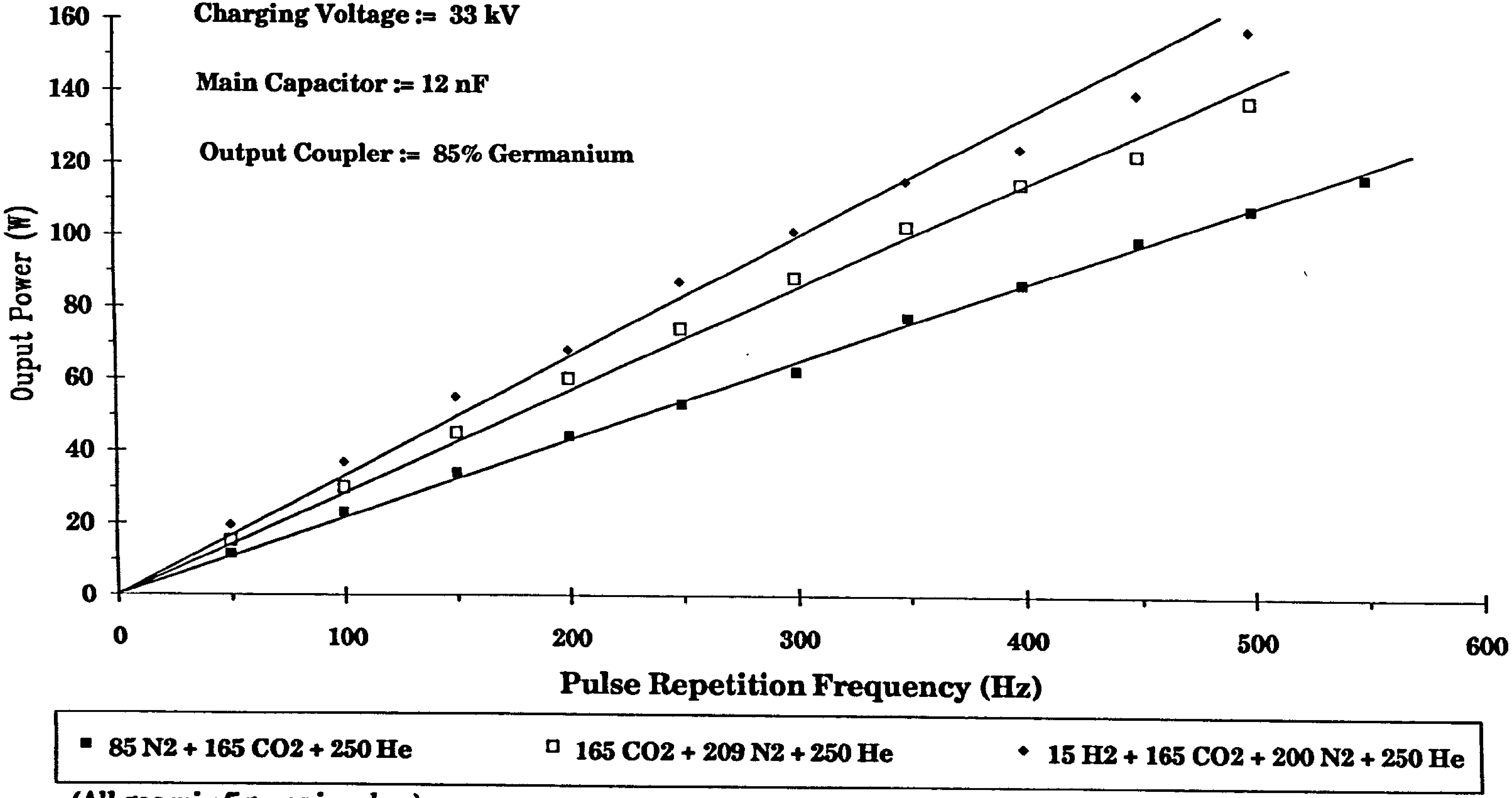

(All gas mix figures in mbar)

REFERENCES

[4.1] G.S.DZAKOWIC & S.A.WUTZKE, J. Appl. Phys., **44**, 5061 (1973)

[4.2] M.J.PECHERSKY, Laser Focus, **17**, 61 (1981)

[4.3] E.P.VELIKHOV, "Molecular Gas Lasers" (MIR Publishers, Moscow, 1981)

[4.4] V.Yu.BARANOV, S.A.KAZSAKOV, D.D.MALYUTA, V.S.MEZHEVOV, A.P.NAPARTOVICH, V.G.NISIEV, M.Yu.ORLOV, A.I.STARODUBTSEV & A.N.STAROSTIN, Appl. Opt., **19**, 930 (1980)

[4.5] B.M.FORESTIER, M.L.SENTIS, S.M.FOURNIER & B.L.FONTAINE, 5th Gas Flow and Chem. Laser Symp., 277, (Oxford, 20→24 Aug. 1984)

[4.6] M.F.QUINN & A.O'HARE, J. Phys. E: Sci. Instrum., **12**, 286 (1979)

[4.7] T.McKEE, D.J.JAMES, W.S.NIP & R.W.WEEKS, Appl. Phys. Lett., **36**, 943 (1980)

[4.8] F.KANNARI, A.SUDA, M.OBARA & T.FUJIOKA, IEEE J. Quant. Elec., **QE-19**, 1587 (1983)

[4.9] J.E.ANDREW & P.E.DYER, Opt. Comm., **54**, 117 (1985)

5. HIGH PRF, MEDIUM POWER XeCl LASER APPLICATIONS

Lasers have proven to be very versatile tools in the use of materials processing: Nd:YAG and CO_2 based systems being the most widely used. These lasers operate in the near- and mid-infrared regions of the spectrum respectively, and hence remove material by thermal mechanisms. The excimer laser, on the other hand, is used to pattern polymeric films by means of ablative etching [5.1 → 5.3]. The non-thermal nature of ablative photo-decomposition (APD) results in an extremely high degree of precision and opens up new possibilities in the area of high resolution patterning for micro-circuit applications [5.2, 5.4 & 5.5]. This ability to ablate polymeric solids via a highly localized, low threshold process, together with the continuing progress being made in raising the repetition rate and average power of excimer lasers, suggests that they could also prove important for cutting, drilling, and micromachining [5.6] of plastic films and structures. Such processing in the near ir spectral region is often difficult because of the high transparency exhibited by many polymers; whereas at CO_2 laser wavelengths the relatively poor spatial resolution, modest absorption, and thermal nature of the interaction limit capabilities.

5.1 ETCH RATES FOR EXCIMER LASER IRRADIATED POLYMERS

Experiments using the high repetition rate XeCl laser were carried out on the cutting of thin polyethylene teraphthalte (PET) films. From previous studies at low prf's, it was known that the etch depth per shot, x, is approximately given by Beer's law [5.2 & 5.7],

$$x = \frac{1}{k} \ln \left(\frac{E}{E_T}\right) \qquad \ldots [5.1]$$

where k is the effective absorption coefficient for uv radiation in the polymer, E_T is the threshold fluence, and E is the incident fluence. The threshold and absorption coefficients are related approximately as kE_T = constant which indicates that a minimum absorbed energy density is required to achieve ablative removal.

For a laser of fixed energy J and focal area of A, the volume of material removed per shot is, from [5.1],

$$v = xA = \frac{A}{k} \ln\left(\frac{J}{AE_T}\right) \qquad \ldots [5.2]$$

This is a maximum when $^{dv}/_{dA} = 0$, giving

$$\frac{1}{k} \ln\left(\frac{J}{AE_T}\right) - \left(\frac{J}{A^2 E_T} \cdot \frac{AE_T}{J} \cdot \frac{A}{k}\right) = 0$$

or

$$\ln\left(\frac{J}{AE_T}\right) = 1$$

This requires that $J = 2.72AE_T$ and thus the optimum fluence for material removal is $E = 2.72E_T$. Therefore, for a given laser energy, the focal area should be chosen to satisfy this condition if efficient processing by material removal is desired.

5.1.1 Cutting of Polyethylene Terephthalate (PET)† Films

If a circular spot of area A_c is used, then the energy required is $J=2.72A_cE_T$. For a 200μm diameter focal spot $A_c=3.14\times10^{-4}cm^2$, and since $E_T\sim170mJ.cm^{-2}$ at 308nm [5.2 & 5.7] then J=0.15mJ. This energy is very low and does not make efficient use of the ~10mJ/pulse that the XeCl laser could deliver at high prf's.

A more appropriate geometry for linear cutting is a line focus of length l and width 2ω, which would also greatly increase the usage of the beam (Fig. 5.1). For example, with a line focus of l=10mm and 2ω=200μm then J=4.62mJ. However, in the line focus geometry an initial 'run-in' distance occurs, during which time full cutting is not achieved (Fig. 5.2). This distance is of the order of the line focus length, l. If d is the film thickness and the etch depth per shot is x, then to achieve penetration requires that $n > {}^{d}/_{x}$ laser pulses are delivered within the time, τ, and that the film moves a distance equivalent to the line focus length l, i.e. $\tau = {}^{l}/_{V_F}$ where V_F is the cutting velocity. Taking $n={}^{d}/_{x}$ and defining the laser prf as ν gives:

$$\nu = \frac{n}{\tau} = \frac{dV_F}{xl}$$

or a cutting velocity of,

$$V_F = \frac{xl\nu}{d} \qquad \ldots (5.3)$$

---

† PET is more widely known under the registered trade names of Melinex® from Imperial Chemical Industries (ICI), and Mylar® from DuPont De Nemeurs Inc..

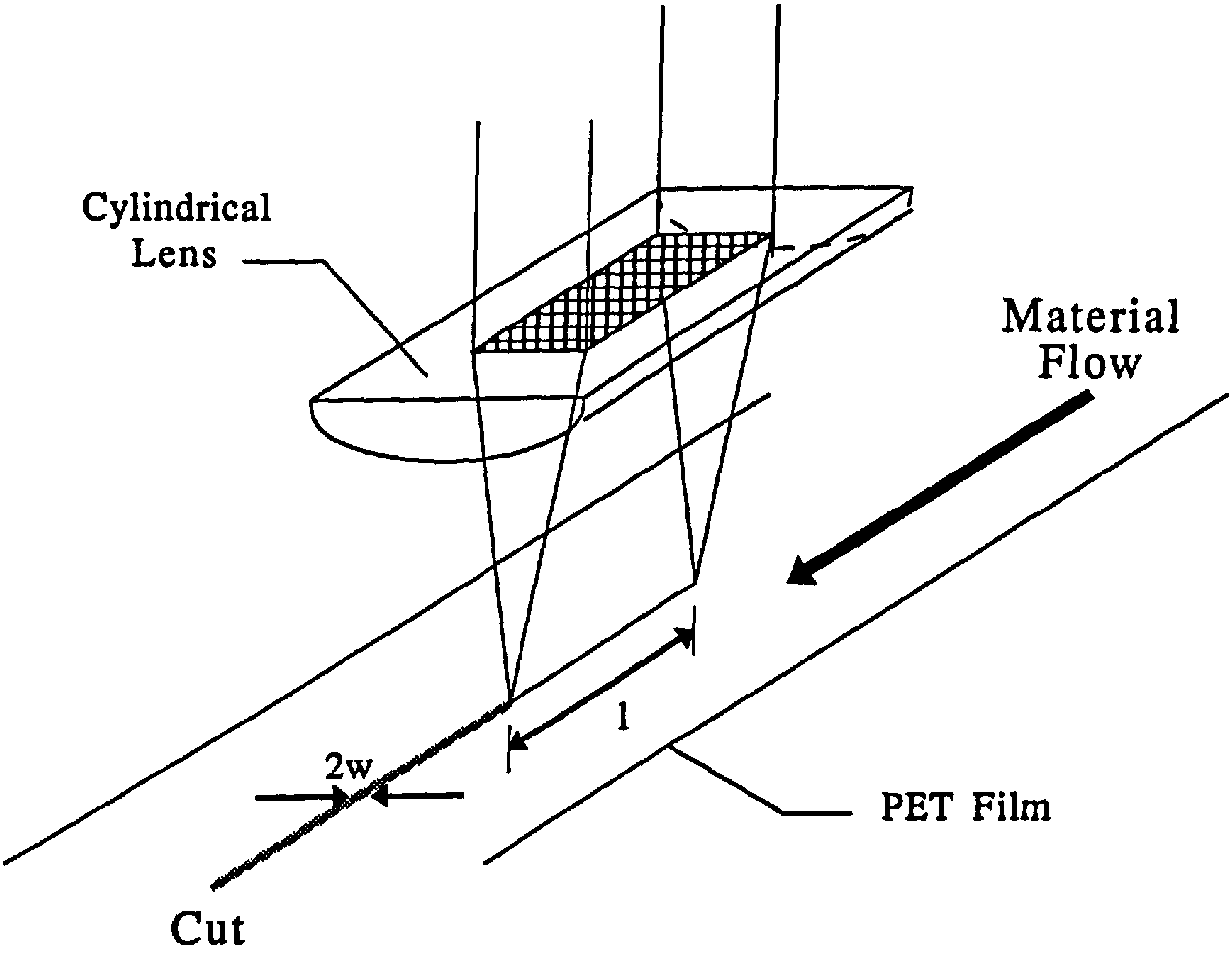

Fig. 5.1 Schematic diagram showing the line focusing geometry used for polymer cutting applications

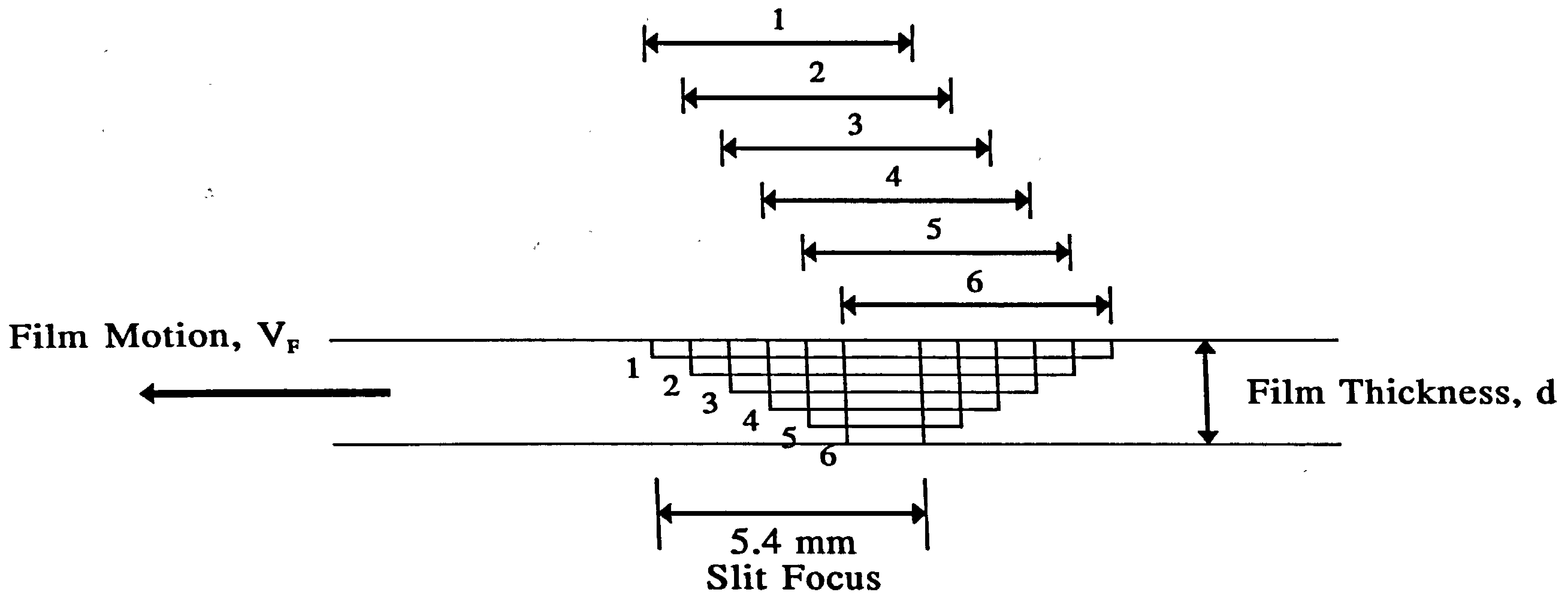

Fig. 5.2 Schematic diagram showing the effect of subsequent pulses on the etch rate for a polymer film moving with velocity V_F

Under optimal conditions $x = {}^{1}/k$ and $J = 5.44\omega l E_T$, so

$$V_F = \frac{1}{k}\,\frac{J\nu}{5.44E_T\omega d}$$

or

$$V_F = \left(\frac{1}{kE_T}\right)\frac{P}{5.44\omega d} \qquad \ldots (5.4)$$

where P is the laser average power, and ${}^{1}/kE_T$ is approximately constant. Since $kE_T \sim 3.4\times10^3$ [5.8], the maximum, power normalised cutting rate is ${}^{V}F/_{P} = 6.4\text{cm.s}^{-1}.\text{W}^{-1}$ for $d=12\mu m$ and $2\omega=140\mu m$.

5.2 EXPERIMENTAL ARRANGEMENT

In these experiments, a constant laser energy of ~12mJ could be maintained at prf's up to 10^3Hz. The use of a circular focal spot would therefore have either meant working with an unacceptably large cut width (~2mm) to attain the optimum fluence, or at an excessively high fluence (~40J.cm^{-2}) with the minimum attainable spot width of ~200µm. In contrast, the line focus gave a maximum fluence of ~1600mJ.cm^{-2}, which was considerably closer to the optimum value.

5.2.1 Optical Arrangement

Here the 8x15mm output beam from the laser was brought to a 5.4mm-long line focus of full width 140µm using an anamorphic focussing system, and the PET film was transported through the focal plane using a variable speed rotating wheel of 40 or 100cm diameter (Fig. 5.3). For a fixed traversal speed the laser prf was then varied until cutting just occured.

5.2.2 Laser Beam Profile Measurements

In any processing application it is useful to know the beam profile, since its uniformity and shape may have a positive or detrimental effect on the process, and may be able to shed some light on the phenomena encountered. The beam profile of the hrr XeCl laser was measured in planes normal and perpendicular to the electrode surfaces in the near field using a slit, of width ~0.1mm, scanned across the beam with an energy meter behind it. The profile in the horizontal (or narrow) direction is shown in Fig. 5.4 and is typical for this type of laser. In the vertical direction (Fig. 5.5), with the cathode at the top, the beam shape is fairly flat in the lower two-thirds, but rises to almost double the amplitude in the top one-third.

The effect of the anarmorphic focussing arrangement on the beam profile was then investigated. Here, it was assumed that the profile in the horizontal plane would not change dramatically since it was quasi-gaussian in nature. Also, it would be difficult to measure it accurately given the size of the slit width used for point-to-point sampling of the beam. Measuring the profile in the vertical direction was carried out producing the results shown in Fig. 5.6. It can be seen that the profile was closely analogous to the near field profile, as one might expect, still retaining the peak from the cathode region of the beam.

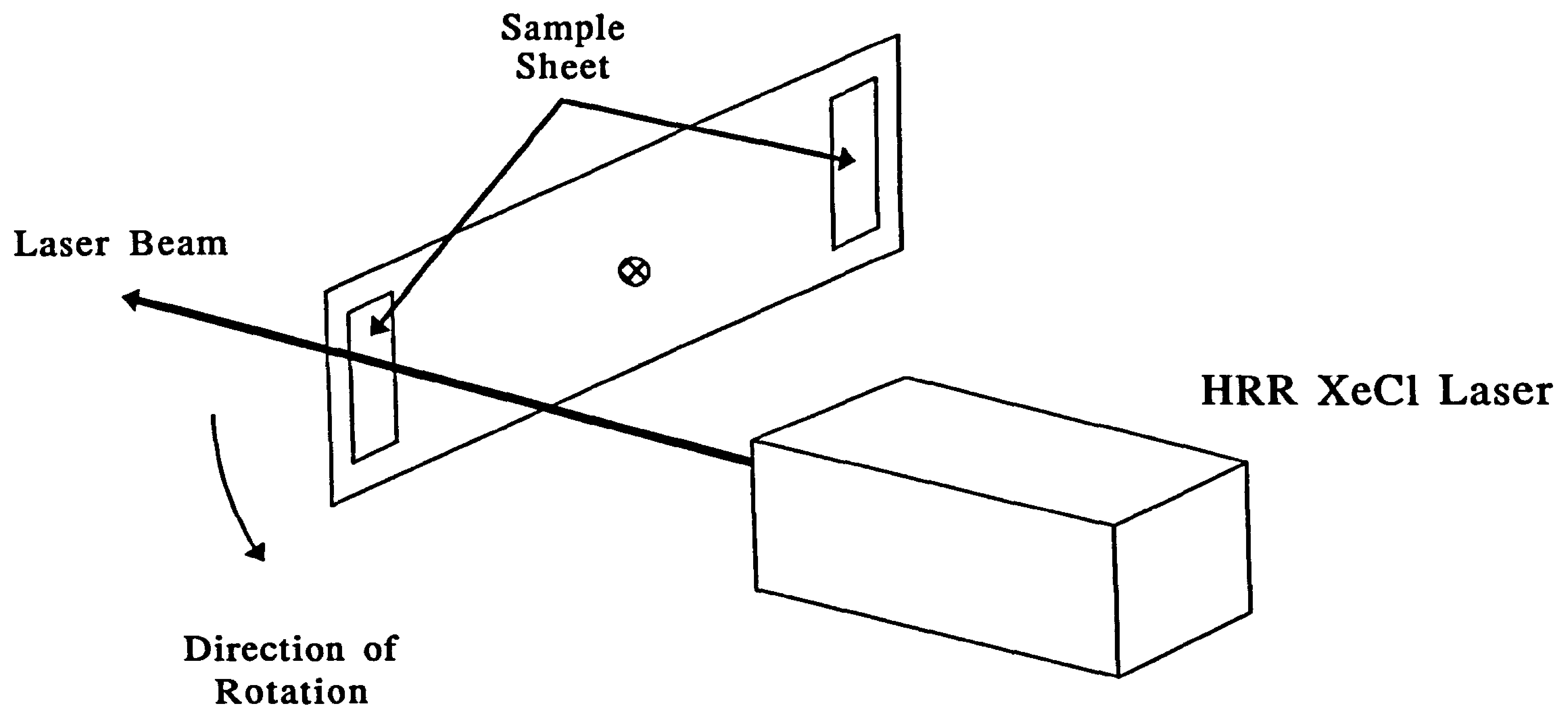

Fig. 5.3 Schematic diagram of the polymer sample translation arrangement

Fig. 5.4 Laser beam profile in the horizontal plane measured in the near field

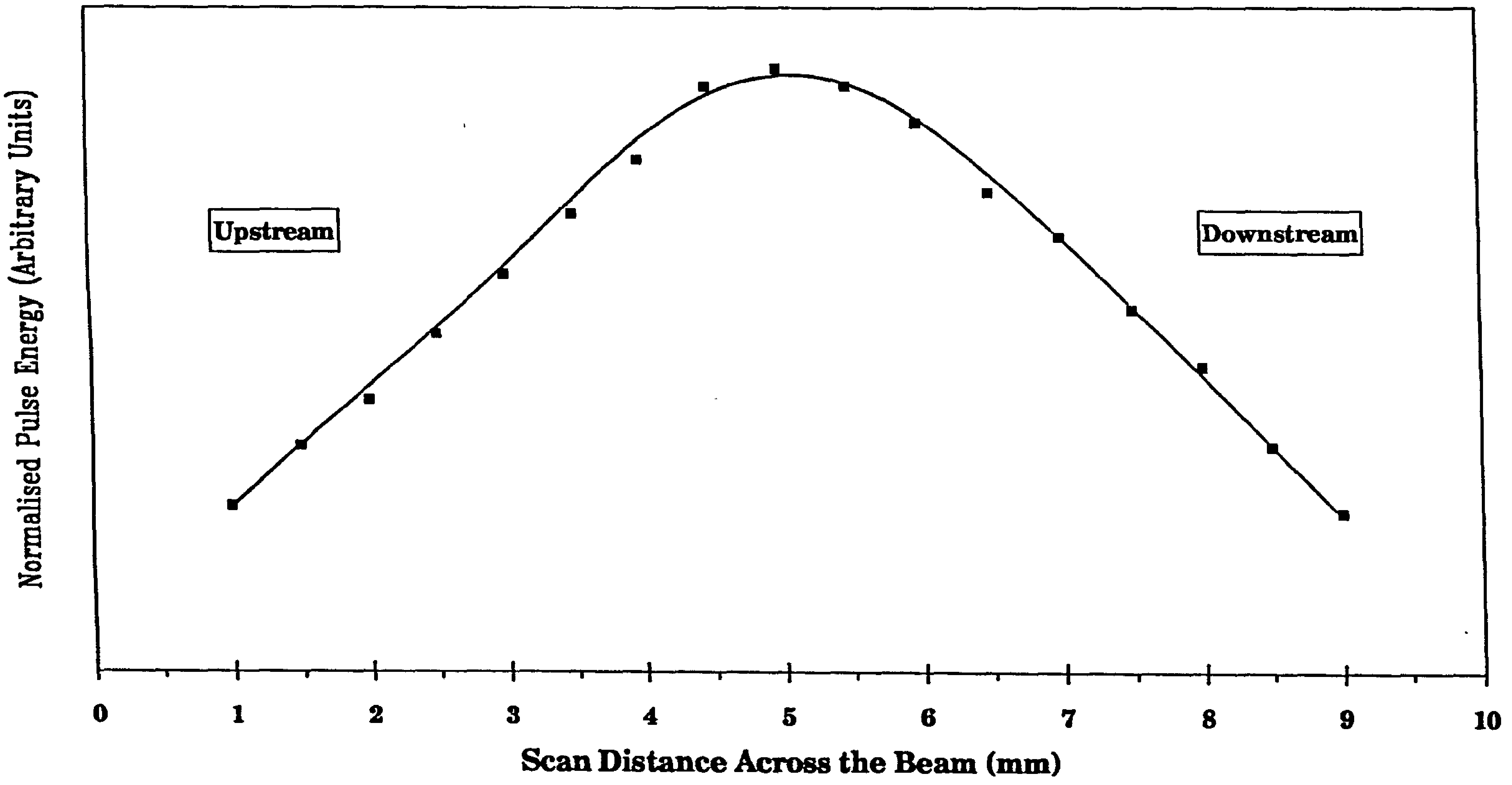

Fig. 5.5 Laser beam profile in the vertical plane measured in the near field

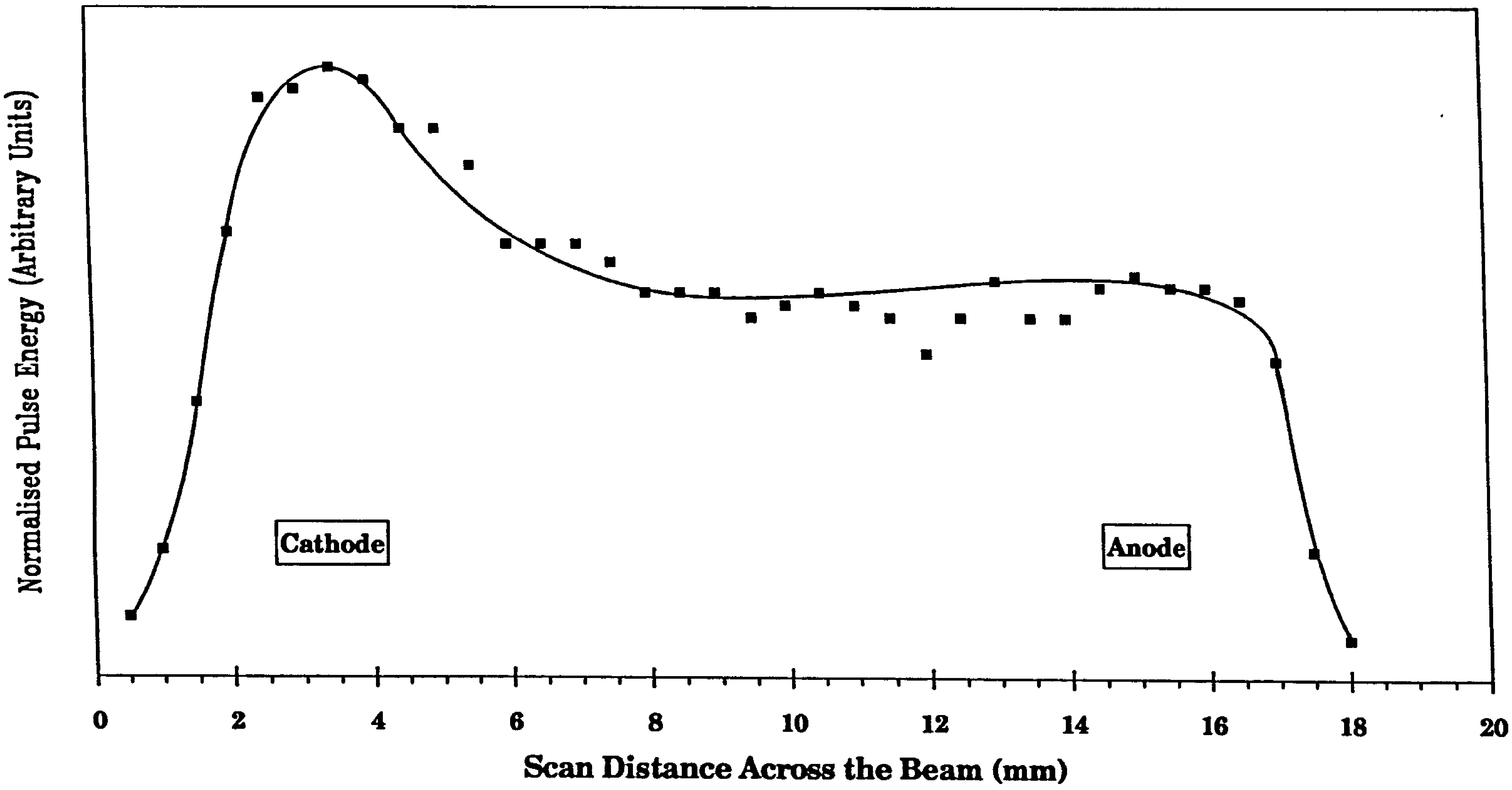

Fig. 5.6 Focussed laser beam profile for various slit widths with the baseline adjusted to show the change in profile

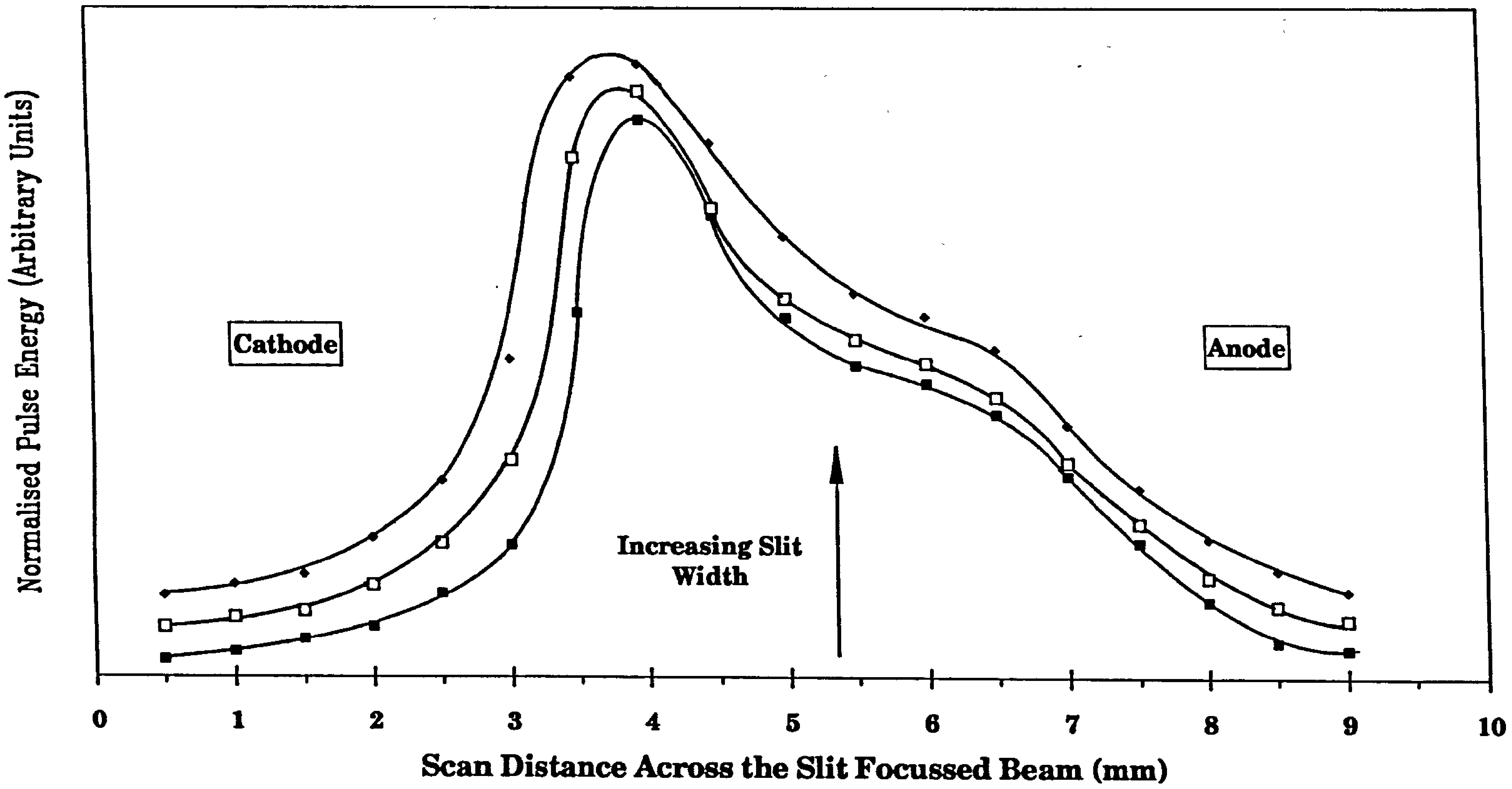

5.3 CUTTING RATES FOR PET FILMS

Results for the maximum cutting rate are shown in Fig. 5.7 for a 12µm thick PET film as a function of XeCl laser prf in the range 5 → 900 Hz, for a fixed pulsed energy of 12 ± 2 mJ/pulse. As can be seen, the linear dependence of the cut rate with prf, as predicted by Eq. (5.4), is obtained for $\nu < 80\,\mathrm{Hz}$ with $^{V_F}/_{P} = 5.5\,\mathrm{cm.s^{-1}.W^{-1}}$. The latter is somewhat lower than that given by Eq. (5.4) since the fluence exceeds the optimum value. For $\nu > 80\,\mathrm{Hz}$ the cut rate deviates from a linear scaling and rises substantially, but then continues to follow a linear dependence for $\nu > 200\,\mathrm{Hz}$.

Experiments were also carried out on stationary PET samples to determine the influence of prf on the number of pulses, n, required to penetrate the film. A fast uv photodiode located behind the film was used to measure the delay time for the onset of laser transmission through the strongly absorbing film (Fig. 5.8), thus signalling penetration, and n calculated from the transmission delay time and known prf. Results for a $d = 50\,\mu\mathrm{m}$ PET film irradiated using the line focus geometry are shown in Fig. 5.9 where the *average* etch depth per pulse defined as $^{d}/_{n}$ is given as a function of prf for two fluences. A significant increase in apparent average etch rate occurs for $\nu > 50\,\mathrm{Hz}$ in keeping with the enhanced cutting rate regime in Fig. 5.7. For $\nu < 50\,\mathrm{Hz}$ the etch rates defined in this way are broadly consistent with previous measurements [5.3] and thus are expected to represent a true ablative material removal rate per pulse, independent of the number of pulses [5.7]. However, at the higher prf's this may no longer be so, since additional factors may contribute to penetration as discussed below.

Fig. 5.7 Maximum cutting rate as a function of prf for a 12µm-thick PET film

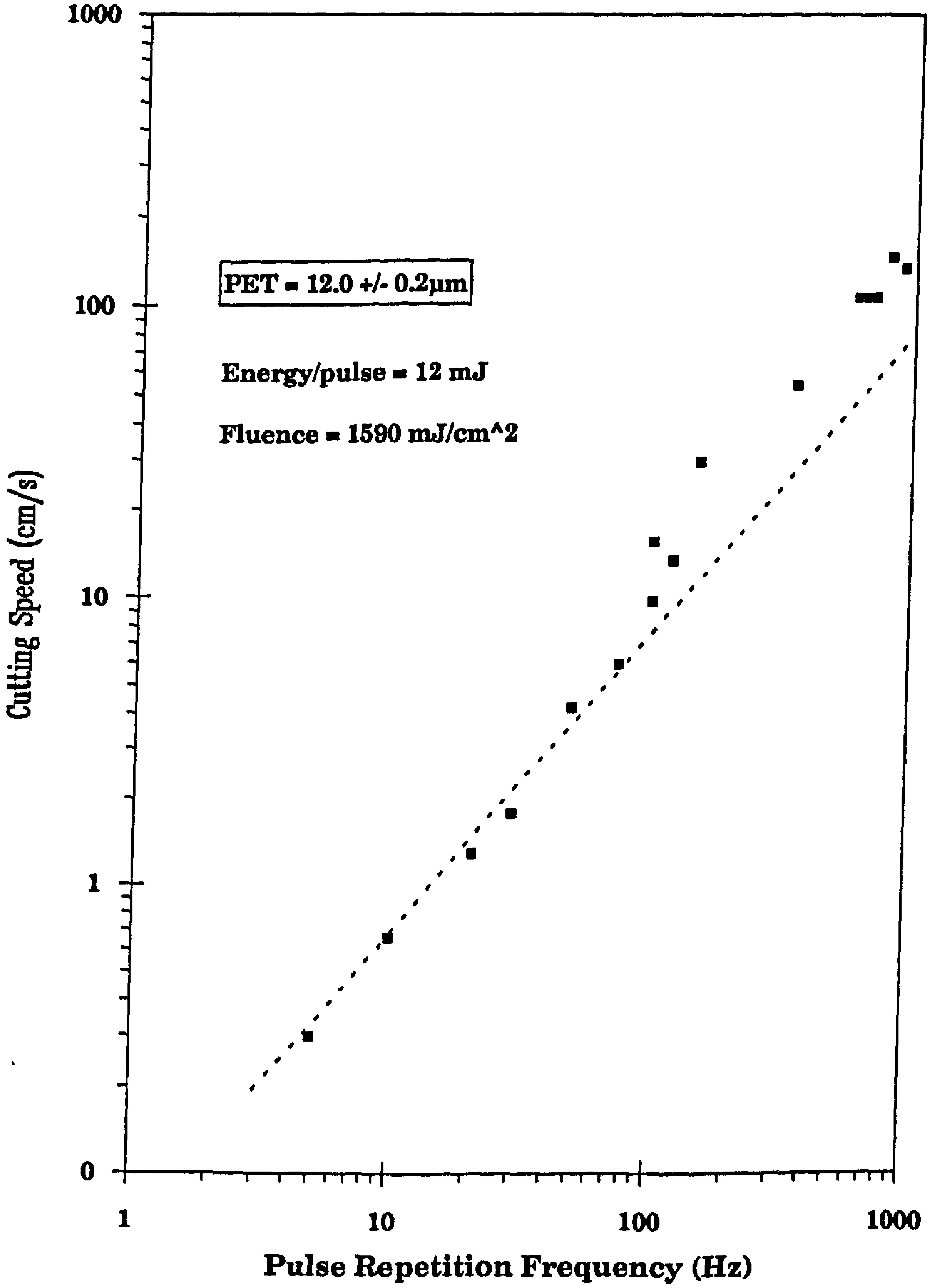

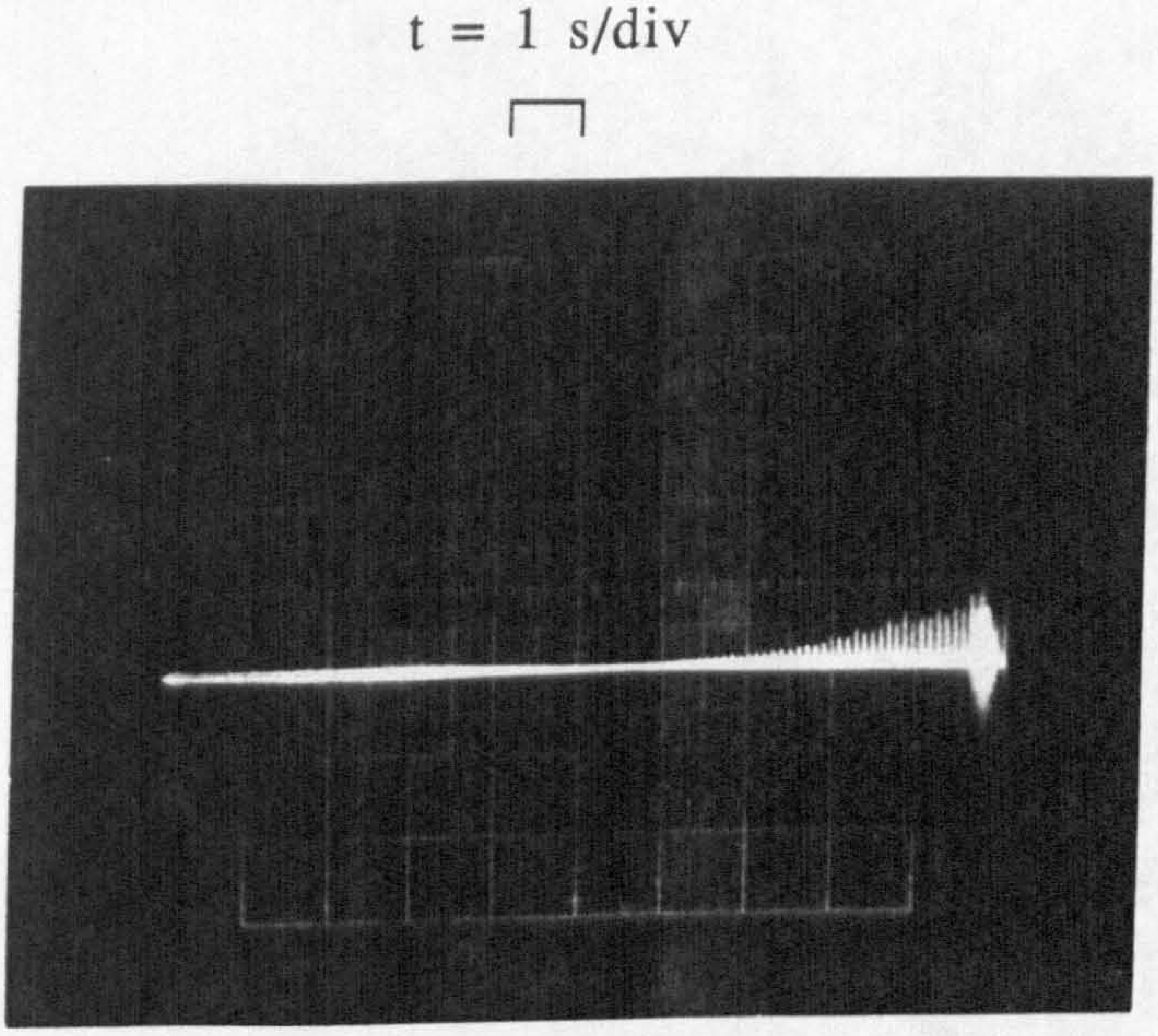

Fig. 5.8 Oscillograph showing the time taken for the laser beam to penetrate a 50μm PET film

Fig. 5.9 Etch depth per pulse for 50 µm PET as a function of PRF for different pulse energies, and hence different fluences.

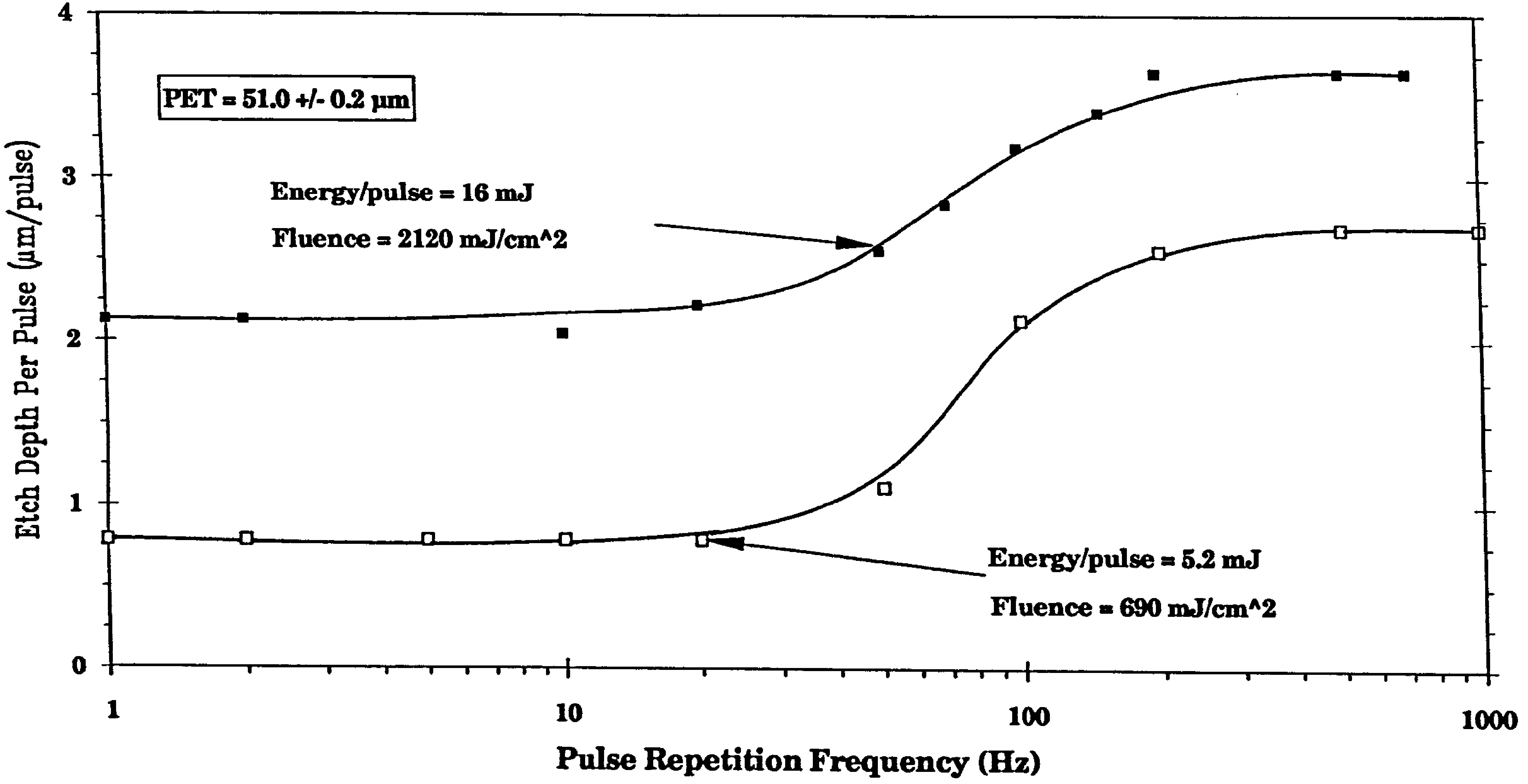

5.3.1 Analysis of the Effects of PRF on the Cutting of Thin PET Films

To obtain a semi-quantitative insight into this behaviour, we consider the heating and characteristic cooling time of the film when irradiated at $E > E_T$. Initially, that is to say during and soon after the laser pulse, absorbed laser energy *not* removed by ablation products, appears as heat in a surface layer $\sim k^{-1}$ deep. If $\omega \gg d$, subsequent thermal conduction will produce uniform heating through the film depth on a time scale for which lateral conduction can be neglected. Since ablation limits the maximum energy loading per unit area of the film to approximately E_T [5.8], the resulting temperature rise of the bulk film in the irradiated zone is given by

$$T_0 \sim \frac{E_T}{cd} \qquad \ldots [5.5]$$

where c is the volume specific heat, and changes in film mass due to ablation are neglected. For $d \sim 12\,\mu m$ the temperature rise is substantial ($T_0 \sim 82\,K$). If this uniformly heated strip of film is treated as a plane heat source, the subsequent temperature/time profile at the centre of the strip due to one-dimensional lateral conduction can be shown [5.9] to be

$$T(t) = T_0 \mathrm{erf}\left(\frac{\tau_c}{t}\right)^{\frac{1}{2}} \qquad \ldots [5.6]$$

where erf is the error function, $\tau_c = \omega^2/4D$ the characteristic cooling time for lateral conduction, and D the thermal diffusivity.

The above equation is assumed applicable for times $t > d^2/4D$, the characteristic time scale to obtain uniform heating through the film thickness. From Eq.(5.6) cumulative heating effects can be expected to become important for laser prf's $\nu > \tau_c^{-1}$, and with $2\omega = 140\,\mu m$ and $D = 10^{-3} cm^2 s^{-1}$ this gives 80 Hz. The increase in cutting efficiency and (static) etch rates for $\nu > 50 \rightarrow 100$ Hz (Figs. 5.7 & 5.9) would thus be consistent with the onset of cumulative heating. There are several ways in which this might modify the interaction:

(i) If, as suggested previously [5.3], ablation is due primarily to a thermal process requiring the attainment of a critical temperature for degradation, then substantial temperature rise due to preceeding pulses would reduce the threshold fluence for subsequent pulses. The etch rate, Eq.(5.1), would then increase with an increasing number of shots in a manner dictated by the temperature/time history of the bulk film. Because of the logarithmic dependence exhibited by Eq.(5.1), large changes in threshold would have to occur to explain the observed results (Fig. 5.9).

(ii) Estimates using Eq.(5.6) show that at high prf's, the partially crystalline PET film will be rapidly raised to its melting temperature [~265°C) throughout its thickness. Under these conditions the substantial surface pressure [5.6] generated by the ablation process may cause the film to be ruptured in the melted region thus causing premature penetration and enhancing the apparent etch-rate.

(iii) Since the PET film is biaxially orientated, heating above the melting temperature may lead to the irradiated zone "opening-up" under the action of internal stress relaxation (heat shrinkage). This possibility is suggested by the electron micrographs in Fig. 5.10, which show the slots cut in stationary 50 μm thick PET film at 10 and 700 Hz. These reveal that the cut width in the high prf case is considerably larger, and that a bead of thickened material develops around the edge of the cut. This would be consistent with local heating above the melt temperature and subsequent melt flow under the action of internal

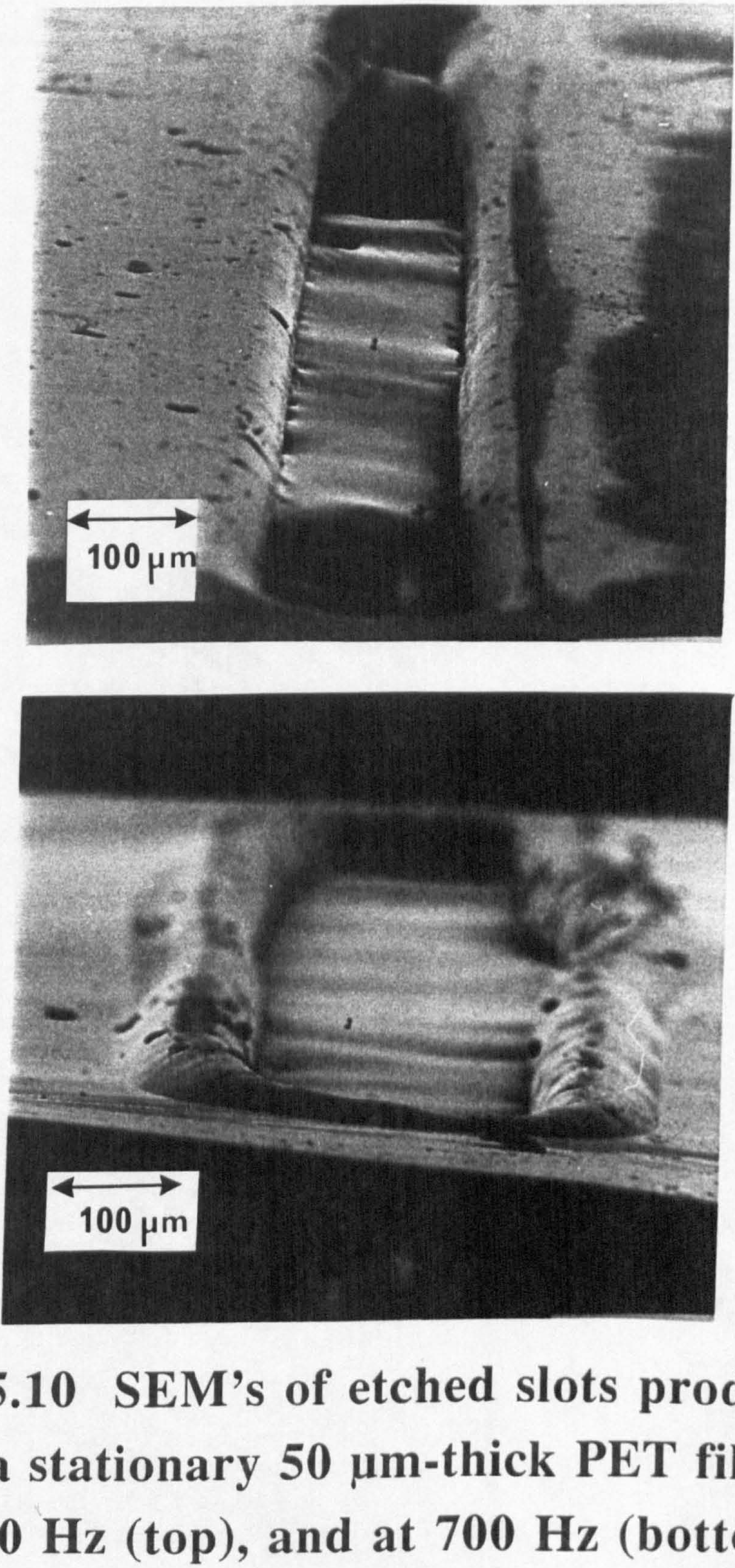

Fig. 5.10 SEM's of etched slots produced in a stationary 50 µm-thick PET film: at 10 Hz (top), and at 700 Hz (bottom)

stresses in the orientated film. A bead is also evident at the edge of film cut at high prf's (Fig. 5.11).

Although it appears that the results presented can be explained by mechanisms related to the onset of cumulative heating, the possibility that the abalation process is modified at high prf's by the build-up of long-lived [~10 ms) photochemically produced species [5.10] cannot at this stage be ruled out. Since such species would be confined to the beam absorption depth, that is to say a few times k^{-1}, a significant increase in the etch rate would follow only if such species produced a large decrease in E_T as discussed in (i) above. Further experiments are required to clarify these issues.

5.4 CONCLUSION

In conclusion, the work described shows that operation of the XeCl laser at high prf has advantages with regard to the cutting efficiency of PET film although under these conditions the interaction and quality of the cut may be more closely similar to that obtained by conventional laser processing. An extension of those studies to shorter excimer wavelengths, where photo processes are more efficient and the threshold fluence and associated thermal loading of the film [5.8] are considerably reduced, will be of interest both to help resolve the ablation mechanism at high prf and to minimise the thermal effects in the interaction zone.

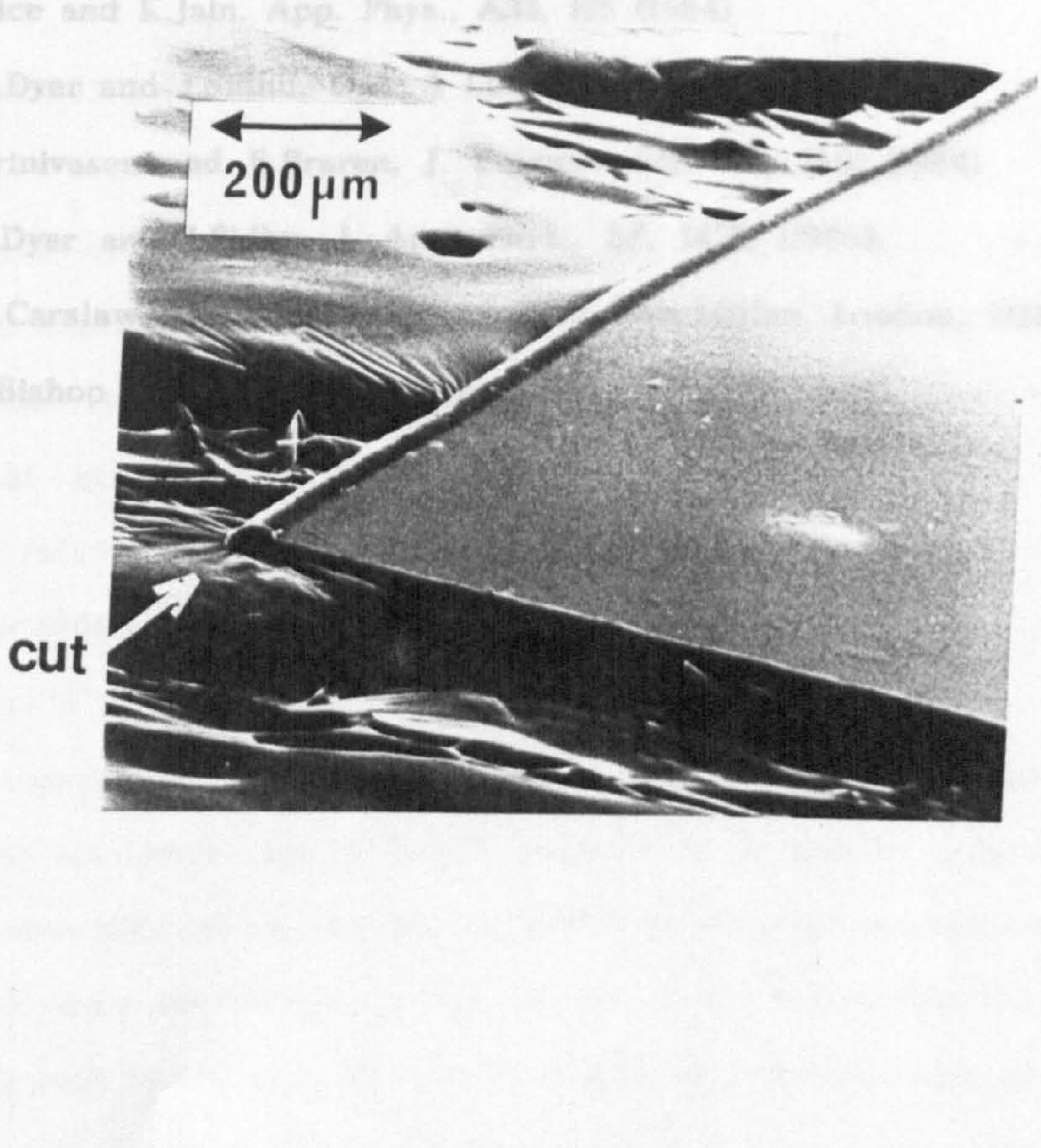

Fig. 5.11 SEM of the edge quality of a cut, produced by a 700 Hz XeCl laser, in a 12 µm thick PET film

REFERENCES

[5.1] R.Srinivasen and V.Mayne-Banton, Appl. Phys. Lett. **41**, 576 (1982)

[5.2] R.Srinivasen, J. Vac. Sci. Technol. **B14**, 923 (1983)

[5.3] J.E.Andrew, P.E.Dyer, D.Forster and P.H.Key, Appl. Phys. Lett. **43**, 717 (1983)

[5.4] T.F.Deutsch and M.W.Geis, J. App. Phys., **54**, 7201 (1983)

[5.5] S.Rice and K.Jain, App. Phys., **A33**, 195 (1984)

[5.6] P.E.Dyer and J.Sidhu, Opt. & Laser Engin., **6**, 67 (1985)

[5.7] R.Srinivasen and B.Braren, J. Polymer Sci., **22**, 2601 (1984)

[5.8] P.E.Dyer and J.Sidhu, J. App. Phys., **57**, 1420 (1985)

[5.9] H.S.Carslaw, The Conduction of Heat (MacMillan, London, 1921)

[5.10] G.J.Bishop & P.E.Dyer, App. Phys. Lett., **47**, 1229 (1985)

6. REVIEW

This review of the thesis has been divided into two sections. The first provides a discussion of the work carried out, reviewing how the design might be done differently today, with an update of the technology specific to high repetition rate excimer lasers. The second section provides the conclusion to the work carried out in this thesis.

6.1 DISCUSSION

Construction of excimer laser gas vessels, and associated gas handling equipment, requires careful selection of materials to ensure that minimal gas contamination will occur. Detailed studies of materials [6.1], and more recently of contaminant generation by these materials [6.2], play an important role in improving the gas lifetime of excimer lasers, and hence their acceptability in the industrial environment.

The laser vessel, used for the work reported in this thesis, was designed and constructed six years ago following the then available information on materials compatibility, and hence was constructed from stainless-steel. The laser vessel was constructed in segments (Fig. 2.5) to facilitate the inclusion of a longer path to the venturi flume if discharge problems occured with the flow not being laminar. However, this proved not to be necessary, at flow velocities of up to ~45m.s^{-1}, for laser operation at prf's of approximately 1kHz (i.e. acoustic noise in the system did not adversely affect the laser performance). Therefore, a more simplified contruction method could possibly be used, for example, a box structure using internal sheet metal to provide the ducting. Difficulties arising from this type of approach, would relate to the wall thickness, and its ability to withstand, and pass, pressure certification tests. The use of strengthening members, however, could result in thinner walls being acceptable. A large diameter cylinder is another possibility, since the cylinder wall could provide the outer side of the ductwork. The use of aluminium would provide a weight advantage if welding difficulties, associated with this material, can be overcome. Aluminium appears to be gas compatible since both of the major manufacturers of commercial excimer lasers use aluminium vessels.

The duct design proved to be efficient, with careful design of the bend radii [6.3] resulting in equal turning vanes not being required, thereby simplifying the construction. The fan section, operating at up to 8000rpm, proved to be reliable once difficulties encountered with the rotary seal had been resolved. Problems did arise with the flow of gas around the wind tunnel, which produced a higher flow velocity at the outside edge. The use of the venturi flume helped minimise the flow gradient across the duct, producing a flow velocity through the electrodes of up to $\sim 45 m.s^{-1}$, and thereby improving the performance of the laser. The inital use of PVC for the venturi flume and in the electrode gantry design proved to have a detrimental effect on the gas lifetime, and was later redesigned using PTFE, the best of the polymer materials available. The other material of choice for use inside excimer vessels is high density alumina (ceramic), which was used in the construction of the corona preionisation bar.

Discharge perturbation studies, using the experimental layout shown in Fig. 4.3, have shown that pressure waves generated by the discharge travel at approximately the speed of sound of the buffer gas. Hence, are essentially acoustic waves rather than shock waves. In the case of helium buffered gas mixtures this was $\sim 1000 m.s^{-1}$, and for neon $\sim 475 m.s^{-1}$. Using the optical detection technique, close agreement was also achieved between the maximum attainable laser prf, and the time taken for the discharge perturbation to cease at a point just beyond the upstream contact surface. Such measurements implied that a clearing ratio of approximately two was required to maintain a stable discharge at prf's <1600Hz.

In any high repetition rate device the high voltage switching component is critical and must be selected with care. The switch chosen for this work was a thyratron, since spark-gaps were not capable of switching reliably at the high repetition rates required (~kHz). Experiments to determine the relative efficiency of the EEV CX-1573 thyratron, used in this thesis, compared to that of a spark-gap, showed that switching losses in both devices account for approximately 25% of the power being switched. The EEV CX-1573 thyratron was a tetrode device, and lasted approximately 25×10^6 pulses in the operating configuration employed.

In the circuit design (Fig. 2.21) and layout, it was necessary to reduce the inductance to a few hundred nano-henries or better, to maximise the output laser pulse energy. Fig. 2.22 shows the layout of the thyratron, and the main discharge capacitor, relative to the electrode gantry, indicating the size of the inductance loop in the finalised design. This design provided a fast ground return, and produced an estimated inductance of ~220nH. Further study of the detailed circuit and discharge parameters would be required for this device in order to minimise significant current ringing which is detrimental to thyratron lifetime. The use of ferrites [6.4] to provide magnetic assistance to the circuit could help minimise current reversal.

Thyratrons are still the switch of choice among the leading excimer laser manufacturers today. In the past, thyratrons such as the CX-1573 had the ability to switch excimer discharge circuits, but, with the high rates of rise of current, the lifetimes were short. This led some manufacturers to use magnetic pulse compression techniques to reduce the rate of rise of current to a level more readily acceptable to the thyratron. Recent work by the thyratron manufacturers, and in particular EEV, has resulted in thyratron lifetimes exceeding 10^{10} pulses on a dummy excimer load. In EEV's case this is achieved by inclusion of hollow anode structures and dispenser cathodes, which extend the lifetime of these components. Other manufacturers, such as EG&G and ITT have in addition increased the size of the cathodes to increase electrode lifetime.

There is also an increasing trend amongst excimer laser developers to move away from thyratron technology to solid state switching devices and systems. This has been made possible by the major leaps in the power handling capabilities of such devices.

The electrode gantry went through several iterations where the electrodes, capacitors, and venturi flume were changed. The original nickel "Chang" profiled electrodes used in the electrode gantry design had problems with heavy discharging, or arcing, at the ends. This was due to the end profiles being semi-circular and not a "Chang" profile, which would be very large given the length of the electrodes. The replacement profiled electrodes in brass worked well because the ends of the electrodes could be hand profiled into an eliptical shape more suitable to the excimer discharge properties. This was not done to the "Chang" profiled electrodes since they were ideal for CO_2 laser operation, and could be used in other systems in the future.

The original Murata internal preionisation capacitors proved to be rugged in construction, but in an effort to increase the number of preionisation sparks it was decided to try capacitors with no epoxy coating. (These custom capacitors were supplied by Morgan-Matroc - formerly Steatite & Porcelain.) Twin preionisation pins per capacitor had been tried with some success, but it was felt that single pins per capacitor provided a more stable preionisation source.

Several preionisation schemes were evaluated in these studies: two used discrete sparks to provide the uv preionisation; one used a corona uv preionisation electrode; and the last, used an axial x-ray preionisation source developed by Raouf [6.5].

The resistively ballasted array, that formed the basis of one of the spark preionisation schemes, did not perform well. Any of the combinations of up- or down-stream arrays and capacitor coupling, outlined in Table 3.2, produced, within the bounds of error, the same output power of 0.65W at 50 Hz. A maximum XeCl ouput power of 5.0W at 450Hz was achieved with both arrays present. The poor performance of this scheme was attributed to the time delay between the first and last spark in firing.

The corona preionisation scheme is very attractive since it has a number of attributes beneficial to excimer discharges. With this source placed behind a suitable mesh, there is the ability to selectively preionise a well defined width of the discharge, ensuring a good uniform glow. Since it is not a spark discharge the current is low, thereby minimising the rate of material removal. Hence, contaminant build-up in the laser vessel is reduced. Unfortunately, although very good discharge quality was achieved, an output power of only 4.6W at 750 Hz was produced.

The most succesful, and most conventional, of the preionisation schemes reported was the capacitively coupled technique. Careful consideration had to be given to the placement of the preionisation sparks relative to the discharge, in order to balance the uniformity of preionisation with the optimum pulse energy. The optimum position was found to be 3cm from the centre of the electrode profile and mid-position between the electrodes. This final geometry used a venturi flume and side walls constructed from PTFE. A maximum power of 22W at 700Hz and 16W at 1000Hz using a 3 HCl : 30 Xe : 3067 Ne (mbar) gas mixture was achieved with this design.

In any future development of a high prf excimer laser, it would be necessary to increase the gain length of the discharge, as well as the inter-electrode spacing. Experiments have shown that increasing the electrode spacing has a marked effect on the pulse energy of the device. Also, the use of high reflectivity output couplers with this laser indicates that there is insufficient gain. Therefore, increasing the discharge (gain) length would be beneficial.

6.2 CONCLUSION

The laser vessel described in this thesis uses a closed-cycle gas flow loop constructed from stainless-steel, for corrosive gas compatibility, has a total volume of 6 litres, and a maximum working pressure of 4 atmospheres. A magnetically coupled tangential fan provides gas flow and, with appropriate flow shaping at the $0.8 \times 1.5 \times 22.0\,\text{cm}^3$ discharge region, the maximum flow velocity attained was $\sim 45\,\text{m.s}^{-1}$ (as measured with a small pitot-static tube). Optical probing of the acoustic and thermal perturbations following the discharges in the system, indicate that the gas clearing ratio is sufficient for a maximum prf of ~1800Hz.

Electrical excitation of the discharge was by a conventional, capacitively coupled, uv spark preionisation arrangement, which provided rapid energy deposition into the discharge. This scheme was adopted following tests, at high prf, on a number of uv preionisation arrangements, including corona and resistively ballasted sparks arrays. The power for the main circuit was derived from a commercial resonant inverter supply, capable of producing $3\,kJ.s^{-1}$ at up to 40kV. A grounded cathode thyratron was used as the switch, providing reliable trouble free operation without the use of magnetic assist or switching. In operation, the laser has proven to be capable of producing 22W at 700Hz with a 10nF charging capacitor, the limiting factor being the available power supply. At 1kHz, output powers of 16W have been attained.

In addition to the uv preionisation schemes investigated for high prf operation, the operation of an axial x-ray preionisation source [6.6] at repetition rates lower than 50Hz was also tried as a means to preionise the discharge. Although a significant axial intensity non-uniformity was present, due to the high divergence from the near point source, a 50% improvement in laser energy was achieved compared to that of the uv preionisation scheme. The development of compact, high prf, x-ray preionisation sources for use in excimer lasers is of particular interest because of the ability to uniformly preionise the discharge region. This would minimise discharge instabilites, and also reduce the amount of gas contaminating debris currently being formed by preionisation sparks, and the discharge itself.

The use of excimer lasers to process polymer films by ablative etching [6.7 → 6.9] has been studied in detail, particularly with a view to exploiting this technique for high resolution patterning of films for microcircuit applications [6.8 & 6.10]. Experiments have been carried out using this laser to cut polyethylene teraphthalate (PET) films at rates up to $1.3\,m.s^{-1}$ [6.11]. The 8 x 15 mm output beam, from the laser, was brought to a 5.4 mm long line focus of full width 140µm, with the PET being transported through the focal plane using a variable speed rotating wheel of 40cm or 100cm diameter. A constant laser energy of 12mJ could be maintained up to prf's of 1kHz producing a fluence of $1600\,mJ.cm^{-2}$ at the focal plane. Results for the maximum cutting rate of 12 and 50µm thick PET film, as a function of XeCl laser prf in the range 5 to 900Hz, has shown that the effective etch rate, and corresponding cutting efficiency, is markedly dependent on prf. It is thought that this dependence is due to cummulative heating of the substrate, when the cooling time of the interaction zone is long compared to the interpulse period. This behaviour has not been observed in previous studies since the laser prf's have generally been restricted to < 10Hz.

High repetition rate devices, operating at moderate power levels, are just becoming commercially available to researchers. Therefore opportunities exist for exploiting this type of device for materials interaction programs (e.g. biological, polymers, etc.).

REFERENCES

[6.1] R.TENNANT, LA-UR-81:559, Los Alamos National Laboratory, NM, (1981)
R.TENNANT, Laser Focus, 17, 65 (1981)

[6.2] J.REID, G.BISHOP, S.HASTIE, B.NORRIS, R.WEEKS, E.WILLIAMS & T.ZNOTINS, SPIE O-E/LASE '89, Los Amgeles (1989)

[6.3] GENERAL ELECTRIC CO., "Fluid Flow Data Book" (1977)

[6.4] R.W.WEEKS & T.J.McKEE, 6th IEEE Pulsed Power Conf., Arlington, Virginia (1987)

[6.5] D.N.RAOUF, "U.V. and X-ray Preionised High-Pressure CO_2 Lasers and Line Narrowing for Spectroscopic Sudies", Ph.D. Thesis, Univ. of Hull (1989)

[6.6] G.J.BISHOP, P.E.DYER, D.N.RAOUF, & B.L.TAIT
Appl. Phys. Lett., **47**, 1045 (1985)

[6.7] R.SRINIVASEN & V.MAYNE-BANTON, Appl. Phys. Lett., **41**, 576 (1982)

[6.8] R.SRINIVASEN, J. Vac. Sci. Tech. B1, **4**, 923 (1983)

[6.9] J.E.ANDREW, P.E.DYER, D.FORSTER & P.H.KEY,
Appl. Phys. Lett., **43**, 717, (1983)

[6.10] T.F.DEUTSCH & M.W.GEIS, J. Appl. Phys., **54**, 7201 (1983)

[6.11] G.J.BISHOP & P.E.DYER, Appl. Phys. Lett., **47**, 1229 (1985)

Appendix - 1

CALCULATION OF THE PRESSURE DROP IN THE RECIRCULATION LOOP

Let us assume that we can use the physical characteristics of the buffer gas (helium or neon), that is to say the other gases in the mix will have little effect. The properties of these gases are given in Table A1.1.

The Reynolds number, R, for the system can be calculated as follows:

$$R = \frac{\rho \, v \, D}{\Gamma}$$

where ρ is the gas density, v the gas flow velocity, $D^{\dagger}$ the pipe equivalent diameter, and Γ the gas viscosity. (N.B. A gas flow velocity of $25\,m.s^{-1}$, sufficient to achieve kHz operation, was used for this calculation.)

(a) Pressure drop in a straight duct.

$$\Delta p = 4 \; f \frac{L}{D} \frac{\rho v^2}{2g} \qquad \text{[A1.1, Section G402.1, p4]}$$

where L is the length of duct, g is the acceleration due to gravity ($g = 9.807\,m.s^{-1}$), and $f = {}^{0.04}/_{R^{0.16}}$, the average friction factor for $R < 10^5$.

[†] D for a rectangular duct of sides a and b is given by,

$$D = \frac{2ab}{(a+b)}$$

for $a = 0.036\,m$, $b = 0.260\,m$ the rectangular dimensions, $D = 0.063\,m$.

Buffer Gas Properties		
	Helium	**Neon**
Density @ STP ($kg.m^{-3}$)	0.178	0.900
Density @ 3 atmos. ($kg.m^{-3}$)	0.534	2.700
Viscosity, Γ ($kg.m^{-1}.s^{-1}$)	19.4×10^{-6}	31.1×10^{-6}

Table A1.1

(b) Pressure drop in 90° bends of rectangular cross-section.

$$\Delta p = C_{B90}\, C_a \frac{\rho v^2}{2g}$$ [A1.1, Section G403.3, p4]

where $C_{B90} = 0.15$, the gross bend factor for $r/a = 1.36$, and $C_a = 0.75$, the loss ratio for $b/a = 7.2$.

(c) Pressure drop in an expanding duct.

$$\Delta p = \eta_p \left(1 - \left(\frac{A_1}{A_2}\right)^2\right) \frac{\rho v^2}{2g}$$ [A1.1, Section G406, p12]

where $\eta_p = \dfrac{C_{pr}}{\left(1 - \left(\frac{A_1}{A_2}\right)^2\right)}$, the nominal pressure efficiency [Section G406, p3],

A_1 is the cross-sectional area at the entrance of the duct ($A_1 = 9.36 \times 10^{-3}$m), A_2 is the cross-sectional area at the exit of the duct ($A_2 = 6.63 \times 10^{-2}$m), and $C_{pr} \sim 0.25$, the pressure recovery coeffcient for $A_2/A_1 = 7.08$.

(d) Pressure drop in a contracting duct.

The pressure loss in contractions are quite low [A.1.2] and can be assumed to be negligible in comparison to other pressure losses.

The total pressure drop for the various ducting components (Fig. 2.4) is given in Table-A1.2 for both buffer gases, helium and neon.

	Helium	**Neon**
Reynolds Number, R	43,353	137,177
Average Friction Factor, f	7.25×10^{-3}	6.03×10^{-3}

Duct Sections	**Pressure Drop (Pa or N.m^{-2})**	
1. Straight (4 cm)	0.313	1.318
2. Straight (4 cm)	0.313	1.318
3. 90° bend	1.914	9.679
4. Straight (4 cm)	0.313	1.318
5. Straight (44 cm)	3.446	14.493
6. Straight (4 cm)	0.313	1.318
7. 90° bend	1.914	9.679
8. Straight (4 cm)	0.313	1.318
9. Straight (4 cm)	0.313	1.318
10. 90° bend	1.914	9.679
11. Straight (4 cm)	0.313	1.318
12. Straight (4 cm)	0.313	1.318
13. Expansion (no venturi)	4.253	21.502
14. Contraction	---	---
Total Pressure Drop (N.m^{-2})	**15.883**	**75.312**

Table A1.2

REFERENCES

[A1.1] GENERAL ELECTRIC CO., "Fluid Flow Data Book" (1977)

[A1.2] W.C.OSBOURNE & C.G.TURNER (Eds.),
"Woods Practical Guide to Fan Engineering", Woods of Colchester (1952)

Appendix - 2

From the flow pressure measurements made with the pitot-static tube and micro-manometer, the following equation was used to derive the gas velocity.

$$\Delta p = \frac{1}{2}\rho v^2$$

where Δp is the gas pressure change monitored on the micro-manometer, ρ is the effective gas density, and v is the gas flow velocity.

Rearranging gives:

$$v = \sqrt{\frac{2\Delta p}{\rho}}$$

Since the pressure measurements were in torr, a conversion factor was used to convert these measurements into SI units, i.e.

$$v\ (\mathrm{m.s^{-1}}) = \sqrt{\left(\frac{2 \times 10^5\ (\mathrm{Pascals/atmos.})}{760\ (\mathrm{torr/atmos.})}\right)} \times \sqrt{\left(\frac{\Delta p\ (\mathrm{torr})}{\rho (\mathrm{kg.m^{-3}})}\right)}$$

Appendix - 3

CIRCUIT INDUCTANCE CALCULATION

The following calculations are based on a set of guidelines that can be found in [A3.1].

Inductance of Loop 1 (see Fig. 2.22)

$$\text{Area, } S_1 = a_1 \times b_1$$
$$= 0.08 \times 0.23$$
$$\underline{S_1 = 1.84 \times 10^{-2}\,\mathrm{m}^2}$$

$$(\pi r_{01}{}^2)_{\mathrm{equiv.}} = S_1 = 1.84 \times 10^{-2}\,\mathrm{m}^2$$
$$\underline{r_{01} = 0.077\,\mathrm{m}}$$

For ${}^{b_1}/{a_1} = 2.88$ and ${}^{h}/{2a_1} = 0.625$ then $K_{L1} \approx 0.85$, from [A3.1, p317].

$$K_{R1} \approx K_{L1}\left(\frac{h}{2r_{01}}\right) \approx 0.55$$

Now,

$$L_1 \approx \mu_0 \frac{S_1}{h} K_{R1}$$
$$\underline{L_1 \approx 127\,\mathrm{nH}}$$

Inductance of Loop 2

$$\text{Area, } S_2 = a_2 \times b_2$$
$$= 0.10 \times 0.17$$
$$\underline{S_2 = 1.70 \times 10^{-2}\,\mathrm{m}^2}$$

$$(\pi r_{02}^{2})_{\mathrm{equiv.}} = S_2 = 1.70 \times 10^{-2}\,\mathrm{m}^2$$

$$\underline{r_{02} = 0.074\,\mathrm{m}}$$

For $b_2/a_2 = 1.70$ and $h/2a_2 = 0.588$ then $K_{L2} \approx 0.65$, from [A3.1, p317].

$$K_{R2} \approx K_{L2}\left(\frac{h}{2r_{02}}\right) \approx 0.55$$

Now,

$$L_2 \approx \mu_0 \frac{S_2}{h} K_{R2}$$

$$\underline{\underline{L_2 \approx 94\,\mathrm{nH}}}$$

Therefore,

$$\underline{\underline{L_{total} = L_1 + L_2 = 221\,\mathrm{nH}}}$$

REFERENCE

[A3.1] KNOEPFEL H., "Pulsed High Magnetic Fields", North Holland (1970)

PUBLICATIONS AND PAPERS ARISING FROM THIS WORK

[1] "Axial x-ray preionised XeCl laser and direct comparison with UV preionisation": G.J.BISHOP, P.E.DYER, D.N.RAOUF & B.L.TAIT, Appl. Phys. Lett., **47**, 1045 (1985)

[2] "Polymer film cutting and ablative etching using a 1-kHz XeCl laser": G.J.BISHOP & P.E.DYER, Appl. Phys. Lett., **47**, 1229 (1985)

[3] "Axial x-ray preionisation of high pressure gas lasers":
G.J.BISHOP, P.E.DYER, D.N.RAOUF & B.L.TAIT,
CLEO '85, Baltimore (1985)

[4] "Performance and characterisation of a high pulse-repetition-frequency (>1kHz) uv-preionised XeCl* laser":
G.J.BISHOP, P.E.DYER, P.MONK, D.N.RAOUF & B.L.TAIT,
Seventh National Quantum Electronics Conference, Malvern (1985)